DESIGNING ADDED FUNCTIONS IN ENGINEERED CEMENTITIOUS COMPOSITES

by

En-Hua Yang

A dissertation submitted in partial fulfillment
of the requirements for the degree of
Doctor of Philosophy
(Civil Engineering)
in The University of Michigan
2008

Doctoral Committee:

Professor Victor C. Li, Chair
Professor Richard E. Robertson
Associate Professor Sherif El-Tawil
Assistant Professor Jerome P. Lynch

To my parents and my wife,

for their greatest love and support.

Acknowledgements

This dissertation has been completed under the guidance of my advisor, Professor Victor C. Li. Without his support, I could have never completed this work. I am deeply indebted to him for his guidence, inspiration, and encouragement in the past five years.

I would like to thank my dissertation committee members, Professors Richard E. Robertson, Associate Professor Sherif El-Tawil, and Assistant Professor Jerome P. Lynch for their valuable comments and encouragement.

To Professor Anthony M. Waas at the Department of Aerospace Engineering, for letting me use the drop weight impact machine, Mr. Amit G Salvi at the Department of Aerospace Engineering, for providing guidance on using the drop weight impact tester, and Professor David Yankelevsky at Technion – Israel Institute of Technology, for collaborating on the impact research.

I must acknowledge the National Science Foundation for funding of Materials Use: Science, Engineering, and Society (MUSES) Biocomplexity Grants CMS-0223971, CMS-0329416, and the Michigan Department of Transportation, particularly Mr. Roger Till, both supported much of my research.

I would like to thank my colleagues at the Advanced Civil Engineering Materials Research Laboratory, Dr. Shuxin Wang and Professor Yingzi Yang for their great help and lessons on how to be not only a good researcher, but a good friend. I would also like to thank Professor Yun Y. Kim, Dr. Martin Weimann, Dr. Mike D. Lepech, Dr. Shunzhi Qian, Professor Mustafa Şahmaran, Professor Andrea Spagnoli, Ms. Mo Li, Ms. Estela

Garces, Mr. Jian Zhou, Mr. Matthew Fadden, and Mr. Ravi Ranade for their friendship and assistance during my studies.

I am grateful to Ms. Debbie Hemmeter, Ms. Janet Lineer, Ms. Reta Teachout, Ms. Linda Fink, Ms. Kimberly Bonner, Ms. Jill Miller and Ms. Patricia Mackmiller for assistance in administrative matters, to Mr. Merrick Burch, Mr. Robert Fischer, Mr. Jan Pantolin, and Mr. Robert Spence for technical support.

Finally, I could never have attempted any of this without the love and support of my parents Sheng-Wei and Yu-Feng, my wife Ching-I, and my son Chi-Ann. I also owe a great deal of gratitude to my aunt Sheng-Li, uncle Sheng-Zhen, and my mother-in-law Yu-Tao, for their support and help over the past few years.

Table of Contents

List of Tables

List of Figures

CHAPTER 1

INTRODUCTION

It is known that structural performance is greatly influenced by the materials used. Within the civil engineering community, the performance-based design concept for structures is getting more and more attention and gradually replacing the conventional prescriptive approach [1]. The performance-based design concept allows for greater flexibility, e.g., in dimensioning and reinforcement detailing by structural engineers. It also allows for a larger degree of freedom in construction material choice. Therefore, high performance civil engineering materials with added functions beyond their basic properties are highly desirable (**Fig. 1.1**). Unfortunately, adding new attributes into material empirically sometimes causes loss of basic properties. The often existed trade-off between new performance requirements and basic material properties posts the challenge of this thesis research.

A good example which shows this trade-off is lightweight concrete. Concrete material with low weight reduces gravity load and seismic internal mass, resulting in

potentially reduced member sizes and foundation forces if the basic material properties can be retained. However, the strength and toughness of lightweight concrete is often greatly reduced because the lightweight aggregate used is usually weaker than cement matrix and provides little resistance to crack propagation.

Due to the low cost and wide availability of raw ingredients along with other advantages (e.g. the ability to be cast and satisfied compressive strength), concrete has been the predominant construction material during the last century. In fact, concrete is the most used man-made material on the planet [2]. As of 2005, about six billion cubic meters of concrete are made each year, which equals one cubic meter for every person on Earth. Concrete is a composite material in which the aggregates (e.g. gravel and sand) are embedded in a binding medium (e.g. cement or binder) that fills the space between the aggregate particles and glues them together.

One major weakness of concrete is the brittle facture behavior in tension, with low tensile strength and ductility. This brittleness has been recognized as a bottleneck hindering structural performances in safety, durability and sustainability. Under extreme loading such as bomb blast and flying object impact, reinforced concrete (R/C) structure can be vulnerable. With limited structural ductility, R/C structures can only absorb a small amount of energy imposed by dynamic loads and catastrophic failure may happen. The lack of structural ductility is due to the brittle nature of concrete in tension which may lead to loss of structural integrity. Many infrastructure deterioration problems and failures can be traced back to the cracking and brittle nature of concrete. For instance, the early formation of shrinkage cracks in R/C structures provide pathways for the penetration of aggressive ions to cause concrete deterioration. Chlorides, oxygen, and

carbonation agents can migrate through cracks and ultimately lead to corrosion of reinforcement. The corrosion of steel reinforcement exposed to water and air penetrated via cracks where the expanding pressure generated by formation of rust leads to concrete spalling and disintegration of R/C structure [3]. Limited durability implies the need for repeated repairs that consumes energy and raw materials and generates emissions of green house gases. The raw ingredients that goes into the making of concrete, in particular, cement is both highly energy intensive and is responsible for about 5% of the anthropogenic CO_2. This trend is decidedly unsustainable. Tensile ductility and tight crack width control are therefore two properties that could contribute to structural safety, durability and sustainability.

The most effective means of imparting ductility into concrete is by means of fiber reinforcement. While the fracture toughness of concrete is significantly improved by fiber reinforcement, most fiber-reinforced concrete (FRC hereafter) still shows quasi-brittle post-peak tension-softening behavior under tensile load where the load decreases with the increase of crack opening. The tensile strain capacity therefore remains low, about the same as that of normal concrete, i.e. about 0.01%.

1.1 High Performance Fiber Reinforced Cementitious Composites

Significant efforts have been made to convert this quasi-brittle behavior of FRC to ductile strain-hardening behavior resembling ductile metal. This new class of cement based material, high performance fiber reinforced cementitious composites (HPFRCC), was first described by Naaman and Reinhardt [4]. HPFRCC is distinguished from an ordinary

FRC by its unique macroscopic pseudo-strain-hardening behavior after first cracking when it is loaded under uniaxial tension.

In most instances, the high performance is achieved through increasing the volume fraction of fiber as much as possible. As the fiber content exceeds a certain value, typically 4-10% depending on fiber type and matrix and interfacial properties, the conventional FRC may exhibit moderate strain-hardening behavior. For example, Cheyrezy et al. [5] developed a high performance concrete comprising organic fibers dispersed in a cement matrix, wherein the matrix is highly compacted by using very hard, small diameter fillers to achieve high strength. Moderate strain-hardening behavior is achieved with strain capacity less than 0.5%, when 4% polyvinyl alcohol fiber by volume fraction is added.

High volume fraction of fiber; however, results in considerable processing problems. Fiber dispersion becomes difficult because of high viscosity of the mix due to the presence of high surface area of the fibers and the mechanical interaction between the fibers, along with the difficulties in handling and placing. Various processing techniques have been proposed to overcome the workability problem. For example, Shah et al. [6] used extrusion process to produce fiber reinforced cementitious composite with strain-hardening behavior in tension wherein more than 4% fiber by volume fraction is used. The tensile strain capacity of such extruded composites is substantially higher than normal cement or mortar, but remains below 1%.

1.2 Engineered Cementitious Composites

Engineered Cementitious Composites (ECC) is a unique representative of HPFRCC, featuring extreme intrinsic tensile ductility and moderate fiber content. ECC exhibits tensile strain-hardening behavior similar to that of ductile metals. The tensile strain capacity of ECC is several hundred times that of normal concrete and the fracture toughness of ECC is similar to that of aluminum alloys [7]. Furthermore, the material remains ductile even when subjected to high shear stresses [8]. The compressive strength of ECC ranges from 40-80 MPa depending on mix composition, the high end similar to that of high strength concrete. High tensile ductility and toughness of ECC material greatly elevates the mechanical performance of reinforced ECC (R/ECC) structure by preventing brittle failure and loss of structural integrity which is usually found in traditional reinforced concrete (R/C) structure under excessive loading. In fact, it has been demonstrated experimentally that R/ECC structural members, such as beams [9], columns [10], walls [11], and connections [12], surpass normal R/C structural members in structural load carrying capacity, deformability, and energy absorption capacity under monotonic and reverse cyclic loading.

The ingredients of ECC are similar to that of normal FRC, except for the absence of coarse aggregates. Notably, ECC utilizes short, randomly distributed fibers with a moderate volume fraction (2% or less in general). With this relatively small amount of short fibers, self-consolidating ECC [13, 14] has been designed for use with regular construction equipment [15]. ECC is currently emerging in full scale structural applications including the composite deck of a cable stayed bridge in Japan [16] **(Fig. 1.2)**. This bridge employed about 800 cubic meters of ECC for the 38mm thick

ECC/Steel composite deck. In the United States, the first full scale ECC link slab has been constructed in Michigan [17] as shown in **Fig. 1.3**.

The high performance, moderate fiber content combination is attained by micromechanics-based composites optimization [18, 19] (see also **Chapter 2**). Micromechanics provides guidance in specific selection and tailoring of the type, size and amount of ingredients. As a result, the fiber, matrix and interface interacts synergistically to produce controlled multiple microcracking when overloaded in tension, while suppressing the localized fracture mode commonly observed in FRC. ECC micromechanics-based design framework elevates the cementitious materials design from conventional trial-and-error empirical combination of individual constituents to systematic engineered selection. Such linkage can be further extended to the structural performance beyond material level and integrate the material design into performance based design concept for structure. The resulting design concept is the Integrated Structures and Materials Design (ISMD) [20]. ISMD combines materials engineering and structural engineering by adopting material properties as the shared link as depicted in **Fig. 1.4**. Therefore, ECC represents not only a material but also a design philosophy.

The micromechanics tailoring nature embodied in ECC material design enables the possibility of adding new performance requirements on top of high ductility. For example, ECCs suitable for spraying [21] and extruding [22] have been developed with appropriate control of rheological properties.

ECCs with high early strength have been developed for rapid repair and retrofit of existing infrastructure [23]. Micromichanics models indicated that the demand of high early strength alters the subtle balance between composites ductility and vital constituent

properties such as fiber/matrix interface bond and matrix toughness, and therefore the potential of strain-hardening may diminish. To battle this trend, focus has been placed on tailoring pre-existing flaw size distribution in matrix. Specifically, plastic beads with specified size and amount are doped into ECC mix design to encourage crack initiation, and therefore the potential of multiple cracking can increase. The resulting high early strength ECC materials are capable of delivering compressive of 21MPA with 3-4 hours after placement and retain long-term tensile strain capacity above 2%.

Lightweight ECCs [24] with densities between 900 and 1800 kg/m^3 have been developed and can offer considerable weight saving. Lightweightness in ECC was achieved by incorporating air-entrainment admixture, polymeric micro-hollow-bubble, natural lightweight aggregates perlite, or glass micro-bubbles. While strain-hardening is readily obtained due to low matrix toughness in lightweight ECCs, the emphasis is placed on the pursuit of tensile and compressive strength. By selecting appropriate lightweight filler, tensile strength of 4 MPa with strain capacity above 4% is proven to be achievable at a density of 1450 kg/m3, along with a compressive strength of 40 MPa.

Within this thesis, a systematic design approach of adding new functions into ECC is proposed and used for ECC design as depicted in **Fig. 1.5**. ECC M45, the most studied ECC material, is used as the starting material for adding new functions. M45 has a tensile strength of 5-6 MPa, a tensile ductility of 3-5%, and a steady-state crack opening of 60 μm. The compressive strength of M45 can reach 60 MPa. The design starts from identifying the performance requirement and determining performance measurement metric. For example, low weight is the performance requirement of lightweight concrete and density can be used to quantify the performance of lightweightness of material. The

next step involves micromechanical model revision incorporating new mechanisms due the new performance requirement if there is any. A good example is designing ECC tensile ductility at high loading rate (**Chapter 5**). Strain rate effects on fiber, matrix and interface due to high rates of loading need to be taken into account and the rate-dependent micromechanics models need to be established. The newly revised micromechanical models along with the performance measurement metric can be then used for composite re-design through ingredients re-selection and/or component re-tailoring. Through this design approach, the resulting ECC material should possess added functions while maintaining its tensile ductility.

1.3 Research Motivation and Objectives

Safety, durability, and sustainable development of future infrastructure systems can be seen as the three major challenges posted for today's civil engineers. Projecting current consumption trends, nearly 2.3 Earths will be needed to support human life by 2050. To battle this trend, a new cadre of researchers and engineers is needed to direct more sustainable development worldwide. This is especially true for civil engineering discipline, as huge flows of construction materials and energy resources for construction projects are consumed each year. The emphasis on sustainability can be seen as a new frontier of civil engineering.

Moreover, structural durability represents another great challenge for civil engineering profession. The American Society of Civil Engineer's 2005 Report Card for America's Infrastructure assigned a national grade of "D" to US infrastructure with a

total investment of US$1.6 trillion needed for repairs. This stresses the need for improving infrastructure durability.

In addition to sustainability and durability, terrorist attacks and natural hazards highlight the need for assuring human safety in large structures under extreme loading such as blasts, impacts, accidental fires, and earthquakes. Within the last two decades, a series of terrorist related acts has occurred in the US, including the World Trade Center bombing in New York City in 1993, the Alfred P. Murrah Federal Building bombing in Oklahoma City in 1996, and the most recent terrorist attack on the World Trade Center in 2001. Other type of dynamic loads, such as seismic loading, can also lead to loss of civilian life and properties. The Northridge earthquake in 1994, for example, killed 72 people, injured 9,000 and caused $25 billion in damage.

The ultimate goal of research in ECC is to improve the safety, durability, and sustainability of infrastructure systems through innovative materials solution. As a step towards achieving this goal, the development of new ECCs with added functions of impact resistance, self-healing, and greenness forms the focus in this dissertation. Together, they demonstrate the efficiency of the design approach outlined in the previous section for added functions into ECC. These three chosen functions and related background motivation for their choice are further described below.

While HPFRCC materials including ECC deliver superior mechanical properties, they usually perform quite poorly in material sustainability indicators. The cement use in typical HPFRCC materials is three to five times that in normal structural concrete. The production of fibers is also energy intensive. Little work has been done to incorporate sustainability performance into HPFRCC material design. As these materials are staged

to large scale application, the social, environmental, and economical cost of the application of these materials must be considered. The specific material function targeted in this dissertation in relation to sustainability is material greenness – i.e. replacing cement by industrial by-products and/or wastes while maintaining, if not improving, ECC material fresh and hardened properties.

Increased durability of reinforced concrete is usually associated with a very compact and dense concrete matrix so that the transport of corrosives to the steel can be greatly reduced [25, 26]. These concepts rely upon the concrete to remain uncracked. In reality; however, reinforced concrete members crack due to both applied structural loading and shrinkage and thermal deformations, which are practically inevitable and often anticipated in restrained conditions [27, 28]. The formation of cracks coupled with a lack of crack width control in brittle concrete leads to increased permeability of cracked concrete. This then gives rise to elevated chloride concentrations, subsequent corrosion and volume expansion of reinforcing steel, and ultimately to disintegration of the matrix. This case highlights a highly durable material which did not translate to highly durable structures due to the presence of cracking under field conditions. The specific material functionality targeted in this dissertation in relation to infrastructure durability is material self-healing – i.e. autogenous healing of cracks so that transport properties of cracked ECC can be reduced and mechanical properties of cracked ECC can be regenerated.

Impact/blast protection is a vital component of any protective structure such as blast walls, barracks, and headquarters. Due to the brittleness of concrete, protective structures made of R/C can be vulnerable under severe impact/blast loads [29]. Brittle failures (e.g. cracking, spalling, fragmentation) of concrete are often observed in R/C

structures when subjected to impact/blast [30], and can lead to severe loss of structural integrity and personnel. The specific material functionality targeted in this dissertation in relation to infrastructure safety is material tensile ductility under dynamic loading – i.e. ensuring extreme tensile strain capacity of ECC even when subjected to high strain rate loading.

The main objective of this research is to explore the possibility of embedding special functions into ECCs which may contribute to the safety, durability, and sustainability of our future infrastructure systems. Specifically, ECC micromechanics-based design theory will be improved in the prediction of crack width and will be extended to dynamic loading condition so that the design theory can be applied even when the material is subjected to extreme loading. The quantitative links to composite performances, in terms of tensile strain capacity, first cracking and ultimate strength, crack width, and compressive strength, will be utilized to guide the development of ECC materials with special functions for prospective applications.

1.4 Research Scope and Dissertation Organization

In this dissertation, development of three new ECCs with special functions, namely green ECC, self-healing ECC, and impact resistant ECC, are presented. While the material tailoring for high ductility is focused upon, the tailoring process is constrained by other performance requirements imposed by the prospective application. Micromechanics tools are employed to understand the influence of each variable in the mix constituents and the results provide a qualitative and quantitative basis for performance optimization. It is recognized that the problems of infrastructure safety, durability and sustainability are

highly complex and interdisciplinary. Complete solution of these problems is beyond the scope of this dissertation research. Instead, this dissertation focuses on providing contributions to these problems through advanced material research. More specifically, this dissertation explores in-depth the development of three added functions – material greenness, material self-healing, and material impact resistance, as illustrated in **Fig. 1.6**. Through these and other examples, it is established that micromechanics can be exploited as a powerful tool for material function design.

In Chapter 2, the theoretical framework of ECC material design previously developed [19, 31-38] is further completed to allow more accurate prediction of crack width. A cohesive traction model is used to study crack propagation mode (Griffith type vs. steady state flat cracking), to verify the condition for steady state crack propagation, and to visualize steady state crack propagation. The flat crack propagation mode provides a means to suppressing the typical single large fracture typical of normal concrete and FRC, and at the same time enabling self-controlled tight crack width. A more complete fiber bridging constitutive model that includes two-way fiber pullout, matrix micro-spalling, and Cook-Gordon effect, mechanisms not accounted for in previous model versions, is established and verified with the experimentally measured $\sigma(\delta)$ curves. The micromechanics-based design theory is then used to tailor a new low cost ECC reinforced with Polypropylene fibers (PP-ECC) as an example to demonstrate the effectiveness of micromechanics approach in composite optimization.

Chapter 3 attempts to tackle one aspect of the sustainability issue in HPFRCCs, which typically have a high cement content. A new set of green ECC is developed taking into account environmental sustainability consideration. Specifically, a high volume of

fly ash is adopted in the development of a green version of ECC. The influence of fly ash content on matrix toughness, interface bond properties, material microstructure, composite performances, and material greenness are investigated in detail. Micromechanics developed in Chapter 2 serves as a tool for smart greening – improving material greenness while maintaining or even elevating desirable material properties. The material sustainability performance is evaluated by material sustainability indicators. The resulting green ECC demonstrates that, when properly tailored, high strain capacity is retainable in the presence of high volume of low quality recycled by-products.

In Chapter 4, the autogenous self healing of ECC exposed to different environmental conditions is reported. The autogenous healing of cracks to block transport of water and corrosives into the composite and down to reinforcing steel is achieved through formation of self-healing compounds such as calcite and hydration products within cracks. Second, self-healing of cracks can regenerate a large portion of material load capacity and stiffness under mechanical loads. This self healing functionality makes ECC a virtually crack-free concrete material by resolving these two damaging phenomena associated with cracks within concrete. The concept of self-healing and its dependence on tight crack width deliberately (micromechanically, Chapter 2) designed into special versions of ECC is explicitly explored and reported in this chapter. The resulting crack-free ECC is expected to greatly promote durability and extend the service lives of concrete structures.

Chapter 5 presents the development of an impact resistant ECC for elevating the impact resistance of structures. The research program starts from investigating the fundamental mechanisms governing rate dependency in the tensile properties of ECC

material. The micromechanics-based rate dependent strain-hardening criteria are established for ECC re-engineered with impact resistance functionality. Specifically, ECC is retailored at the microstructural scale to maintain its tensile ductility under high strain rate loading. The resulting material is used to build simple structural elements including thin ECC circular plate, ECC beam, reinforced ECC (R/ECC) panel, and R/ECC beam for drop weight impact testing to verify the structural performance. It is shown that ECC designed for high rate loading can effectively suppress the brittle fracture failure mode, and therefore enhance the structural performance in terms of structural load and energy absorption capacity under drop weight impacts.

Overall conclusions from this study are summarized in Chapter 6, and some future works worthy of further investigations are outlined.

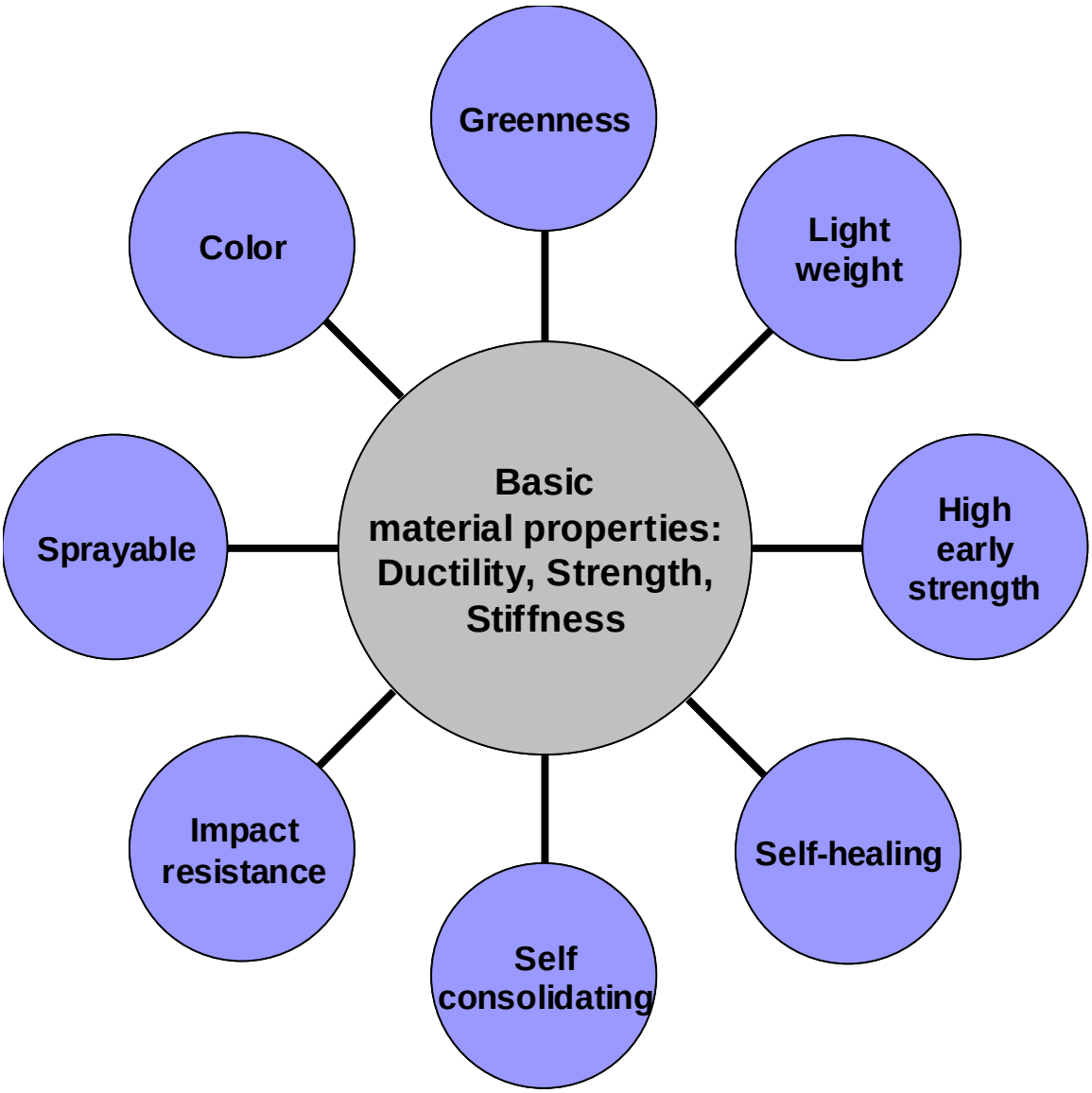

Fig. 1.1 – Illustration of materials with added functions

Fig. 1.2 – Mihara Bridge with ECC/steel composite deck opened to traffic in April 2005, Japan

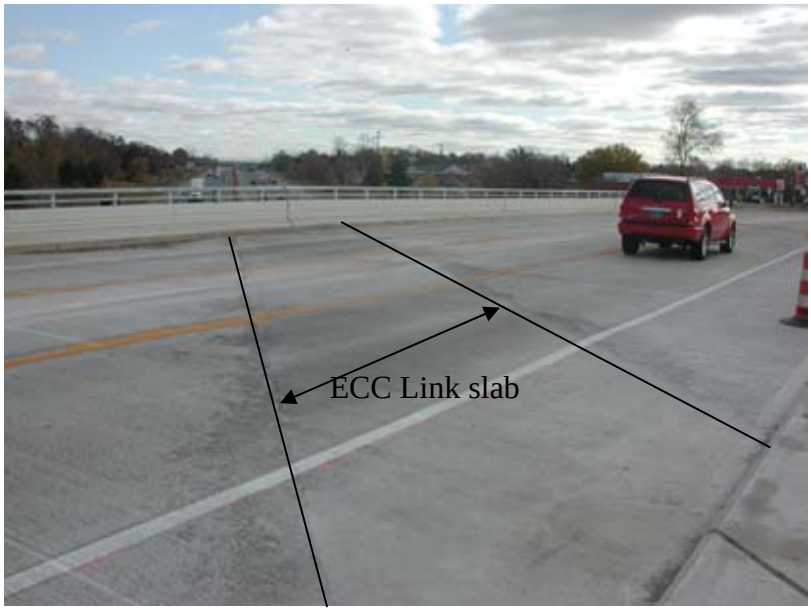

Fig. 1.3 – ECC link slab on the Grove Street Bridge over I-94 opened to traffic in October 2005, Michigan.

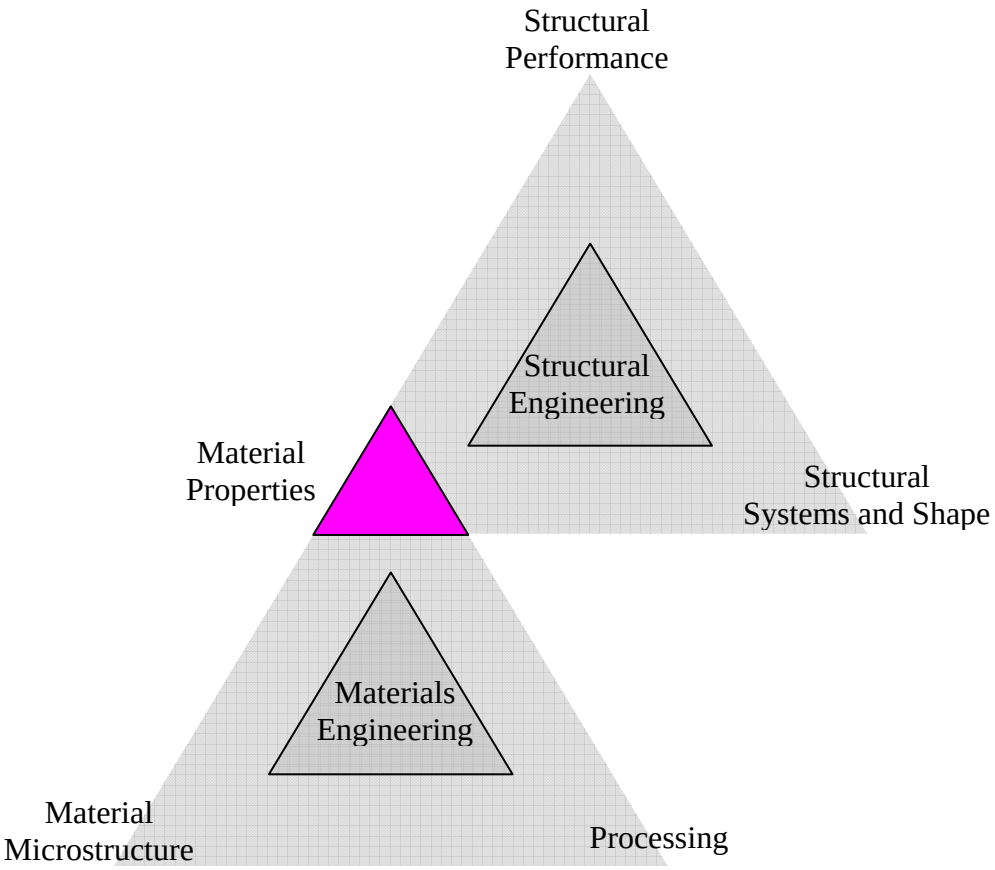

Fig. 1.4 – Integrated Structures and Materials Design

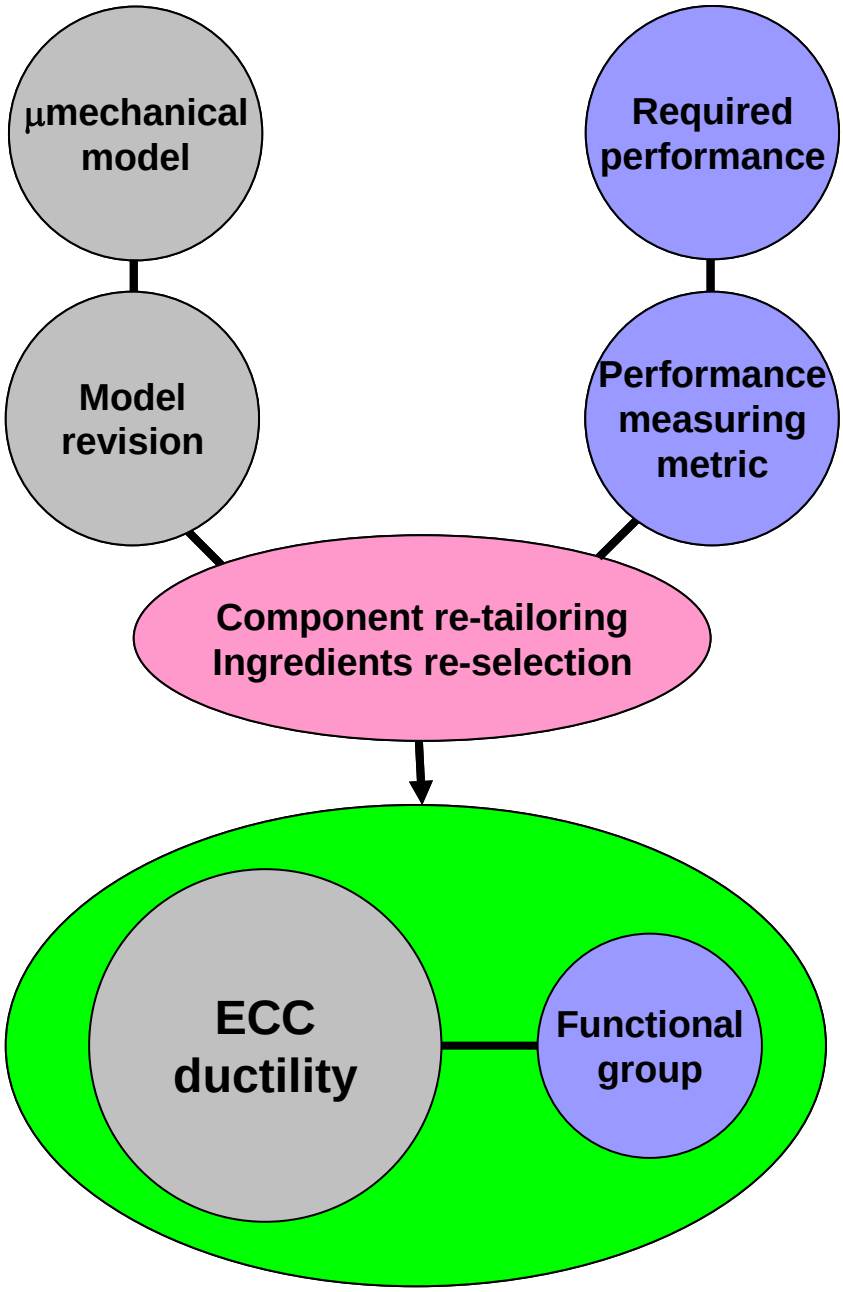

Fig. 1.5 – Generalized design approach of adding new functions into ECC

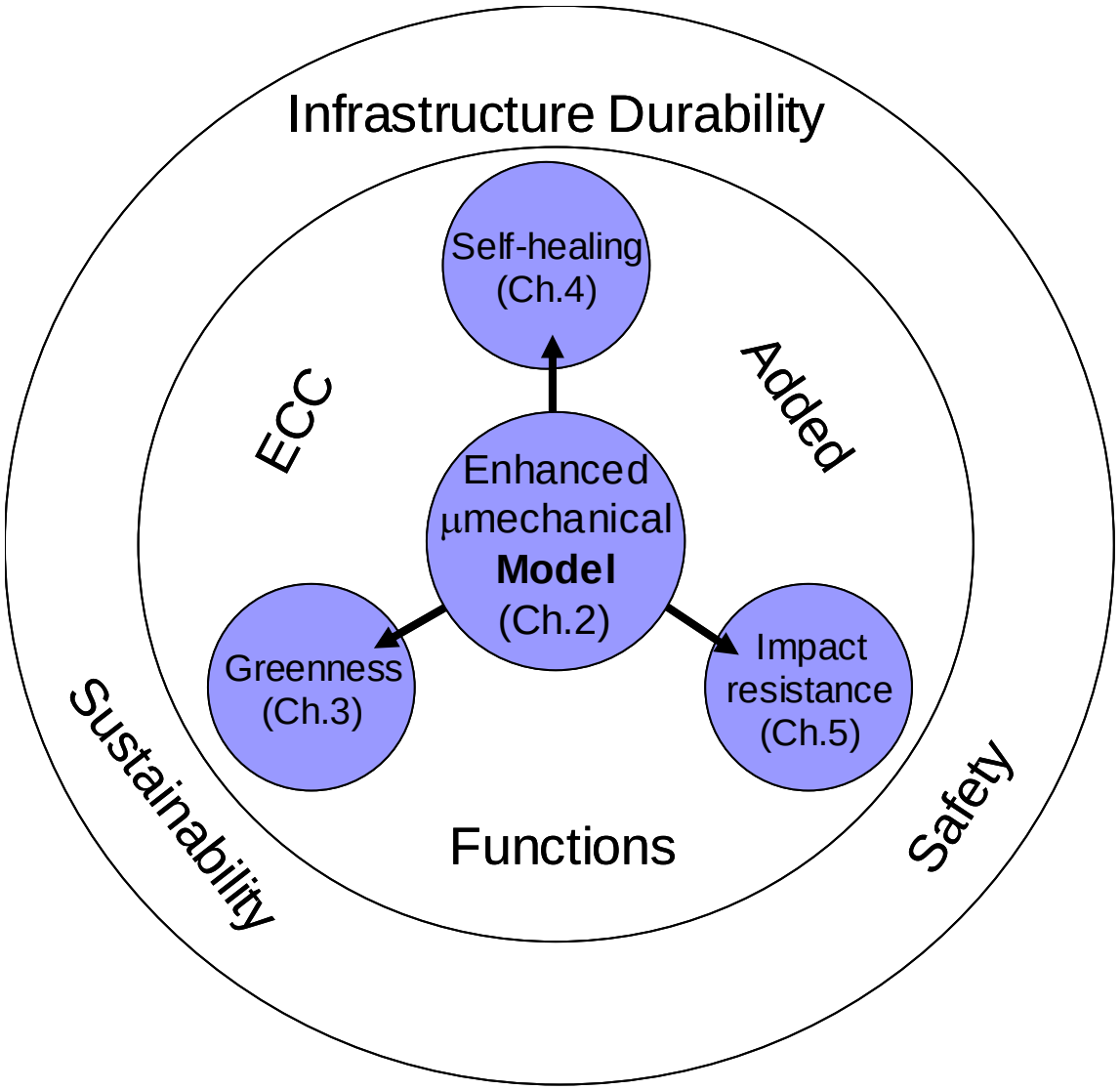

Fig. 1.6: Dissertation framework

Reference

[1] SEAOC, "Vision 2000: A framework for performance based engineering of buildings," *Structural Engineers Association of California*, Sacramento, CA, 1995

[2] Lomborg, B., *The Skeptical Environmentalist: Measuring the Real State of the World*,

[3] ACI_Committee_224, "ACI Report 224R-80," *Concrete International*, vol.2, no.10, pp.35-75, 1980

[4] Naaman, A.E., and Reinhardt, H.W., "Characterization of High Performance Fiber Reinforced Cement Composites HPFRCC," *High Performance Fiber Reinforced Cementitious Composites*, pp.1-23, 1996

[5] Cheyrezy_et_al., Concrete comprising organic fibers dispersed in a cement matrix, concrete cement matrix and premixes, *French Patent WO 99/58468*, 1999

[6] Shah_et_al., Method of making extruded fiber reinforced cement matrix composites, *US Patent No. 5891374*, 1999

[7] Maalej, M., Hashida, T., and Li, V.C., "Effect of Fiber Volume Fraction on the Off-Crack Plane Energy in Strain-Hardening Engineered Cementitious Composites," *Journal of American Ceramics Society*, vol.78, no.12, pp.3369-3375, 1995

[8] Li, V.C., Mishra, D.K., Naaman, A.E., Wight, J.K., LaFave, J.M., Wu, H.C., and Inada, Y., "On the Shear Behavior of Engineered Cementitious Composites," *J. of Advanced Cement Based Materials*, vol.1, no.3, pp.142-149, 1994

[9] Li, V.C.a.W., S., "Flexural Behavior of GFRP Reinforced Engineered Cementitious Composites Beams," *ACI Materials Journal*, vol.99, no.1, pp.11-21, 2002

[10] Fischer, G., and Li, V.C., "Effect Of Matrix Ductility On Deformation Behavior of Steel Reinforced ECC Flexural Members Under Reversed Cyclic Loading Conditions," *ACI Structural Journal*, vol.99, no.6, pp.781-790, 2002

[11] Kesner, K., and Billington, S.L., "Experimental Response of Precast Infill Panels Made with DFRCC," *DFRCC-2002 International Workshop*, Takayama, Japan, pp.289-298, 2002

[12] Parra-Montesinos, G., and Wight, J.K., "Seismic Response of Exterior RC Column-to-Steel Beam Connections," *Journal of Structural Engineering*, vol.126, no.10, pp.1113-1121, 2000

[13] Kong, H.J., Bike, S., and Li, V.C., "Constitutive Rheological Control to Develop a Self-Consolidating Engineered Cementitious Composite Reinforced with Hydrophilic Poly(vinyl alcohol) Fibers," *Journal of Cement and Concrete Composites*, vol.25, no.3, pp.333-341, 2003

[14] Fischer, G., Wang, S., and Li, V.C., "Design of Engineered Cementitious Composites (ECC) for processing and workability requirements," *Proceeding of BMC-7*, Warsaw, Poland, pp.29-36, 2003

[15] Li, V.C., Lepech, M., and Li, M., *Field Demonstration of Durable Link Slabs for Jointless Bridge Decks Based on Strain-Hardening Cementitious Composites*. 2005, Michigan DOT report.

[16] Kunieda, M., and Rokugo, K., "Recent Progress on HPFRCC in Japan," *Journal of Advanced Concrete Technology*, vol.4, no.1, pp.19-33, 2006

[17] Michigan_DOT, "Bridge Decks Going Jointless: Cementitious Composites Improve Durability of Link Slabs," *Construction and Technology Research Record*, vol.100, pp.1-4, 2005

[18] Li, V.C., "Engineered Cementitious Composites - Tailored Composites Through Micromechanical Modeling," in *Fiber Reinforced Concrete: Present and the Future*, N. Banthia, A. Bentur, and A. Mufti Ed., Canadian Society for Civil Engineering, Montreal, pp.64-97, 1997

[19] Lin, Z., and Li, V.C., "Crack Bridging in Fiber Reinforced Cementitious Composites with Slip-Hardening Interfaces," *Journal of Mechanics and Physics of Solids*, vol.45, no.5, pp.763-787, 1997

[20] Li, V.C., "Integrated Structures and Materials Design," *RILEM Structures and Materials*, 2006

[21] Kim, Y.Y., Fischer, G., Lim, Y.M., and Li, V.C., "Mechanical Performance of Sprayed Engineered Cementitious Composite (ECC) Using Wet-mix Shotcreting Process for Repair," *ACI Materials J.*, vol.101, no.1, pp.42-49, 2004

[22] Stang, H., and Li, V.C., "Extrusion of ECC-Material," *in Proc. of High Performance Fiber Reinforced Cement Composites 3 (HPFRCC 3)*, 1999

[23] Wang, S., and Li, V.C., "High Early Strength Engineered Cementitious Composites," *ACI Materials J.*, vol.103, no.2, pp.97-105, 2006

[24] Wang, S., and Li, V.C., "Lightweight ECC," *in Proceedings of High Performance Fiber Reinforced Cementitious Composite (HPFRCC 4)*, Ann Arbor, Michigan, pp.379-390, 2003

[25] Oh, B.H., Cha, S.W., Jang, B.S., and Jang, S.Y., "Development of high-performance concrete having high resistance to chloride penetration," *Nuclear Engineering and Design*, vol.212, Switzerland, pp.221-231, 2002

[26] Beeldens, A.L., "Durability of high strength concrete for highway pavement restoration," *CONSEC '01: Third International Conference on Concrete Under Severe Conditions*, Vancouver, Canada, pp.1230-1238, 2001

[27] Mihashi, H., and De Leite, J.P.B., "State-of-the-Art Report on Control of Cracking in Early Age Concrete," *Journal of Advanced Concrete Technology*, vol.2, no.2, pp.141-154, 2004

[28] Wittmann, F.H., "Crack formation and fracture energy of normal and high strength concrete," *Sadhana*, vol.27, no.4, pp.413-423, 2002

[29] Magnusson, J., and Hallgren, M., "Reinforced High Strength Concrete Beams Subjected to Air Blast Loading," *Structures and Materials*, vol.15, pp.53-62, 2004

[30] Clifton, J.R., "Penetration Resistance of Concrete – A Review," *National Bureau of Standards, special publication 480-45*, Washington DC, 1984

[31] Li, V.C., and Leung, C.K.Y., "Steady State and Multiple Cracking of Short Random Fiber Composites," *ASCE J. of Engineering Mechanics*, vol.188, no.11, pp.2246-2264, 1992

[32] Li, V.C., and Wu, H.C., "Conditions for Pseudo Strain-Hardening in Fiber Reinforced Brittle Matrix Composites," *J. Applied Mechanics Review*, vol.45, no.8, pp.390-398, 1992

[33] Wang, Y., Backer, S., and Li, V.C., "A Statistical Tensile Model of Fiber Reinforced Cementitious Composites," *J. Composites*, vol.20, no.3, pp.265-274, 1989

[34] Li, V.C., Wang, Y., and Backer, S., "Effect of Inclining Angle, Bundling, and Surface Treatment on Synthetic Fiber Pull-Out from a Cement Matrix," *J. Composites*, vol.21, no.2, pp.132-140, 1990

[35] Li, V.C., "Post-Crack Scaling Relations for Fiber-Reinforced Cementitious Composites," *ASCE J. of Materials in Civil Engineering*, vol.4, no.1, pp.41-57, 1992

[36] Maalej, M., Li, V.C., and Hashida, T., "Effect of Fiber Rupture on Tensile Properties of Short Fiber Composites," *ASCE J. of Engineering Mechanics*, vol.121, no.8, pp.903-913, 1995

[37] Lin, Z., Kanda T., and Li, V.C., "On Interface Property Characterization and Performance of Fiber Reinforced Cementitious Composites," *J. Concrete Science and Engineering*, vol.1, pp.173-184, 1999

[38] Wang, S., *Micromechanics-Based Matrix Design for Engineered Cementitious Composites*, Ph.D. Dissertation, Department of Civil and Environmental Engineering, University of Michigan, Ann Arbor, 222 pp, 2005

CHAPTER 2

ECC Micromechanics Based Design Theory

Micromechanics models of ECC were first established in early 90's [1, 2], in attempt to link the material microstructures to composite multiple cracking and tensile strain-hardening behavior. Efforts to perfect the models have continued since then. In this chapter, ECC design framework – scale linking is described first, followed by a brief review of strain-hardening criteria. Condition for steady state crack propagation is verified and simulated numerically by nonlinear fracture mechanics approach, using finite element method and cohesive traction model. Review of fiber bridging constitutive model is then shown and compared with experimental results for model validation. At the end of this chapter, a new ECC adopting high tenacity polypropylene fibers developed through the guidance of ECC micromechanics-based design theory is described.

2.1 ECC Design Framework – Scale Linking

ECC tensile strain hardening is a result of realizing and tailoring the synergistic interaction between fiber, matrix, and interface. Micromechanics has been used as a tool to link material microstructures to ECC tensile strain hardening behavior. Desirable tensile strain capacity several hundred times that of normal concrete can be achieved by tailoring material microstructures once the established linkages are utilized in material component tailoring. Therefore, scale linking (**Fig. 2.1**) represents the design philosophy behind the development of ECC in which investigation of microscale phenomena and tailoring material microstructure are the keys to understanding and designing desirable composite macroscale behavior.

As shown in **Fig. 2.1**, ECC shows multiple cracking and tensile strain hardening in composite macroscale (mm – cm). One scale below is the mesoscale (μm – mm). In this scale, fibers bridge across the crack and fiber bridging spring law governs the bridging behavior. Still one scale down is the material microstructure (nm – μm) which consists of fiber, matrix, and interface. Micromechanics model links microscale constituent parameters to fiber bridging constitutive behavior in the mesoscale. Steady state crack analysis connects fiber bridging property to tensile strain hardening in composite macroscale. Once established, the model-based linking provides a backward path for material microstructure/ingredient tailoring which allows systematic composite optimization for maximum tensile ductility with the minimum amount of fibers (Sec. 2.5). Microstructure tailoring includes deliberate selection or modification of fiber, matrix, and interface properties, including the addition of nano-size particles (e.g. carbon and nano-fibers) and fiber surface coating. This conceptual framework represents a holistic

approach in composite design accounting for the interaction between the fiber, matrix, and interface.

2.2 Strain Hardening Criteria

ECC is a fiber reinforced brittle mortar matrix composite and the pseudo strain-hardening behavior in ECC is achieved by sequential development of matrix multiple cracking (**Fig. 2.2**). The fundamental requirement for multiple cracking is that steady state crack propagation prevails under tension, which requires the crack tip toughness J_{tip} to be less than the complementary energy J'_b calculated from the bridging stress σ versus crack opening δ curve, as illustrated in **Fig. 2.3** [3, 4].

$$J_{tip} \le \sigma_0 \delta_0 - \int_0^{\delta_0} \sigma(\delta) d\delta \equiv J_b^{'} \tag{2.1}$$

$$J_{tip} = \frac{K_m^2}{E_m} \tag{2.2}$$

where σ_0 is the maximum bridging stress corresponding to the opening δ_0, K_m is the matrix fracture toughness, and E_m is the matrix Young's modulus. **Eqn. 2.1** employs the concept of energy balance during flat crack extension between external work, crack tip energy absorption through matrix breakdown (matrix toughness), and crack flank energy absorption through fiber/matrix interface debonding and sliding. This energy-based criterion determines the crack propagation mode (steady state flat crack or Griffith crack).

The stress-crack opening relationship $\sigma(\delta)$, which can be viewed as the constitutive law of fiber bridging behavior, is derived by using analytic tools of fracture mechanics, micromechanics, and probabilistics. In particular, the energetics of tunnel

crack propagation along fiber/matrix is used to quantify the debonding process and the bridging force of a fiber with given embedment length [5]. Probabilistics is introduced to describe the randomness of fiber location and orientation with respect to a crack plane. The random orientation of fiber also necessitates the accounting of the mechanics of interaction between an inclined fiber and the matrix crack. As a result, the $\sigma(\delta)$ curve is expressible as a function of micromechanics parameters, including interface chemical bond G_d, interface frictional bond τ_0, and slip-hardening coefficient β accounting for the slip-hardening behavior during fiber pullout. In addition, snubbing coefficient f and strength reduction factor f' are introduced to account for the interaction between fiber and matrix as well as the reduction of fiber strength when pulled at an inclined angle. Besides interfacial properties, the $\sigma(\delta)$ curve is also governed by the matrix Young's modulus E_m, fiber content V_f, and fiber diameter d_f, length L_f , and Young's modulus E_f.

Another condition for the pseudo strain-hardening is that the matrix tensile cracking strength σ_c must not exceed the maximum fiber bridging strength σ_0.

$$\sigma_c < \sigma_0 \tag{2.3}$$

where σ_c is determined by the matrix fracture toughness K_m and pre-existing internal flaw size a_0. While the energy criterion (**Eqn. 2.1**) governs the crack propagation mode, the strength-based criterion represented by **Eqn. 2.3** controls the initiation of cracks. Satisfaction of both **Eqn. 2.1** and 2.**3** is necessary to achieve ECC behavior; otherwise, normal tension-softening FRC behavior results. Details of these micromechanical analyses can be found in previous works [5, 6].

Due to the randomness nature of preexisting flaw size and fiber distribution in ECC, a large margin between J'_b and J_{tip} is preferred. The pseudo strain-hardening (PSH)

performance index has been used to quantitatively evaluate the margin and is defined as follows [7].

$$PSH\ energy = \frac{J_b^{'}}{J_{tip}}$$
$$PSH\ strength = \frac{\sigma_o}{\sigma_c} \tag{2.4}$$

Materials with larger PSH index should have better chance of saturated multiple cracking. The saturation of multiple cracking is achieved when microcracks are more or less uniformly and closely spaced (at around 1-2mm), and cannot be further reduced under additional tensile loading of a uniaxial tensile specimen. Robustness of tensile ductility refers to the consistency of tensile capacity from one specimen to another. To measure the extent of saturation of multiple cracking, PSH intensity has been used and is defined as crack spacing ratio [7].

$$PSH\ \ Intensity = \frac{x_d^{test}}{x_d} \tag{2.5}$$

where x_d is the theoretical crack spacing calculated from mechanics [2, 8] and x_d^{test} is the crack spacing measured experimentally. Crack spacing here is defined as the distance between two adjacent cracks. The minimum value of PSH intensity is 1 which indicates a fully saturated multiple cracking state. According to Aveston et al [9], the PSH intensity should fall between 1 and 2 for saturated PSH behavior.

The micromechanics-based strain-hardening criteria, **Eqn. 2.1** and 2.**3**, are used as guidance for ECCs design in the following chapters. The evaluation of PSH and PSH Intensity is helpful in quantifying the saturation of multiple cracking and the robustness of tensile ductility for the newly developed ECCs.

2.3 Numerical Study on Steady State Crack Propagation

In some composite systems when the applied ambient stress exceeds the matrix cracking strength, a flat crack can form after initiating from a defect site and extends infinitely through the matrix. In this scenario, the crack opening δ and the ambient loading σ_∞ remain constant and bridging ligaments sustain and pass the load without rupturing and diminishing. This behavior is known as steady state crack propagation. Further loading causes crack initiation from another defect site and subsequent flat crack propagation occurs. Repeated formation of such steady state cracks results in multiple cracking and strain-hardening of the composite. This deformation mechanism has been observed experimentally in several reinforced brittle matrix composites [10-12] and is important for the converting brittle materials into ductile materials in tension as discussed in Sec. 2.2.

Steady state crack propagation in the present study is defined as crack extension under constant ambient load independent of crack length. Specifically, the crack propagates at constant crack width, i.e. in a flat crack mode, **Fig. 2.4(a)**, with crack flanks bridged by fibers. Under this circumstance, the crack tip advances without knowing any difference in its surrounding environment, including the loading, crack shape, stress and strain fields, and boundary conditions. Conversely, extension of a Griffith type crack, **Fig. 2.4(b)**, is accompanied by a continuous drop in ambient load and a widening in crack opening. We define here a "Griffith type crack" as essentially a Griffith crack which has part of the crack opening profile near the crack tip region modified by the presence of cohesive traction due to matrix retention and/or fiber bridging, but otherwise the same as a standard Griffith crack. Although steady state cracking theory has been established for

many years, it has not yet been observed experimentally due to test difficulties. In this study, a numerical approach will be employed to validate the condition for steady state cracking and to simulate steady state crack propagation.

In the following subsections, the condition for steady state crack propagation is reviewed first. The cohesive traction model which is employed in the finite element analyses to calculate the cracking behavior is then shown, followed by the discussion of results on the Griffith type and the steady state crack propagation.

2.3.1 Condition for Steady State Crack Propagation

The theoretical foundation of multiple cracking was first studied by Aveston et al. [9] who analyzed this phenomenon for an aligned continuous fiber reinforced brittle matrix composite. Later, Marshall and Cox [3] employed the J-integral method to calculate steady state cracking stress σ_{ss} and proposed a more general solution for the condition of steady state cracking:

$$\sigma_{ss}\delta_{ss} - \int_0^{\delta_{ss}} \sigma(\delta)d\delta = J_{tip} \tag{2.6}$$

where J_{tip} is the crack tip toughness and $\sigma(\delta)$ is the spring law of the material elements bridging the crack surfaces (**Fig. 2.3**). As described in the previous section, **Eqn. 2.6** can also be derived based on the energy balance concept and expresses the energy exchange per unit crack advance during steady state crack propagation. The left hand side of **Eqn. 2.6** may be interpreted as the net energy input by external work (first term) less the energy consumed by the bridging elements which open from 0 to δ_{ss} (second term), and represents the complementary energy of the $\sigma(\delta)$ curve (shaded area in **Fig. 2.3**). Hence,

Eqn. 2.6 dictates that the net energy available for driving the crack must be equal to the crack tip toughness during steady state crack extension. This is an alternative definition of steady state cracking in the present context. That is, the net energy available to drive the crack tip propagation is invariant with the crack length.

Recognizing that the left hand side of **Eq. 2.6** reaches a maximum, J'_b, steady state cracking is guaranteed when

$$J'_b \equiv \sigma_0 \delta_0 - \int_0^{\delta_0} \sigma(\delta) d\delta \geq J_{tip} \tag{2.7}$$

where J'_b is the maximum complementary energy defined as the hatched area in **Fig. 2.3**.

Equation 2.7 has been recognized as an important criterion in designing strain hardening fiber reinforced brittle matrix composites as described in Sec. 2.2. Li et al. utilized this criterion in conjunction with a $\sigma(\delta)$ formulated for short randomly distributed fibers [5] in the successful development of ECC with 5% tensile strain capacity [13].

2.3.2 Cohesive Traction Model with Two Interface Types

To simulate the behavior of crack extension, the cohesive traction model provides an effective approach and relatively precise solution [14]. In this study, the cohesive traction model was realized by employing interface element with the user-defined cohesive traction law in the crack plane. The simulations were performed using a commercial FEM software DIANA. The interface element with the user-defined cohesive traction law is a standard element formulation in DIANA.

Details of the model is given in **Figure 2.5**. A two dimensional plate with 160mm in width and 100.5mm in length is modeled using the finite element method. Due to x- and y-axis symmetries, only a quarter of the plate is modeled. The boundary

conditions are fixed in the y direction for the bottom line and fixed in the x direction for the left sideline. The plate is subject to an ambient uniaxial tensile load σ_∞. The matrix element is assumed to act linear-elastically. Interface elements are used to simulate the developing crack and are assigned the user-defined cohesive traction law as material property. Except for those elements representing a pre-existing crack, they are assumed to be linear elastic until a predefined tensile strength f_t is reached. After that, the cohesive behavior follows the imposed cohesive traction law. Specifically, two sets of interface elements are deliberately employed as shown in **Fig. 2.5**. Interface 1 and 2 can be assigned different operative traction behavior for different investigation purposes. For example, a zero bridging in interface 1 and a matrix retention law in interface 2 represents a traction-free center through-crack in a two dimensional plate. Matrix retention is used to represent the break-down tension-softening behavior of the matrix (see **Fig. 2.6**). As another example, interface 1 and 2 can be assigned a bridging law and a total cohesive traction curve, respectively. In this scenario, interface 1 represents a cracked interface but still with cohesive traction associated with bridging only (e.g. fiber) and interface 2 is an (as yet) uncracked interface with assigned cohesive traction combining both matrix retention and fiber bridging action. Interface 2 effectively becomes part of interface 1 when matrix retention is exhausted as the crack opening increases. The philosophy behind this approach reflects the recognition that the matrix breakdown and the bridging (e.g. fiber) are two separate and distinct physical processes. This is consistent with the bridged crack concept first suggested by Marshall and Cox [3].

In the following subsections, several scenarios (i.e. Griffith type cracking and steady-state crack propagation) are examined by incorporating this cohesive traction model.

2.3.3 Analyses of Griffith Type Crack Propagation

Base on the theory embodied in **Eqn. 2.7**, if the condition of steady-state cracking is not satisfied, a Griffith type crack, with enlarging crack opening δ as a function of crack length, should result. For the Griffith type crack, the near tip crack opening profile is not described by the typical elliptical shape as in the case of the classical Griffith crack, due to cohesive traction which reduces the opening. **Figure 2.6** shows a bridging constitutive law and a matrix retention law in which J'_b (0.5 J/m^2) is less than J_{tip} (5 J/m^2), so that **Eqn. 2.7** is violated. The value of J_{tip} can be calculated from the area under the matrix retention curve. The value of J'_b is the area to the left of the bridging law up to the peak bridging stress.

Figure 2.7 shows the computational results when the above cohesive tractions are assigned to interface 1 and 2. The computation was conducted by load control and an arch-length method [15] was used as the solution method. The arch-length method which is automatically implemented in DIANA has the advantage of solving problems with high nonlinearity which is likely to be the case in the present study. As can be seen in **Fig. 2.7(a)**, after the peak load, a descending ambient stress σ_∞ is accompanied by a continuously increasing mid-crack opening δ_m (measured at the center of the crack). **Fig. 2.7(b)** plots a quarter of the crack opening profile after the peak load. By symmetry, an enlarging oval shape crack forms with a descending σ_∞. The concave shape near the

crack tip region (circular part in **Fig. 2.7(c)**) is a result of matrix retention and bridging traction. **Fig. 2.7(c)** shows δ_m versus crack length (L, measured in terms of the length of interface with $\delta > 0$) curve. By plotting $\Delta\delta_m/\Delta L$ (secant slope calculated from two adjacent data points) versus L curve as shown in **Fig. 2.7(d)**, it is found that the change in mid crack opening per unit crack advance ($\Delta\delta_m/\Delta L$) approaches a constant (0.09) which implies a continuously widening crack as the crack tip extents. Continuously enlarging in crack opening causes the exhausting of bridging, and therefore it has to be a Griffith type crack.

It may be argued that the Griffith type cracking behavior described above is a result of low bridging strength (σ_0 = 1MPa) compared to the matrix strength (f_t = 5MPa). However, another computation attempt shows that even when the bridging strength (σ_0 = 6MPa) is larger than the matrix strength (f_t = 5MPa) as shown in **Fig. 2.8(a)**, crack propagation remains in a Griffith type mode. For this case, J'_b (3 J/m^2) is set to remain lower than J_{tip} (5 J/m^2) so that the steady state criterion (**Eqn. 2.7**) is still violated. **Fig. 2.8(b)** plots the computed ambient load versus the mid-crack opening curve. Again, a continuously increasing crack opening is observed beyond the peak load. At a certain point, the crack opening exceeds 10 μm, which indicates the exhausting of the bridging capacity (**Fig. 2.8(a)**) and a traction free Griffith type crack results.

From the above analyses, it is concluded that no mater how strong the fiber bridging is, a Griffith type crack will form as long as **Eqn. 2.7** is violated, that is, when the complementary energy J'_b is smaller than the matrix toughness J_{tip}. In ductilizing brittle matrix composites, this result reveals an important information that a composite with strong bridging is not necessary a tough material. That is, simply having a first

crack strength lower than the maximum bridging capacity is not sufficient for multiple cracking. **Eqn. 2.7** from energy balance concept is also necessary. This concept; however, has not been widely accepted by researchers.

2.3.4 Analysis of Steady State Crack Propagation

To verify the condition of steady state cracking, a bridging curve with larger J'_b is assigned to interface 1. **Figure 2.9** gives the matrix retention and the bridging constitutive laws. In this case, J'_b is 12 J/m^2 which is larger than J_{tip} (5 J/m^2) so that **Eqn. 2.7** is satisfied. Further, $f_t < \sigma_0$.

It has to be pointed out that and the numerical simulation of steady state crack propagation requires special considerations. Mathematically speaking, steady state cracking represents infinite solutions in terms of crack length for a given load. In other words, infinite equilibrium states of different crack length can be found at the steady state cracking stress (σ_{ss}). However, it is impossible for a FEA program to find more than one solution/equilibrium state. An alternate way to simulate steady state cracking is to calculate the cracking strength of the plate for different crack lengths, specifically, different length of interface 1 on which only fiber bridging (no matrix retention) is imposed. A constant ambient load for different imposed crack lengths, if found, implies steady state crack propagation. This concept is somewhat analogous to the displacement control method utilized in many FEA. Instead of controlling displacement; however, we vary crack length to find the corresponding equilibrium state.

Figure 2.10 shows the computational results of the plate with different length of interface 1 ranging from 4mm to 44mm. As can be seen in **Fig. 2.10(a)**, a stable crack

growth is found before the peak load. After that, a descending ambient stress accompanied by an increase in crack length indicates unstable cracking. However, this unstable crack propagation is bounded and the ambient stress approaches a constant value (σ_{ss}) with further crack extension. **Figure 2.10(b)** displays a quarter of the crack opening profile after the peak load. Interestingly, the crack starts with an oval shape and tends to propagate in a flat manner after a certain length of propagation. **Figure 2.10(c)** and **(d)** show the $\delta_m - L$ and the $\Delta\delta_m/\Delta L - L$ curves, respectively. It can be seen that the crack opening approaches a constant (δ_{ss}) when the crack tip moves forward and $\Delta\delta_m/\Delta L$ approaches zero which suggests the cessation of crack widening as it extends in length. These observations confirm the attainment of steady state cracking.

According to the condition of steady state cracking (**Eqn. 2.6**), the complementary energy J'_b should equal the matrix toughness J_{tip} at steady-state. From the computational results shown above, the crack opening at steady state δ_{ss} in this case is 2.582 μm (**Fig. 2.10(c)**). Using this information combined with the given bridging law $\sigma(\delta)$, the complementary energy J'_b at steady state can be calculated and the value is 4.9992 J/m^2, which is very close to the theoretical value ($J'_b = J_{tip} = 5$ J/m^2). Through this check, the condition for steady state cracking is further confirmed.

From the above discussions, it is clear that appropriate bridging traction relations, in contrast to strong bridging, are required in order to achieve steady state crack propagation and to ductilize brittle matrix composite. This fact has been recognized and implemented in designing ECC. In ECC, the complementary energy (J'_b) was maximized through tailoring proper fiber/matrix interface properties. On the other hand, J_{tip} can be minimized through matrix modification. **Equation 2.7** allows a systematic

means of searching for optimal combinations of matrix toughness (J_{tip}) and fiber bridging properties (J_b').

2.3.5 Summary

This study demonstrates and simulates steady state crack propagation in composites utilizing a numerical approach. The numerical results establish without a doubt that the steady state cracking criterion is a fundamental principle that must be satisfied for ductilizing brittle matrix composites via multiple cracking. As also demonstrated from experimental research [13], deliberate control of the bridging law through tailoring of the composite constituents, as governed by the steady state cracking criterion, is key to attaining ductile composites.

The cohesive traction model with two interface types provides good results in simulating single crack propagation for a broad range of composite materials. This model may be extended to simulate the multiple cracking and strain hardening behavior of reinforced brittle matrix composites.

2.4 Fiber Bridging Constitutive Model of ECC

As can be seen, the fiber bridging constitutive law $\sigma(\delta)$ is employed in both strian-hardening criteria. It determines the complementary energy J_b' in **Eqn. 2.1** as well as the maximum bridging strength σ_0 in **Eqn. 2.3**. Therefore, the $\sigma(\delta)$ relationship critically controls the tensile strain-hardening behavior of ECC.

Fiber bridging constitutive law $\sigma(\delta)$ describes the relationship between the bridging stress σ transferred across a crack and the opening of this crack δ. In the development of ECC, the $\sigma(\delta)$ relationship is of primary importance. It relates to material microstructure (micro-scale) on one hand, and governs composite tensile strain-hardening behavior (macro-scale) on the other. Therefore, control of $\sigma(\delta)$ curve through tailoring material microstructure is the key to successfully design ECC material properties in general, and tensile properties, i.e. tensile strain capacity and ultimate tensile strength, and steady state crack width in particular. The tensile properties of ECC are important to the structural safety at ultimate limit state as the steady state crack width is to the structural long-term durability.

In the following subsections, review of the bridging model of ECC is shown first. Comparison between experimental and predicted $\sigma(\delta)$ curves is then reported to verify the fidelity of the model.

2.4.1 Fiber Bridging Model

ECC is a cement-based composite and usually reinforced with short (6-12mm), randomly distributed small diameter (10-100μm) micro-fibers. The construction of fiber-bridging constitutive law starts from modeling a single fiber pullout behavior against the surrounding matrix. The $\sigma(\delta)$ relationship can then be obtained by averaging the contributions from fibers with different embedment length and orientation across the crack plane. Due to the absence of coarse aggregate in ECC mix design, aggregate bridging is not considered in the present study.

Modeling of Single Fiber Behavior

When a fiber is subjected to a pullout force, it must first debond from the surrounding matrix before it can be pulled out. The debonding process may be viewed as crack propagation along the interface tunnel from near the matrix crack surface toward the embedded end. After debonding, the interface is purely governed by frictional force. Such tunneling crack problem was studied by Lin and Li [16]. Assuming constant frictional stress τ_0 and debonding fracture energy G_d (also referred to as chemical bond in this paper), during debonding stage (short-range relative sliding) the single fiber-bridging stress $\sigma_{debonding}$ versus the fiber displacement (at exit point) relative to the matrix crack surface u is given by

$$\sigma_{debonding} = 2\sqrt{(\tau_0 u + G_d)\frac{2E_f(1+\eta)}{d_f}} \tag{2.8}$$

where E_f and d_f are fiber Young's modulus and diameter, respectively, and η is a parameter expressing the ratio of the effective (accounting for volume fraction) fiber stiffness to effective matrix stiffness. η approaches to zero as the fiber content becomes small.

After debonding is completed, the fiber is in the pullout stage. For some types of fiber, particularly PVA fiber, significant slip-hardening response was observed during long-range pullout. Assuming the frictional stress is linear to the slip distance with coefficient β (referred as slip-hardening coefficient [16]), the fiber stress $\sigma_{pullout}$ during pullout stage can be expressed as

$$\sigma_{pullout} = \frac{\tau_0}{d_f}(L_e - u - \delta_c)\left(1 + \frac{\beta(u-\delta_c)}{d_f}\right) \tag{2.9}$$

$$\delta_c = \frac{2\tau_0 L_e^2(1+\eta)}{E_f d_f} + \sqrt{\frac{8G_d L_e^2(1+\eta)}{E_f d_f}} \tag{2.10}$$

where L_e is the fiber embedment length and δ_c corresponds to the displacement at which full-debonding is completed. A schematic illustration of single fiber pullout behavior is shown in **Fig. 2.11**. At the end of debonding, there is a sudden load drop due to unstable extension of the tunnel crack. Subsequently, the fiber is held back in the matrix only by frictional bonding. The magnitude of the drop can be used to calibrate the chemical bond G_d [17]. During the debonding and pullout stages, the fiber may rupture if the load P exceeds the fiber tensile strength, which is often the case in PVA-ECC system due to strong slip-hardening effect [17].

In short fiber composite systems such as ECC, fibers are oriented at an arbitrary angle ϕ relative to the crack plane ($\phi = 0$ when fiber is perpendicular to the plane and $\phi = \pi/2$ when fiber is parallel to the plane). Misaligned fibers are subjected to additional frictional stress due to the interaction with the matrix when the fiber exits the matrix. For flexible polymeric fiber, Morton and Groves [18] and Li et al. [19] suggested the following empirical relation to account for the increase of bridging force P due to an inclination angle ϕ by making analogy to an Euler friction pulley at the fiber exit point,

$$P(\phi) = P(0)e^{f\phi} \tag{2.11}$$

where $f > 0$ is referred to as the snubbing coefficient.

Some types of fiber have strength which are vulnerable to bending and lateral stress. Macroscopically, these fibers exhibit strength reduction when loaded at an inclined angle to the crack plane. For PVA fiber, Kanda and Li [7] introduced a strength reduction coefficient f' to account for this effect in the following form,

$$\sigma_{fu}(\phi) = \sigma_{fu}(0)e^{-f'\phi} \tag{2.12}$$

where σ_{fu} is the fiber rupture strength

Two-way Fiber Pullout Consideration

Many reinforcing fibers for cementitious composites, such as polyethylene fiber, polypropylene fiber, and smooth steel fiber, do not exhibit significant slip-hardening response, i.e. β approaches 0 or even goes negative (**Fig. 2.11**). Consequently, for bridging fibers, after complete debonding of the short embedment side, the long embedment side remains anchored since the load begins to drop. The increase of crack opening causes the short embedment side to be pulled out, and the elastic stretch of the long embedment side is negligible. The scenario; however, may be different in PVA fiber system, where strong slip-hardening behavior is present. Redon and Li [17] suggested that slip-hardening of PVA fiber in a cement matrix was due to an abrasion and jamming effect during sliding of the fiber in the matrix tunnel. **Figure 2.12** shows typical responses of single PVA fiber pulled out from ECC mix 45 (M45) matrix. When the embedment length is small (e.g. L_e = 0.597 mm), the fiber can be pulled out from the matrix completely. When the embedment length is large (e.g. L_e = 1.18 mm), the fiber ruptures. The most significant observation however is that due to strong slip-hardening behavior the pullout load (after full debonding, first peak) can be much higher than the load at the completion of debonding. For PVA fibers bridging a crack, therefore, after the completion of debonding at short embedment side, the long embedment side may continue debonding and eventually enter the pullout stage such that two-way fiber pullout occurs. In this case, the contributions of slip displacement from both sides of the fiber

across the crack to the total crack opening δ should be included. The possibility of two-way fiber debonding and pull-out was originally suggested by Wang et al [20].

The modeling of two-way fiber pullout is illustrated in **Fig. 2.13**. For given crack opening δ, the contribution δ_L and δ_S from the long embedment segment (length L_L) and the short embedment segment (length L_S), respectively, can be calculated from the fiber load balance,

$$\delta = \delta_L + \delta_S \tag{2.13}$$

$$\delta_L = \delta_S \qquad \text{for } \delta < 2\delta_{0S} \tag{2.14}$$

$$P_d(\delta_L) = P_p(\delta_S, L_S) \qquad \text{for } \delta_S > \delta_{0S} \text{ and } \delta_L < \delta_{0L} \tag{2.15}$$

$$P_p(\delta_L, L_L) = P_p(\delta_S, L_S) \qquad \text{for } \delta_L > \delta_{0L} \text{ and } \delta_L < \delta_{0L} \tag{2.16}$$

The debonding load P_d and pullout load P_p are given by

$$P_d(\delta) = \pi\sqrt{(\tau_0\delta + G_d)\frac{E_f d_f^3(1+\eta)}{2}} \tag{2.17}$$

$$P_p(\delta, L) = \pi\tau_0(L - \delta + \delta_0)(d_f + \beta(\delta - \delta_0)) \tag{2.18}$$

where δ_0 is the crack opening corresponding to complete debonding,

$$\delta_0(L) = \frac{2\tau_0 L^2(1+\eta)}{E_f d_f} + \sqrt{\frac{8G_d L^2(1+\eta)}{E_f d_f}} \tag{2.19}$$

$$\delta_{0L} = \delta_0(L_L) \tag{2.20}$$

$$\delta_{0S} = \delta_0(L_S) \tag{2.21}$$

Matrix Micro-spalling Consideration

Matrix micro-spalling at the fiber exit is commonly observed in random fiber reinforced brittle matrix composites, including PVA-ECC [7]. When the pullout force at the fiber exit is misaligned with the orientation of the embedded segment, stress concentration at the bearing point causes local failure of supporting matrix. The size of the spalled matrix piece is governed by the fiber diametera and bearing force which is a function of external load on the fiber, matrix strength, matrix stiffness, and inclination angle.

A semi-empirical equation for estimating the spalling size s was proposed by Wang [21] as following,

$$s = \frac{P \sin\left(\frac{\phi}{2}\right)}{k d_f \sigma_m \cos^2\left(\frac{\phi}{2}\right)} \tag{2.22}$$

where P is the external force acting on the fiber; ϕ is the fiber inclination angle; σ_m is the matrix tensile strength, and k is the spalling coefficient (**Fig. 2.14**). k is a dimensionless constant related to fiber geometry and matrix stiffness, and can be calibrated by experimental observation. In this equation, the spalling size is assumed to be proportional to the external load on fiber exit and inversely proportional to matrix tensile strength and fiber diameter. The trigonometric terms reflect the force decomposition and geometric feature of the bearing portion of the matrix. An illustration of **Eqn. 2.22**, by plotting spalling size s against force P and inclination angle ϕ, is shown in **Fig. 2.14**. For typical forces in PVA fibers in ECC, the predicted spall size (for k = 500) is in the range of 0-28 μm, consistent with those observed experimentally.

Physically, matrix micro-spalling relieves stress concentration particularly on stretched bridging fibers. As illustrated in **Fig. 2.15**, spalling also changes the fiber inclination angle ϕ to a smaller ϕ'. Since the strength of PVA fiber degrades significantly at high inclination angle, the existence of matrix spalling serves to delay fiber rupture and allows larger crack opening as well as higher peak bridging stress.

Microscopic observation indicates that the spalling size s of PVA-ECC ranges from several micrometers to several tens of micrometers and is mostly limited by the fiber diameter. In PVA-ECC system, considering a typical steady-state crack width of 60 μm, the maximum elastic stretch of the fiber segments freed from spalling (i.e. total length 2s) will not exceed 2 μm at the peak load, which is negligible compared to the steady state crack opening. Therefore, the elastic deformation of the fiber segments freed from spalling can be neglected without significant influence on the model accuracy. With this simplification, the modeling of single fiber-bridging behavior with consideration of both two-way pullout and matrix spalling can be reduced to the problem of two-way pullout with a modified δ. As illustrated in **Fig. 2.15**, for a given crack opening δ,

$$\delta' = \sqrt{4s^2 + 4s\delta\cos\phi + \delta^2} \tag{2.23}$$

$$\phi' = \sin^{-1}\left(\frac{\delta\sin\phi}{\delta'}\right) \tag{2.24}$$

$$\delta_{eff} = \delta' - 2s \tag{2.25}$$

where δ_{eff} will replace δ in **Eqn. 2.13** and s is given by **Eqn. 2.22**. Single fiber-bridging behavior $P(\delta)$ can be then obtained by evaluating **Eqns. 2.13 – 2.25**.

Averaging – Modeling of Fiber Randomness

The randomness of fiber location and orientation is accounted for in the modeling of the $\sigma(\delta)$ relation by adopting probability density functions that describe the spatial variability of the fibers [19]. **Equation 2.26** shows the formulation of bridging stress σ versus crack opening δ relation. $P(z, \phi)$ is the bridging force contributed by a single fiber with centroidal distance z and orientation angle ϕ relative to the crack plane. $p(z, \phi)$ is the probability density function of fiber with distance z and orientation ϕ. A_f and V_f are the cross-sectional area and volume fraction of fiber, respectively.

$$\sigma(\delta) = \frac{1}{A_f V_f} \int P(z,\phi) p(z,\phi) dz d\phi \tag{2.26}$$

In general, the probability density functions of z and ϕ are independent of each other. For the case of 3-D uniform random distribution, $p(z, \phi)$ can be expressed as follows

$$p(z,\phi) = p(z)p(\phi) \tag{2.27}$$

$$p(z) = \frac{1}{l_f} \qquad -\frac{l_f}{2} \le z \le \frac{l_f}{2} \tag{2.28}$$

$$p(\phi) = \sin(\phi) \qquad 0 \le \phi \le \frac{\pi}{2} \tag{2.29}$$

The random distribution assumption is generally valid in ECC materials, where short fiber and low fiber volume fraction, typically no more than 2%, are adopted. Mix rheology of ECC is also engineered such that uniform fiber distribution is readily achievable without clustering. The fiber orientation however may be constrained, for instance in spray process where ECC is applied layer by layer. In the case of 2-D random distribution, the orientation probability of fiber can be expressed as

$$p(\phi) = \frac{2}{\pi} \qquad 0 \le \phi \le \frac{\pi}{2} \tag{2.30}$$

The composite fiber-bridging behavior $\sigma(\delta)$ relation is available through averaging of all fiber force on the crack plane, as defined by **Eqn. 2.26**. In this study, **Eqn. 2.26** and **Eqns. 2.13 – 2.25** are numerically evaluated. Small increment in δ was chosen to ensure accuracy.

Cook-Gordon Effect Consideration

Another mechanism which contributes to additional compliance in the $\sigma(\delta)$ curve is the Cook-Gordon effect. Cook-Gordon effect describes a premature fiber/matrix interface debonding normal to the fiber axis caused by a tensile stress located ahead of a blunt matrix crack propagating towards a fiber under remote tensile load as depicted in **Fig. 2.16(a)**. Therefore, fiber debonding takes place ahead of the matrix crack, resulting in stretching of a free fiber segment α (Cook-Gordon parameter) and additional crack opening δ_{cg} as shown in **Fig. 2.16(b)**. Li et al. [22] assumed that this phenomenon applies to all fibers regardless of orientation, so that δ_{cg} can be directly computed from the bridging force P. For a single fiber, the additional displacement may be estimated as follows,

$$\delta_{cg} = \frac{4\alpha P}{\pi d_f^2 E_f} \tag{2.31}$$

Noting that when P is independent of ϕ and z, the integration of **Eqn. 2.26** gives the number of fibers bridging across the crack per unit area times P.

$$\sigma = P\frac{A_f}{V_f}\int p(z,\phi)dzd\phi \equiv PN_B \tag{2.32}$$

where N_B is the number of fiber-bridging across the crack per unit area and can be defined as

$$N_B = \frac{A_f}{V_f}\int p(z,\phi)dzd\phi = \frac{A_f}{V_f}\eta_B \tag{2.33}$$

where

$$\eta_B \equiv \int p(z,\phi)dzd\phi \tag{2.34}$$

defines the efficiency of bridging in terms of the amount of fibers bridging across a crack with respect to orientation effect. The P – δ_{cg} relationship for a single fiber, **Eqn. 2.31**, may be substituted into **Eqn. 2.26**. That is:

$$\delta_{cg} = \frac{\alpha\sigma}{V_f E_f \eta_B} \tag{2.35}$$

so that the total crack opening δ_{tot} is approximately given as

$$\delta_{tot} = \delta + \delta_{cg} \tag{2.36}$$

with δ related to σ by **Eqn. 2.26** and **Eqns. 2.13 – 2.25**, and δ_{cg} given by **Eqn. 2.35** above. This procedure allows us to calculate the fiber-bridging stress σ indirectly as a function of the total crack opening δ_{tot}. The flow chart of the numerical procedure for computing the bridging stress vs. crack opening displacement relationship can be found in **Fig. 2.17**.

2.4.3 Experimental Validation of σ(δ) Curve

Experimental Determination of σ(δ) Curve

To verify the fiber-bridging model, deformation-controlled tensile tests were conducted on notched coupon specimens to measure the $\sigma(\delta)$ relationship of PVA-ECC. Due to the multiple cracking nature of PVA-ECC with close crack spacing (1mm on average), it is

challenging to measure the $\sigma(\delta)$ curve over a single crack. (A reasonably sized gauge length will cover the opening displacements of a number of subparallel microcracks, and therefore masks the true value of δ.) An alternative way to fulfill the purpose of verifying the model experimentally is to reduce the fiber content (< 2 vol.%) so that single cracking occurs. Although interfacial bond properties may change due to the reduction of fiber, the mechanisms, i.e. two way fiber pullout, Cook-Gordon effect, etc., which govern the fiber bridging behavior should nominally be unaltered. Once the validity of the fiber-bridging model is proven, the $\sigma(\delta)$ curve of higher fiber content can be calculated by using the corresponding micromechanics parameters.

In this study, PVA-ECC mix 45 (M45) which is the most widely used ECC in the field was adopted for measuring the $\sigma(\delta)$. The mix proportion of M45 can be found in **Table 2.1**. The ingredients of PVA-ECC include Type I ordinary Portland cement, ASTM Class F fly ash, fine silica sand with a mean size of 110 μm, water, superplasticizer, and PVA fibers. Generally, the fiber content in PVA-ECC is 2 vol.%. In this study, M45 matrix with 0.5 vol.% and 0.1 vol.% were used in order to generate a single crack under uniaxial tensile loading. The dimensions of the PVA fiber are 12 mm in length and 39 μm in diameter on average. The nominal tensile strength of the fiber is 1600 MPa and the density of the fiber is 1300 kg/m^3. The fiber is surface-coated by oil (1.2% by weight) in order to reduce the fiber/matrix interfacial bond strength. This decision was made through ECC micromechanics material design theory and has been experimentally demonstrated from previous investigations [13, 23].

A Hobart mixer with 10L capacity was used in preparing the PVA-ECC mixes. Solid ingredients, including cement, fly ash, and sand, were first mixed for a couple of

minutes. Water and superplasticizer were then added into the dry mix and mixed for another three minutes. The liquefied fresh mortar matrix should reach a consistent and uniform state before adding fibers. After examining the mortar matrix and making sure that there is no clump at the bottom of the mixer, PVA fibers were slowly added into the mortar matrix and mixed until all fibers are evenly distributed. The mixture was then cast into coupon molds. The specimens were demolded after 24 hours, and air cured at 50±5% RH, 23±2 ^{0}C until the age of 28 days for testing.

Notched coupon specimens with thickness 13mm, width 76mm, and height 90mm were used to conduct uniaxial tensile test at the age of 28 days. The 2mm wide circumferential notch was produced before testing by a diamond saw. Deep notches (6mm) were generated at two laterals for crack initiation and shallow notches (2mm) were produced on the front and back surfaces as crack guides (**Fig. 2.18**). A servohydraulic testing system was used in deformation-controlled mode to conduct the uniaxial tensile test. The loading rate used was 0.0001 mm/s to simulate a quasi-static loading condition. Aluminum plates were glued both sides at the ends of coupon specimens to facilitate gripping. Two extensometers with 5mm gauge length were attached to the laterals of the specimen and across the notches to measure the crack opening δ. The test setup is shown in **Fig. 2.19**. The crack opening was extracted from the total average displacement across the crack measured by the two extensometers and elastic deformation outside the crack but within the 5mm gauge length was subtracted out.

Determination of micromechanics parameters

As can be seen, the $\sigma(\delta)$ model is related to a set of micromechanics parameters, including interface chemical bond G_d, interface frictional bond τ_0, and slip-hardening coefficient β accounting for the slip-hardening behavior during fiber pullout. In addition, snubbing coefficient f and strength reduction factor f' are introduced to account for the interaction between fiber and matrix as well as the reduction of fiber strength when pulled at an inclined angle. Besides the interfacial properties, $\sigma(\delta)$ curve is also governed by the matrix Young's modulus E_m, matrix tensile strength σ_m, matrix spalling coefficient k, fiber content V_f, fiber diameter d_f, length L_f , and Young's modulus E_f, apparent fiber strength σ_{fu}, and Cook-Gordon parameter α.

In order to calculate the analytical $\sigma(\delta)$ curve, micromechanics parameters of ECC were independently measured or deduced. **Tables 2.2** and **2.3** summarize the values of those micromechanics parameters used in the model calculation. Among them, all fiber parameters E_f, L_f, and d_f are measurable with good accuracy. The apparent fiber strength σ_{fu} and fiber strength reduction coefficient f' were measured by single fiber in-situ strength test [7] and interface properties τ_0, G_d, and β were measured by single fiber pullout test [17]. To measure the interfacial bond properties of ECC with different fiber volume content, M45 mortar matrix with the presence of 0.1, 0.5, and 2 vol.% PVA fibers were cast into molds and single PVA fiber was surrounded by the ECC matrix. As can be seen from **Table 2.3**, interfacial bond strength reduces with the increase of fiber volume content. This may be attributed to the higher air content and therefore loose pore structure in ECC when the fiber volume increases.

Wu [2] measured f values using the early developing version of the PVA fiber that has only 0.5% oiling coating instead of 1.2% used in the current commercialized PVA REC-15 fiber, and found that the f value ranged from 0.2 to 0.8. Considering that snubbing coefficient is closely related to fiber surface frictional coefficient, which decreases significantly with increase of oiling coating content [23], the lower end value of snubbing coefficient f = 0.2 is hence assumed in this study.

Matrix Young's modulus E_m was determined from the initial slope of the tensile stress-strain curve and the matrix tensile strength σ_m was deduced based on a wedge splitting test. The wedge splitting test [24] measured the matrix fracture energy and σ_m was calculated by means of inverse analysis [25, 26]. Factor k can be calibrated by measuring the spalling size. Matrix micro-spalling was collected during the uniaxial tensile test and the maximum size of matrix micro-spalling was 30 μm. Matrix spalling coefficient k = 500 is chosen such that the maximum spalling size calculated from **Eqn. 2.22** (see **Fig. 2.14**) will not exceed the size observed in microscopic observation, i.e. 30 μm in PVA-ECC system.

To determine the Cook-Gordon parameter α, Bentur [27] suggested $\alpha = 2d_f$ to $10d_f$ for steel fiber in neat cement paste. Li et al. [22] adopted $\alpha = 15d_f$ for polypropylene fiber-reinforced concrete and found that resulting $\sigma(\delta)$ curve matched those of experimental data very well. For the PVA-ECC, a smaller Cook-Gordon parameter is expected due to the hydrophilic nature of PVA fiber which may introduce a stronger interface chemical bond between fiber and matrix. For lack of more precise experimental evidence, the low end suggested by Bentur, $\alpha = 2d_f$ is adopted in this study.

Comparison between model prediction and experimental results

The analytical $\sigma(\delta)$ curve can be calculated as long as all micromechanics parameters are determined. 2-D random fiber distribution (**Eqn. 2.30**) was assumed in calculating the fiber-bridging model for comparison with experimental $\sigma(\delta)$ curves measured from coupon specimens. Because the thickness of the coupon specimen is small (13 mm) when compared with fiber length (12 mm), fiber is most likely distributed in a 2-D randomness manner. **Figure 2.20** shows the predicted fiber-bridging constitutive law (solid line) for M45 with V_f = 0.5 and 0.1 vol.%, respectively. In calculating these two curves, all micromechanics parameters for model input are listed in **Tables 2.2** and **2.3**. Post-cracking $\sigma(\delta)$ curve (hollow circular dots) measured experimentally are also plotted together with the model prediction in **Fig. 2.20** for comparison purpose. At least 6 uniaxial tensile tests were conducted and reported in **Fig. 2.20** for each fiber volume.

The scattered $\sigma(\delta)$ curves obtained from experiments are results of material inhomogeneity, e.g. varying number of bridging fiber across crack plane for the six different specimens. Although the peak bridging stress varies in a wider range, the corresponding crack opening δ remains fairly constant. This is likely a result that with larger number of fibers, a higher load can be reached, but the crack opening will be limited by an effectively stiffer (averaged) fiber spring. This observation is also consistent with the two sets of experimental data of $V_f = 0.1$ and $V_f = 0.5$. As can be seen, the predicted $\sigma(\delta)$ curves which represent the mean fiber-bridging constitutive law fit well with experimental observations and the validity of this newly developed $\sigma(\delta)$ model is therefore confirmed.

2.4.3 Discussion

The middle curve in **Fig. 2.21(a)** displays the predicted mean $\sigma(\delta)$ curve of PVA-ECC M45 with V_f = 2 vol.% based on the corresponding micromechanics parameters and fiber-bridging model. As can be seen, the peak bridging stress is 6.7 MPa and the corresponding crack opening is 130 μm. These values are considerably larger than the observation from composite tensile test result, in which composite ultimate tensile stress is around 5 MPa and the average crack opening is around 60 μm as depicted in **Fig. 2.2**.

The middle curve in **Fig. 2.21(a)** displays the predicted mean $\sigma(\delta)$ curve of PVA-ECC M45 with V_f = 2 vol.% based on the same micromechanics parameters and fiber-bridging model. As can be seen, the peak bridging stress is 6.7 MPa and the corresponding crack opening is 130 μm. These values are considerably larger than the observation from composite tensile test result, in which composite ultimate tensile stress is around 5 MPa and the average crack opening is around 60 μm as depicted in **Fig. 2.2**.

It should be pointed out that in the composite tensile test, multiple crack surfaces are generated during the strain-hardening stage and the final failure plane is the one with the weakest bridging (lowest tensile strength capacity). If material inhomogeneity in ECC is inevitable, the observed 5 MPa ultimate tensile stress in the composite tensile test (**Fig. 2.2**) actually represents the lowest peak fiber-bridging stress. This observed value (5 MPa) is 25% less than the calculated peak bridging stress (6.7 MPa) and is likely attributed to varying number of bridging fiber from one crack plane to another. To simulate this variation, $\sigma(\delta)$ curves with V_f = 1.5 vol.% (25% less) and 2.5 vol.% (25% more) were calculated using the same set of micromechanics parameters as 2 vol.% except the fiber volume was changed as the lower and higher bonds of bridging,

respectively. These three curves represent the variation of σ(δ) curve in PVA-ECC M45, among the multiple crack planes.

Following the discussion above, the weakest fiber-bridging σ(δ) curve is expected to dominate the composite tensile behavior. Damage localization in ECC occurs as soon as the weakest bridging plane reaches its peak bridging stress (5 MPa for M45). **Figure 2.21(b)** displays a magnified view of **Fig. 2.21(a)**. As can be seen, crack opening δ for each σ(δ) curve at σ = 5 MPa varies from 37 μm to 133 μm with a mean of 62 μm. This predicted mean crack opening is remarkably consistent with the average crack opening observed from the composite uniaxial tensile test (**Fig. 2.2**).

To evaluate contributions to the σ-δ of each of the three newly introduced mechanisms, theoretical σ(δ) curves calculated by various models are presented in **Fig. 2.22**. When only one-way pullout is considered, e.g. previous simplified model by Lin et al. [5], the predicted peak bridging stress and corresponding crack opening are 6.2 MPa and 93 μm respectively. If two-way pullout is accounted for but without considerations of spalling and Cook-Gordon effects, a peak stress 6.3 MPa is attained at crack opening of 130 μm. When both two-way pullout and matrix spalling are considered but without consideration of Cook-Gordon effect, the model predicts a peak stress 6.7 MPa at 131 μm. If all three newly introduced mechanisms are accounted for, the predicted peak bridging stress and corresponding crack opening are 6.7 MPa and 133 μm respectively. A direct comparison between these four curves reveals that two-way pullout is most responsible for overcoming the underprediction of crack opening in PVA-ECC system using the previous model version. The contribution of matrix spalling to crack opening is rather small. Matrix spalling, which effectively reduces the inclination angle for individual

fibers, delays fibers to rupture, and therefore raises the peak bridging stress. In contrast, if there is no matrix spalling, fiber with large inclination angle will rupture at much earlier stage due to higher fiber strength reduction. Cook-Gordon effect does not show remarkable impact on crack opening due to the assumption of small Cook-Gordon parameter $\alpha = 2d_f$ which is likely the case for the hydrophilic PVA fiber. However, the Cook-Gordon effect may play an important role in other fiber-reinforced ECC systems, such as polyethylene (PE) and polypropylene (PP) fibers, in which the fiber/matrix interface chemical bond is much weaker (close to zero due to the hydrophobic nature of PE and PP fibers) and a larger Cook-Gordon parameter α is expected.

2.4.4 Summary

An analytical fiber-bridging model was reviewed and experimentally verified in this subsection. The new model improves over an earlier version by including three new mechanisms of fiber/matrix interactions in order to accurately predict the $\sigma(\delta)$ curve of ECC in general, and improve accuracy of crack opening prediction in particular. For the PVA-ECC system, it was found that two-way fiber pullout mechanism is most responsible for enhancing the correction prediction of the crack opening. The predicted crack opening based on this model can reproduce those in PVA-ECC composite tests when variability in bridging fiber volume from one crack plane to another is recognized.

Although this model is suitable especially for the PVA-ECC system, it is likely applicable to other fiber systems as long as the appropriate governing fiber/matrix interaction mechanisms are captured. This revised fiber-bridging model will greatly improve ECC micromechanics-based material design theory in terms of crack width

(which strongly governs structural durability) and composite tensile ductility (which strongly governs structural load carrying capacity and deformability).

2.5 Micromechanics-based Composite Optimization and Component tailoring

This subsection give specific examples of fiber, matrix, and interface tailoring. Special attention is given to polyvinyl alcohol (PVA) fiber as this fiber has been one of the dominant synthetic fibers used in the fiber cement industry and to polypropylene (PP) fiber which appears to gain increasing acceptance with property improvements in recent years. A a new version of ECC incorporating high tenacity polypropylene fiber is developed as a result.

It is well known that fibers are essential for the ductile performance of fiber cement, a composite with a highly brittle matrix. In the past, this ductile performance has been supported by the use of low cost asbestos fiber in relatively large amount, 9 to 14% by weight [28]. With the world-wide trend of banning asbestos fiber due to concerns of impact on human health, the industry is increasingly turning to synthetics. Some synthetic fibers can be relatively expensive, while others appear to limit the composite performance. However, synthetic fibers offer the opportunity for tailoring – in fiber length and diameter, mechanical characteristics, surface treatment, etc. It is only natural, therefore, to ask the question how fiber cement should be designed, so that optimal composite performance is achieved at the lowest cost.

The micromechanical model for randomly oriented discontinuous fiber reinforced brittle matrix composites described in the previous subsections may shed light on fiber

cement optimization. Specifically, this model can be used to address optimal mix composition of fiber, matrix and interface characteristics in order to achieve maximum tensile ductility while minimizing the amount of fiber. Emphasis is placed on the need for a holistic approach in composite design. Further, the model can be used to guide the tailoring of fiber characteristics, including surface treatment, or the tailoring of the matrix composition, including the use of artificial defects.

2.5.1 Illustration of Model-Based Composite Optimization

As described in the previoius subsections, the micromechanics-based strain-hardening model links material microstructures and composite behavior and serves as a tool to guide composite optimization through properly tailored fiber, matrix, and interface properties. In this subsection, illustration of model for composite optimization is described. Focus is placed on thin sheet cement composites reinforced with randomly oriented discontinuous PP fibers or PVA fibers.

Figure 2.23 shows the calculated critical fiber volume as a function of interface frictional bond for achieving saturated multiple cracking and tensile strain-hardening behavior of a PP fiber (control PP) reinforced thin sheet cement composite based on the micromechanics model with 2-D fiber orientation assumption. The 2-D fiber orientation assumption is particularly applicable for the thin sheet fiber cement due to process induced fiber layering and sheet thickness smaller than fiber length. The two curves in **Fig. 2.23(a)** relating V^f_{crit} to τ_0 were calculated by specifying all other micromechanical parameters (**Table 2.4**) and plugging them into the strain-hardening criteria, i.e. energy

criterion and strength criterion in **Eqns 2.1** and **2.3**, respectively. The micromechanical parameters were independently measured or deduced [28, 29].

Due to the random nature of pre-existing flaw size and fiber distribution in cement composites, a large margin between J'_b and J_{tip} as well as σ_{fc} and σ_0 is preferred. Materials with larger values of PSH indices should have a better chance of saturated multiple cracking. Unsaturated PSH behavior often leads to small tensile strain capacity and large variability of tensile ductility of the composites. It has been demonstrated experimentally that polyethylene (PE) fiber reinforced cement composites with performance indices $J'_b/J_{tip} > 3$ and $\sigma_0/\sigma_{fc} > 1.2$ produce saturated PSH behavior [7]. However, for the PVA fiber reinforced cement composites, the crack patterns observed required modification of the σ_0/σ_{fc} index to be greater than 1.45 instead of 1.2 [2]. This is due to higher rupture tendency, i.e. lower fiber strength and higher interfacial bonds for the PVA fiber, when compared with PE fiber. This results in larger variation in the bridging capacity, thus requiring higher margin between the first crack and the peak bridging strength. A similar argument applies to the PP fiber reinforced composites. Here, although the interfacial bond properties of PP fiber cement are similar to that of PE fiber cement (due to the hydrophobic surface of both fibers), the fiber strength of PP is much lower than that of PE [7]. In this study, a PSH strength index $\sigma_0/\sigma_{fc} > 2$ is assumed for the PP fiber system. Further experimental confirmation of this assumption is required. To ensure saturated multiple cracking for the PVA and PP fiber composites, these modified values of performance indices (PSH strength value = 1.45 and 2 for PVA and PP respectively; PSH energy value = 3 for both) will be utilized in the following calculations.

As can be seen from **Fig 2.23(a)**, V^f_{crit} calculated from the strength criterion approaches a constant at high frictional bond and sharply increases at low friction area (τ_0 < 0.3 MPa). The bridging strength is known to be governed by fiber strength, fiber volume, and interfacial properties, e.g. τ_0 and G_d. At higher interfacial friction; however, fiber rupture dominates over fiber pull-out so that the bridging strength becomes insensitive to τ_0. Because fiber strength is given, fiber volume approaches to a steady value in order to satisfy the strength criterion (σ_0 = 5MPa). At low friction; however, fiber pull-out prevails over fiber rupture and bridging strength is now insensitive to the fiber strength and governed by fiber volume and τ_0. High amount of fiber is therefore required to obtain adequate bridging strength of 5MPa.

Interestingly, a concave V^f_{crit} curve was obtained based on the energy criterion. The energy criterion requires the complementary energy of $\sigma(\delta)$, hatched area in **Fig. 2.3**, to reach a specified value (15 J/m^2) in order to ensure robust steady-state cracking. In general, the bridging strength decreases with reduction of τ_0, resulting in low J'_b at low τ_0 region. At high τ_0 end, the stiffness of the fiber bridging "springs" (i.e. the initial slope of the $\sigma(\delta)$) keeps rising, resulting in a decrease in J'_b also. High fiber fraction is therefore required at both high and low τ_0 in order to satisfy the 15 J/m^2 complementary energy. An optimum point, i.e. a balanced interfacial friction (τ_0 around 0.25 MPa) which meets the specified J'_b at minimum fiber fraction, exists in the energy curve.

Strain-hardening behavior relies on the satisfaction of both the strength and energy criteria. Therefore, the minimum fiber amount to achieve saturated multiple cracking is the combination of the two curves whichever has higher V^f_{crit} as depicted in **Fig. 2.23(b)**. The combined curve shown in **Fig. 2.23(b)** indicates that the optimum

point for the strain-hardening behavior of this control PP-fiber cement falls in the range of 3.5 vol.% fiber content with 1.5 MPa interface frictional bond strength. However, due to the hydrophobic nature of PP fiber, the interfacial bonds are usually very weak, e.g. $G_d \sim 0$ J/m^2 and τ_0 is usually in the range of 0.2 – 0.3 MPa [28]. Therefore, much higher fiber content (7 – 13 vol.%) is usually adopted in ductile PP-fiber cement materials [30, 31].

Low tensile strength has been recognized as a major drawback of PP fiber. High tenacity PP fiber was therefore developed. **Fig. 2.24** shows the effect of fiber strength on V^f_{crit} vs τ_0 curves. These curves were calculated using the same set of micromechanical parameters as for the control PP fiber, except that the fiber strength was increased to 928 MPa [29]. As can be seen, enhanced fiber strength greatly reduces V^f_{crit} at higher friction ($\tau_0 > 0.3$ MPa) for both the strength and energy curves as well as the combined curve. Meanwhile, for the strong PP case, strength criterion overrides the energy criterion and dominates the combined V^f_{crit} curve in the range of τ_0 from 0 to 5 MPa. For ordinary high tenacity PP fiber with frictional bond between 0.2 and 0.3 MPa; however, V^f_{crit} over 4% is still needed to achieve robust strain-hardening. To take advantage of the improved fiber strength in high tenacity PP fiber, it is also necessary to increase the interface frictional bond τ_0 to around 1 MPa or above. This example underlines the importance of understanding the governing mechanisms through micromechanics-based models in design of ductile composites.

Figure 2.25 illustrates the effect of fiber length on the V^f_{crit} curve. All micromechanical parameters used in calculating the long PP fiber case are identical with the control PP fiber except that the fiber length is changed from 8 mm to 19 mm. In

contrast to increase of fiber strength, both individual strength- and energy-based curves and the combined curve of long PP fiber drop significantly at the low τ_0 end ($\tau_0 < 1$ MPa) and do not change much when τ_0 is beyond 1 MPa. This calculation indicates that increase of fiber length is especially beneficial for fiber reinforced composite with low interfacial friction in achieving strain-hardening behavior, which is the case for the normal PP-fiber cement. However, realistically feasible fiber length may be limited by processing requirements.

PVA fiber featuring high stiffness, high tensile strength, and strong interfacial bonding has been one of the dominant synthetic fibers used in the fiber cement industry. The relative high cost of PVA fiber prohibits usage of high fiber fraction in the cost-sensitive construction industry. Therefore, composite optimization of PVA-fiber cement becomes even more critical and valuable. **Table 2.5** lists the micromechanical parameters used in calculating the V^f_{crit} plots for the PVA-fiber cement [21, 23]. The high interface chemical bond $G_d = 5$ J/m^2 measured is due to the hydrophilic nature of virgin PVA fiber (G_d5PVA) with surrounding cement matrix. Crack tip bridging by such fibers results in a high matrix cracking strength of 4.5 MPa [21, 23]. **Figure 2.26** shows V^f_{crit} as a function of τ_0 for the control PVA fiber (G_d5PVA) cement system. As can be seen, the energy criterion overwhelms the strength criterion and governs the composite behavior. Due to the strong hydrophilic tendency of the surface of PVA fiber, a high interface frictional bond is usually found, e.g. τ_0 can be as high as 5.7±0.6 MPa [32]. Therefore, increase of PVA fiber (G_d5PVA) strength is expected to greatly reduce V^f_{crit}. In contrast, increase of PVA fiber (G_d5PVA) length will not improve the composite

ductility much due to high τ_0 in the PVA fiber (G_d5PVA) cement system (similar to that shown in **Fig. 2.25** for PP fiber at high τ_0).

An alternative route would be to alter the chemical bonding as illustrated in **Fig. 27**. The micromechanical parameters used in calculating the V^f_{crit} plots for G_d2PVA fiber system are identical with the control PVA system (G_d5PVA), except that the chemical bond was lowered from 5 to 2 J/m^2 and the matrix cracking strength was reduced from 4.5 MPa to 3.5 MPa due to the lower G_d [21, 23]. As can be seen, lowering G_d greatly shifts the energy curve down at all τ_0 and the strength curve is also dragged down mainly caused by the reduction of σ_0 (from 6.5 to 5 MPa allowed by the reduction in σ_{fc}). In the case of G_d2PVA, the combined curve indicates that lowering G_d is an effective way to reduce the V^f_{crit} at all τ_0 for achieving tensile strain-hardening behavior.

In the previous discussion, focus has been placed on altering the fiber and interface properties in order to shift the V^f_{crit} curve down. In fact, matrix tailoring, e.g. manipulating the pre-existing flaw size distribution and the matrix fracture toughness, can be the third element in this micromechanics-based composite optimization [21]. For a brittle matrix composite, the stress to initiate a crack from a pre-existing defect, the cracking strength σ_{fc} is largely determined by the largest flaw normal to the maximum principle tensile stress. The maximum fiber bridging stress σ_0 imposes a lower bound on the critical flaw size such that only flaws larger than this critical size can be activated and contribute to multiple cracking. Insufficient number of such flaws in the matrix causes unsaturated multiple cracking, and therefore a larger PSH strength index (σ_0/σ_{fc}) is required for saturated multiple cracking. A practical approach to controlling the pre-existing flaws, i.e. introducing artificial defects with prescribed size distribution, has

been demonstrated and proved an efficient way to achieving robust strain-hardening behavior [33]. **Figure 2.28** displays the effect of introducing artificial flaws into matrix. All micromechanical parameters are identical with G_d2PVA except that a smaller performance index (σ_0/σ_{fc} is set to be 1.15 instead of 1.45) was used to reflect the higher probability of reaching saturated multiple cracking with emplacement of artificial flaws. Note that the performance index J'_b/J_{tip} remains the same because implantation of artificial defects does not affect the propagation of cracks. Therefore, the same energy curves can be expected for the G_d2PVA(flaw) case in **Fig. 2.28(a)**. As can be seen, strength curve shifts down and the combined curve in **Fig. 2.28(b)** indicates that the minimum V^f_{crit} can be further lowered due to intentionally implanting of artificial defects into the matrix.

Another approach to matrix modification is to limit the matrix toughness J_{tip}. **Figure 2.29** illustrates the effect of matrix toughness on the V^f_{crit} plot. The micromechanical parameters are identical with G_d2PVA except a lower J_{tip} (5 → 3.3 J/m2) and σ_{fc} (3.5 → 2.5 MPa) were used. The same performance indices (J'_b/J_{tip} = 3 and σ_0/σ_{fc} = 1.45) were adopted to calculate the strength and energy curve in **Fig. 2.29(a)**. It is clear that both the energy and strength curves as well as the combined curve shift down at all range of τ_0. It can be concluded that low matrix toughness is beneficial for multiple cracking. However, excessively low matrix toughness may lead to low compressive strength, and is generally not desirable.

2.5.2 Examples of Composite Optimization

The previous section illustrates the concepts of composite optimization by means of micromechanics-based strain-hardening model. Through the guidance of the model, composite tensile strain-hardening behavior can be achieved by adopting minimum amount of fiber with properly tailored fiber, matrix, and interface. In this section, examples are given to demonstrate the practice of composite optimization of PVA and PP fiber reinforced cement composites, respectively.

As depicted in **Fig. 2.26(b)**, virgin PVA fiber has strong interfacial chemical and frictional bonds, which demands high amount of fiber (4 – 6 vol.%) in order to achieve strain-hardening behavior. From micromechanics model (**Fig. 2.27(b)**), lowering chemical and frictional bonds are effective approaches to reduce V^f_{crit}. This can be realized by modifying the surface properties of PVA fiber. It is known that the strong interfacial bonds of PVA fiber are introduced by its hydrophilic surface. Therefore, a feasible way to reduce the hydrophilic tendency would be coating the surface of PVA fiber with a thin layer of oiling agent [23]. **Figure 2.30** shows the effect of surface coating on interfacial bonding. As can be seen, both the chemical and frictional bonds drop significantly with increase amount of surface oiling (wt.%). When the oil content reaches 0.8 to 1.2%, the τ_0 and G_d drops to 1-2 MPa and about 2 J/m^2, respectively. According to **Fig. 2.27(b)** – G_d2PVA , such interface property values are optimal for design of a ductile fiber cement with 2 vol.% fiber content.

Figure 2.31 displays the predicted σ-δ curves of virgin PVA fiber (control) as well as surface-coated (1.2 wt.% oiling agent) PVA fiber based on the micromechanics model. The micromechanical parameters used in calculating the $\sigma(\delta)$ are listed in **Table**

2.6. Meanwhile, the resulting complementary energy and peak bridging strength of $\sigma(\delta)$ are also reported in **Table 2.6**. As can be seen, J'_b and σ_0 of the control PVA system do not satisfy the strain-hardening criteria. The surface-coated PVA system; however, can meet both the strength and energy requirement. The tensile stress-strain curve of control PVA and 1.2% surface-coated PVA fiber reinforced cement composites are shown in **Fig. 2.32**, respectively. As can be seen, significant improvement in terms of tensile ductility was found in the surface-coated PVA fiber system, which validates the effectiveness of micromechanics model and demonstrates the feasibility of composite optimization.

For the PP fiber system, increase of fiber strength along with higher frictional bond τ_0 could be an efficient way to improve composite ductility as illustrated in **Fig. 2.24(b)**. The weak bonding of ordinary PP fibers can be attributed to their low surface energy (hydrophobic character) and low surface roughness. It has been reported that surface treatment with plasma can increase the surface energy of hydrophobic fiber, and therefore interfacial bonding [34]. Another approach would be to produce PP fibers whose sheath layer composition, and thus surface properties, differs from their core [29].

High tenacity PP fibers with different sheath material and/or surface coating produced by Redco, Belgium and Brasilit, Brazil were used in producing PP-ECC. The structure of high tenacity PP fiber with sheath and/or surface coating can be found in **Fig. 2.33**. As can be seen, high molecular weight PP resin is used in the core to achieve high stength. Geometry of spinning melting heads, spinning holes of spinning melting heads, and cooling rate can also affect fiber strength. Different additives may be used in the sheath layer to have different surface energy and roughness, and therefore changing the interfacial bond strength with cement matrix. The thickness of the sheath layer can also

affect the interfacial bond strength. However, increase in the thickness of the sheath layer usually causes strength reduction and cost increase. Therefore, one should always on the one hand optimize the sheath layer for interfacial bond strength to cement, while minimizing the loss of strength and the cost increase associated with the presence of additives, on the other hand. Besides adding additive into the sheath layer, surface coating also help improve interfacial bond strength and easy to implement. A broad range of additives in view of their contribution to increasing the interfacial bond strength and improving the fiber cement properties, with or without additional surface coating has been investigated [29].

Table 2.7 illustrates the interfacial bond strength, as measured by the single fiber pullout tests, of several high tenacity PP fibers with and without different types of treatment. As can be seen, proper treatment can increase the interfacial frictional bond strength significantly, from 0.2 MPa and up to 1.51 MPa. As indicated in **Fig. 2.24(b)**, increase of fiber strength as well as adequate frictional bond strength above 1MPa are required to achieve strain-hardening behavior. Therefore, use of high tenacity PP fibers with improved bond strength to produce strain-hardening PP-ECC are very promising.

Figure 2.34 shows the predicted σ-δ curves of control PP fiber system along with the copolymer C PP fiber system. The micromechanical parameters for these two systems are listed in **Table 2.8**. As can be seen, the strength and τ_0 are greatly improved and the copolymer C PP fiber satisfy the strain-hardening criterion at 2 vol.% fiber fraction, which is identical with the prediction in **Fig. 2.24(b)**.

Based on the guidance of the micromechanical model, strain-hardening PP-ECC incorporating 2 vol.% high tenacity PP fiber has been developed. **Figure 2.25** shows the

tensile stress-strain curve of six PP fiber cements, in which **(a)** incorporated an ordinary high tenacity PP fiber (HTPP 1) as a control, and **(b)** to **(f)** adopted treated high tenacity PP fibers with improved bond strength (HTPP 2 to 6). HTPP 2 to 4 are produced by Redco, Belgium and HTPPs 5 and 6 are supplied by Brasilit, Brazil. The mechanical, geometric, and bond properties of those PP fibers can be found in **Table 2.9**. Notice that a longer fiber length was intentionally chosen for the ordinary high tenacity PP fiber. The analysis in **Fig. 2.25** indicates that longer fiber length is beneficial for fibers with low frictional bond, which is the case of ordinary high tenacity PP fiber. Therefore, use of longer fiber gives a better chance for the tensile strain-hardening behavior in ordinary high tenacity PP fiber cement. However, longer fiber length can greatly reduce the workability and introduce poor fiber dispersion. In this study, an ordinary high tenacity PP fiber with 12mm in length was used in order to obtain decent workability and fiber dispersion. Same mix proportaion was used to produce the six PP fiber cements and the mix proportiaon can be found in **Table 2.10**.

Despite the use of long fiber, ordinary high tenacity PP fiber cement still shows tension softening behavior as illustrated in **Fig. 2.35(a)**. For HTPP 2 to 6 fiber cements; however, strain-hardening behavior with great improvement in the tensile ductility (2-6%) was obvious. Among PP-ECC 2 to 4 adopting HTPP fibers produced by Redco, Belgium, it is interesting to show that PP-ECC 4 has the highest composite tensile strength as well as the highest tensile strain capacity despite the fact that the HTPP 4 fiber itself has the lowest fiber strength among those high tenacity PP fibers. This may be attributed to a stronger interfacial bonding within PP-ECC 4 resulting in a higher bridging strength and a larger complementary energy. **Figure 2.36** displays the crack pattern of PP-ECC 2 to 4.

Uniformly distributed and saturated cracks were found in all three PP-ECCs. From the crack spacing and crack width, it suggests that HTPP 4 has the strongest interfacial bonds and HTPP 3 has the weakest interfacial bonds. This observation further confirms and explains the composite behavior as indicated above. Therefore, fiber strength is not the only factor that dominates the composite behavior. Control of the synergistic interaction between fiber, matrix, and interface is the key to optimize composite behavior. **Figure 2.37** shows the bending behavior of PP-ECC 2 to 4. Again, PP-ECC 4 has the best bending ductility and bending strength. PP-ECCs 5 and 6 using HTPPs 5 and 6 produced by Brasilt, Brazil also show tensile strain-hardeing behavior (**Fig. 2.35(e)** and **(f)**). The properties of HTPPs 5 and 6 are identical expect for the longer fiber length of HTPP 6. It is not surprising that PP-ECC 6 has much improved tensile ductility than that of PP-ECC 5. As predicted from the micromechanics model **Fig. 2.25**, longer fiber length promotes strain-hardening as interfacial frictional bond is below 1 MPa which is the case for the brasilit HTPP fibers (0.7MPa).

Table 2.11 gives the cost comparison of PVA fibers and HTPP fibers and the resulting PVA-ECC and HTPP-ECC. As can be seen, the cost of HTPP-ECC is drastically reduced about 60% that of PVA-ECC. The wider availiability of HTPP fibers and the cost benefit of HTPP-ECC make it a desirable alternative in replace of current PVA-ECC. With a further imporvement of tensile and compressive strength of HTPP-ECC, it can be expected that this new version of ECC will have a good chance to be widely adopted in the full scale field applications.

2.5.3 Summary

Micromechanics-based model linking characteristics of composite constituents to composite tensile strain-hardening behavior can be used for systematic optimization of composite tensile ductility while minimizing the fiber content. This approach is holistic, simultaneously taking into account the interacting effects of fiber, matrix, and interface properties on composite response. Due to the large number of micromechanical parameters (thirteen) governing composite response, this micromechanics-based approach for composite optimization is much more efficient than the traditional empirical trial-and-error approach.

It is shown that in general, the strength and energy criteria must be considered to ensure adequate initiation of multiple cracks, and that cracks initiated propagate in the flat steady-state cracking mode, in order to achieve saturated multiple cracking so that a robust ductile composite is assured. In the case of (control) PP-fiber cement, the critical fiber content to achieve strain-hardening is governed by both the strength and energy criteria, depending on the interfacial frictional bond strength. In the case of (strong) PP-fiber cement, the critical fiber content is controlled only by the strength criterion. In the case of (control) PVA-fiber cement; however, the critical fiber content is dominated by the energy criterion.

The micromechanical-based model can be translated into specific guidance for composite component tailoring. Parametric studies reveal that enhanced fiber strength may benefit composite ductility at high interfacial friction condition. In contrast, increase of fiber length promotes composite multiple-cracking behavior primarily at low τ_0 region. Lowering interface chemical bond usually decreases the critical fiber volume for

achieving tensile strain-hardening. Matrix tailoring, including intentionally implanting artificial defects and reduction of matrix toughness, can be an alternative for composition optimization.

The micromechanics-based model suggests very different engineering strategies for different types of fiber systems. In the case of PVA fiber, surface treatment leading to a reduction of bond properties is beneficial to composite ductility. Specifically, G_d and τ_0 values of 1.6 J/m^2 and 1.1 MPa leads to a composite with high tensile ductility at fiber content of 2 vol.%. In contrast, increase in frictional bonding greatly enhances composite performance when PP fiber is utilized. Here, τ_0 of 0.7 to 1.5 MPa for an enhanced fiber strength of 750-850 MPa is recommended. Experimental data show significant improvements in composite ductility when these fibers are properly tailored, thus confirming the effectiveness of the micromechanics approach. Although applied to two specific fiber types, the theoretical tools developed are expected to be applicable to a wide range of fiber types and brittle matrix types.

2.6 Conclusions

In this chapter, ECC micromechanics-based design theory are overviewed. A numerical model is used to study crack propagation mode (Griffity type vs. steady state flat cracking) and the condition for steady state crack propagation, $J'_b > J_{tip}$, is verified through the simulation. An improved fiber bridging constitutive model considering two-way fiber pullout, matrix micro-spalling, and Cook-Gordon effect is proposed and verified with experimentally measured $\sigma(\delta)$ curves. The new model significantly

improves the prediction of steady state crack opening, one of the major performance concerns in material design for durability. ECCs incorporating high tenacity PP fibers are developed through the guidance of micromechanics-based design theory. This demonstrates the effectiveness of micromechanics approach in composite optimization.

Table 2.1 – Mix proportions of PVA-ECC (M45)

V_f (vol.%)	Cement (kg/m^3)	Fly Ash (kg/m^3)	Sand (kg/m^3)	Water (kg/m^3)	SP (kg/m^3)	PVA Fiber (kg/m^3)	Total (kg/m^3)
2	571	685	456	332	6.8	26	2076.8
0.5	571	685	456	332	6.8	6.5	2057.3
0.1	571	685	456	332	6.8	1.3	2052.1

Table 2.2 – Micromechanics parameters used as model input

Fiber parameters				Interface parameters			Matrix parameters		
d_f (μm)	L_f (mm)	E_f (GPa)	σ_{fu} (MPa)	f	f'	α (μm)	E_m (GPa)	σ_m (MPa)	k
39	12	22	1060	0.2	0.33	78	20	5	500

Table 2.3 – Interfacial properties of ECC

Matrix type	τ_0 (MPa)	G_d (J/m^2)	β
0.1 vol.% PVA	1.91	1.24	0.63
0.5 vol.% PVA	1.58	1.13	0.60
2 vol.% PVA	1.31	1.08	0.58

Table 2.4 – Micromechanical parameters used in calculating V^f_{crit} of PP-fiber cement

	Fiber parameters				Interface parameters				Matrix parameters	Energy criterion		Strength criterion	
	d_f (μm)	L_f (mm)	E_f (GPa)	σ_{fu} (Mpa)	G_d (J/m^2)	β	f	f'	E_m (GPa)	J_{tip} (J/m^2)	J'_b (J/m^2)	σ_{fc} (MPa)	σ_0 (MPa)
Control PP	16.6	8	11.6	400	0	0.005	0.39	0.1	20	5	15	2.5	5
Long PP	16.6	19	11.6	400	0	0.005	0.39	0.1	20	5	15	2.5	5
Strong PP	16.6	8	11.6	928	0	0.005	0.39	0.1	20	5	15	2.5	5

Table 2.5 – Micromechanical parameters used in calculating V^f_{crit} of PVA-fiber cement

	Fiber parameters				Interface parameters				Matrix parameters	Energy criterion		Strength criterion	
	d_f (μm)	L_f (mm)	E_f (GPa)	σ_{fu} (MPa)	G_d (J/m^2)	β	f	f'	E_m (GPa)	J_{tip} (J/m^2)	J'_b (J/m^2)	σ_{fc} (MPa)	σ_0 (MPa)
G_d5 PVA	39	12	42.8	1070	5	0.05	0.5	0.32	20	5	15	4.5	6.5
G_d2 PVA	39	12	42.8	1070	2	0.05	0.5	0.32	20	5	15	3.5	5
G_d2PVA (flaw)	39	12	42.8	1070	2	0.05	0.5	0.32	20	5	15	3.5	4
G_d2PVA (lowJ_{tip})	39	12	42.8	1070	2	0.05	0.5	0.32	20	3.3	10	2.5	3.5

Table 2.6 – Micromechanical parameters used in calculating σ(δ) curve of PVA fiber cement

	Fiber parameters					Interface parameters					Matrix parameters	Model results	
	V_f (vol.%)	d_f (μm)	L_f (mm)	E_f (GPa)	σ_{fu} (MPa)	G_d (J/m^2)	τ_0 (MPa)	β	f	f'	E_m (GPa)	J'_b (J/m^2)	σ_0 (MPa)
Virgin PVA	2	39	8	42.8	1070	5.29	2.93	2.92	0.5	0.32	20	8.8 *(15)	5.6 *(6.5)
1.2% Coated PVA	2	39	8	42.8	1070	1.61	1.11	1.15	0.5	0.32	20	43.0 *(15)	5.1 *(5)

*( ): Required minimum J'_b and σ_0 for tensile strain-hardening behavior of PVA-fiber cement (see Sec. 2.5.1)

Table 2.7 – Influence of the sheath composition and surface coating on the interfacial frictional and chemical bonds (After [29])

Additive in Sheath	Surface Coating	τ_0 (MPa)	G_d (J/m^2)
No	No	0.22	-
No	Yes	0.4-0.72	-
Mineral Filler	No	0.64	-
Copolymer A	No	0.82	-
Copolymer B	No	1.51	1.4
Copolymer C	Yes	1.02	-
Copolymer D	Yes	0.76-1.1	0.07-0.1

Table 2.8 – Micromechanical parameters used in calculating $\sigma(\delta)$ curve of PP-fiber cement

	Fiber parameters					Interface parameters					Matrix parameters	Model results	
	V_f (vol.%)	d_f (μm)	L_f (mm)	E_f (GPa)	σ_{fu} (MPa)	G_d (J/m^2)	τ_0 (MPa)	β	f	f'	E_m (GPa)	J'_b (J/m^2)	σ_0 (MPa)
Control PP	2	11	8	11.6	400	0	0.22	0.005	0.39	0.1	20	24.8 *(15)	2.2 *(5)
Copolymer PP	2	11	8	11.6	749	0	1.02	0.005	0.39	0.1	20	54.6 *(15)	5.3 *(5)

*( ): Required minimum J'_b and σ_0 for tensile strain-hardening behavior of PP-fiber cement (see Sec. 2.5.1)

Table 2.9 – Mechanical, geometric, and interfacial bond properties of six high tenacity PP (HTPP) fibers

Fiber Type	σ_f (MPa)	ε_f (%)	L_f (mm)	d_f (μm)	τ_0 (MPa)	G_d (J/m^2)	Note	Supplier
HTPP 1	928	-	12	16.6	0.2	-	ordinary HTPP	-
HTPP 2	770	19.1	6	11.9	0.4-1.5	0.07-1.4	sheath and/or coating	Redco, Belgium
HTPP 3	880	25.7	6	12.1				
HTPP 4	880	17.6	6	11.2				
HTPP 5	850	21	6	12	0.7	-	coating	Brasilit, Brazil
HTPP 6	850	21	10	12				

Table 2.10 – Mix design of PP fiber cement (unit: kg/m^3)

Cement	Fly ash	Water	SP	PP fiber
412	1154	363	6.6	18

Table 2.11 – Cost comparison of PVA-ECC and HTPP-ECC

Fiber Type	PVA	HTPP
Fiber Provider	Kuraray, Japan	PGI, USA Brasilit, Brazil Redco, Belgium
Cost of Fiber ($/kg)	6.6	3
Cost of resulting ECC ($/kg)	350	150

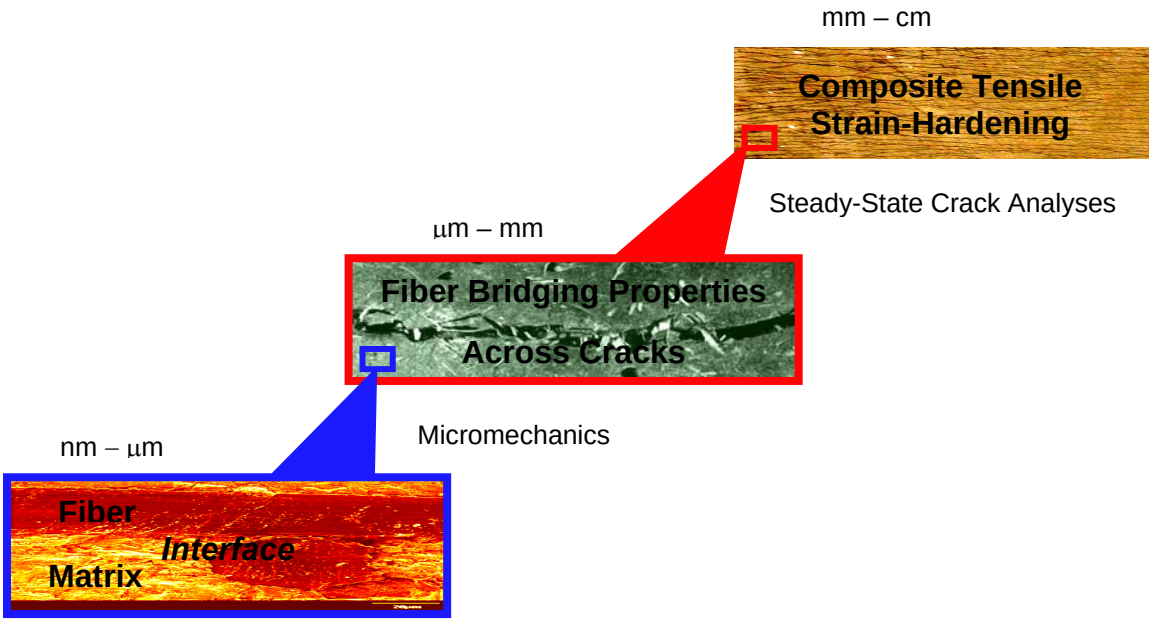

Fig. 2.1 – Scale linking in ECC

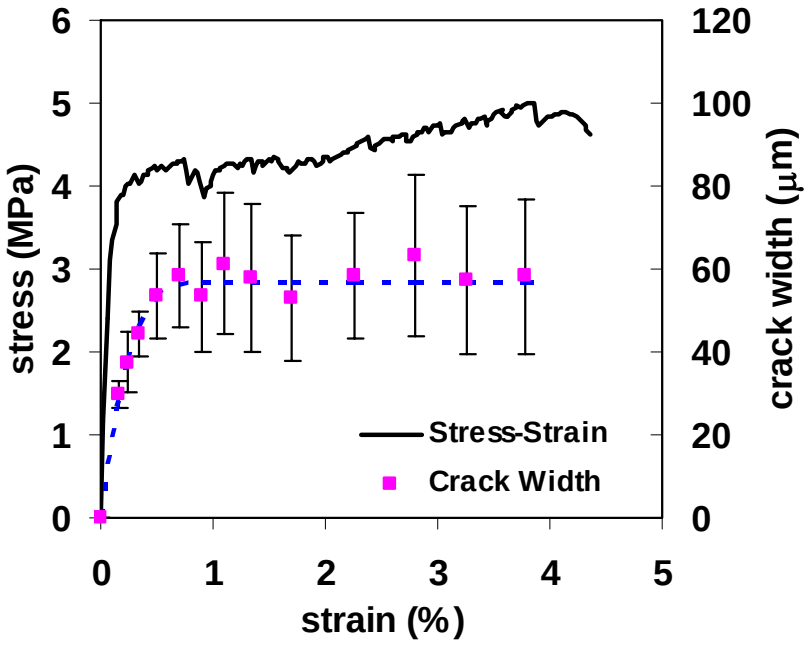

Fig. 2.2 – Typical tensile stress-strain-crack width relationship of PVA-ECC M45

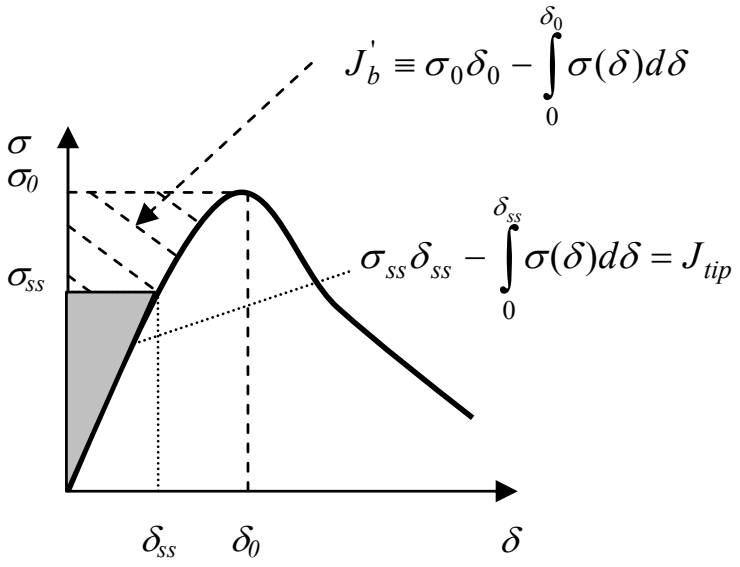

Fig. 2.3 – Typical σ(δ) curve for tensile strain-hardening composite. Hatched area represents complimentary energy J'_b. Shaded area represents crack tip toughness J_{tip}.

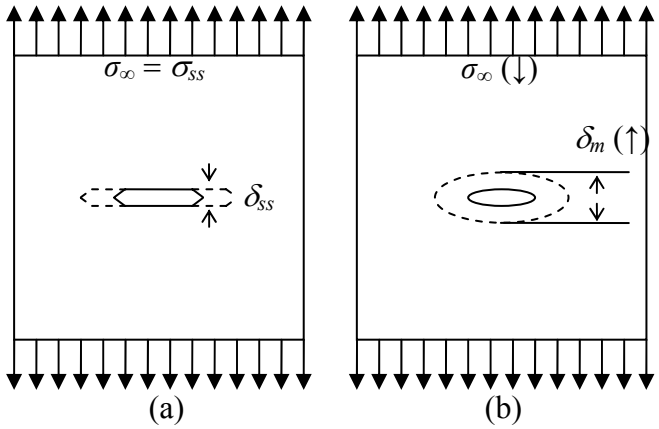

Fig. 2.4 – (a) Steady-state cracking with constant ambient load σ_{ss} and constant crack opening δ_{ss} (flat crack); and (b) Griffith crack (an oval shape crack) with a descending ambient load and a widened crack opening

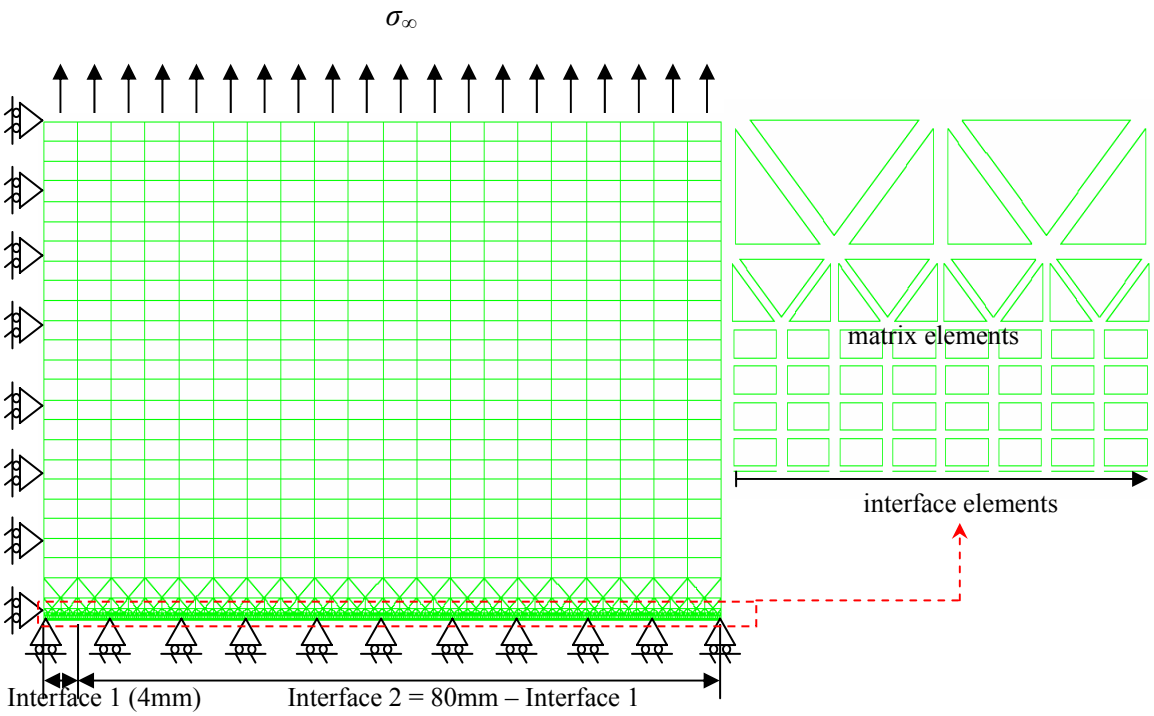

Fig. 2.5 – Cohesive traction model with two interface types

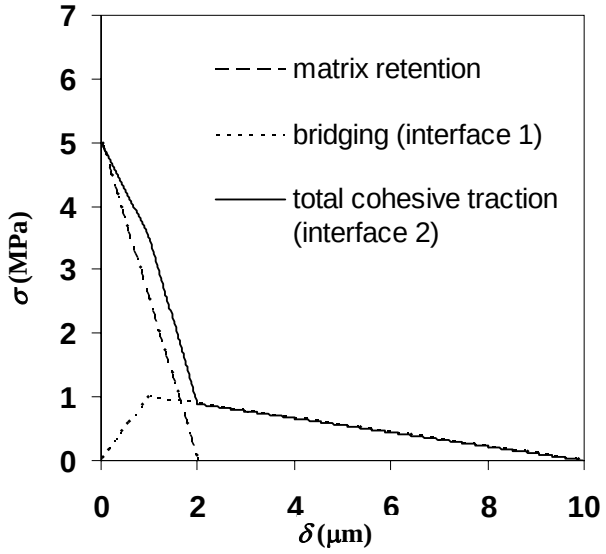

Fig. 2.6 – Matrix retention and bridging constitutive laws in which $J'_b < J_{tip}$

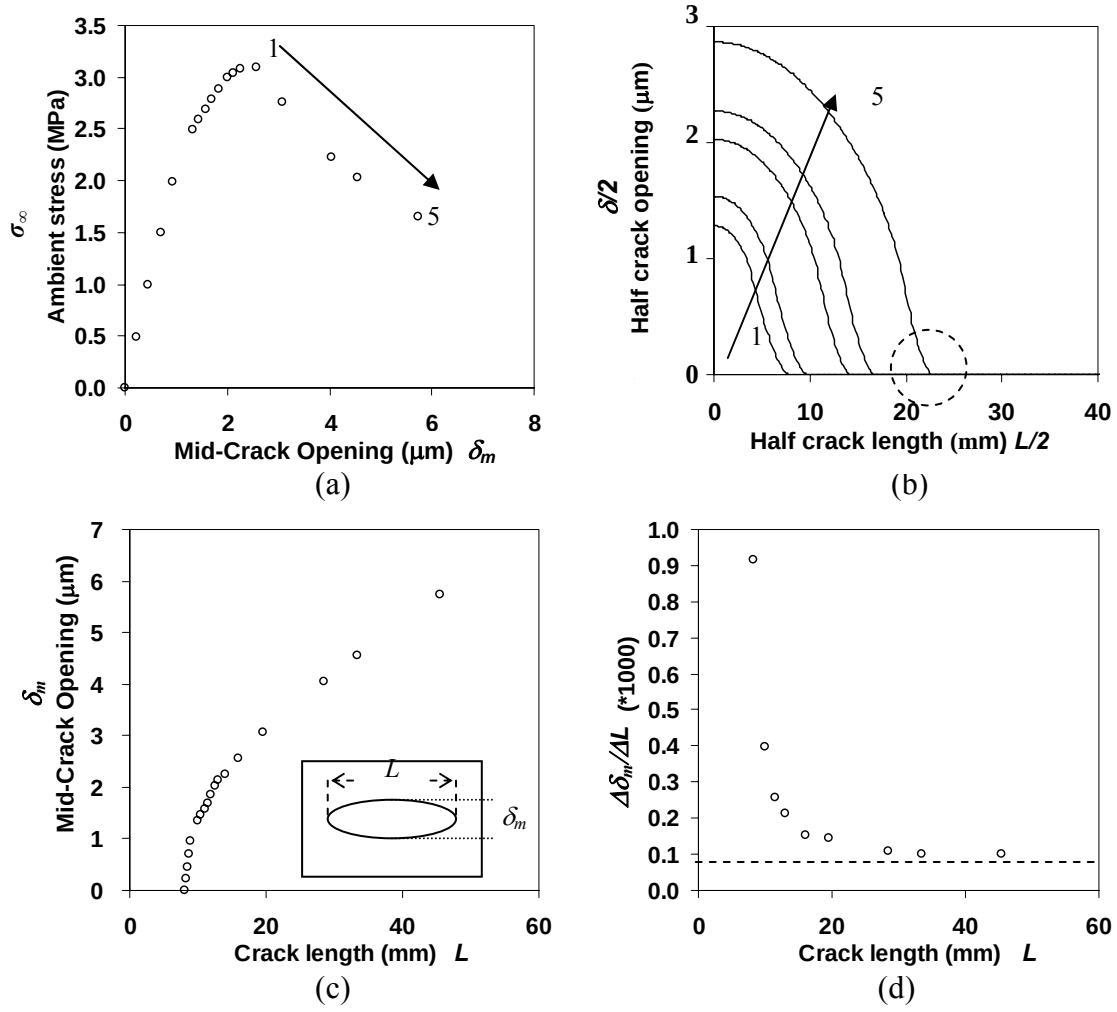

Fig. 2.7 – Computational results of Griffith type cracking where cohesive tractions in figure 4 are applied to interface 1 and 2, respectively.

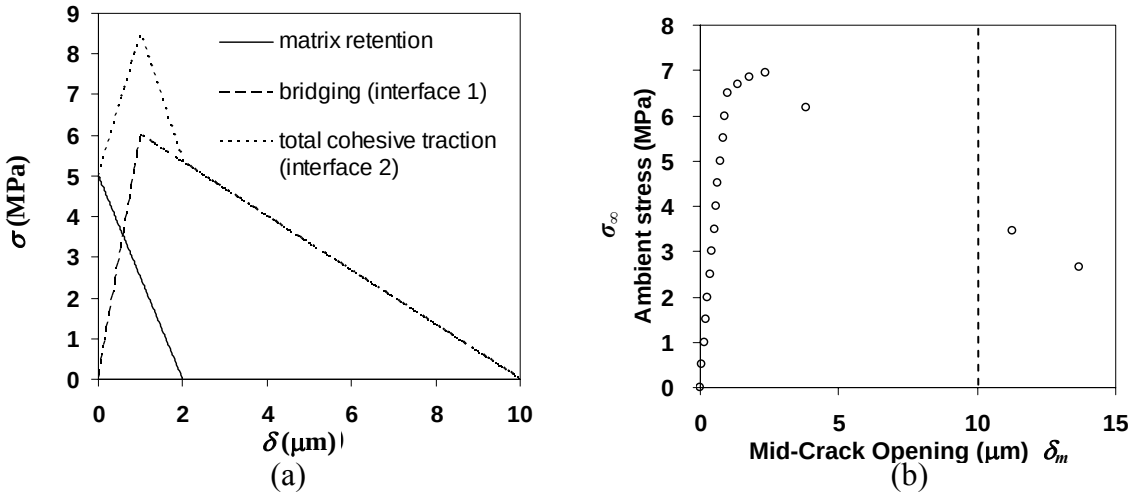

Fig. 2.8 – (a) Matrix retention and bridging constitutive laws in which $J'_b < J_{tip}$ but with substantial bridging strength and (b) computational result of $\sigma_\infty - \delta_m$

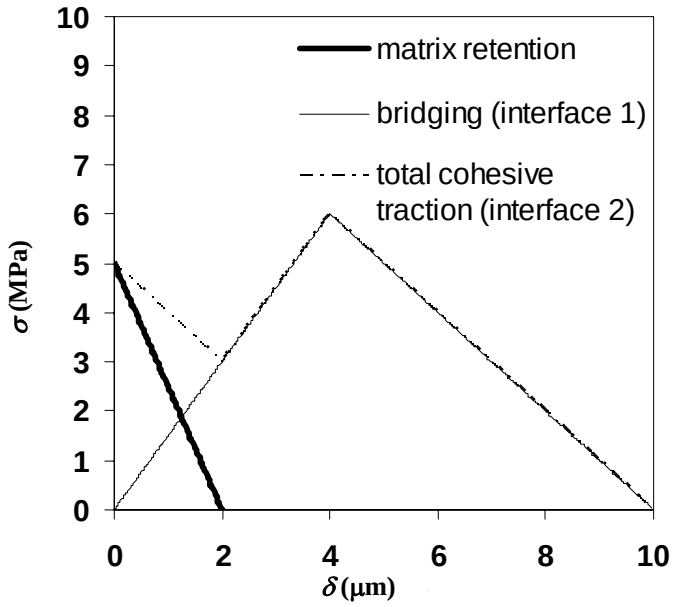

Fig. 2.9 – Matrix retention and bridging constitutive laws in which $J'_b > J_{tip}$

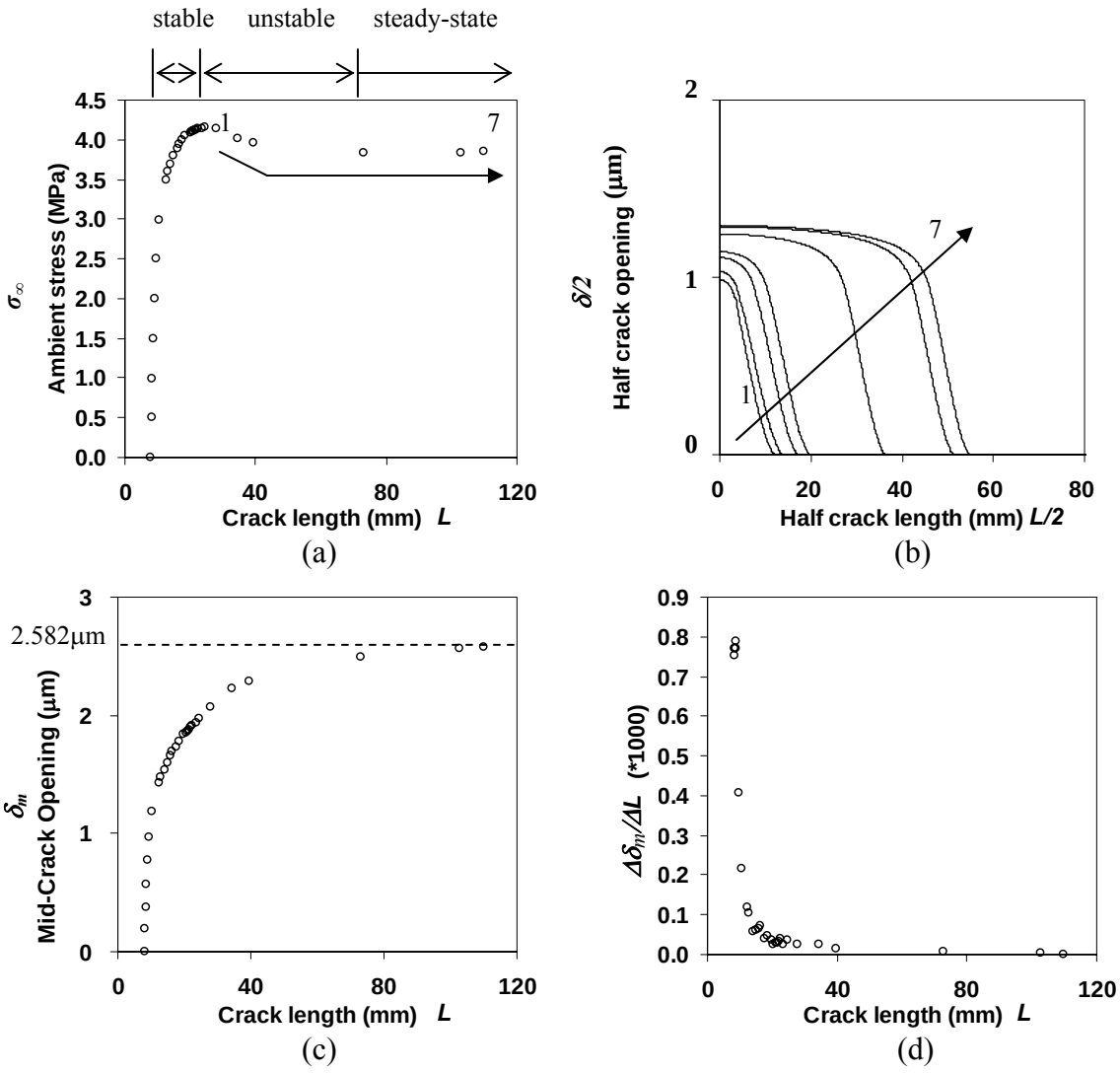

Fig. 2.10 – Computational results of steady-state cracking. Stage numbers represent the ambient stress states in (a) and the corresponding crack profiles are shown in (b). Mid-crack opening behavior is shown in (c) and (d).

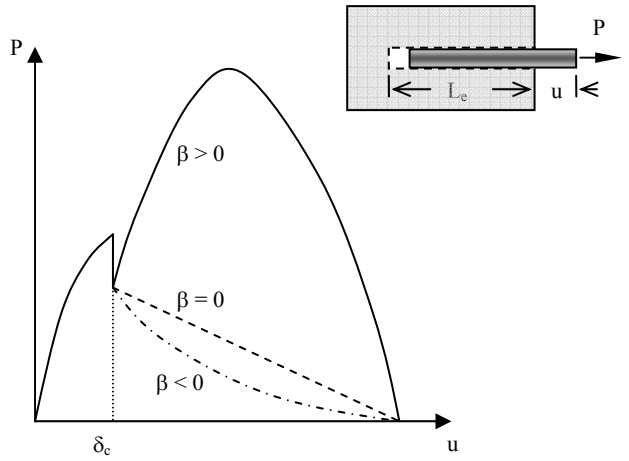

Fig. 2.11 – Single fiber pullout behavior (β > 0) slip-hardening; (β = 0) interface friction is independent to slip distance; and (β < 0) slip-softening

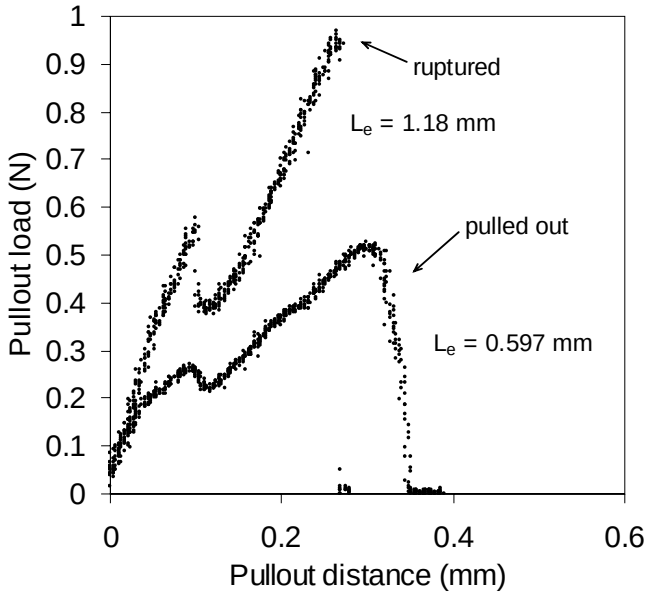

Fig. 2.12 – Single fiber pullout curves of PVA-ECC M45 (fiber diameter 39 μm) (After [21])

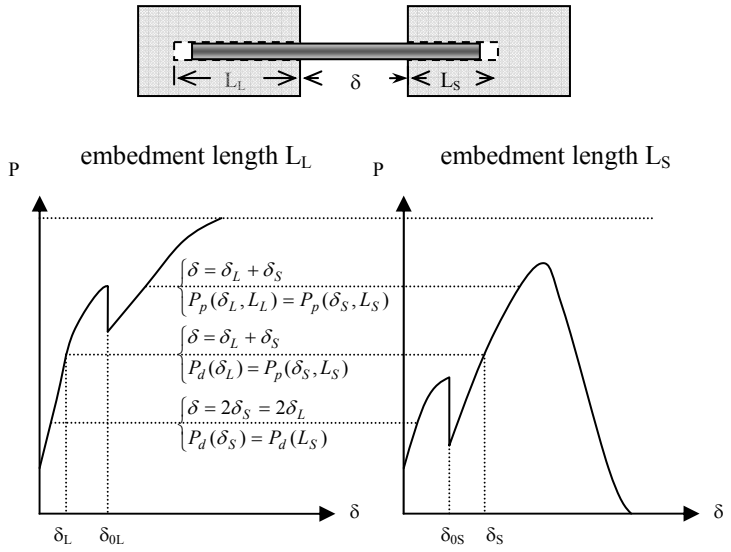

Fig. 2.13 – Modeling of two-way pullout: (left) load vs. displacement curve of the long embedment side; (right) load vs. displacement curve of the short embedment side

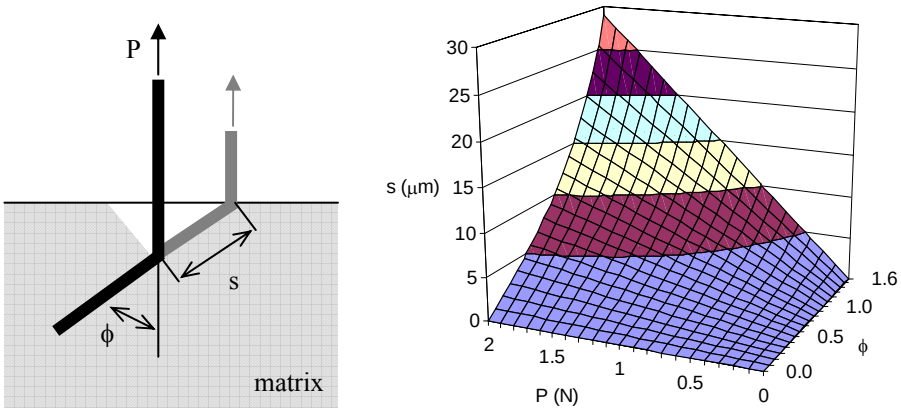

Fig. 2.14 – Dependence of matrix spalling size s on inclination angle ϕ and fiber load P (Eqn. (17), assuming matrix tensile strength σ_m = 5 MPa, fiber diameter d_f = 39 μm, and spalling coefficient k = 500) (After [21])

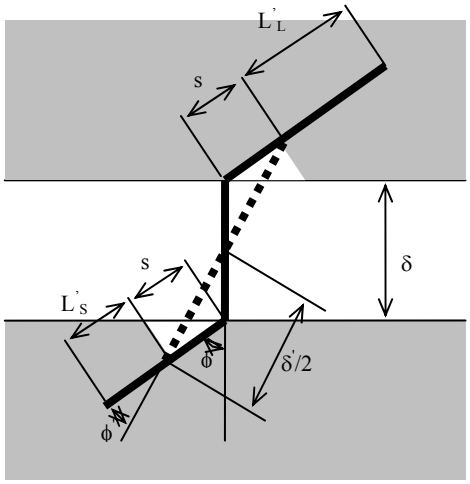

Fig. 2.15 – Schematic of inclined bridging with matrix spalling

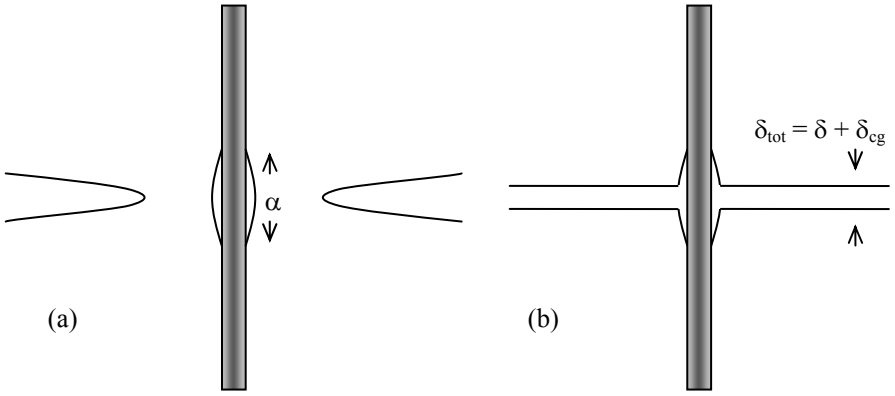

Fig. 2.16 – Cook-Gordon effect (a) induces fiber-matrix separation due to the tensile stress in the horizontal direction associated with the elastic crack tip field of the approaching matrix crack, and (b) leads to an additional crack opening δ_{cg} due to elastic stretching of the fiber segment α in addition to the δ associated with interface frictional debonding.

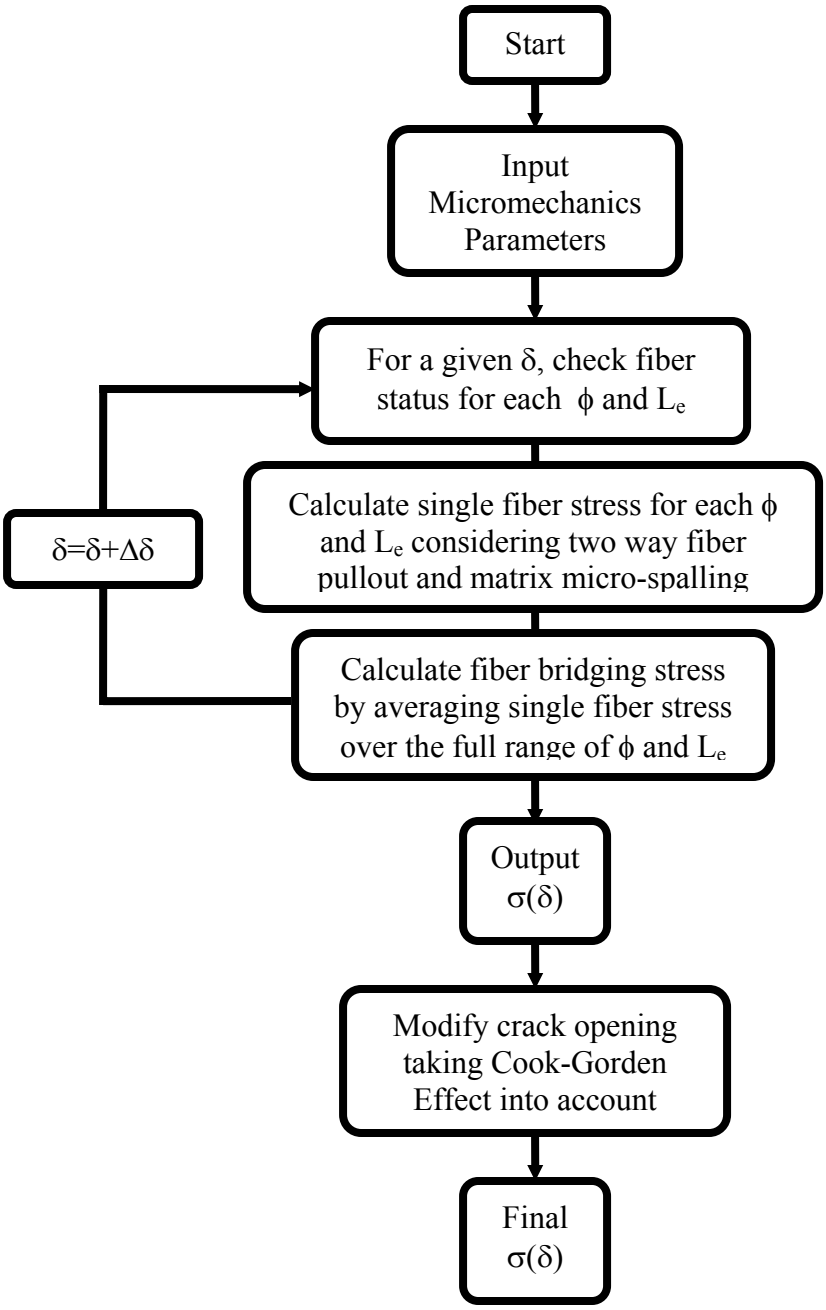

Fig. 2.17 – Flow chart of the numerical procedure for computing σ(δ)

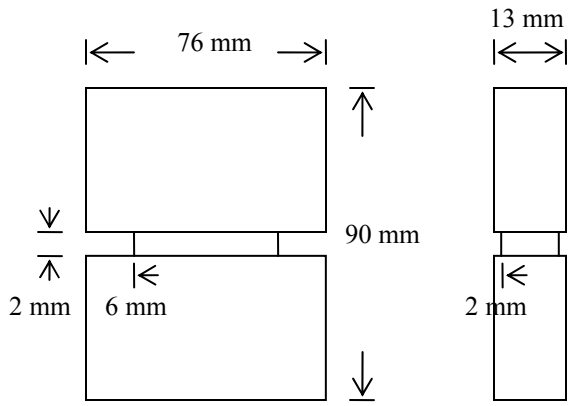

Fig. 2.18 – Dimensions of notched coupon specimen

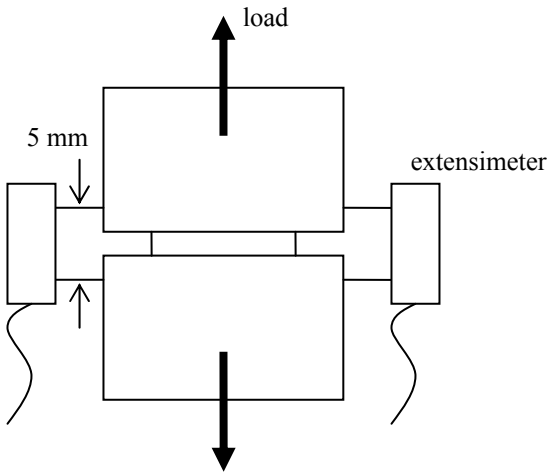

Fig. 2.19 – Setup of uniaxial tensile test for experimental determination of $\sigma(\delta)$ curve

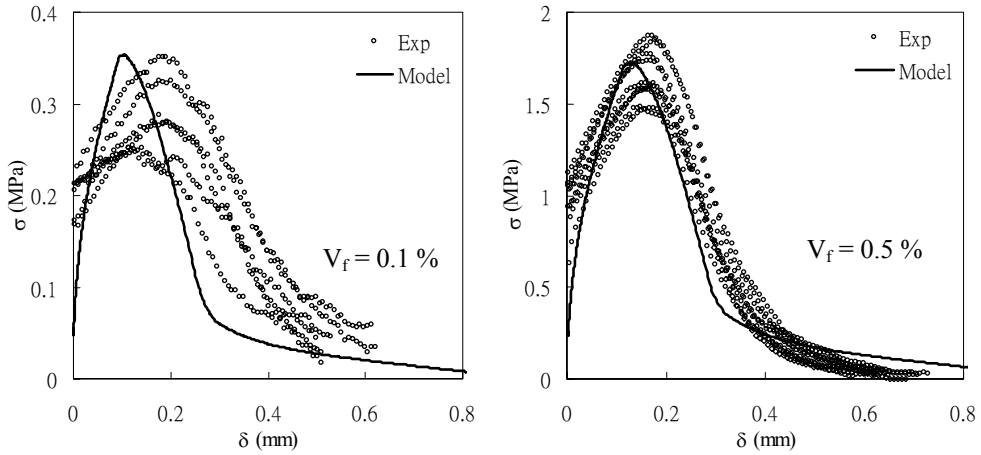

Fig. 2.20 – Comparison of σ(δ) curves obtained from uniaxial tensile tests and from model predictions of PVA-ECC for (a) V_f = 0.1 vol.% and (b) V_f = 0.5 vol.%

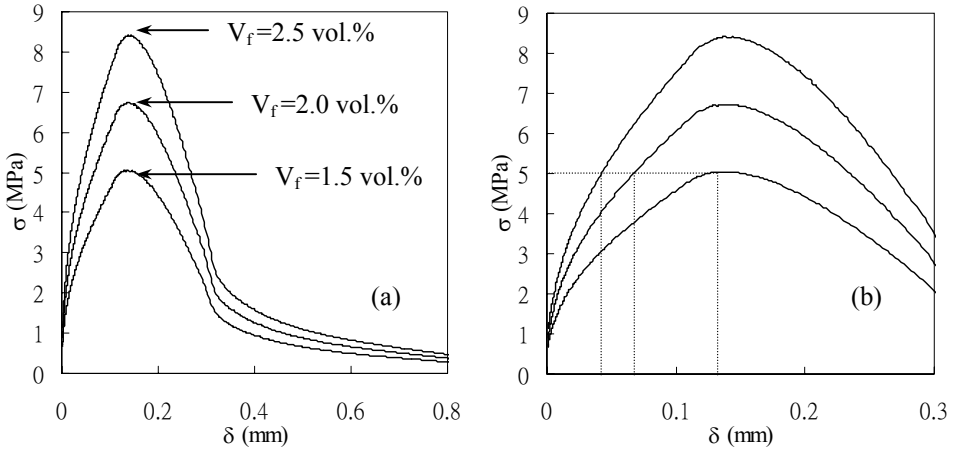

Fig. 2.21 – (a) Predicted σ(δ) curve of PVA-ECC M45 with V_f = 2 vol.% (full span), and (b) magnified view of (a) (δ = 0 ~ 0.3 mm). The three curves in each plot are generated assuming fiber volume variation due to processing of ECC composites, see text.

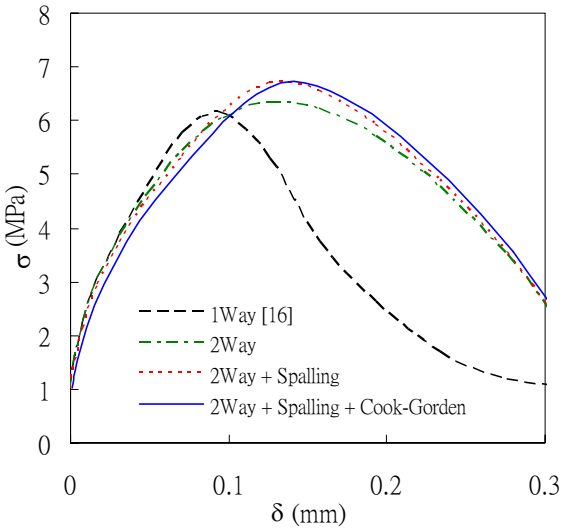

Fig. 2.22 – Theoretical bridging stress vs. crack opening relation of PVA-ECC calculated by various models.

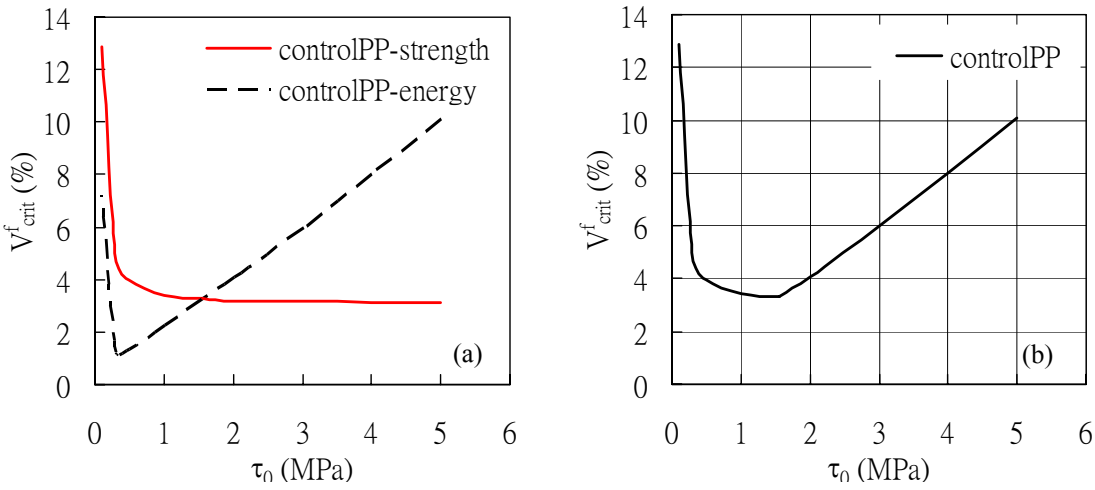

Fig. 2.23 – Micromechanical model calculated V^f_{crit} as a function of τ_0 for strain-hardening (control) PP-fiber cement determined by (a) the energy and the strength criterion respectively and (b) the combined effect

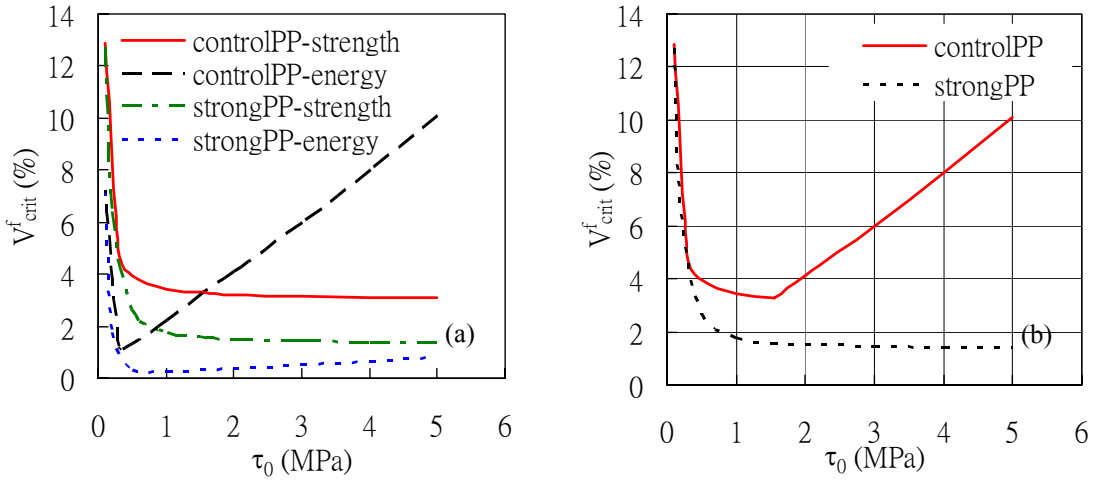

Fig. 2.24 – Effect of fiber strength on V^f_{crit} determined by (a) the energy and the strength criterion respectively and (b) the combined effect

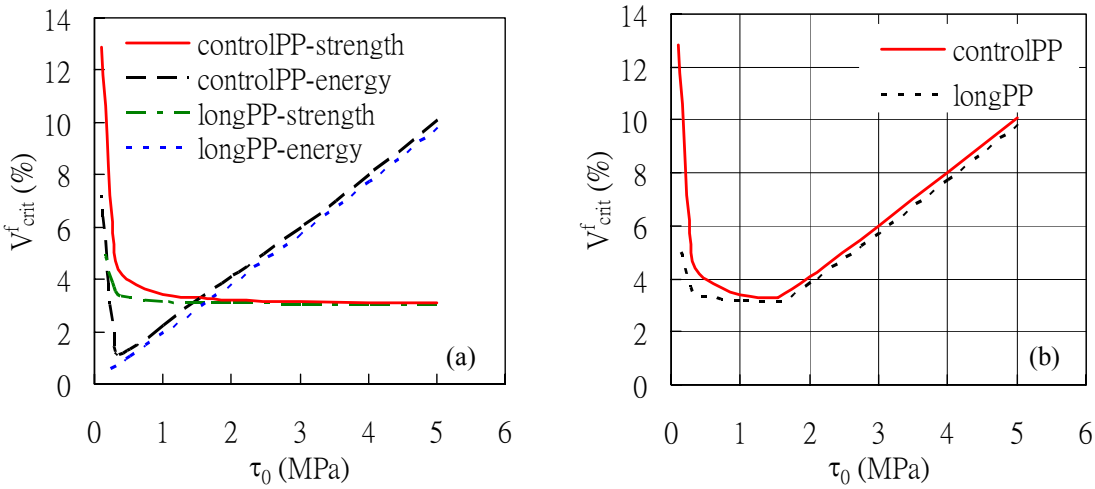

Fig. 2.25 – Effect of fiber length on V^f_{crit} determined by (a) the energy and the strength criterion respectively and (b) the combined effect

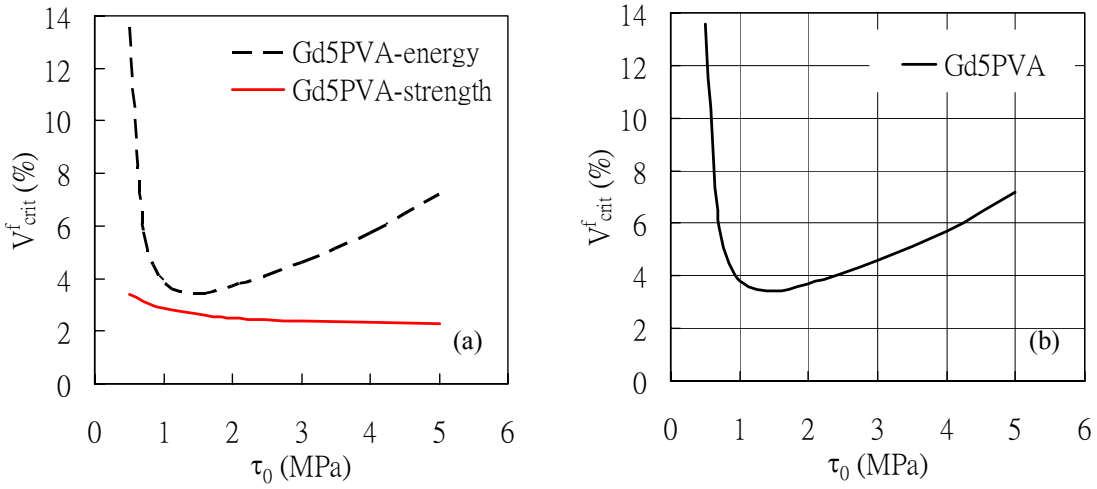

Fig. 2.26 – Micromechanical model calculated V^f_{crit} as a function of τ_0 for strain-hardening (control) PVA-fiber cement determined by (a) the energy and the strength criterion respectively and (b) the combined effect

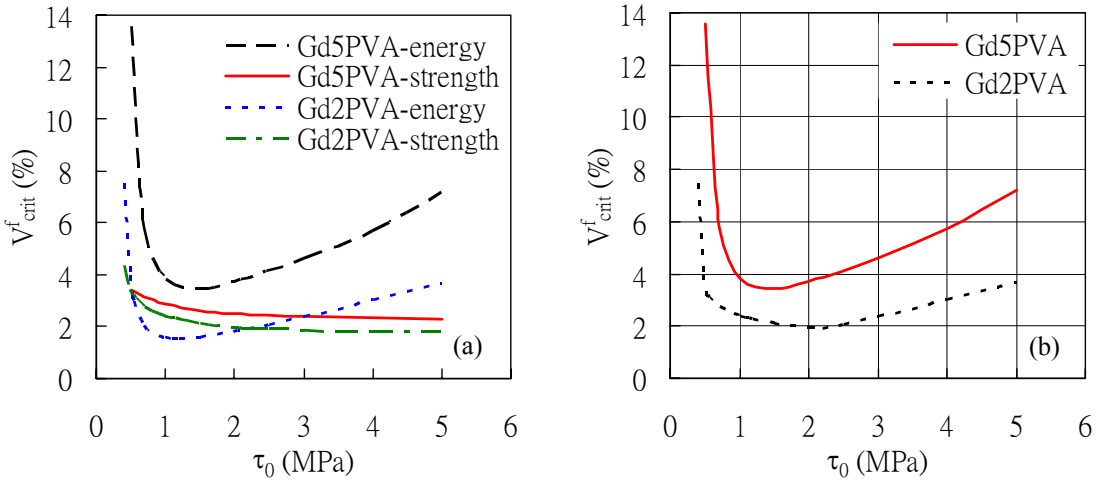

Fig. 2.27 – Effect of interface chemical bond on V^f_{crit} determined by (a) the energy and the strength criterion respectively and (b) the combined effect

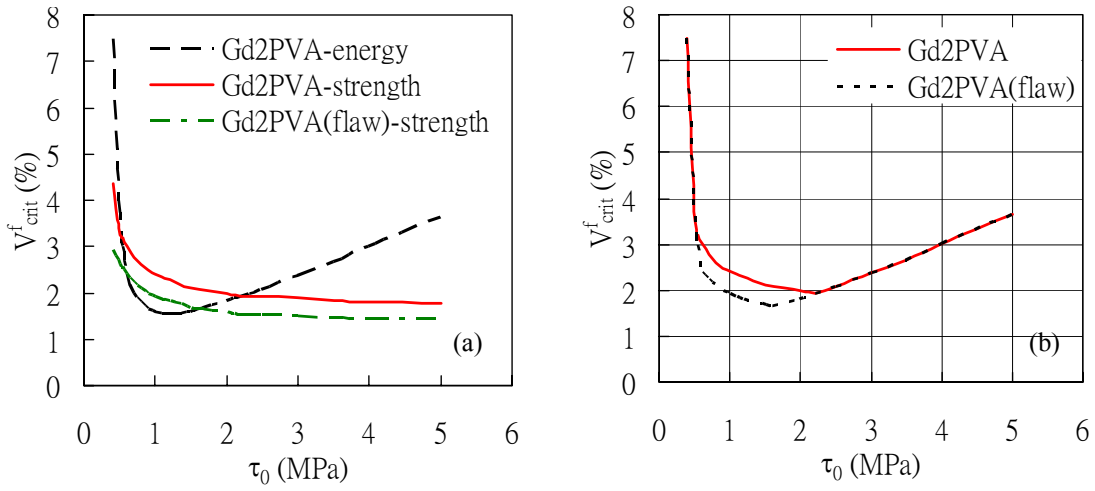

Fig. 2.28 – Effect of planting artificial flaws in matrix on V^f_{crit} determined by (a) the energy and the strength criterion respectively and (b) the combined effect

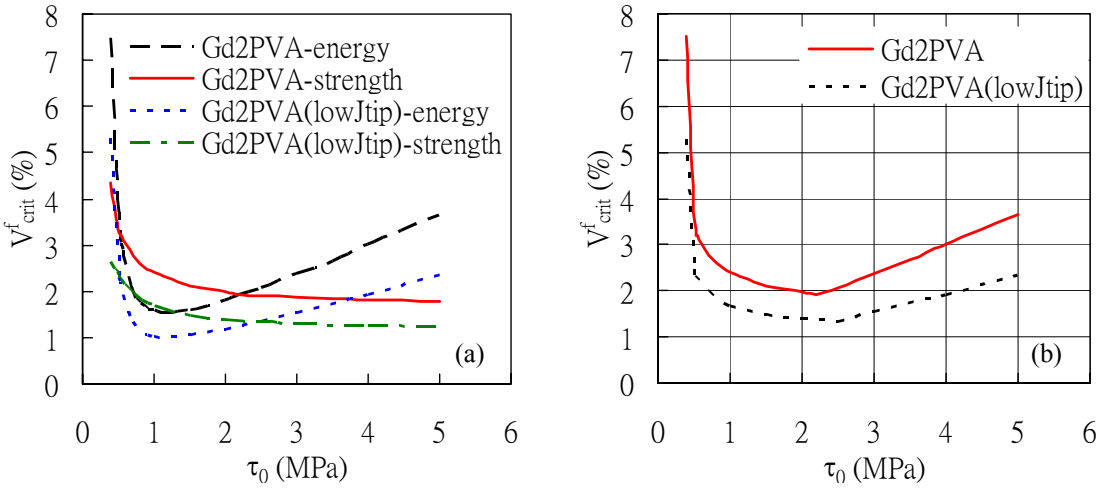

Fig. 2.29 – Effect of matrix toughness on V^f_{crit} determined by (a) the energy and the strength criterion respectively and (b) the combined effect

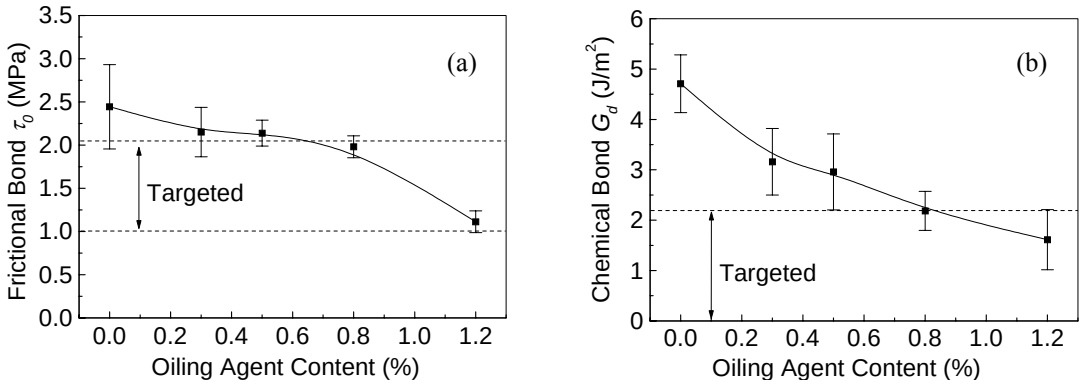

Fig. 2.30 – Effect of coating content on interface (a) frictional bond and (b) chemical bond (After [23])

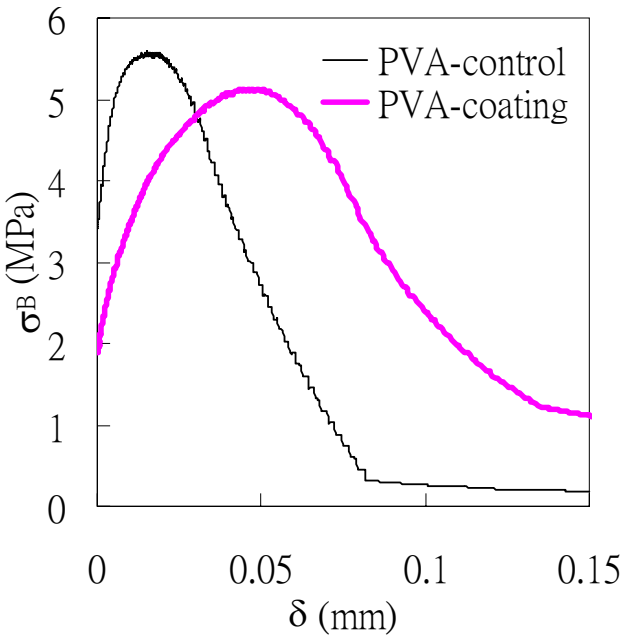

Fig. 2.31 – Effect of interface tailoring on predicted σ(δ) curve of PVA-fiber cement

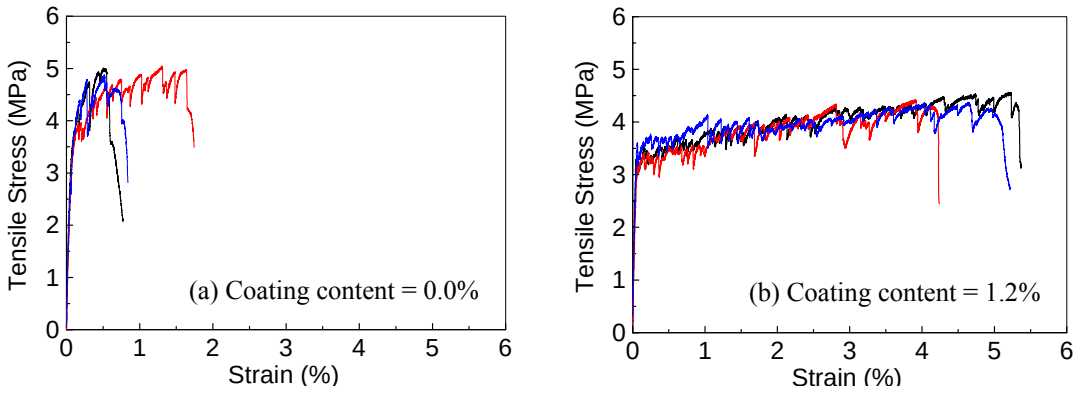

Fig. 2.32 – Effect of interface tailoring on composite tensile stress-strain behavior of PVA-fiber cement – three curves in each plot represents three repeatable test results (After [23])

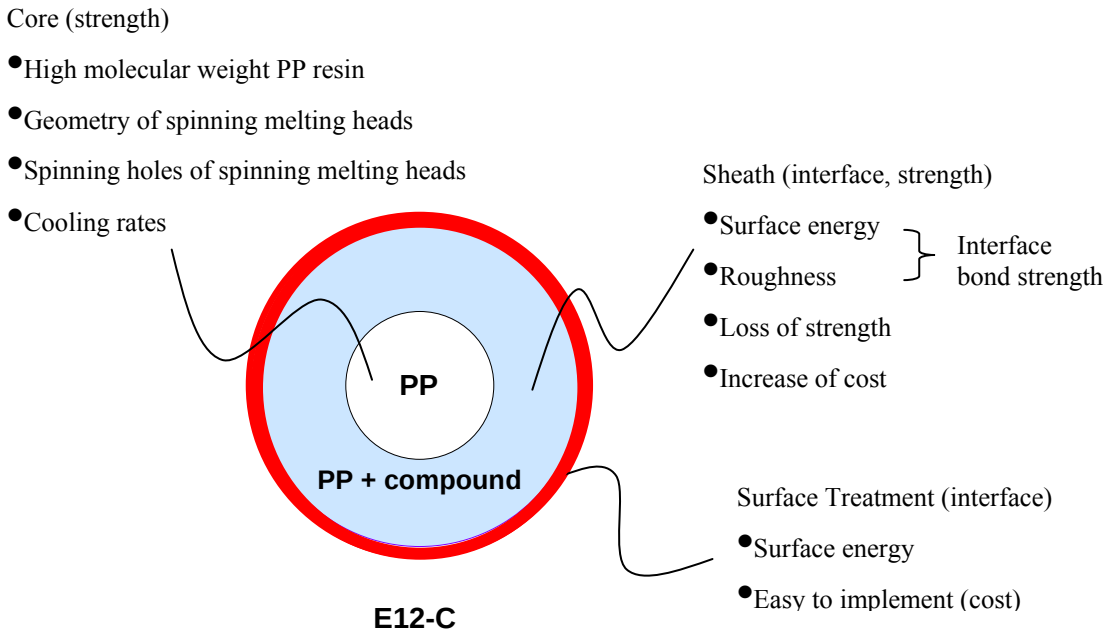

Fig. 2.33 – Structure of high tenacity PP copolymer fiber (After [29])

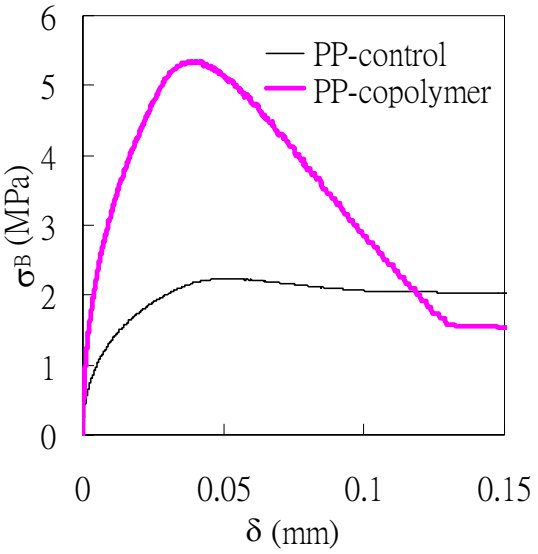

Fig. 2.34 – Effect of fiber and interface tailoring (high tenacity copolymer fiber) on σ(δ) curve of PP-fiber cement

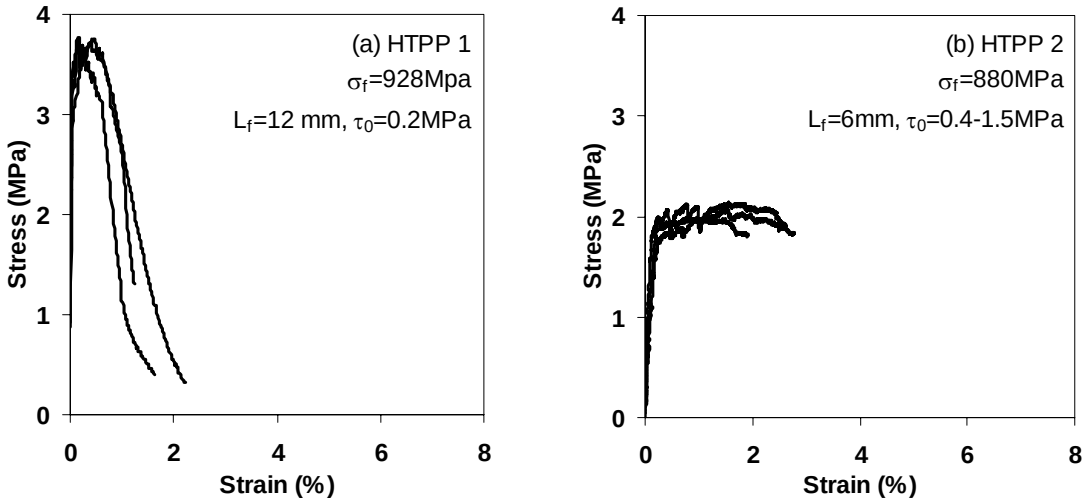

Fig. 2.35 (a) and (b) – Tensile stress-strain curves of PP fiber cement. (a) Tension softening of ordinary high tenacity PP fiber cement 1, and (b) tensile strain-hardening of PP-ECC 2 adopting treated high tenacity PP fiber 2.

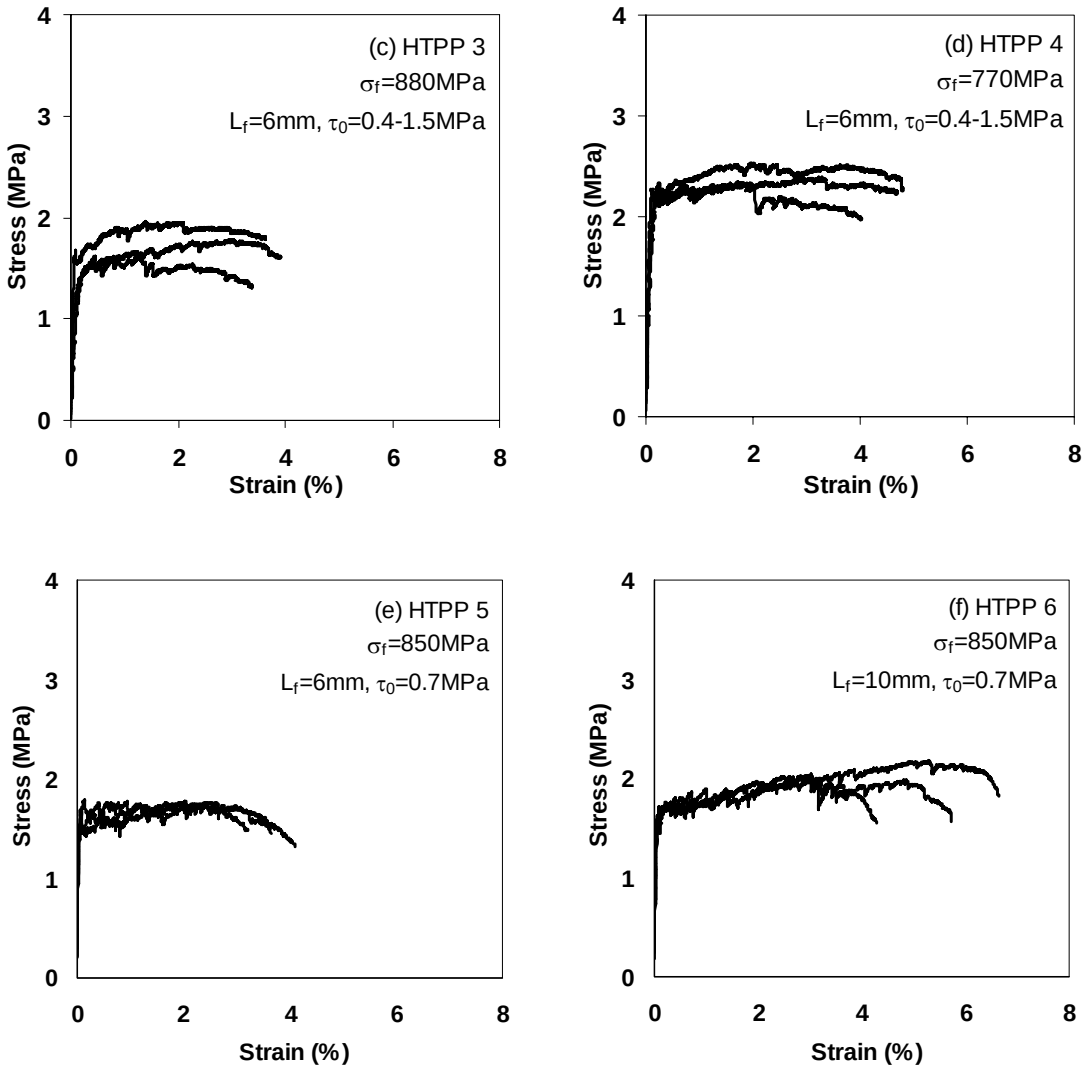

Fig. 2.35 (c) to (f) – Tensile stress-strain curves of PP fiber cement. (c) to (f) Tensile strain-hardening of PP-ECCs adopting treated high tenacity PP fibers 3 to 6.

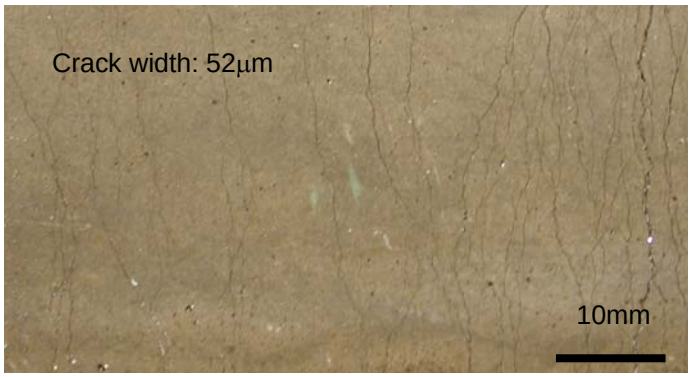

HTPP 2

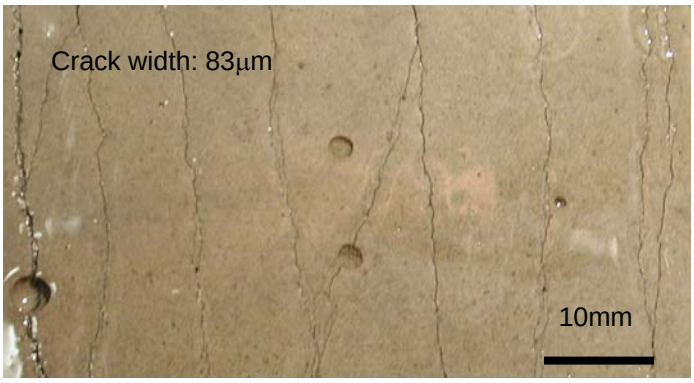

HTPP3

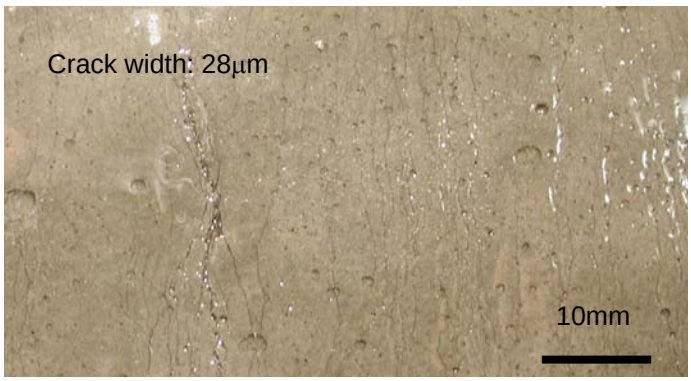

HTPP 4

Fig. 2.36 – Crack pattern of tensile strain-hardening PP-ECC 2 to 4

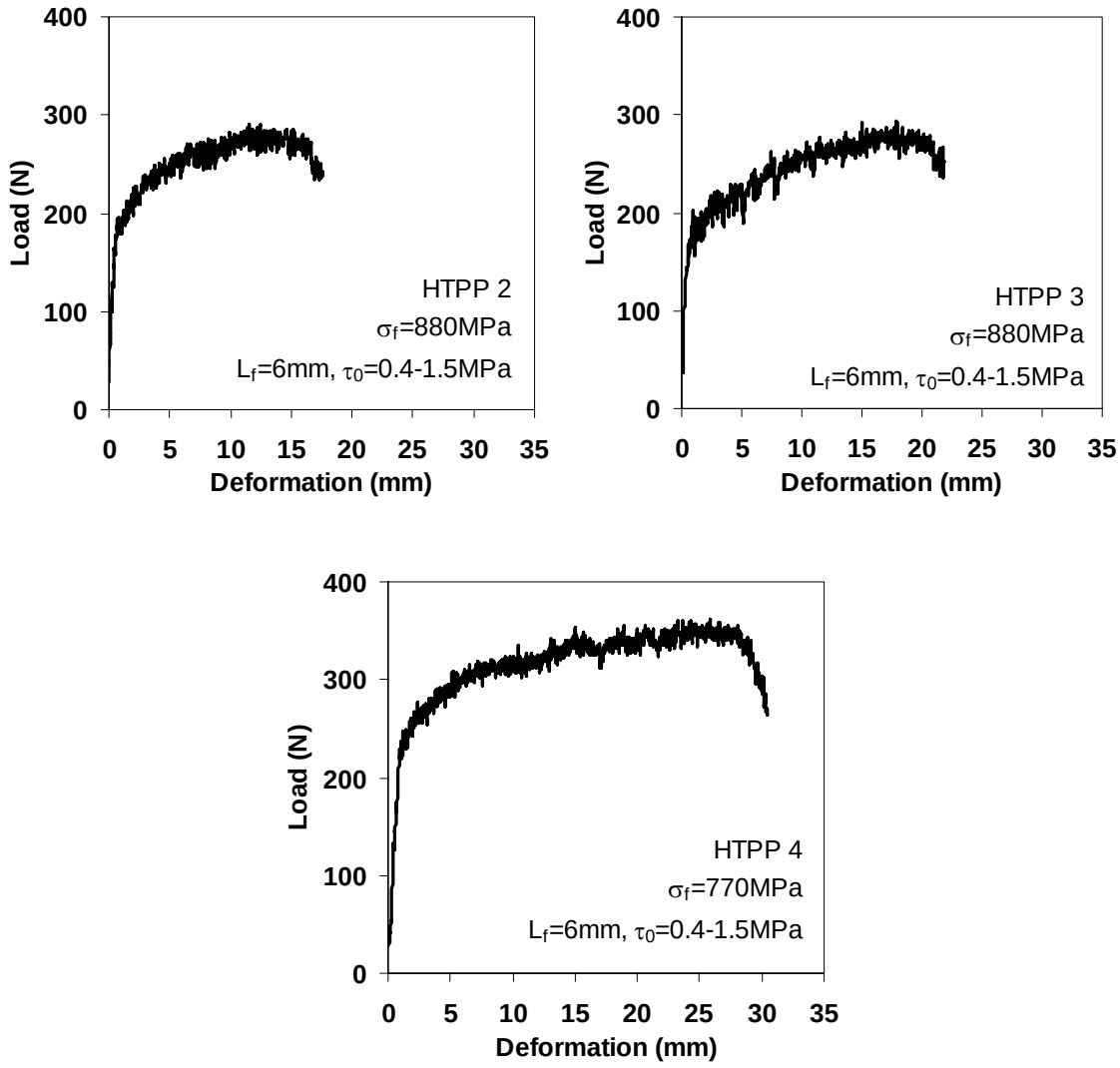

Fig. 2.37 – Four point bending load-deformation of PP-ECC 2 to 4

References

[1] Li, V.C., and Leung, C.K.Y., "Steady State and Multiple Cracking of Short Random Fiber Composites," *ASCE J. of Engineering Mechanics*, vol.188, no.11, pp.2246-2264, 1992

[2] Li, V.C., and Wu, H.C., "Conditions for Pseudo Strain-Hardening in Fiber Reinforced Brittle Matrix Composites," *J. of Applied Mechanics Review*, vol.45, no.8, pp.390-398, 1992

[3] Marshall, D.B., and Cox, B.N., "A J-Integral Method for Calculating Steady-State Matrix Cracking Stresses in Composites," *Mechanics of Materials*, no.8, pp.127-133, 1988

[4] Li, V.C., and Leung, C.K.Y., "Theory of Steady State and Multiple Cracking of Random Discontinuous Fiber Reinforced Brittle Matrix Composites," *Journal of Engineering Mechanics*, vol.118, no.11, pp.2246-2264, 1992

[5] Lin, Z., T. Kanda, and V.C. Li, "On Interface Property Characterization and Performance of Fiber-Reinforced Cementitious Composites," *Journal of Concrete Science and Engineering*, no.1, pp.173-184, 1999

[6] Li, V.C., "Post-Crack Scaling Relations for Fiber-Reinforced Cementitious Composites," *Journal of Materials in Civil Engineering*, vol.4, no.1, pp.41-57, 1992

[7] Kanda, T., *Design of Engineered Cementitious Composites for Ductile Seismic Resistant Elements*, Ph.D. Dissertation, Department of Civil and Environmental Engineering, University of Michigan, Ann Arbor, 329 pp, 1998

[8] Wu, H.C., and Li, V.C., "Snubbing and Bundling Effects on Multiple Crack Spacing of Discontinuous Random Fiber-Reinforced Brittle Matrix Composites," *Journal of American Ceramics Society*, vol.75, no.12, pp.3487-3489, 1992

[9] Aveston, J., Cooper, G., and Kelly, A., "Single and Multiple Fracture," *Properties of Fiber Composites*, Guildford, UK, pp.15-24, 1971

[10] Majumdar, A.J., "Glass Fiber Reinforced Cement and Gypsum Products," *Proc R Soc*, vol.A319, pp.69, 1970

[11] Phillips, D.C., "The Fracture Energy of Carbon-Fiber Reinforced Glass," *J Mat Sci* vol.7, pp.1175-1191, 1972

[12] Marshall, D.B., and Evans, A.G., "Failure Mechanisms in Ceramic-Fiber/Ceramic-Matrix Composites," *J Amer Ceram Soc*, vol.68, pp.225-231, 1985

[13] Li, V.C., Wang S, and Wu C, "Tensile Strain-hardening Behavior of PVA-ECC," *ACI Materials Journal*, vol.98, no.6, pp.483-492, 2001

[14] Hillerborg, A., Modeer, M., and Petersson, P.E., "Analysis of Crack Formation and Crack Growth in Concrete by Means of Fracture Mechanics and Finite Elements," *Cement Conc Res*, vol.6, pp.773-782, 1976

[15] Cook, R.D., Malkus, D.S., Plesha, M.E., and Witt, R.J., *Concepts and Applications of Finite Element Analysis*, Wiley Publication, 2002

[16] Lin, Z., and Li VC, "Crack Bridging in Fiber Reinforced Cementitious Composites with Slip-Hardening Interfaces," *Journal of Mechanics and Physics of Solids*, vol.45, no.5, pp.763-787, 1997

[17] Redon, C., Li, V.C., Wu, C., Hoshiro, H., Saito, T., and Ogawa, A., "Measuring and Modifying Interface Properties of PVA Fibers in ECC Matrix," *ASCE Journal of Materials in Civil Engineering*, vol.13, no.6, pp.399-406, 2001

[18] Morton, L., and Groves, G.W., "The Effect of Metal Wires on the Fracture of a Brittle Matrix Composite," *Journal of Material Science*, no.11, pp.617-622, 1976

[19] Wang, Y., and Backer S, and Li VC, "A Statistical Tensile Model of Fiber Reinforced Cementitious Composites," *Journal of Composites*, vol.20, no.3, pp.265-274, 1990

[20] Wang, Y., Li VC, and Backer S, "Modeling of Fiber Pull-out From a Cement Matrix," *Int'l J. of Cement Composites and Lightweight Concrete*, vol.10, no.3, pp.143-149, 1988

[21] Wang, S., *Micromechanics Based Matrix Design for Engineered Cementitious Composites*, Ph.D. Dissertation, Departmental of Civil and Environmental Engineering, University of Michigan, Ann Arbor, 221 pp, 2005

[22] Li, V.C., Stang H, and Krenchel H, "Micromechanics of Crack Bridging in Fibre-Reinforced Concrete," *Materials and Structures*, no.26, pp.486-494, 1993

[23] Li, V.C., C. Wu, S. Wang , A. Ogawa and T. Saito, "Interface Tailoring for Strain-hardening PVA-ECC," *ACI Materials Journal*, vol.99, no.5, pp.463-472, 2002

[24] Bruehwiler, E., and Wittmann, F.H., "The Wedge Splitting Test, A New Method of Performing Stable Fracture Mechanics Test," *Engineering Fracture Mechanics*, vol.35, no.1-3, pp.117-125, 1990

[25] Ostergaard, L., *Early-Age Fracture Mechanics and Cracking of Concrete - Experiments and Modeling*, Ph.D. Dissertation, Department of Civil Engineering, Technical University of Denmark, 2003

[26] Ostergaard, L., Lange, D., and Stang, H., "Early-Age Stress-Crack Opening Relationships for High Performance Concrete," *Cement and Concrete Composites*, vol.26, no.5, pp.563-572, 2004

[27] Bentur, A., *personal communication*. 1992.

[28] Kim, P.J., *Micromechanics Based Durability Study of Lightweight Thin Sheet Fiber Reinforced Cement Composites*, Ph.D. Dissertation, Department of Civil and Environmental Engineering, University of Michigan, Ann Arbor, 486 pp, 1999

[29] De Lhoneux, B., R. Kalbskopf, P. Kim, V. Li, Z. Lin, D. Vidts, S. Wang, and H. Wu, "Development of High Tenacity Polypropylene Fibres for Cementitious Composites," *Proceedings of the JCI International Workshop on Ductile Fiber Reinforced Cementitious Composites (DFRCC) - Application and Evaluation* -, Takayama, Japan, pp.121-132, 2002

[30] Stang, H., B. Mobasher, B., and S.P. Shah, "Quantitative Damage Characterization in Polypropylene Fiber Reinforced Concrete," *Cement and Concrete Research*, vol.20, no.4, pp.540-558, 1990

[31] Takashima, H., K. Miyagai, T. Hashida, and V.C. Li, "A Design Approach for the Mechanical Properties of Polypropylene Discontinuous Fiber Reinforced Cementitious Composites by Extrusion Molding," *Journal of Engineering Fracture Mechanics*, vol.70, pp.853-870, 2003

[32] Wu, C., *Micromechanical Tailoring of PVA-ECC for Structural Applications*, Ph.D. Dissertation, Departmental of Civil and Environmental Engineering, University of Michigan, Ann Arbor, 238 pp, 2001

[33] Li, V.C., and Wang, S., "Microstructure Variability and Macroscopic Composite Properties of High Performance Fiber Reinforced Cementitious Composites," *Probabilistic Engineering Mechanics*, vol.21, no.3, pp.201-206, 2006

[34] Li, V.C., H.C. Wu, and Y.W. Chan, "Effect of Plasma Treatment of Polyethylene Fibers on Interface and Cementitious Composite Properties," *Cement and Concrete Composites*, vol.18, no.4, pp.223-237, 1996

CHAPTER 3

ADDING GREENNESS IN ECC

In the development of HPFRCC, material sustainability is seldom a concern and high cement content is commonly seen in mixture designs. In this chapter, a new set of ECC is developed taking into account environmental sustainability consideration. Specifically, a large amount of cement is substituted by recycled class F fly ash (up to 85% by weight). While micromechanics is applied in many aspects of the material design process, emphasis of this study is placed on the effect of fly ash content on altering material microstructure and mechanical properties. Experimental results show that HVFA ECCs, while incorporating high volumes of recycled fly ash, can retain a long term tensile ductility around 2-3%. Significantly, both crack width and free drying shrinkage are reduced with increase of fly ash amount, which may benefit the long-term durability of HVFA ECC structures. Micromechanics analysis indicates that the increase of fiber/matrix interface frictional bond in HVFA ECCs is responsible for the tight crack width. In addition, HVFA ECCs show a robustness improvement by achieving more

saturated multiple cracking, while reducing environmental impact through use of industrial waste stream material in replacement of cement. The resulting HVFA ECCs are expected to promote infrastructure sustainability through simultaneous enhancements of material greenness and infrastructure durability through tight crack width control.

3.1 Introduction

Concrete is the most popular construction material and more than 11.4 billion tons of concrete is consumed annually worldwide [1]. It has been reported that 2.2 billion tons of cement was produced in the year 2005 [2]. The demand for cement increases with time and it was estimated that each ton of cement produced generates an equal amount of carbon dioxide [3]. The production of cement is responsible for 5% of global greenhouse gas emission created by human activities [4]. Therefore, incorporation of sustainability consideration into the design of civil engineering materials is urgently needed.

High Performance Fiber-Reinforced Cementitious Composites (HPFRCC) can significantly contribute to enhancing the service life of civil infrastructure. Among them, ECC is a noticeable representative with unique tensile properties. As described in chapter 1, ECC is currently emerging in full scale structural applications [5, 6]. As broadening application of ECC materials is emerging, it is imperative to incorporate environmental consideration into their development. Compared with normal concrete, early versions of ECC use more cement due to the absence of coarse aggregate in the mixture design. High cement content usually introduces higher hydration heat, autogenous shrinkage, and cost. Moreover, the associated increase in primary energy and emission of carbon

dioxide create a negative environmental impact. A plausible solution would be to replace a large portion of cement in ECC by industrial by-product, e.g. coal combustion products, without sacrificing its mechanical properties in general, and tensile ductility in particular.

Fly ash is a by-product of coal burning power plant and is usually considered a waste material. While more than 600 million tons of fly ash is generated each year worldwide, 80% is disposed by landfill. With pozzolanic and cementitious properties, it has been used as a substitute for cement in concrete. Traditionally, the replacement of cement by fly ash is limited to about 10% to 25% of the total cementitious materials [7, 8]. With the progress in water reducing chemical additives, high volume fly ash (HVFA) structural concrete with reasonable compressive strength and workability was introduced [9]. The term HVFA concrete is used to recognize a concrete material which has more fly ash than cement [8].

It has been reported that concrete incorporating HVFA has significant improvement in mechanical properties and durability. Specifically, HVFA concrete has higher elastic modulus, lower shrinkage and creep, excellent freezing and thawing resistance, lower water permeability, and lower chloride-ion penetration [10, 11]. This is mainly attributed to the secondary hydration that fly ash can provide, and therefore resulting in a dense matrix. The practical use of HVFA concrete in full-scale structures was recently reported by Mehta [12].

Previous research has developed green ECCs incorporating different types of fly ash, i.e. bottom ash, class F fly ash, class C fly ash, and fine fly ash, with a fly ash to cement ratio (F/A) up to 1.5 [13]. However, the cement content of green ECCs is still twice that of normal concrete. This study focuses on incorporating high dosage of class F

fly ash in ECC with a fly ash to cement ratio (FA/C) up to 5.6, in which the cement content is 40% less than normal concrete, and its resulting reduction in environmental impacts. The choice of class F fly ash is due to its abundant availability (practical consideration) and less energy-intensity (i.e. less post-processing) when compared with bottom ash and fine fly ash, respectively.

ECCs with high volume low calcium fly ash replacement (up to 85% replacement by weight) are proposed. This study focuses on the experimental characterization of mechanical properties and drying shrinkage behavior of high volume class F fly ash ECCs (HVFA ECC) and the effects of fly ash content in altering composite microstructures and environmental sustainability indicators. The ECC material design framework was described in **Chapter 2**. This design framework is useful both as a guidance for HVFA ECC design and in understanding the experimental data on HVFA ECC tensile property characteristics. In the following sections, experimental investigation is described. HVFA ECC properties in terms of compressive strength, tensile stress-strain behavior, tensile ductility, crack width, robustness, and free drying shrinkage are reported. The microstructures of HVFA ECC are also investigated and related to composite macro behavior through micromechanics theory of ECC. Finally, material sustainability indicators (MSI) are reported.

3.2 Experimental Program

Materials

Previous research [13] incorporating fly ash into ECC design (FA/C = 0 to 1.5) indicates

that use of fly ash reduces matrix toughness and fiber/matrix interfacial chemical bond which makes the satisfaction of the energy criterion for strain hardening (**Eqn. 2.1)** easier to attain, and is therefore beneficial for ECC strain-hardening behavior. The use of higher fly ash content should make this effect more profound, and therefore eight HVFA ECCs with various fly ash contents (fly ash to cement ratio, FA/C, ranges from 1.2 to 5.6 by weight) were examined in this research. The amount of fly ash used is limited by the compressive strength of HVFA ECCs as discussed in **Sec. 3.3**.

The mix design of HVFA ECCs can be found in **Table 3.1**. Type I ordinary Portland cement (OPC) was used in all mixtures. The fly ash used was an ASTM class F fly ash from Texas and the physical properties and chemical compositions of the fly ash are listed in **Table 3.2**. 76.37% of the fly ash particle size is smaller than 45 μm. A fine silica sand with a maximum grain size of 250 μm (0.01 in.) and a mean size of 110 μm (0.004 in.) was adopted in ECC mixtures. The size distribution of this quartz sand is listed in **Table 3.3**. In all mixtures, the water to cement (w/c) ratio was controlled at 0.25 ± 0.01. Slight adjustment in the amount of superplasticizer and w/c in each mixture was performed to achieve consistent rheological properties for better fiber distribution and workability. All HVFA ECCs; therefore, have similar fresh properties with self-consolidating performance (70 cm in pancake flow size). While various fiber types have been used in the past, a Polyvinyl Alcohol (PVA) fiber was used at a moderate volume fraction of 2% in this study. The dimensions of the PVA fiber are 8 mm (0.315 in.) in length and 39 μm (0.0015 in.) in diameter on average. The nominal tensile strength of the fiber is 1600 MPa (11 psi) and the density of the fiber is 1300 kg/m^3 (2192 lb/yd^3). The fiber is surface-coated by oil (1.2% by weight) in order to reduce the fiber/matrix

interfacial bond strength. This decision was made through ECC micromechanics material design theory and has been experimentally demonstrated from previous investigations [14, 15].

Mixing and Curing

A Hobart mixer with 13L (0.46 ft^3) capacity was used in preparing all ECC mixtures. Solid ingredients, including cement, fly ash, and sand, were first mixed for a couple of minutes. Water and superplasticizer were then added into the dry mixture and mixed for another three minutes. The liquefied fresh mortar matrix should reach a consistent and uniform state before adding fibers. After examining the mortar matrix and making sure there is no clump in the bottom of the mixer, PVA fibers were slowly added into the mortar matrix and mixed until all fibers are evenly distributed. The mixture was then cast into molds. Specimens were demolded after 24 hours. After demolding, specimens were first cured in sealed bags at room temperature (20 ± 3^oC) for another 6 days and then cured in air at room temperature before testing. The relative humidity (RH) of the laboratory air is 45% ± 5%.

Specimens

Compressive test was carried out for each mix at the age of 3, 28, and 90 days. Cylinders measuring 75 mm (3 in.) in diameter and 150 mm (6 in.) in length were used in this study. The ends of cylinders were capped with a sulfur compound to ensure a flat and parallel surface and a better contact with the loading device.

Coupon specimens measuring 152mm (6 in.) by 76mm (3 in.) by 13mm (0.5 in.)

were used to conduct uniaxial tensile test for each mix at the age of 3, 28, and 90 days. In addition to the tensile stress-strain curve, crack width, another important tensile characterization of ECC material concerning durability [16, 17], was also examined. A servohydraulic testing system was used in displacement control mode to conduct the tensile test. The loading rate used was 0.0025 mm/s (0.0001 in/s) to simulate a quasi-static loading condition. Aluminum plates were glued both sides at the ends of coupon specimens to facilitate gripping. Two external linear variable displacement transducers were attached to the specimen with a gauge length of approximately 50 mm (2 in.) to measure the specimen deformation.

The matrix fracture toughness K_m at the age of 28 days was measured by the three point bending test according to ASTM E399 standard. Beam specimens measuring 305 mm (12 in.) in length, 76 mm (3 in.) in height, and 38 mm (1.5 in.) in thickness were cast from selected mixtures (mix 1, 2, 3, 5, and 7) without adding fibers. The span of support is 254 mm (10 in.) and the notch depth to height ratio is 0.5.

Single fiber pullout test was performed for mix 1, 2, 3, 5, and 7 at the age of 28 days to quantify fiber/matrix interfacial properties as a function of fly ash content. Three important interfacial parameters, including chemical bond strength G_d, frictional bond strength τ_0, and slip hardening coefficient β, were determined through this test. Specimen preparation, test configuration, data processing, and calculation of interfacial parameters can be found in Ref. [18]. The interfacial parameters along with other micromechanics parameters were then used to calculate the fiber bridging law $\sigma(\delta)$. The resulting complimentary energy J'_b calculated from the $\sigma(\delta)$ curve combined with the matrix fracture toughness J_{tip} obtained from the K_m measurement were used as inputs to

evaluate material behavior, i.e. strain-hardening or tension softening, and to calculate the PSH index.

Free drying shrinkage measurements were made for all eight HVFA ECCs as a function of drying time. Tests were conducted according to ASTM C157/C157M-99 and C596-01 standards, except that the storing of the specimens before test was modified. The specimens were cured in sealed bags for 7 days before they were moved to laboratory air (Temperature: 22±3^{o}C, RH: 45±5%) and the measurement was started. Free drying shrinkage deformation was monitored until hygral equilibrium was reached.

3.3 Results and Discussion

The compressive strength of eight HVFA ECCs with different fly ash contents at the age of 3, 28, and 90 days are summarized in **Fig. 3.1** and **Table 3.4**. Each data point is an average of at least 3 compressive tests. As can be seen from the curve, the replacement of cement by class F fly ash generally reduces the compressive strength of ECC at all ages. However, even at 75% replacement of cement (FA/C = 2.8), the compressive strength of ECC at 28 days can still reach 35MPa (5075 psi) which exceeds the nominal compressive strength for normal concrete (30 MPa [4350 psi]). No significant strength gain is found in HVFA ECCs between 28 to 90 days. Fly ash is usually considered a beneficial ingredient for long term strength development in concrete due to its pozzolanic properties. In HVFA ECC; however, the specimens were cured in air after 7 days sealed curing. Related research indicated that hydration of cement will stop completely when the internal humidity in hardened cement paste falls below 80 percent [19]. Therefore,

the loss of internal humidity in low water-cementitious ratio HVFA ECCs would likely arrest further hydration.

Figure 3.2 shows the representative 28 days tensile stress-strain curves of HVFA ECCs. Tensile ductility at different ages is summarized in **Table 3.5** and is plotted against FA/C illustrated in **Fig. 3.3**. Each data point in **Fig. 3.3** is an average of 4 or more uniaxial tensile tests. From the uniaxial tensile test, all HVFA ECCs exhibit tensile strain hardening behavior at different ages and the tensile strain capacity reaches 2-3% at the age of 90 days. This indicates that the most unique property of ECC, tensile ductility, is retained and is not sacrificed by replacing cement with large amount of class F fly ash. However, there is a general tendency of tensile strength reduction with increasing amount of fly ash.

Crack width of ECC at material hardening stage does not depend on structural geometry and has been recognized as an important material property [20]. The imposed deformation is accommodated by ECC multiple cracks with more or less constant crack width during the strain-hardening stage. The magnitude of crack width controls many transport properties in cracked concrete materials and has a direct impact on durability [16, 17]. **Table 3.7** and **Fig. 3.4** give the effect of fly ash content on the residual crack width at different ages. The term residual crack width indicates that crack width is measured from the unloaded specimen after the uniaxial tensile test. Each data point in **Fig. 3.4** is an average of 4 or more coupon specimens and 20+ crack width are measured from each specimen.

It was found that the crack width reduces as fly ash content increases at all ages. The drop is significant especially in early ages (3 days, **Fig. 3.5**). The larger crack width

at early age is likely a result of lower bridging stiffness prior to full development of interfacial bond properties when load is applied to the specimen. This behavior has been observed in other laboratory tests [21] and in the field [22]. At the age of 28 days, the residual crack width of some HVFA ECCs can be lower than 10 μm (0.0004 in.). This observation suggests that HVFA ECC will most likely have lower permeability and better durability even in the presence of microcracks when compared with cracked concrete in which the crack width is not self-controlled and is usually in the range of several hundred micrometers to several millimeter. In addition, crack width was identified as a key factor in self-healing of ECC [23, 24]. Tight crack width in HVFA ECC is likely to promote self-healing behavior.

Single fiber pullout test was carried out in order to reveal the effect of fly ash content on fiber/matrix interfacial properties and on crack width control of HVFA ECCs. Single fiber pullout specimen were cast from selected mixtures (mix 1, 2, 3, 5, and 7) and tested after curing for 28 days. Results are presented in **Fig. 3.6**. As can be seen, the chemical bond G_d drops with increase of fly ash content. Lower G_d indicates easier interface debonding without fiber breaking. This is a result of lower hydration degree in fiber/matrix interface as more cement is replaced by fly ash. High volume fraction of low calcium class F fly ash serves as inner filler and reduces the possibility of developing a strong chemical bond.

Interestingly, the frictional bond τ_0 shows a reverse trend. High τ_0 indicates a strong holding force in the interface and resistance to fiber sliding. As a result, crack width reduction is attained at higher fly ash content. A possible mechanism that contributes to higher τ_0 may be that unhydrated fly ash with smooth spherical shape (**Fig.**

3.7(a)) and small particle size (76.37% < 45 μm [0.0018 in.]) increases the compactness of ITZ [25], and therefore increases interface frictional bond. **Figure 3.7(b)** illustrates the densely packed fiber/matrix interface in HVFA ECC. This picture was taken from a HVFA ECC with 85% replacement of cement (FA/C = 5.6) by a scanning electron microscope (SEM) at an age of 90 days. The dark grove shows the impression left by a fiber (removed before taking this image) on the fiber/matrix interface (marked by the dash line). The circled area shows the morphology right beneath the fiber/matrix interface. To a certain degree, it reflects the microstructure of the ITZ. It is clear that many unhydrated fly ash particles serving as inner fillers are distributed in the matrix and densely pack the interface zone. In addition, unlike chemical bond which relies on chemical reaction, this physical packing mechanism should be less dependent on age, and therefore crack width in high volume fly ash ECC remains tight at early ages. This is particularly valuable in the event that tensile stress build up occurs due to restrained autogenous shrinkage in the first few days after ECC placement. The slip-hardening coefficient was found to be independent of fly ash content as shown in **Fig. 3.6(c)**.

Figure 3.8 gives the result of PSH index of HVFA ECCs as a function of fly ash contents at the age of 28 days. To calculate the PSH index, the complementary energy J'_b was read out from the $\sigma(\delta)$ curve which was calculated from the measured interfacial properties (described above) through micromechanics models and the matrix toughness J_{tip} is determined by **Eqn. 2.2** using experimentally measured matrix fracture toughness K_m (**Fig. 3.9**) and the matrix Young's modulus. As can be seen, HVFA ECCs have PSH indexes larger than one, which means the satisfaction of **Eqn. 2.1**, consistent with the observation that all HVFA ECCs exhibited tensile strain-hardening behavior. Moreover,

ECC with higher fly ash content has higher value of PSH index, which indicates a larger margin between J'_b and J_{tip} and implies a better chance of saturated multiple cracking, i.e. a more robust multiple cracking behavior in HVFA ECCs. The larger PSH index value for mixes with higher FA content is mainly due to the lower G_d and higher τ_o.

The implication of FA content on composite strain-hardening tendency was further confirmed by plotting the inverse of PSH intensity index, $(\text{PSH intensity})^{-1}$, against FA/C as depicted in **Fig. 3.8**. The PSH intensity index was evaluated based on the observed crack spacing x_d^{test} measured from the uniaxial tensile tests and the theoretical crack spacing x_d calculated from the mechanics of matrix stress buildup through interfacial shear stress transfer. Detailed calculation of x_d can be found in Ref. [26]. The maximum value of $(\text{PSH intensity})^{-1}$ is 1 which indicates a fully saturated multiple cracking. Larger $(\text{PSH intensity})^{-1}$ value represents more saturate and robust multiple cracking behavior (i.e. robust tensile strain capacity). Indeed, PSH index is positively correlated with $(\text{PSH intensity})^{-1}$ as shown in **Fig. 3.8**, and therefore PSH index can be used as an indicator in the future to identify the saturation of multiple cracking and the robustness of ECC tensile ductility. Robustness improvement of HVFA ECC in terms of tensile strain capacity is evident due to easy saturation of multiple cracking and is almost linearly proportional to the fly ash content as illustrated in **Fig. 3.8**.

The smaller crack width and closer crack spacing in ECC mixes containing a larger amount of FA combines to give a 28 day tensile strain capacity that remains about constant at ~2-3% as mentioned earlier.

Figure 3.10 shows the free drying shrinkage deformation measurement of HVFA ECCs. Because of the absence of coarse aggregate, drying shrinkage deformation of

ECC (1500 – 1800 με) [27] is higher than normal structural concrete (600 – 800 με) [27, 28]. The general trend in **Fig. 3.10** shows that fly ash can effectively reduce drying shrinkage deformation in ECC material. Similar result has been reported for HVFA concrete [29]. In the present study, 50% reduction of free drying shrinkage of ECC was found when fly ash to cement ratio was increased from 1.2 to 5.6. A possible mechanism is that unhydrated fly ash particles serve as fine aggregates (**Fig. 3.7(b)**) to restrain the shrinkage deformation [8, 30].

To quantify the greenness of HVFA ECCs, Material Sustainability Indicators (MSI) are adopted in this study [31]. MSIs are calculated based on material and energy flow in the production process, and expressed in terms of energy consumption, waste, and pollutant releases including solid waste, carbon dioxide, nitrogen oxides, sulfur oxides, particulate matter, water usage, hydrocarbon demand, and others. Four assumptions are made in calculating the contribution of fly ash to MSI. First, fly ash is a waste material that would be disposed of. Second, fly ash does not carry any environmental burdens associated with coal combustion. Third, reusing fly ash is given a credit for saving landfill space. Fourth, there is no processing on fly ash after leaving the power plant. **Table 3.7** summarizes three major MSIs of representative HVFA ECCs. MSIs of conventional concrete are also computed for comparison purpose. In calculating solid waste, fly ash is assigned a negative value since recycling removes fly ash from the waste stream. In general, MSIs decrease with increase of FA/C, which indicates a greener material at higher fly ash content. Due to the presence of fiber, HVFA ECCs consume more energy than concrete. In terms of solid waste and carbon dioxide generation; however, the material sustainability performance of HVFA ECCs surpassed conventional

concrete.

Although MSIs provide a simple platform for comparing greenness of different materials, true assessment of sustainability should be performed based on life cycle analysis of a specific type of infrastructure. Case study [32, 33] has shown that over a complete life cycle a bridge using durable ECC link slab is significantly more sustainable than the same structure using concrete link slab due to lower maintenance and construction congestion costs. Lower maintenance costs of bridges incorporating ECC link slabs can reduce life cycle agency costs by 27%. Lower construction congestion resulting from fewer construction events can reduce user costs, such as lost driver wages, by 14%. Less construction material and fewer vehicles caught in traffic reduce lifecycle environmental cost burdens by 28%. Overall this results in a decrease in life cycle cost from $22 million for the conventional bridge to $18.5 million for the ECC link slab bridge, a 16% reduction in total costs. Additionally, the adoption of ECC link slabs represents a 39% decrease in carbon dioxide emissions over the complete service lifecycle, a 40% reduction in NMHC releases, a 39% reduction in Methane, a 44% decrease in PM_{10} emissions, and a 48% decrease in sulfur dioxide emissions, a precursor to acid rain.

3.4 Conclusions

A set of HVFA ECCs with different amounts of fly ash replacement is developed. This study demonstrates the feasibility of creating greener ECC, which maintains the tensile ductility characteristics but also incorporates sustainability consideration. In particular,

the following conclusions can be drawn:

1. Increase of fly ash content generally reduces the compressive strength of ECC. At FA/C equals 2.8; however, the compressive strength at 28 days can still reach 35 MPa, which is the regular strength grade for concrete in many applications. HVFA ECCs with different compressive strength may be selected for use in different applications.
2. All HVFA ECCs show tensile strain-hardening behavior, with PSH indexes larger than one. At the age of 90 days, the tensile ductility of HVFA ECCs can still reach the long term stabilized value of 2-3%.
3. Tensile strength tends to be reduced with increasing fly ash content. As of FA/C is increased from 1.2 to 5.6, the tensile strength reduced from 5-6 MPa to 3-4 MPa.
4. High fly ash content tends to reduce the crack width in ECC. It is found that high interface frictional bond τ_0 restrain the slippage of fiber and is responsible for the tight crack width. Microstructure analysis reveals that the higher τ_0 is a result of densely packed interface transition zone by unhydrated fly ash particles. Tight crack width has been shown to promote self-healing in ECC and greatly benefit the durability of ECC infrastructure.
5. Increasing the amount of fly ash in HVFA ECCs tends to improve robustness (reduced variability) of tensile ductility, based on the current analysis. Furthermore, the PSH index may be used as a robustness indicator in terms of ECC tensile ductility.
6. Incorporating high volumes of fly ash in ECC generally reduces the free drying shrinkage. In this study, 50% reduction of free drying shrinkage is found when

FA/C increases from 1.2 to 5.6.

7. In MSIs analysis, HVFA ECCs remain more energy intensive than conventional concrete. However, the production of HVFA ECCs results in negative solid waste and in some cases lower carbon dioxide emission compare to that of conventional concrete.

Incorporating waste stream material ingredients does not necessarily mean lower composite material performance, as long as the governing mechanisms for possible deterioration are controlled. In the present study, using recycling class F fly ash actually improves many properties of ECC, especially reduced drying shrinkage, tighter crack width and more robust tensile strain ductility. However, as is expected, the use of fly ash does limit the compressive strength and tensile strength of ECC. Therefore, understanding the underlying micromechanics of critical composite properties is the key to successfully take sustainability into consideration in the design of construction materials.

Table 3.1 – Mix proportion of HVFA ECCs

Mix	FA/C	Cement, kg/m^3 (lb/yd^3)	Fly Ash, kg/m^3 (lb/yd^3)	Sand, kg/m^3 (lb/yd^3)	Water, kg/m^3 (lb/yd^3)	SP, kg/m^3 (lb/yd^3)	PVA Fiber, kg/m^3 (lb/yd^3)	Total, kg/m^3 (lb/yd^3)
1	1.2	571 (962)	685 (1154)	456 (768)	332 (559)	6.80 (11.46)	26 (43.8)	2077 (3500)
2	1.6	477 (804)	763 (1286)	456 (768)	330 (556)	6.05 (10.19)	26 (43.8)	2060 (3471)
3	2.0	412 (694)	824 (1388)	456 (768)	326 (549)	5.52 (9.30)	26 (43.8)	2051 (3456)
4	2.4	362 (610)	870 (1466)	456 (768)	323 (544)	5.10 (8.59)	26 (43.8)	2042 (3441)
5	2.8	324 (546)	906 (1527)	456 (768)	320 (539)	5.29 (8.91)	26 (43.8)	2037 (3432)
6	3.2	292 (492)	935 (1575)	456 (768)	312 (526)	5.52 (9.30)	26 (43.8)	2027 (3415)
7	3.6	266 (448)	959 (1616)	456 (768)	309 (521)	5.80 (9.77)	26 (43.8)	2022 (3407)
8	5.6	190 (320)	1063 (1791)	456 (768)	300 (506)	6.45 (10.87)	26 (43.8)	2032 (3424)

Table 3.2 – Physical properties and chemical compositions of fly ash

SiO_2, %	55.71	Moisture Content, %	0.16
Al_2O_3, %	22.56	Loss on Ignition, %	0.41
Fe_2O_3, %	5.61	Amount Retained on #325 Sieve, %	23.63
Sum, %	83.88	Specific Gravity	2.29
CaO, %	10.44	Autoclave Soundness, %	0.02
MgO, %	1.78	Strength Activity Index w/ Portland Cement at 7 days, % of Control	77.1
SO_3, %	0.54		
Na_2O, %	0.24	Strength Activity Index w/ Portland Cement at 28 days, % of Control	85.5
K_2O, %	0.79		
Total Alkalies, %	0.76	Water Required, % of Control	94.6
Available Alkalies, %	0.26		

Table 3.3 – Size distribution of silica sand

< 150 μm (0.0059 in.), %	< 100 μm (0.0039 in.), %	< 75 μm (0.0030 in.), %	< 53 μm (0.0021 in.), %
93	77	33	8

Table 3.4 – Compressive strength, MPa (Ksi) of HVFA ECCs at different ages

FA/C / Age (days)	1.2	1.6	2.0	2.4	2.8	3.2	3.6	5.6
3	30.6±2.1 (4.4±0.3)	26.3±1.0 (3.8±0.2)	16.9±0.4 (2.4±0.1)	17.1±0.4 (2.5±0.1)	14.6±3.2 (2.1±0.5)	17.0±0.5 (2.5±0.1)	15.0±0.2 (2.2±0.0)	8.2±0.2 (1.2±0.0)
28	52.6±0.2 (7.6±0.0)	47.5±0.4 (6.9±0.1)	34.2±2.8 (5.0±0.2)	38.4±1.6 (5.6±0.2)	35.2±1.3 (5.1±0.2)	26.7±4.4 (3.9±0.6)	23.9±1.0 (3.5±0.1)	21.4±1.0 (3.1±0.1)
90	54.0±1.4 (7.8±0.2)	49.0±4.8 (7.1±0.7)	35.5±2.9 (5.2±0.1)	43.4±0.6 (6.3±0.1)	38.9±1.1 (5.6±0.2)	28.2±1.2 (4.1±0.2)	25.9±0.1 (3.8±0.0)	22.2±1.4 (3.2±0.2)

Table 3.5 – Tensile strain capacity (%) of HVFA ECCs at different ages

FA/C / Age (days)	1.2	1.6	2.0	2.4	2.8	3.2	3.6	5.6
3	4.6±1.3	4.2±0.8	4.1±0.2	4.3±1.0	4.4±0.3	4.3±1.1	4.0±0.3	3.8±0.4
28	2.7±1.1	3.7±0.6	3.0±1.1	2.9±0.8	3.0±0.7	2.7±0.7	2.5±0.3	3.3±0.2
90	1.8±0.9	3.0±1.4	3.1±1.5	2.3±0.7	3.3±1.4	2.9±0.9	2.6±1.2	3.4±0.6

Table 3.6 – Residual crack width (μm) after tensile test of HVFA ECCs at different ages

FA/C / Age (days)	1.2	1.6	2.0	2.4	2.8	3.2	3.6	5.6
3	84±32	60±7	33±6	28±6	16±4	13±5	12±2.5	13±2
28	31±6	36±12	15±3	22±6	15±8	8±2	8±1	15±2
90	17±5	26±10	16±6	16±8	11±3	8±2	7±1	9±1

Table 3.7 – Material sustainable indicators (MSIs) of conventional concrete and HVFA ECCs

	Total Energy, MJ/L (MJ/gal)	Solid Waste, kg/L (lb/gal)	Carbon Dioxide, g/L (lb/gal)
Conventional Concrete	2.46 (9.32)	0.2 (1.669)	373.28 (3.12)
HVFA ECC (FA/C = 1.2)	5.99 (22.69)	-0.46 (-3.84)	628.16 (5.24)
HVFA ECC (FA/C = 3.6)	4.35 (16.48)	-0.84 (-7.01)	350.79 (2.93)
HVFA ECC (FA/C = 5.6)	3.91 (14.81)	-0.95 (-7.93)	276.95 (2.31)

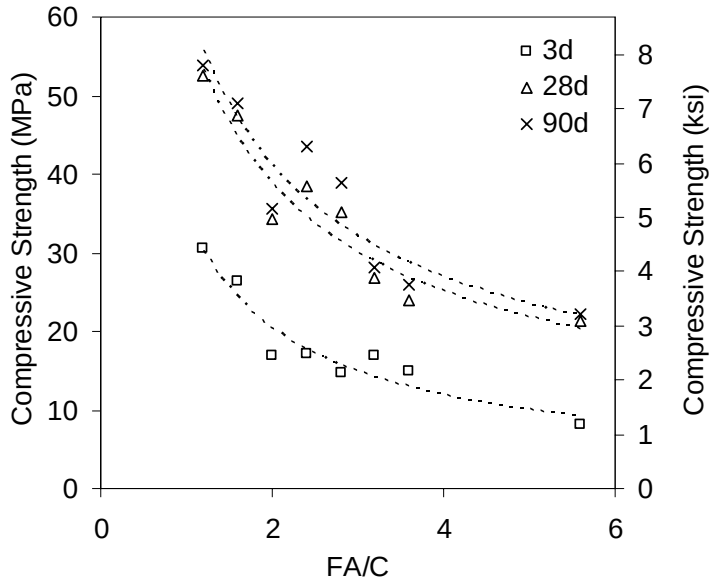

Fig. 3.1 – Compressive strength of HVFA ECC as a function of fly ash content at different ages.

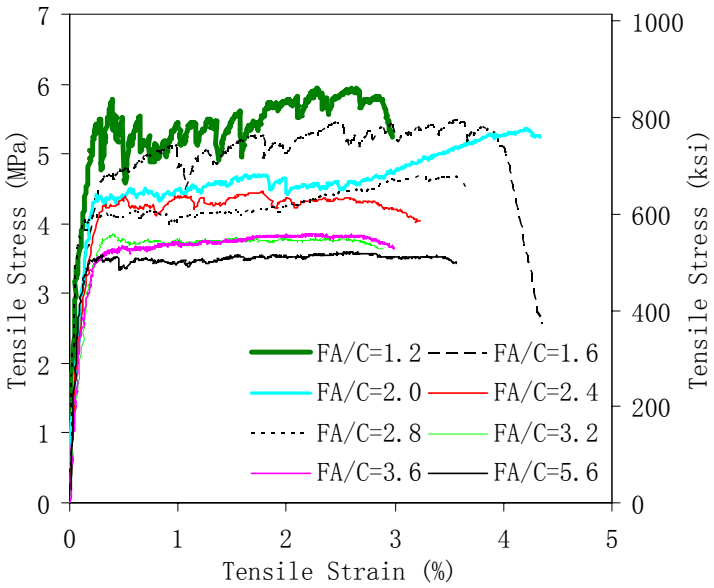

Fig. 3.2 – Tensile stress-strain curves of HVFA ECCs at the age of 28 days.

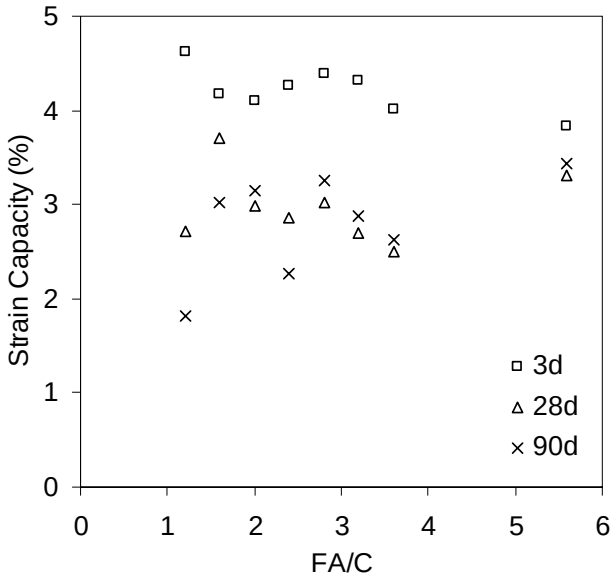

Fig. 3.3 – Tensile ductility of HVFA ECC as a function of fly ash content at different ages.

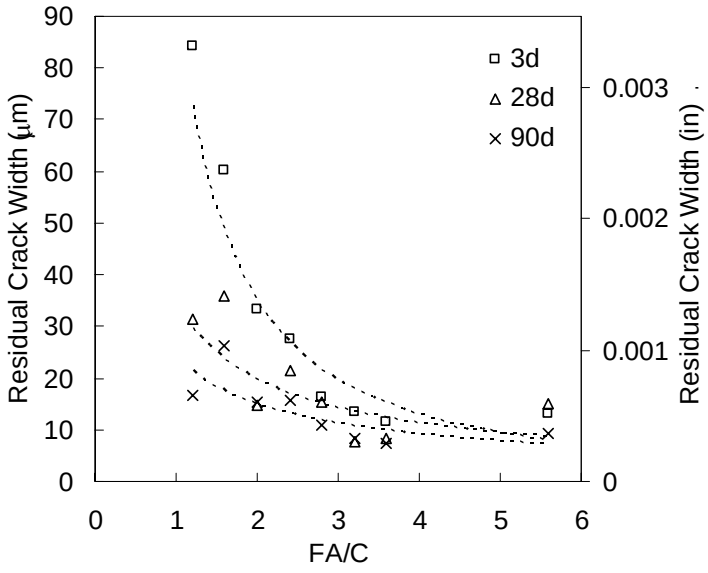

Fig. 3.4 – Residual crack width of HVFA ECC as a function of fly ash content at different ages.

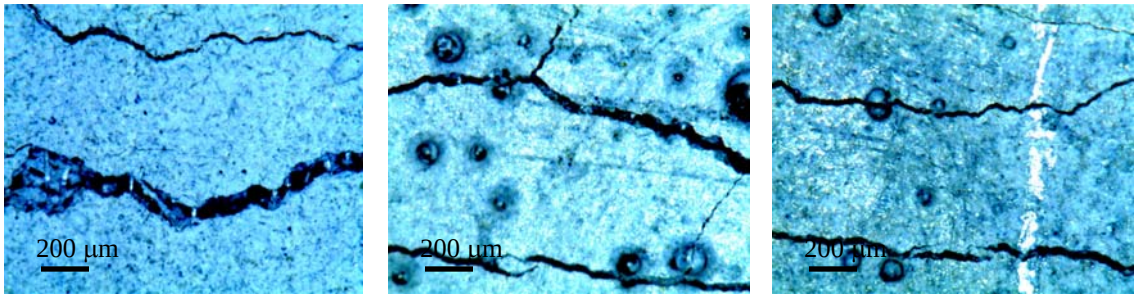

(a) (b) (c)

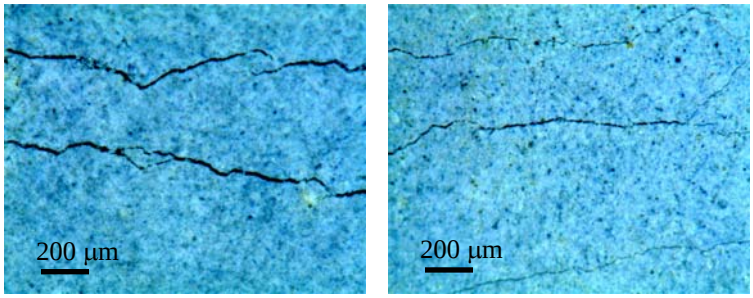

(d) (e)

Fig. 3.5 – Microscopic photos of residual crack width of HVFA ECCs at the age of 3 days where FA/C are (a) 1.2, (b) 1.6, (c) 2.0, (d) 2.8, and (e) 3.6, respectively.

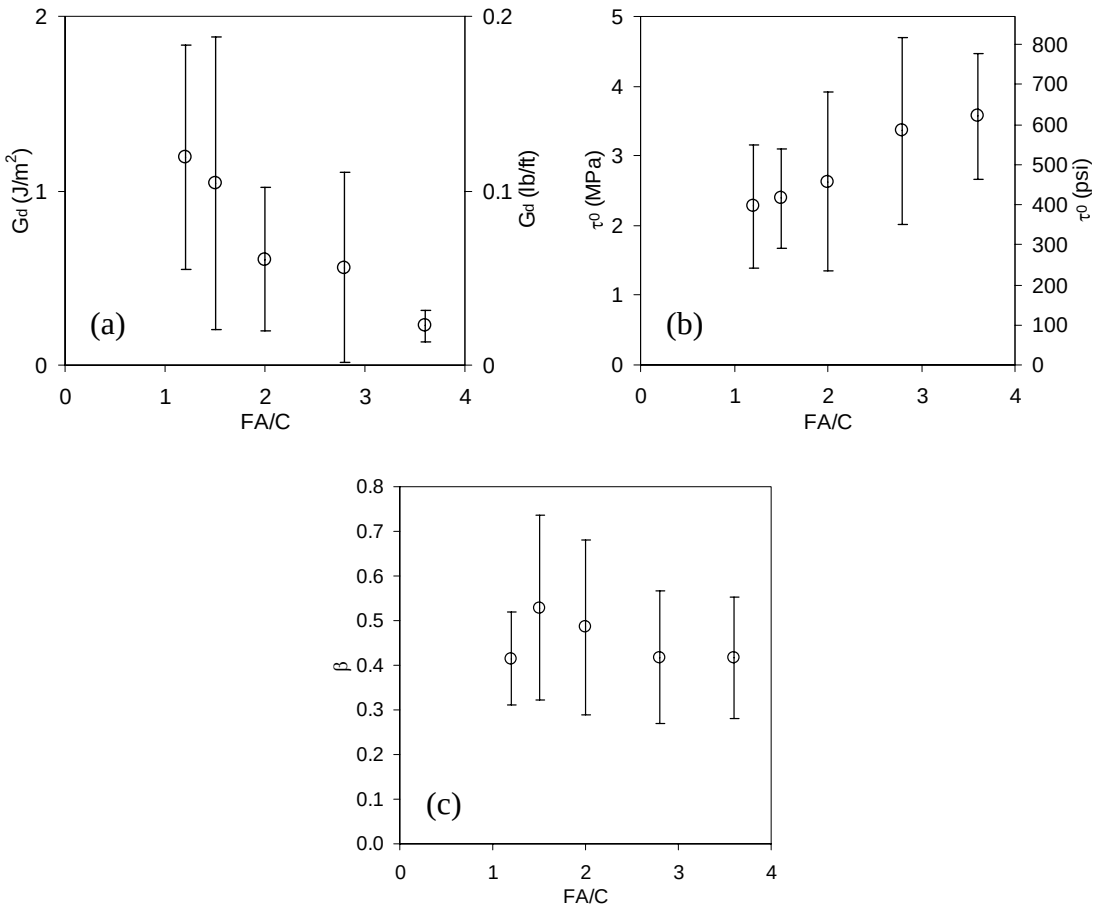

Fig. 3.6 – (a) Chemical bond strength, (b) frictional bond strength, and (c) slip-hardening coefficient of HVFA ECC as a function of fly ash content at the age of 28 days.

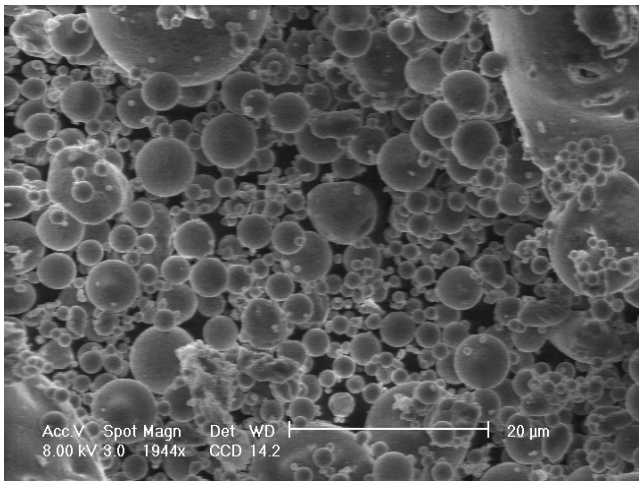

(a)

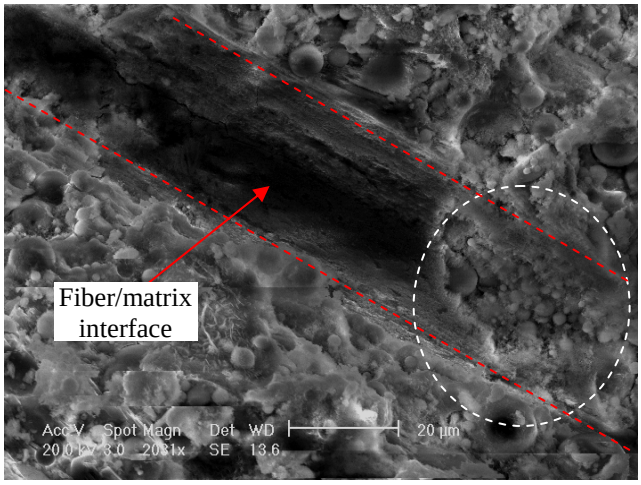

(b)

Fig. 3.7 – SEM photos of (a) class F fly ash and (b) ITZ of HVFA ECC with 85% replacement of cement at the age of 90 days.

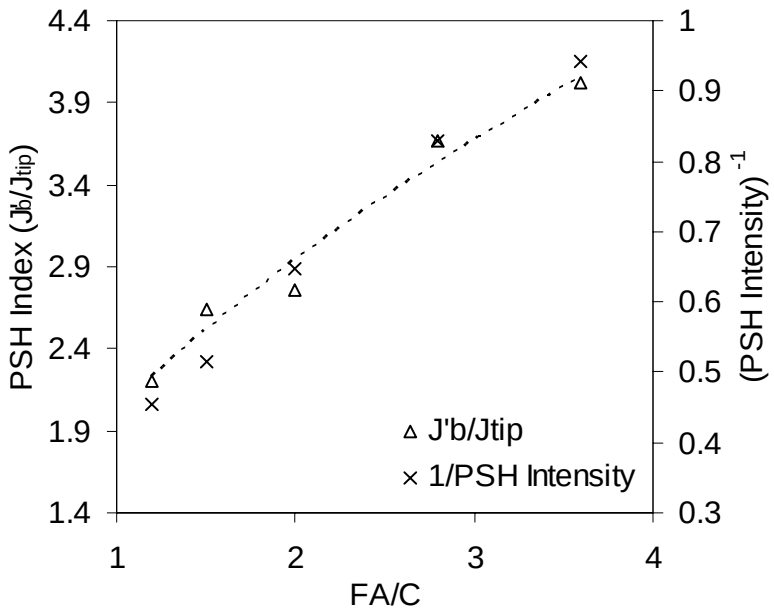

Fig. 3.8 – PSH and PSH intensity indexes of HVFA ECCs at the age of 28 days.

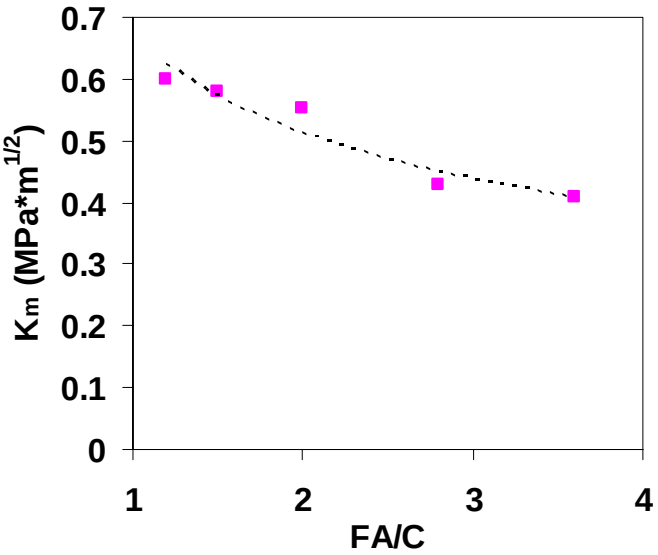

Fig. 3.9 – K_m as a function of fly ash content at the age of 28 days.

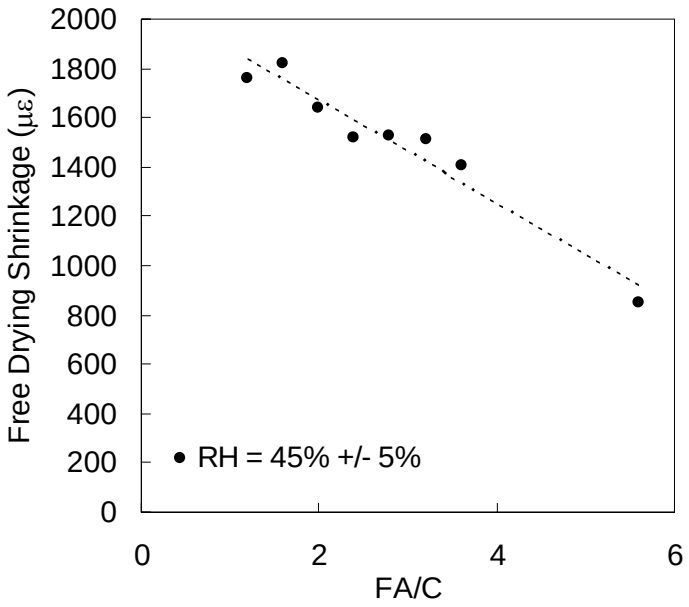

Fig. 3.10 – Free drying shrinkage of HVFA ECC as a function of fly ash content.

References

[1] Metha, P.K., "Reducing the Environmental Impact of Concrete," *Concrete International*, vol.23, no.10, pp.61-66, 2001

[2] USGS, *Mineral Commodity Summaries*. 2006.

[3] van Oss, H.G., and A.C. Padovani, "Cement Manufacture and the Environment. Part I: Chemistry and Technology," *Journal of Industrial Ecology*, vol.6, no.1, pp.89-105, 2002

[4] Battelle, *Climate Change*, in *Toward a Sustainable Cement Industry*. 2002, World Business Council on Sustainable Development (WBCSD).

[5] Kunieda, M., and Rokugo, K., "Recent Progress on HPFRCC in Japan," *Journal of Advanced Concrete Technology*, vol.4, no.1, pp.19-33, 2006

[6] Michigan_DOT, "Bridge Decks Going Jointless: Cementitious Composites Improve Durability of Link Slabs," *Construction and Technology Research Record*, no.100, pp.1-4, 2005

[7] Reiner, M., and Rens, K., "High-Volume Fly Ash Concrete: Analysis and Application," *Pract. Periodical on Struct. Des. and Constr.*, vol.11, no.1, pp.58-64, 2006

[8] Zhang, M.N., "Microstructure, Crack Propagation, and Mechanical Properties of Cement Pastes Containing High Volumes of Fly Ashes," *Cement and Concrete Research*, vol.25, no.6, pp.1165-1178, 1995

[9] Malhotra, V.M., *Superplasticized Fly Ash Concrete for Structural Concrete Applications*, in *Concrete International*. Dec. 1986. p. 28-31.

[10] Sivasundaram, V., Carette, G.G., and Malhotra, V.M., "Mechanical Properties, and Resistance to Diffusion of Chloride Ions of Concretes Incorporating High Volumes of ASTM Class F Fly Ashes from Seven Different Sources," *ACI Materials Journal*, vol.88, no.4, pp.407-416, July-Aug. 1991

[11] Bilodeau, A., Sivasundaram, V., Painter, K.E., and Malhotra, V.M., "Durability of Concrete Incorporating High Volumes of Fly Ash from Sources in the U.S.," *ACI Materials Journal*, vol.91, no.1, pp.3-12, Jan.-Feb. 1994

[12] Mehta, P.K., and Manmohan, D., *Sustainable High-Performance Concrete Structures*, in *Concrete International*. 2006. p. 37-42.

[13] Wang, S., *Micromechanics Based Matrix Design for Engineered Cementitious Composites*, Ph.D. Dissertation, Department of Civil and Environmental Engineering, University of Michigan, Ann Arbor, 2005

[14] Li, V.C., Wang, S., and Wu, C., "Tensile Strain-hardening Behavior of PVA-EDD," *ACI Materials Journal*, vol.98, no.6, pp.483-492, 2001

[15] Li, V.C., Wu, C., Wang, S., Ogawa, A., and Saito, T., "Interface Tailoring for Strain-hardening PVA-ECC," *ACI Materials Journal*, vol.99, no.5, pp.463-472, 2002

[16] Lepech, M., and Li, V.C., "Water Permeability of Cracked Cementitious Composites," *Proceeding of Eleventh International Conference on Fracture*, Turin, Italy, 2005

[17] Lepech, M., and Li, V.C., "Durability and Long Term Performance of Engineered Cementitious Composites," *Proceedings of International RILEM Workshop on HPFRCC in Structural Applications*, Honolulu, Hawaii, pp.165-174, 2005

[18] Redon, C., Li, V.C., Wu, C., Hoshiro, H., Saito, T., and Ogawa, A., "Measuring and Modifying Interface Properties of PVA Fibers in ECC Matrix," *Journal of Materials in Civil Engineering*, vol.13, no.6, pp.399-406, 2001

[19] Midness, S., Young, J.F., and Darwin, D., *Concrete*, Second Ed., Prentice Hall, 2002

[20] Weimann, M.B., and Li, V.C., "Hygral Behavior of Engineered Cementitious Composites (ECC)," *International for Restoration of Buildings and Monuments*, vol.9, no.5, pp.513-534, 2003

[21] Li, V.C., Yang, E., and Li, M., *Field Demonstration of Durable Link Slabs for Jointless Bridge Decks Based on Strain-Hardening Cementitious Composites - Phase III: Shrinkage Control*. 2007, MDOT Progress Report 2.

[22] Li, V.C., Lepech, M., and Li, M., *Field Demonstration of Durable Link Slabs for Jointless Bridge Decks Based on Strain-Hardening Cementitious Composites*. 2005, Michigan DOT report.

[23] Yang, Y., Lepech, M., and L, V.C., "Self-healing of ECC Under Cyclic Wetting and Drying," *Proceedings of Int'l Workshop on durability of reinforced concrete under combined mechanical and climatic loads*, Qingdao, China, pp.231-242, 2005

[24] Li, V.C., and Yang, E., "Self Healing in Concrete Materials," in *Self Healing Materials: An Alternative Approach to 20 Centuries of Materials Sciences*, S. van der Zwaag Ed., Springer, pp.161-193, 2007

[25] Kayali, O., "Effect of High Volume Fly Ash on Mechanical Properties of Fiber Reinforced Concrete," *Materials and Structures*, vol.37, no.269, pp.318-327, 2004

[26] Wu, H.C., and Li, V.C., "Snubbing and Bundling Effects on Multiple Crack Spacing of Discontinuous Random Fiber-Reinforced Brittle Matrix Composites," *Journal of American Ceramics Society*, vol.75, no.12, pp.3487-3489, 1992

[27] Wang, S., and Li, V.C., "Polyvinyl Alcohol Fiber Reinforced Engineered Cementitious Composites: Material Design and Performance," *Proceedings of International RILEM Workshop on HPFRCC in Structural Applications*, Honolulu, Hawaii, pp.65-74, 2005

[28] Mindess, S., Young, J.F., and Darwin, D., *Concrete*, Second Ed., Prentice Hall, 2002

[29] Atis, C.D., "High-Volume Fly Ash concrete with High Strength and Low Drying Shrinkage," *Journal of Materials in Civil Engineering*, vol.15, no.2, pp.153-156, 2004

[30] Bisallion, A., Rivest, M., and Malhotra, V.M., "Performance of High-Volume Fly Ash Concrete in Large Experimental Monoliths," *ACI Materials Journal*, vol.91, no.2, pp.178-187, 1994

[31] Li, V.C., Lepech, M., Wang, S., Weimann, M., and Keoleian, G., "Development of Green ECC for Sustainable Infrastructure System," *International Workshop on Sustainable Development and Concrete Technology*, Beijing, China, pp.181-192, 2004

[32] Keoleian, G.A., Kendall, A., Dettling, J.E., Smith, V.M., Chandler, R., Lepech, M.D., and Li, V.C., "Life Cycle Modeling of Concrete Bridge Design: Comparison of Engineered Cementitious Composite Link Slabs and Conventional Steel Expansion Joints," *ASCE J. Infrastructure Systems*, vol.11, no.1, pp.51-60, 2005

[33] Lepech, M.D., *A Paradigm for Integrated Structures and Materials Design for Sustainable Transportation Infrastructure*, Ph.D. Dissertation, Department of Civil and Environmental Engineering, University of Michigan, Ann Arbor, 355 pp, 2006

CHAPTER 4

DESIGNING SELF-HEALING FUNCTION IN ECC

The chemical make-up and physical properties, self-controlled tight crack width and high tensile ductility in particular, of ECC makes self-healing prevails in a variety of environmental conditions even when the composite is deliberately damaged by tensioning to several percent strain. Self-healing takes place automatically at cracked locations without external intervention. Self-healing in terms of mechanical and transport properties recovery of pre-damaged (by pre-cracking) composite is revealed in a variety of environmental exposures, include wetting and drying cycles, conditioning temperature, water permeation, and chloride submersion. The establishment of self-healing in ECC looks to improve the long term ductility and durability of ECC after cracking, and to establish a much more durable civil engineering material subjected to various environmental conditions.

4.1 Introduction

Cracks can occur during any stage of the life of a concrete structure. They can be due to the concrete material itself as in the case of volume instabilities, or due to external factors such as excessive loading, harsh environmental exposure, poor construction procedures, or design error. These cracks have many negative effects on the mechanical performance and durability of concrete structures. The development of concretes which can automatically regain this loss of performance is highly desirable. Along these lines, self-healing of cracked concrete, commonly known as autogenous healing, is an often studied phenomenon.

The phenomenon of self-healing in concrete has been known for many years. It has been observed that some cracks in old concrete structures are lined with white crystalline material suggesting the ability of concrete to seal the cracks with chemical products by itself, perhaps with the aid of rainwater and carbon dioxide in air. Later, a number of researchers [1, 2] in the study of water flow through cracked concrete under a hydraulic gradient, noted a gradual reduction of permeability over time, again suggesting the ability of the cracked concrete to self-seal itself and slow the rate of water flow. The main cause of self-sealing was attributed to the formation of calcium carbonate, a result of reaction between unhydrated cement and carbon dioxide dissolved in water [1]. Thus, under limited conditions, the phenomenon of self-sealing in concrete is well established. Self-sealing is important to watertight structures and to prolonging service life of infrastructure.

In recent years, there is increasing interest in the phenomenon of mechanical property recovery in self-healed concrete materials. For example, the resonance

frequency of an ultra high performance concrete damaged by freeze-thaw actions [3], and the stiffness of pre-cracked specimens [4] were demonstrated to recover after water immersion. In another investigation, the recovery of flexural strength was observed in pre-cracked concrete beams subjected to compressive loading at early age [5]. In these studies, self-healing was associated with continued hydration of cement within the cracks. As in previous permeability studies, the width of the concrete cracks, found to be critical for self-healing to take place, was artificially limited using feedback controlled equipment and/or by the application of a compressive load to close the preformed crack. These experiments confirm that self-healing in the mechanical sense can be attained in concrete materials.

Deliberate engineering of self-healing in concrete was stimulated by the pioneering research of White and co-workers [6, 7] who investigated self-healing of polymeric material using encapsulated chemicals. A number of experiments were conducted on methods of encapsulation, sensing and actuation to release the encapsulated chemicals [8-12] into concrete cracks. For example, Li et al [10] demonstrated that air-curing polymers released into a crack could lead to a recovery of the composite elastic modulus. The chemical release was actuated by the very action of crack formation in the concrete, which results in breaking of the embedded brittle hollow glass fibers containing the polymer. Thus, the healing action took place where it was needed. Another approach, taken by Nishiwaki et al [13], utilized a repair agent encapsulated in a film pipe that melts under heating. A heating device was also embedded to provide heat to the film pipe at the cracked location when an electric current is externally supplied. Yet another approach, suggested by the experiments of Bang et al [14] and Rodriguez-Navarro et al

[15], used injected micro-organisms to induce calcite precipitation in a concrete crack. These novel concepts represent creative approaches to artificially induce the highly desirable self-healing in concrete materials.

From a practical implementation viewpoint, autogenous self-healing is most attractive. Compared with other engineering materials, concrete is unique in that it intrinsically contains micro-reservoirs of unhydrated cement particles widely dispersed and available for self-healing. In most concrete and particularly in those with a low water/cement ratio, the amount of unhydrated cement is expected to be as much as 25% or higher. These unhydrated cement particles are known to be long lasting in time. Autogenous self-healing is also economical, when compared with chemical encapsulation or other approaches that have been suggested. As indicated above, the phenomenon of autogenous self-healing has been demonstrated to be effective in transport and mechanical properties recovery. Unfortunately, the reliability and repeatability of autogenous self-healing is unknown. The quality of self-healing is also rarely studied, and could be a concern especially if weak calcite is dependent upon for mechanical strength recovery. Perhaps the most serious challenge to autogenous healing is its known dependence on tight crack width, likely less than 150 microns, which is very difficult to achieve in a consistent manner for concrete in the field. In practice, concrete crack width is dependent on steel reinforcement. However, the reliability of crack width control using steel reinforcement has been called into question in recent years. The latest version of the ACI-318 code has all together eliminated the specification of allowable crack width. Thus, a number of serious material engineering challenges await autogenous

healing before this phenomenon can be relied upon in concrete structures exposed to the natural environment.

To create practical concrete material with effective autogenous self-healing functionality, the following six attributes are considered particularly important. For convenience, we label a material with all these six attributes of autogenous self-healing as "robust".

- *Pervasiveness*: Ready for activation when and where needed (i.e. at the crack when cracking occurs),
- *Stability*: Remain active over the service life of a structure that may span decades,
- *Economics*: Economically feasible for the highly cost-sensitive construction industry in which large volumes of materials are used daily,
- *Reliability*: Consistent self-healing in a broad range of typical concrete structure environments,
- *Quality*: Recovered transport and mechanical properties as good as pre-damage level, and
- *Repeatability*: Ability to self-repair for multiple damage events.

Previous researchers have engaged in limited studies in the phenomenon of concrete self-healing, the formation of self-healing products, and the necessary conditions to experience self-healing in concrete materials. These studies have resulted in identifying three general criteria which are critical to exhibit reliable autogenous self-healing – presence of specific chemical species, exposure to various environmental conditions, and small crack width. These are summarized below. In some instances these findings are contradictory, as in the case of maximum allowable crack width in

which some specify maximum crack widths of 10μm while others specify 300μm to exhibit self-healing in various environmental conditions.

- Essential environmental exposure – Water (submerged) [16, 17], environmental pH [18, 19], wet-dry cycles (capillary suction) [20], temperature above 80ºC [2], temperature above 300 ºC [21]
- Essential chemical species – Bicarbonate ions (HCO_3^-) [1, 19, 22], carbonate ions (CO_3^{2-}) [1, 19, 22], free calcium ions (Ca^{2+}) [1, 19, 22], unhydrated cement (C_3A) [21, 23], free chloride ions (Cl^-) [24-26]
- Maximum crack width – 5 to 10μm [27], 53μm [28], 100μm [2], 150μm [10], 200μm [1], 205μm [29], 300μm [16]

While the individual findings may differ, trends within these studies are clear. First, self-healing can occur in a variety of environmental conditions ranging from underwater to cyclic wet-dry exposures. These conditions are readily available for many infrastructure types. Second, adequate concentrations of certain critical chemical species are essential to exhibit self-healing mechanisms. This too, is readily available due to the chemical make up of cementitious materials and incomplete hydration, as well as the presence of CO_2 in air and NaCl in seawater and deicing salt. Finally, and potentially most important, is the requirement for tight crack widths below roughly 150μm, possibly 50μm. This condition is difficult to achieve consistently, and explains why reliable formation of self-healing products in most concrete structures has not been realized. This set of material physical and chemical properties, and exposure conditions, may serve as a reference base towards systematic design of robust self-healing concrete.

Very little work has been carried out in determining the quality of self-healing and its repeatability.

In this chapter, autogenous recovery of mechanical properties and transport properties of ECC is reported. ECC has been deliberately engineered to possess self-controlled crack width that does not depend on steel reinforcement or structural dimensions [10]. Instead, the fibers used in ECC are tailored [10] to work with a mortar matrix in order to suppress localized brittle fracture in favor of distributed microcrack damage, even when the composite is tensioned to several percent strain. ECC with crack width as low as 20 microns have been made [30]. This crack width can be seen as an inherent material property, similar to compressive strength or elastic modulus. The ability of ECC to maintain extremely tight crack width in the field has been confirmed in a bridge deck patch repair [31] and in an earth retaining wall overlay [32]. With this characteristic, ECC material should have a great potential to engage self-healing in a variety of environmental conditions, even when the composite is tensioned to several percent strain.

The deliberately pre-cracked ECC specimens were exposed to various commonly encountered environments, including water permeation and submersion, wetting and drying cycles, and chloride ponding. The mechanical properties studied include dynamic modulus, tensile stiffness, strength, and ductility. The transport properties studied include water permeability and chloride diffusivity. Self-healing ECC looks to improve structural durability and sustainability.

In the following sections, examination methods of self-healing (e.g. resonant frequency test, uniaxial tensile test, and water permeability test) are described first,

followed by the investigation of the effect of crack width on self-healing. ECC self-healing in terms of reducing transport properties and recovering mechanical properties subjected to different environmental exposures are reported. In the last section, self-healing of ECC at early ages is investigated and prested.

4.2 Self-Healing Examination Methods

In the published literature, a number of techniques have been used to detect self-healing and/or to quantify the quality of self-healing in cementitious materials. Permeability test and acoustic emission technology are two common such techniques [1, 2, 24-27, 29, 33-36]. In many studies, a falling head or constant head test is used to examine the extent of self-healing by monitoring the flow rate or quantity of water passing through the cracked specimens. The change in the coefficient of permeability of concrete with respect to time is used to measure the amount of self-healing which has occurred. Typically, a gradual reduction in this coefficient is used to infer self-healing taking place in the specimen. This approach is restricted to describing self-healing of transport property through permeation, and also requires that the promotion of self-healing derive from fluid (typically water which may carry dissolved CO_2) flow through the crack. Formation of chemical products such as calcite in the crack has been cited as a reason for increase of sealing function over time [1, 2, 24, 25, 33]. The permeability test is typically used to examine self-healing of a single crack although it can be applied to water permeability through multiple cracks.

Acoustic emission technology based on ultrasonic pulse velocity (UPV) measurements has also been used to assess crack healing. Although UPV measurement can detect the occurrence of crack healing, it has been shown that this method cannot accurately determine the extent of crack healing [29]. Resonant frequency or dynamic modulus measurements [26, 27, 37, 38] and pulse echo technique [21, 29] have also been used by a number of researchers to quantify the self-healing process. Recently, one-sided stress wave transmission measurements were used to characterize the process of self-healing. Based on the experimental observation; however, this transmission measurement is unable to clearly distinguish among crack widths above 100μm [29]. The advantage of these techniques is that they can be conducted relatively fast. However, these methods cannot explicitly differentiate between the nature of self-healing – recovery of mechanical and/or transport properties – taken place. Material bulk properties are inferred from the test data.

In order to develop a more comprehensive understanding of self-healing in ECC, four methods have been used in examining its self-healing behavior. The dynamic modulus measurements provide a quick means to assess the presence of self-healing. The uniaxial tension test is used to determine self-healing of mechanical properties. Water permeability is used to examine the recovery of transport property through permeation. Surface chemical analysis, i.e. Energy Dispersive X-ray Spectroscopy (EDX), and Environmental Scanning Electron Microscopy (ESEM) are used to analyze the chemical composition and morphology of self-healing product. Each of these test methods is described in more detail below. Together, they show unequivocally the presence of self-healing in ECC in both the transport sense and in the mechanical sense.

4.2.1 Dynamic Modulus Measurement

The material dynamic modulus measurement based on ASTM C215 (Standard Test Method for Fundamental Transverse, Longitudinal, and Torsional Resonant Frequency of Concrete Specimens) appears to be a particularly promising technique to monitor the extent and rate of autogenous healing. This test method (ASTM C215), which relies on changes in resonant frequency, has proven a good gauge of material degradation due to freeze thaw damage and is specifically referenced within ASTM C666 for freeze thaw evaluation. Rather than quantifying damage; however, it has been adapted to measure the extent and rate of self-healing in cracked concrete [38], when healing is seen as a reduction in material damage.

Prior to using resonant frequency as an accurate measure of "healing" within a cracked ECC specimen, it is essential to verify it as a valid measurement of internal damage/healing. Therefore, a series of ECC specimens measuring 230mm by 76mm by 13mm were prepared and subjected to varying levels of strain deformation ranging from 0% to 4% (i.e. different damage level) under uniaxial tension at the age of 28 days. After unloading, the resonant frequency of each cracked specimen was determined.

From this series of tests, a relationship between tensile strain (i.e. damage) and change in resonant frequency was determined. Further, this relation extends to the number of cracks within a specimen versus resonant frequency. These relations are shown in **Figs. 4.1(a) and (b)**, respectively. The resonant frequency has been normalized by that at zero strain, i.e. the resonant frequency measured with the virgin ECC without preloading. These figures show a distinct bi-linear relationship between the resonant frequency and the tensile strain deformation or number of cracks. Below approximately

1% strain, a sharp drop in resonant frequency with strain/crack number can be seen, while above 1% strain this trend softens. The bi-linear relationship may be attributed to the increase in number and crack width of the multiple-microcracks at low strain level, while only increase in crack number at steady state crack width has been observed after about 1% strain. These results indicate that a change of resonant frequency can be used to quantify the degree of damage (i.e. tensile strain beyond the first crack) to which an ECC specimen has been subjected. Therefore, this technique should prove useful in quantifying both the rate (with respect to cycles of exposures) and extent of self-healing, or "negative damage", within cracked ECC specimens.

4.2.2 Uniaxial Tensile Test

Unlike conventional concrete material, tensile strain-hardening behavior represents one of the most important features of ECC material. To assess the quality of self-healing in such materials, the magnitude of recovered mechanical properties were measured under uniaxial tensile loading. First, deliberate damage were introduced by tensioning a coupon specimen to pre-determined strain levels followed by unloading. After exposure to a healing environment, the specimen is then reloaded in direct tension to analyze the recovery magnitude of tensile strength, stiffness and strain capacity in ECC as shown in **Fig 4.2**. These properties were then compared with those measured before damage (in the case of elastic stiffness) and with those after damage but before self-healing. A servohydraulic testing system was used in displacement control mode to conduct the tensile test. The loading rate used was 0.0025 mm/s to simulate a quasi-static loading condition. Aluminum plates were glued both sides at the ends of coupon specimens to

facilitate gripping. Two external linear variable displacement transducers were attached to the specimen to measure the specimen deformation.

4.2.3 Water Permeability Test

Water permeability test was carried out to measure the transport property, permeability coefficient, of material either virgin (uncracked), preloaded (cracked/damaged), or rehealed specimen. To conduct permeability test, two experimental setups were used. A falling head test was used for specimens with a low permeability, while a constant head test was used for specimens (such as those with large crack width) with a permeability too high to practically use the falling head test. These two setups are shown schematically in **Figs 4.3(a) and (b)**, respectively. The falling head and constant head permeability test setups have been adapted from Wang et al. [35] and Cernica [39].

The permeability of specimens in the falling head test can be determined using **Eqn 4.1** [39], while the permeability of specimens in the constant head test can be determined using **Eqn 4.2** [39].

$$k = \frac{a \cdot L}{A \cdot t_f}\left(\frac{h_0}{h_f}\right) \tag{4.1}$$

$$k = \frac{V \cdot L}{A \cdot h_0 \cdot t_f} \tag{4.2}$$

where k is the coefficient of permeability, a is the cross sectional area of the standpipe, L is the specimen thickness in the direction of flow, A is the cross sectional area subject to flow, t_f is the test duration, h_0 is the initial hydraulic head, h_f is the final hydraulic head, and V is the volume of liquid passed through the specimen during the test.

This permeability test technique was adopted to examine the self-healing in the form of automatic sealing of the microcracks induced by preloading. In this manner, autogenous healing leading to recovery of resistance to water transport via permeation is investigated.

4.2.4 Microscopic Observation and Analysis

The quality of healing is likely influenced by the type of self-healing products formed inside the crack. Analyses of these products were conducted using ESEM and EDX techniques. The crystalline and chemical properties of self-healing products were determined. These techniques are particularly useful in verifying the chemical makeup of self-healing compounds, essential in identifying the chemical precursors to self-healing and ensuring their presence within the composite.

4.3 Environmental Exposures

As described in the previous section, the robustness of self-healing should be examined under a variety of environmental exposures typically experienced by concrete infrastructure systems. In the investigation of self-healing of ECC, various environmental exposures regimes have been adopted. These include cyclic wetting and drying, conditioning temperature, and immersion in water or chloride solution. Specifics of the exposure regimes are summarized below:

- CR1 (water/air cycle) subjected pre-cracked ECC specimens to submersion in water at 20ºC for 24 hours and drying in laboratory air at 21±1ºC, 50±5% RH for 24 hours,

during which no temperature effects are considered. This regime is used to simulate cyclic outdoor environments such as rainy days and unclouded days.

- CR2 (water/hot air cycle) consisted of submersion of pre-cracked ECC specimens in water at 20ºC for 24 hours, oven drying at 55ºC for 22 hours, and cooling in laboratory air at 21±1ºC, 50±5% RH for 2 hours. This regime is used to simulate cyclic outdoor environments such as rainy days followed by sunshine and high temperatures in summer.
- CR3 (90%RH/air cycle) consisted of specimen storage in 90±1%RH curing cabin at 20ºC for 24 hours, and cooling in laboratory air at 21±1ºC, 50±5%RH for 24 hours. This regime is used to simulate high humidity outdoor environments but with no exterior water available.
- CR4 (water submersion) consisted of submersion in water at 20ºC till the predetermined testing ages. This regime is used to simulate ECC in some underwater structures.
- CR5 (air) considered direct exposure to laboratory air at 21±1 ºC, 50±5%RH till the predetermined testing ages. This exposure is used as the control regime.
- CR6 (water permeation) consisted of continuous permeation through cracked ECC specimen in water at 20ºC till the predetermined testing ages. This regime is used to simulate environmental conditions of infrastructure in continuous contact with water with a hydraulic gradient, such as water tank, pipelines, and irrigation channels.
- CR7 (chloride solution submersion) considered direct exposure of pre-cracked ECC specimens to a solution with high chloride content. This regime is used to simulate the exposure to deicing salt in transportation infrastructure or parking structures, or in

concrete containers of solutions with high salt content.

4.4 Effect of Crack Width on Self-Healing

To examine the effect of crack width on self-healing, mortar coupon specimens measuring 230 mm by 76 mm by 13 mm reinforced with a small amount (0.5 vol.%) of polyvinyl alcohol (PVA) fiber were prepared. These specimens were deliberately made to exhibit tension-softening response typical of normal fiber reinforced concrete so that a single crack of controlled crack width can be introduced. Each specimen was first preloaded under uniaxial tension to produce a single crack with a crack width between 0 μm and 300 μm. Negligible closing of the crack was detected upon unloading. After unloading, the specimens were exposed to ten wetting and drying cycles (CR1). Resonant frequency and permeability coefficient were measured after preloading and ten wetting and drying cycles (CR1) to monitor the self-healing of specimen with different crack widths.

Figure 4.4 shows the resonant frequency of single-crack specimens before and after wet-dry cycles as a function of crack width. The y-axis gives the resonant frequency of preloaded specimens before and after the prescribed wet-dry exposure, normalized to the resonant frequency of uncracked (virgin) material. Therefore, 100% represents a total recovery of the resonant frequency. It is expected that further hydration and moisture content changes in the undamaged portion of the specimen during the specimen exposure regimes may contribute to some fraction of the resonant frequency recovery. In other words, even with no rehealing of cracks, the resonant frequency may

be expected to rise somewhat after a specimen has been conditioned. To account for this, the averaged resonant frequency of virgin uncracked specimens under the same 10 cyclic exposure regimes (10 cycles of CR1) was used in the normalization. Each data point represents the average of three test results.

As seen in **Fig. 4.4**, the resonant frequency of specimens after 10 cyclic wet-dry exposures can recover up to 100% of the uncracked value provided that crack widths are kept below 50 microns. With an increase of crack width; however, the degree of material damage indicated by the drop in resonant frequency increases and the extent of self-healing diminishes. When the crack width exceeds 150 microns, the specimen resonant frequency remains unchanged after undergoing the wet-dry cycle exposure, signifying the difficulty of repairing microstructural damage within these cracked materials.

Along with the resonant frequency monitoring, permeability tests were conducted on those single cracked specimens after 10 wet-dry cycles. **Figure 4.5** summarizes the permeability coefficient of preloaded specimen after 10 cyclic exposures as a function of crack width. Although it is known [40] that self-healing can occur during the very act of performing a permeability test, the data shown here were initial values so that permeability changes during the test were deliberately excluded. Thus any self-healing detected here were due to the wet-dry cycle exposures. From **Fig. 4.5**, it can be seen that after exposure, the permeability of specimens with crack widths below 50 microns is essentially identical to that of virgin uncracked specimens, which represents a full recovery of transport property, permeability. With increasing crack width, the permeability increases exponentially.

The resonant frequency measurements and the permeability measurements together suggest that autogenous self-healing within cement-based materials in both mechanical and transport properties can be achieved, provided that damage must be restricted to very tight crack widths, below 150 microns and preferably below 50 μm. This extremely tight crack width is difficult to attain reliably in most concrete materials, even when steel reinforcement is used. However, tailorable ECC materials with inherent tight crack width control have been intentionally designed to meet this rigorous requirement.

4.5 Autogenous Healing of ECC

The mix proportions of ECC material used in this investigation are given in **Table 4.1**. The ECC material utilized for these studies has a tensile strain capacity of 3% and an average steady state crack width of 60 microns. To prepare the ECC, Type I ordinary portland cement, sand with 110μm average grain size, Class F normal fly ash supplied by Boral Materials Technologies, 12mm Kuralon-II REC-15 polyvinly alcohol fibers supplied by Kuraray Company, and a polycarboxylate-based high range water reducer (ADVA® Cast 530) from W.R. Grace & Co. were used. A series of coupon specimens were cast from a single batch prepared using a forced-based Hobart mixer. The fresh ECC was then covered with plastic sheets and demolded after 24 hours. The specimens were left to air cure under uncontrolled conditions of humidity and temperature until the specific test age.

4.5.1 Recovery of Dynamic Modulus

Dynamic modulus measurement was used to monitor the rate and extent of self-healing. ECC coupon specimens measuring 230 mm by 76 mm by 13 mm were prepared and preloaded to different predetermined uniaxial tensile strain levels from 0.3% to 3% at the age of six months. On unloading, a small amount of crack closure about 15% was observed. To account for this, all crack width measurements were conducted in the unloaded state. **Table 4.2** shows the average number of cracks within two pre-loaded specimen series and their corresponding crack widths over a gauge length of 100mm. The maximum, rather than the average crack width, is reported here to highlight the extremely tight crack widths inherent in ECC as compared to concrete. While self-healing in structures will take place in the loaded state, this unloading has minimal impact on ECC self-healing capabilities as cracks in ECC material subjected to tensile load typically exhibits a similar width to that in the unloaded state, between 60μm and 80μm on average [41]. After unloading, these specimens were subsequently exposed to ten wet-dry cycles (CR1 or CR2). The resonant frequencies of the pre-crack specimens were measured after each wetting and drying cycle to monitor the extent and rate of self-healing in ECC. Uniaxial tensile tests were conducted to measure the recovered tensile mechanical properties of ECC specimens after completing the ten wet-dry cycles.

From **Figs. 4.6(a)** and **(b)**, it can be seen that the resonant frequencies of all preloaded ECC specimens gradually recovers under cyclic wetting and drying. The shaded band indicates the range of resonant frequencies of virgin ECC specimens which had undergone the same cyclic wetting and drying exposure regime. Ultimately, the resonant frequencies stabilize after 4 to 5 cycles. These results demonstrate that roughly

4 to 5 wetting-drying cycles are adequate to engage noticeable self-healing of cracked ECC material. Specimens subjected to higher tensile strains exhibit a lower initial frequency after cracking, due to a wider crack width and a larger number of cracks, and ultimately lower recovery values after wetting-drying cycles.

Figures 4.7(a) and **(b)** show the extent of self-healing within preloaded ECC specimens. By calculating the ratio of the resonant frequency after ten wet-dry cycles to the resonant frequencies of virgin ECC specimens which had undergone the same cyclic wetting and drying exposure regimes, the extent of self-healing can be deduced. It was found that the resonant frequencies for CR1 tests after pre-loading were 40~82% of initial, while after wet-dry cycles had regained stiffness to 87~100% of initial values. For CR2 specimens, the resonant frequencies after pre-loading were 31~83% of the initial value, and after self-healing had stabilized at 77~90% of initial.

Of particular interest is the relation between the extent of self-healing and level of strain in the preloaded ECC specimens under CR1. Pre-loaded testing series with tensile strain of 0.5% exhibited a reduction in resonant frequency of only 18%, while those pre-loaded to 3% strain showed an initial reduction of 60%. Self-healing in 0.5% strained specimens showed rebounded resonant frequencies back to 100% of initial values, while specimens pre-loaded to 3% strain returned to only 87% of initial frequencies. This phenomenon is captured in **Fig. 4.8**, which highlights the rebound in resonant frequency versus number of cracks within the ECC specimen. As the number of cracks grows, both the rate and amount of self-healing grows. However, the ultimate self-healed condition may not be as complete as in specimens strained to a lower deformation. This is likely due to the presence of a greater number of cracks within the highly strained specimens.

Within self-healed ECC specimens, the material which heals the cracks is typically much weaker than the surrounding mortar matrix. With an increasing number of cracks, while the opportunity for a greater amount of healing exists, the likelihood of healing all these cracks to a level similar to the uncracked state drops. Therefore, the accompanying reduction in ultimate self-healing state (i.e. final resonant frequency) with an increase in preloaded tensile strain level is not altogether surprising.

In addition to this, a noticable difference exists in the extent of self-healing within specimens subjected to CR1 and CR2. This is most evident in **Figs. 4.7(a) and (b)**. While most specimens subjected to CR1 recovered their full initial RF, those subjected to CR2 did not. This may be due to the temperature effects associated with the CR2 exposure regime. After submersion in water at 20ºC, these specimens are then oven dried at 55ºC. During this process, moisture escapes from the specimens through evaporation. As the water evaporates, steam pressure builds up within the pores, resulting in internal damage and potential microcracking. This additional damage which takes place during the self-healing process, coupled with the initial damage due to cracking, may handicap CR2 specimens and ultimately result in lower amounts of self-healing when compared to CR1 specimens.

4.5.2 Recovery of Tensile Properties

After exposure (CR1 or CR2) and examining resonant frequency (Sec. 4.5.1), uniaxial tensile tests were conducted again in the rehealed specimens. In the stress-strain curve of the reloading stage, the permanent residual strain introduced in the preloading stage is not accounted for.

Figures 4.9 and 4.10 show the preloading tensile stress-strain curves of ECC specimens as well as the reloading tensile stress-strain curves of rehealed ECC specimens after exposure cycles CR1 and CR2, respectively. In the stress-strain curve of the reloading stage, the permanent residual strain introduced in the preloading stage is not accounted for. For the CR1 test series, the first-cracking strength of nearly all specimens after self-healing falls below the first-cracking strength of the virgin specimens (before any damage was induced). The tensile strain capacity after self-healing for these specimens ranges from 1.7% to 3.1%. For the CR2 test series, once again the first-cracking strength of all specimens after self-healing remains below the first-cracking strength of virgin specimens. The tensile strain after self-healing for CR2 specimens ranges from 0.8% to 2.2%. However, the ultimate strengths after self-healing are actually higher than those of the pre-loaded specimens, especially for the specimens pre-loaded to 2-3%.

The higher ultimate strength and lower tensile strain capacity for specimens subjected to CR2 compared to those in CR1 is attributed to the higher temperature exposure (55 ^{o}C) in the CR2 exposure regime. With this temperature increase, the moisture in the specimens will migrate out and may result in a process similar to steam curing. Therefore, hydration of unreacted cement and fly ash will be accelerated. This results in a higher matrix toughness and fiber/matrix interfacial bond which is expected to contribute to higher ultimate strength and a reduction in tensile strain capacity according to micromechanics theory [35] of ECC.

Figure 4.11 shows the tensile properties of ECC specimens which have been preloaded to 3% strain levels, then unloaded, and immediately reloaded. Thus these

specimens have no opportunity to undergo any self-healing. As expected, there is a remarkable difference in initial stiffness between a virgin specimen and a pre-loaded damaged specimen without any rehealing. This is due to the re-opening of cracks within pre-loaded specimen during reloading. The opening of these cracks offers very little resistance to load, as the crack simply opens to its previous crack width. Once these cracks are completely opened; however, the load capacity resumes, and further tensile straining of the intact material (between adjacent microcracks) can take place. By comparing the material stiffness of self-healed specimens in **Figs. 4.9 and 4.10** with that shown for the pre-loaded specimens without self-healing in **Fig. 4.11**, it can be seen that a significant recovery of the stiffness of ECC specimens after self-healing (**Fig. 4.12)** is present. In other words, self-healing of ECC material can result not only in possible sealing of cracks as shown by others, but in true rehabilitation of tensile properties, in this case the initial stiffness of the material under tensile load. This may be the first instance where a clear recovery of mechanical property through autogenous healing is demonstrated.

This finding in recovery of mechanical properties is also supported by the rebound of resonant frequency seen in the self-healed ECC specimens. As outlined in ASTM C215, resonant frequency is directly related to the dynamic modulus, or stiffness, of a material. The self-healing shown through resonant frequency measurements is consistent with that shown in the regain of initial stiffness of tensile coupons. This congruent finding can be used to validate the results of both test series, resonant frequency and direct tension testing.

Figure 4.13 shows an ECC specimen subjected to tensile loading after undergoing self-healing through the CR1 exposure regime. This specimen was initially subjected to 2% strain before being exposed to wet-dry cycles. The distinctive white residue, characteristic of crystallization of calcium carbonate crystals, is abundant within the crack and near the crack face on the specimen surface. Further, it can be seen that the majority of cracks which form in self-healed specimens tend to follow previous crack lines and propagate through the self-healed material. This is not surprising due to the relatively weak nature of calcium carbonate crystals in comparison to hydrated cementitious matrix. The lower first cracking strength in the rehealed specimen (**Figs. 4.9 and 4.10**) is also attributed to that the first crack in the rehealed specimen under tension starts from the self-healed material (calcium carbonate) which has a lower strength compared to adjacent hydrated cementitious matrix.

However, this is not always the case. As can be seen in **Figs. 4.14 and 4.15**, new cracks and crack paths have been observed to form adjacent to previously self-healed cracks which now show little or no new cracking. The possibility of this event depends heavily upon the cracking properties of the matrix adjacent to the self-healing, and the quality of the self-healing material itself. However, this phenomenon serves as testament to the real possibilities of full recovery of mechanical properties via self-healing within ECC material. Certainly, the rehealed crack shown in **Fig. 4.14** was transmitting tensile load high enough to cause new cracking in its neighborhood.

4.5.3 Recovery of Transport Properties

Lepech [42] and Sahmaran [10] observed autogenous healing of ECC when conducting water permeability test and salt ponding test, respectively. This section reviews and summarizes the recovery of transport properties due to ECC self-healing.

Reduction of permeability coefficient in cracked ECC due to self-healing

Permeability specimens were cast into coupon plates with cross sectional dimensions of 13mm by 76mm and 305 mm in length. The specimens were preloaded to the predetermined tensile strain. Prior to the permeability testing (CR6), ECC specimens were kept in water for 14 days to ensure complete water saturation. The edges of the coupon specimen were sealed with epoxy to facilitate unidirectional flow through the cross section. Due to the length of time associated with this type of testing, crack width permeability measurements were performed in the unloaded state.

Figure 4.16 shows the rate of permeation through the ECC specimens dropped drastically from the initial values until asymptotically reaching the recorded value, even though the crack widths during permeability testing do not change. This phenomenon can be partially attributed to achieving complete saturation and further densification of the matrix throughout the testing period. However, ECC specimens were saturated in water for 14 days prior to permeability testing at an age of 28 days. By the time of testing, the specimens should have been nearly, if not completely, saturated and continued to undergo little matrix hydration.

Throughout the course of permeability testing, a white residue formed within the cracks and on the surface of the specimens near the cracks. These formations are shown

in **Fig. 4.17**. **Figure 4.17(a)** shows a saturated ECC specimen immediately prior to the beginning of permeability testing, while **Fig. 4.17(b)** shows the same specimen after permeability testing. The white residue forms both within the cracks, and within the pores on the surface of the ECC specimen. The effect of self-healing of cracks on permeability has been investigated by other researchers [1], and may be significant in the permeability determination of cracked ECC. This can be attributed primarily to the large binder content and relatively low water to binder ratio within the ECC mixture. The presence of significant amounts of unhydrated binders allows for autogeneous healing of the cracks when exposed to water. This mechanism is particularly evident in cracked ECC material due to the small crack widths which facilitate self-healing. However, this phenomenon is not observed while cracked ECC specimens are simply saturated in water (CR4). During the 14 days of saturation prior to permeability testing, cracked ECC specimens showed no signs of autogeneous healing of the cracks. After only 3 days in the permeability testing apparatus, evidence of self-healing became apparent. A similar phenomenon was also seen when cracked ECC specimens were partially submerged in water. Crack healing was only exhibited near the surface of the water, while no healing was observed above or below the water surface.

Surface chemical analysis (EDX) of the self-healing ECC specimens using an ESEM show that the crystals forming within the cracks, and on the surface adjacent to the cracks, are hydrated cement products, primarily calcium carbonate (**Fig 4.18**). These crystal formations within the self-healed cracks are shown in **Fig 4.19**. To facilitate healing of the cracks, and promote formation of calcium carbonate, a flow of water containing carbonates or bicarbonates must be present. Within the permeability testing,

these carbonates were introduced by the dissolution of CO_2 in air into the water which flows through the specimens. In the case of the partially submerged specimens, the small amount of carbon dioxide dissolved at the water surface was sufficient to cause limited self-healing at that location. However, in the absence of this constant carbonate supply, as in the saturation tanks prior to permeability testing, no self-healing of the ECC microcracks can occur. Ultimately, the formation of these crystals slows the rate of permeation through the cracked composite and further reduces the permeability coefficient.

Reduction of diffusion coefficient in ECC due to self-healing

Autogenous self-healing was also observed in an attempt to measure the diffusion coefficient of damage ECC specimen by means of the chloride ponding test. Salt ponding test in accordance with AASHTO T259-80 (Standard Method of Test for Resistance of Concrete to Chloride Ion Penetration) was conducted to evaluate another transport property, effective diffusion coefficient, of material either virgin (uncracked), preloaded (damaged/cracked), or rehealed specimen. After ponding for a certain period (30 days for the pre-loaded specimen and 90 days for the virgin specimen), the salt solution was removed from the prism surface. Powder samples were taken from the specimen for chloride analysis at various depths from the exposed surface. Total chloride (acid-soluble) content by weight of material at each sampling point was examined according to AASHTO T 260-97 (Standard Method of Test for Sampling and Testing for Chloride Ion in Concrete and Concrete Raw Materials).

The chloride profiles were then input into statistical and curve-fitting software. **Eqn 4.3**, Crank's solution to Fick's second law, was fitted to the data. The regression analysis yielded the values of the effective diffusion coefficient (D_e) and surface chloride concentration (C_s) for the specimen.

$$C(x,t) = C_s\left[1 - erf\left(\frac{x}{2\sqrt{D_e t}}\right)\right] \tag{4.3}$$

where

C(x,t) = chloride concentration at time t at depth x

C_s = surface chloride concentration

D_e = effective chloride diffusion coefficient

t = exposure time

erf( ) = error function

In conducting the ponding test, ECC prism specimens measuring 356mm by 76mm by 51mm were prepared. In addition to ECC material, mortar prisms were also tested for comparison purpose. The mortar prisms were reinforced with three levels of steel mesh in order to preload the specimen to a predetermined deformation. At the age of 28 days, prisms surface were abraded using a steel brush as required by AASHTO T259-80. The prisms were preloaded using four point bending test to a predetermined deformation. The ponding test was then performed in the unloaded state. Plexiglass was used around the side surfaces of the prism to build an embankment for holding chloride solution on the exposed surface of prisms. At 29 days of age, a 3% of NaCl solution was ponded on the cracked surface of prisms. In order to retard the evaporation of solution, aluminum plates were used to cover the top surface of the specimens.

Table 4.3 shows the preloaded beam deformation (BD) value, their corresponding average crack widths (CW), depths and number of cracks for prism specimens. Two virgin prisms from each mixture were tested without preloading for control purpose. Note that preloading of the mortar beams were limited to 0.83 mm due to the large crack width (~ 400 μm) and crack depth 70 mm generated in these specimens. In the ECC specimens, the crack width remains at about 50 μm even after beam deformation at 2 mm. The crack length becomes impossible to measure accurately due to the tight crack width. **Table 4.3** also shows the corresponding number of cracks for prism specimens at each beam deformation value. As seen from this table, when the deformation applied to the prism specimens is increased, the number of cracks on ECC is clearly increased but the crack width did not change for the different deformation values. Micromechanically designed ECC changes the cracking behavior from one crack with large width to multiple smaller cracks.

Figure 4.20 shows the relationship between the effective diffusion coefficient of chloride ions and the beam deformation level, for mortar and ECC specimens. Despite the same or higher magnitude of imposed overall deformation and higher crack density, the ECC specimens reveal an effective diffusion coefficient considerably lower than that of the reinforced mortar because of the tight crack width control. Especially for the higher deformation level, the effective diffusion coefficient of mortar increased exponentially with beam deformation. The effective diffusion coefficient of ECC; however, increased linearly with the imposed deformation value, because the number of microcracks on the tensile surface of ECC is proportional to the imposed beam deformation. The total chloride concentration profiles perpendicular to the crack path

indicate no significant chloride penetration even at large imposed deformation (2 mm) for ECC specimens.

The reason for the relatively low diffusion coefficient of cracked ECC specimens is not only due to the tight crack width but also the presence of self-healing of the microcracks. While no self-healing was found when the specimen was submersed in water as decribed in the previous water permeability test, a distinct white deposit was visible over the crack surface at the end of one-month salt solution exposure period (**Fig. 4.21**). This can be attributed to the prescence of NaCl ion which promotes leaching of calcuim hydroxide [35] into cracks and sealed the cracks. An ESEM observation of the fractured surface of ECC across a healed crack is shown in **Fig. 4.22**. These observations indicate that microcracks of ECC exposed to NaCl solution healed completely after exposure for 30 days to NaCl solution.

4.5.4 Summary

From the resonant frequency (after wet-dry cycle exposure) and permeability measurements, it appears that a maximum crack width of 50 micron is necessary to achieve full recovery of mechanical and transport properties in ECC material. Between 50 and 150 microns, partial recovery can be attained.

Under both water/air cycle and water/hot air cycle environments, a recovery of resonant frequent above 80% is achievable for ECC specimens pre-tensioned to as much as 3% strain. Most self-healing appear to occur within the first 4-5 cycles. Under these same conditions, 100% recovery of the initial elastic modulus can be attained. Further the original ultimate tensile strength and strain capacity are retained after rehealing.

However, the first crack strength may be lower especially for those specimens with large prestraining, probably due to the weakness in some partially healed crack planes. In this case, crack formation upon reloading will likely take place where a partially healed crack is present. For specimens with lower amount of prestraining, complete rehealing occurs so that new cracks are observed near rehealed cracks upon reloading. This is in spite of the fact that the products formed inside the cracks are calcites known to be relatively weak. It is possible that the bridging fibers serve as nucleation sites for the calcite crystals while simultaneously act as reinforcements. Further study on the details of reheal product formation process is needed.

Both transport properties, permeability and chloride diffusion, showed a decrease over time. Precracked ECC specimens exposed to water flow in the permeability experiments showed rehealing through calcite formation, while precracked ECC specimens exposed to salt water ponding showed rehealing through calcium hydroxide formation.

From these studies, it becomes evident that self-healing both in the mechanical and transport sense is present in ECC. The deliberate engineering of ECC to maintain extremely tight crack width even under large imposed deformation as carried out in these experiments, is largely responsible for the quality of autogenous self-healing in this material. The low water/binder ratio in addition to the large amount of fly ash also aids in promoting self-healing via continued hydration and pozzolanic activities. These activities are expected to extend indefinitely since unhydrated cement and unreacted fly ash in concrete materials are known to have a long shelf-life.

Similar to all concrete materials, the micro-reservoirs of unhydrated cement and unreacted fly ash in ECC ensures self-healing to be pervasive throughout a structure. The very act of creating a crack is expected to provide advective-diffusive forces that drives free calcium ions towards the crack surface and enhances the tendency to form rehealing products in the crack in the presence of water and dissolved CO_2. This suggests that chemicals are always intrinsically present where it is needed for self-healing. (External water and CO_2 in air is expected to be plentiful especially for transportation infrastructure.) Unlike other concrete materials, ECC has the ability to self-control crack width down to the 60 μm range and below, which drastically enhances the reliability of self-healing, as demonstrated in the test results described for a variety of exposure environments in this article. Also demonstrated is the quality of rehealing especially for ECC specimens preloaded to below 1% tensile strain. Recovery of mechanical and transport properties reaching 80% or above is evident. Additional research is needed to confirm the repeatability of the self-healing functionality in ECC subjected to tensile load cycles.

4.6 Self-Healing of ECC at Early Ages

Due to the improvement of processing [43] and a new generation of high range water reducing admixtures, high strength concrete [44] incorporating high cement content along with low water-cement ratio [45] and/or a well-graded particle size distribution [46] has been developed. High strength concrete has been widely used in civil infrastructure [47] and is expected to elevate structure mechanical performance and to improve durability of

reinforced concrete structures due to the dense concrete matrix, i.e. a very compact microstructure expected to lower permeability and reduce transport of corrosives to the steel. However, a number of investigations [48, 49] revealed that high cement content and low water-cement ratio distinctly raise the cracking potential at early age due to the increase of chemical and autogenous shrinkage and brittleness of high strength concrete. For example, Shah et al. reported a 30% increasing in free drying shrinkage of a high strength concrete (f'c = 90MPa at 28 days), resulting in advanced crack formation at the 6^{th} days (normal concrete control test showed crack formation at the 10^{th} day). when Those early age cracks provide pathways for the penetration of aggressive ions, and therefore greatly reduce the time to initiation of corrosion of steel reinforcement and shorten the service life of infrastructure as a consequence.

Various methods have been attempted to cope with cracking of high strength concrete at early ages [50]. For structural engineers, efforts have been placed on detailing the rebar reinforcement, including increase of reinforcing ratio and the arrangement of transversal or confinement reinforcement. For materials engineers, various kinds of fibers, fiber mesh, shrinkage reducing agent, polymers, crack sealer, and curing admixture have been applied for crack control. These approaches are effective in certain situations but their efficacy and consistency remain to be proven in other situations. Therefore, the development of concrete materials which can automatically regain this loss of performance after early age cracking is highly desirable.

The compressive strength of ECC ranges from 50 to 80 MPa depending on mix composition, putting ECC into the class of high strength concrete materials, but without the associated brittleness. In this study, autogenous healing of cracked ECC (cracks were

generated by pre-loading) at early ages was experimentally investigated and verified. Focus has been placed on early age self-healing behavior under various environmental exposures, including drying action of wind and sun and wetting by rain runoff or snowmelt. Cyclic wetting and drying at controlled temperatures was used as an accelerated test method to simulate outdoor environmental conditions. Experimental investigations on the extent and rate of self-healing for ECC material pre-loaded to various strain levels to deliberately induce various levels of damage, along with the mechanical properties of ECC after self-healing, are presented.

4.6.1 Experimental Program

The mix proportion of ECC material follows **Table 4.1**. To prepare the material, a force-based Hobart mixer with 20L capacity was used in preparing a single batch of ECC material. The fresh mixture was then cast into coupon molds measuring 300 mm by 76 mm by 12.5 mm. The fresh ECC specimens were covered with plastic sheets and demolded after 24 hours. After demolding, specimens were air cured at 50±5 %RH, 21±1^{o}C for 2 days. Uniaxial tensile tests were then conducted on the 3rd day to pre-load/pre-crack ECC specimens at specified tensile deformation, i.e. 0.3%, 0.5%, 1%, 2%, and 3%. When the tensile strain reached the predetermined value, the tensile load was released, and the specimens were removed from the tensile test machine to prepare for predetermined exposure regime, i.e. CR1, CR2, CR3, CR4, and CR5. **Table 4.4** shows the average number of cracks and their corresponding maximum crack widths over a gauge length of 100 mm. All crack width measurements are conducted in the unloaded state.

4.6.2 Recovery of Dynamic Modulus

Test results from the resonant frequency tests are given in **Figs. 4.23** and **4.24**. Each data point is a mean value of two specimens. **Figure 4.23** plots the resonant frequency versus the number of cyclic exposure. It demonstrates the rate/process of autogenous healing of cracked ECC specimens under different environmental exposures. The shaded area indicates the range of resonant frequencies of virgin (no preloading induced damage) ECC specimens which had undergone the same exposure regime.

Among the five exposure regimes, CR1 (water/air cycle), CR2 (water/hot air cycle), and CR4 (water) significantly promote the autogenous healing of cracked ECCs at early ages, and roughly 4 to 5 exposure cycles are necessary to engage noticeable autogenous healing of cracked ECC material. Unlike self-healing at later age in which the presence of both water and carbon dioxide are necessary to form calcium carbonate, early age self-healing occurs even when the specimen is submersed in water (CR4). This may be attributed to continuous hydration of damaged ECC to form C-S-H gel at early ages when plenty of water is provided under CR4. In general, specimens subjected to higher preloaded tensile strain exhibit lower initial frequency due to a higher degree of damage, and ultimately lower recovery values after environmental exposure. However, the resonant frequency can almost recover to the RF value of virgin ECC specimens in CR4 (water) even for specimens with large predetermined tensile deformation. Interestingly, although CR3 (90%RH/air cycle) subjected ECC specimens to a high humidity environment, RF recovery was limited. The resonant frequency of cracked ECC specimens exposed to air (CR5) did not show any distinct change with environmental exposures.

By calculating the ratio of the resonant frequency after ten wet-dry cycles to the resonant frequencies of virgin ECC specimens which had undergone the same exposure regimes, the extent of self-healing can be deduced as shown in **Fig. 4.24**. After exposure regime 1 (CR1), the normalized RF regained to 62~96% of initial values for the various preloading level, in contrast to the 39~77% the preload specimens without self-healing. For the CR2 (water/hot air cycle) specimens, the resonant frequencies after pre-loading were 43~73% of the initial value, and after self-healing had stabilized at 76~93% of initial. Regarding the recovery of RF, the effect of CR1 (water/air cycle) is similar to that of CR2 (water/hot air cycle). For CR4 (water) specimens, the resonant frequencies after pre-loading were 62~83% of the initial value, and after self-healing attained 95~100% of initial, in which the RF of most cracked ECC specimens approached those of virgin specimens. Almost no self-healing occurred in cracked ECC specimens when exposed to air (CR5). For CR3 (90%RH/air cycle) specimens, the resonant frequencies after pre-loading were 40~73% of the initial value, and after self-healing had recovered to 42~78% of initial. Again, limited self-healing was evident in high humidity condition. Similar result on the effect of high humidity on self-healing of concrete has been reported by other researchers [51, 52].

Based on the above observations it can be concluded that the presence of water is the most critical factor in engaging autogenous healing of ECC at early ages (e.g. CR1, CR2, and CR4). Further hydration of unhydrated cement particle is faster in water and, also, water encourages the dissolving and leaching of calcium hydroxide from the concrete matrix near the crack surface, a precondition for the formation of self-healing products. More importantly, very little carbonation can take place in air because only

carbon dioxide dissolved in the surface films of water is available [52]. Carbon dioxide in gaseous form does not react with calcium hydroxide. It can be noted that submersion in water (CR4) results in weight change of ECC specimens at early age which can increase the resonant frequency. The higher resonant frequency resulted from water absorption within concrete have also been reported in other literature [53] and it was attributed to entry of interlayer water into Tober-morite gel and to much more cracks full of water. In this investigation, the rank of different exposure regime in their effectiveness in recovery of resonant frequency of ECC at early ages is CR4 (water) > CR1 (water/air cycle) ~ CR2 (water/hot air cycle) > CR3 (90%RH/air cycle) > CR5 (air). However, due to the water absorption side-effect described above, the effectiveness of self-healing under CR4 need to be investigated further in order to assess the true self-healing in mechanical properties, stiffness in particular, as presented below.

4.6.3 Recovery of Tensile Properties

Although resonant frequency test serves as a means of rapid assessment, it only provides an indication of the level of recovery after self-healing. In order to analyze the recovery magnitude of tensile stiffness, ductility and strength, uniaxial tensile test was conducted. **Figure 4.25** shows the representative reloading tensile stress-strain curves of preloaded ECC specimens after cyclic exposure (10 cycles) along with the tensile stress-strain curve of pre-loading. In the stress-strain curve of the reloading stage, the permanent residual strain introduced in the preloading stage is not accounted for.

Stiffness

As can be seen from **Fig. 4.25**, the slope of the initial raising branch of the tensile stress-strain curve, i.e. stiffness, is different between the preloading and reloading curves. The slope of the preloading curve represents the stiffness of virgin ECC material and the slope of the reloading curve of CR5 (air) may be considered as the stiffness of cracked ECC without any healing. It is clear that the stiffness of the unhealed specimen was drastically reduced due to the presence of the microcrack damage generated during preloading. However, and as can be expected, the amount of stiffness reduction diminishes as the preloading (strain) magnitude decreases. After rehealing (under CR1 to CR4), the material regained a certain degree of its original stiffness depending on different environmental exposures. In some cases, the stiffness can almost fully recover.

Figure 4.26 displays the stiffness ratio as a function of preloading strain and exposure regimes. Stiffness ratio is defined as the ratio of the stiffness of the reloading curve to the stiffness of the preloading curve. As can be seen, low initial damage level, i.e. low pre-determined tensile deformation, has high stiffness ratio under all five exposure regimes. For example, the stiffness ratio at preloading strain of 3% ranges from 5% to 30%, while the stiffness ratio at preloading strain of 0.3% ranges from 30% to 100%. In general, CR2 (water/hot air cycle) exhibits the highest stiffness ratio of ECC specimen and CR5 (air) shows the lowest stiffness ratio. The stiffness of ECC material with low preloaded strain can recover completely under CR1 (water/air cycle) and CR2 (water/hot air cycle). At high preloaded stains, however, CR2 (water/hot air cycle) shows a better recovery than CR1 (water/air cycle). This might be attributed to the enhanced hydration due to exposure to higher temperature in CR2.

Interestingly, unlike the result observed from the resonant frequency measurements, CR4 (water) does not show the most significant stiffness recovery among the five environmental conditions. This can be explained by the high internal moisture and actions of excessive water inside the self-healed ECC specimen continously immersed in water (CR4). It should be point out that self-healed ECC specimens in CR4 (water) were reloaded immediately after a long time exposure to water and the internal relative humidity is close to 100%. It has been reported that harden cement paste with a huge internal surface area exhibits intense fluid-matrix interactions [54]. Moisture induced micro-forces, include molecular adsorption forces along pore walls, capillary pressures in capillary pores, and interlayer fluid pressures (swelling pressure) due to the presence of interlayer hydrate water in nanopores, arise as a result of repulsive forces between water molecules and keeping the pore walls at a certain distance. The induced forces are known to be extremely sensitive to fluid saturation level. CSH (Calcium-Silicate-Hydrate) as main binder ingredients in cement is composed of laminar sheets with interlayer absorbed water. The microscopic swelling pressure increases with increasing degree of saturation of water. The repulsive forces push the laminar sheets apart and the cohesive forces among the hydrated products of cement decrease. The water molecules will decrease the surface energy of the hydrated products of cement and the van der Waals' bonding among the hydrated products of cement [55]. Therefore, higher degree of saturation of water obviously results in a reduction of the stiffness of wet ECC specimen. It was concluded that resonant frequency measurements although providing a rapid test method can not precisely assess the quality of self-healing in some cases. Based on the uniaxial tensile test results which gives the true qualification of self-

healing, the rank in the stiffness ratio of cracked ECC at early ages is CR2 (water/hot air cycle) > CR1 (water/air cycle) > CR4 (water) > CR3 (90%RH/air cycle) > CR5 (air).

Tensile strain capacity

Figure 4.27 shows the result of tensile strain capacity of pre-cracked ECC subjected to different environmental exposures. After 10 cycles of exposure subsequent to different levels of induced damage, all specimens retain tensile strain capacity above 1.5%, a ductility distinctly higher than normal concrete. Among the five exposure regimes, CR5 (air) results in the highest tensile strain capacity and CR2 (water/hot air cycle) results in the lowest one. This is a direct reflection of the effect of hydration degree of the mortar matrix on ECC tensile strain capacity due to different exposure regimes at early age. Recall that specimens subjected to CR2 are submersed in water and then dried in air at 55 ^{o}C. With this temperature increase, the moisture in the specimens will migrate out and may result in a process similar to steam curing. Therefore, hydration of unreacted cement and fly ash will be accelerated, leading to an increased strength of ECC matrix and fiber/matrix interfacial bonding (due to a strong hydrophilic nature of PVA fiber), especially at early ages. The increase of matrix cracking strength prevents crack initiating and propagation from defect sites and excessively strong interfacial bonding increases the tendency of fiber rupture [10]. Both mechanisms cause a negative impact on the development of multiple micro-cracking, and therefore lower tensile ductility observed as a consequence. In contrast, specimens exposed to CR5 (air) have a lower matrix cracking strength because hydration reduces or even stops when the internal humidity goes down.

Tensile strength

The ultimate tensile strength, which is governed by the fiber bridging strength, of all ECC specimens at reloading are larger than the preloading tensile strength and this is most likely the effect of continued hydration process at early ages, i.e. increased fiber bridging strength with further hydration [35]. In particular, the ultimate strength after self-healing for CR2 (water/hot air cycle) is much higher than that of the pre-loaded specimens (**Fig. 4.25**) which again implies an accelerated hydration process leading to a stronger fiber/matrix interfacial bonding when ECC specimens are subjected to CR2 (water/hot air cycle).

4.6.4 Microstructure observations

Figure 4.28(a) shows an ECC specimen subjected to 2% tensile pre-loading and **Fig. 4.28(b)** displays the same spot on the specimen surface after undergoing autogenous healing through submersion in water (CR4). The distinctive white residue (reheal product) is abundant within the crack and near the crack face on the specimen surface. **Figure 4.29** gives a close-up view of the reheal product and its EDX spectrum. As can be seen, calcium is the main elemental composition of the reheal product. By conducting EDX quantification for oxides, the amount of calcium carbonate ($CaCO_3$) can be estimated by combining equal amount of CaO and CO_2. Interestingly, excessive CaO was found which implies the existence of calcium hydroxide (CaOH). Therefore, it is likely that the reheal product at early age is a compound of calcium carbonate (precipitation/crystallization) and calcium hydroxide (further hydration). Further

investigation by x-ray diffraction analysis is necessary in the future in order to reveal the precise chemical composition of reheal products.

4.6.5 Summary

This section presents the findings of an investigation on autogenous healing of ECC subjected to different environmental exposures at early ages. The inherent tight crack width less than 60 μm, make ECC an ideal material to engage in robust self-healing at early age under proper environmental exposures when compared with concrete. Self-healed ECC shows substantial recovery of RF loss from damage (resonant frequency test) as well as adequate mechanical performance (uniaxial tensile test). It can be expected that autogenous healing of ECC will greatly benefit the long-term durability and safety of civil infrastructure. This study represents a systematic revelation of mechanical (not just transport) properties in cementitious material, and through the use of commonly encountered exposure environments in the experiments, demonstrates the realization potential of self-healing in concrete structures. A number of other specific conclusions can be drawn:

- Four to five cycles are necessary for engaging self-healing of ECC at early age under CR1 (water/air cycle), CR2 (water/hot air cycle), and CR4 (water). For different environmental exposures, water is the most determining environmental factor to engage autogenous healing of ECC at early ages.
- In general, ECC with lower initial damage level, i.e. low pre-determined tensile deformation, has higher level of recovery for the same exposure regime. This confirms that the tighter the crack width and the lower the crack number, the higher

the probability of self-healing. Crack width below 150 μm and preferably 50 μm leads to highly robust self-healing [10]. This tight crack width, while difficult to control in normal concrete even with steel reinforcements, are readily attained in ECC when straining is below 1 %.

- Resonant frequency measurement can be used as a rapid screening of the presence or absence of self-healing. This measurement reflects averaged bulk property change in the specimen under the different exposure conditions. Uniaxial tensile test, while more cumbersome, gives a true assessment of the quality of self-healing of the microcracks, and provides quantitative measurements of recovered mechanical properties.
- Under proper exposure, self-healing can distinctly enhance the stiffness of cracked ECC resulting in the true mechanical self-healing of the composites. In some cases, the stiffness of the cracked ECC can recover completely.
- The tensile strain capacity of all re-healed ECCs remains above 1.5%, even higher if the residual strain due to preloading damage is accounted for.
- Higher exposure temperature (CR2) tends to promote the degree of hydration at early age, and therefore increase matrix toughness as well as fiber/matrix interfacial bonding. This results in higher tensile strength and lower tensile strain capacity of self-healed ECC subjected to CR2 (water/hot air cycle).
- From the EDX, the reheal product at early age is likely a compound of calcium carbonate (precipitation/crystallization) and calcium hydroxide (further hydration). Further investigation by x-ray diffraction analysis is necessary in the future to reveal the chemical composition of reheal products.

Based on this study which employs a variety of environmental exposure, self-healing of microcracks in ECC is expected to overcome the problem of early age cracking in high performance concrete materials for infrastructures exposed to water, e.g. transportation infrastructure such as roadways and bridges. Thus ECC combines high ductility, high strength, and self-healing capability. Further studies in the field should be conducted to confirm this expectation in actual structures exposed to natural environments.

4.7 Conclusions

In this chapter, recent finding on autogenous healing of ECC are reported and summarized. Several techniques are adopted to quantify the quality of ECC self-healing. Resonant frequency measurement is used as a quick assessment of self-healing. Uniaxial tensile test is used to evaluate the mechanical properties recovery of rehealed ECC. Water permeability and salt ponding tests are adopted to examine the transport properties recovery. ESEM and EDX are used to observe the morphology and to conduct chemical analysis of healing products. It was concluded that tight crack width below 150 μm and preferably below 50 μm is critical to engage noticeable self-healing in cement-based material. ECC with self-controlled tight crack width shows distinct self-healing and recovery of mechanical and transport properties under different environmental exposures both at early and later ages. Based on the ESEM and EDX analyses, it is likely that the reheal product is a mix of calcium carbonate and calcium hydroxide. The proportion of each species is dependent on different environmental conditions. Further investigation is

necessary in the future in order to reveal the precise chemical composition of reheal products.

Table 4.1 – Mix Proportions of ECC

Materials	Cement	Aggregate	Fly ash	Water	HRWR	Fiber
Unit weight (kg/m3)	578	462	694	319	17	26

Table 4.2 – Crack characteristics of pre-loaded ECC

Tensile strain (%)	**Number of cracks**	**Maximum crack widths (μm)**
3	39	90
2	27	60
1	15	60
0.5	7	70
0.3	5	50

Table 4.3 – Crack widths, numbers and depths of preloaded ECC and mortar prisms (After [10])

Material	Beam Deformation (mm)	Average Crack Width (μm)	Crack Depth (mm)	Crack Number
Mortar	0.5	~50	20	1
	0.7	~150	36	1
	0.8	~300	55	1
	0.83	~400	70	1
ECC	0.5	~0	N/A	0
	1.0	~50	N/A	15
	1.5	~50	N/A	21
	2.0	~50	N/A	35

Table 4.4 – Crack characteristics of pre-load ECC

Tensile strain (%)	3	2	1	0.5	0.3
Number of cracks	41	24	16	7	5
Maximum crack width (μm)	95	70	60	50	50

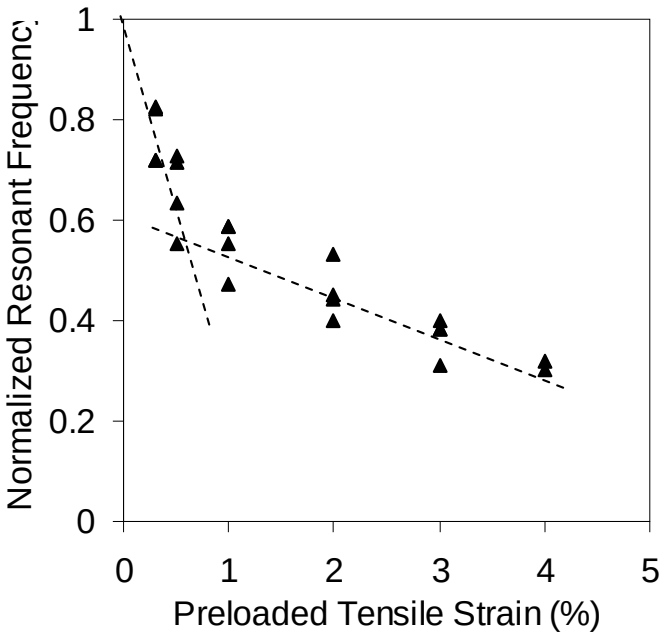

(a) Resonant frequency as a function of preloaded tensile strain

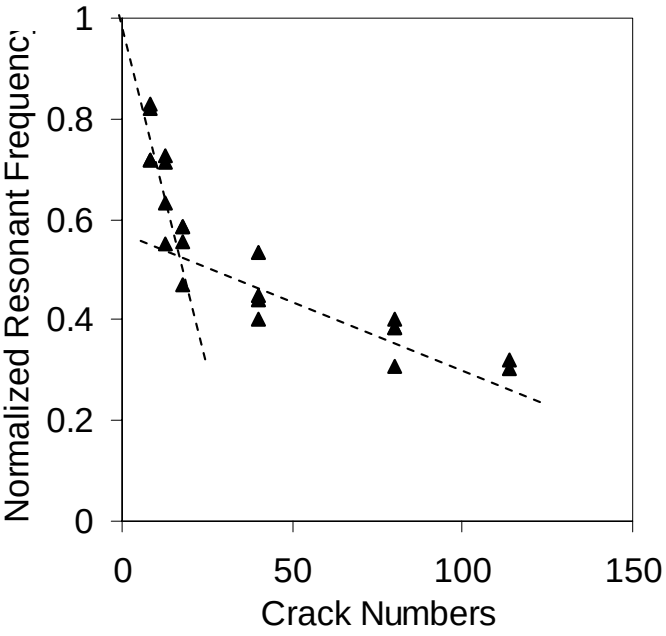

(b) Resonant frequency as a function of crack numbers

Fig 4.1 – Resonant frequency as an indicator of ECC material damage (i.e. tensile strain deformation beyond elastic stage)

Fig 4.2 – Setup of the uniaxial tensile test

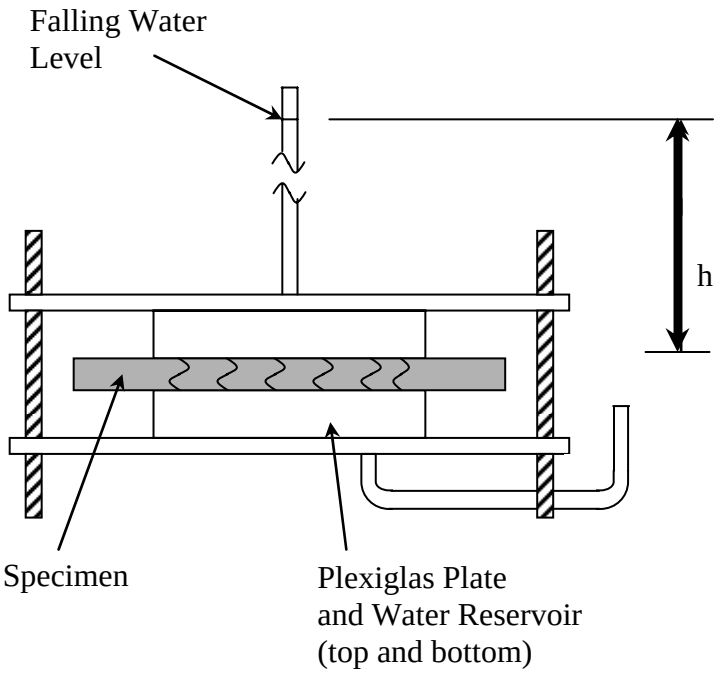

(a) Falling head permeability test setup

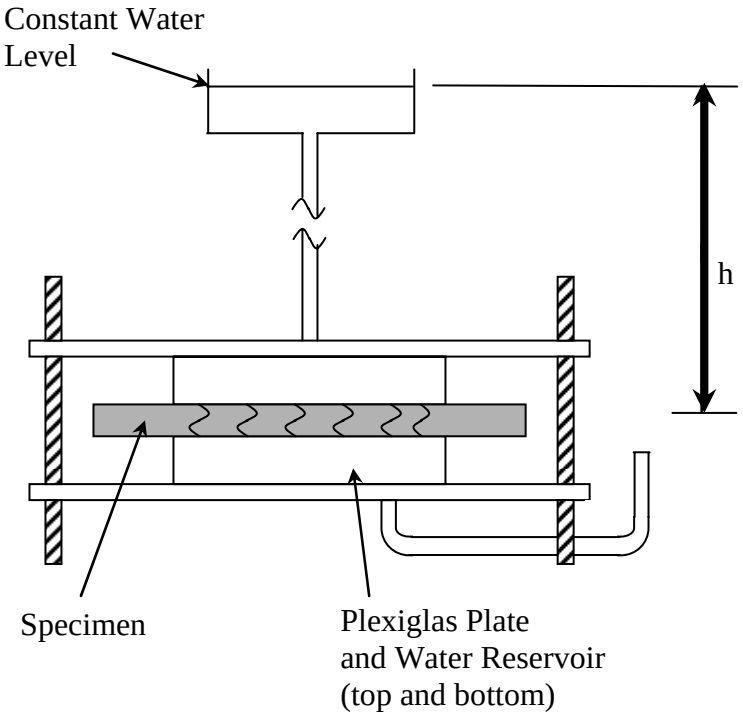

(b) Constant head permeability test setup

Fig 4.3: Permeability test setups

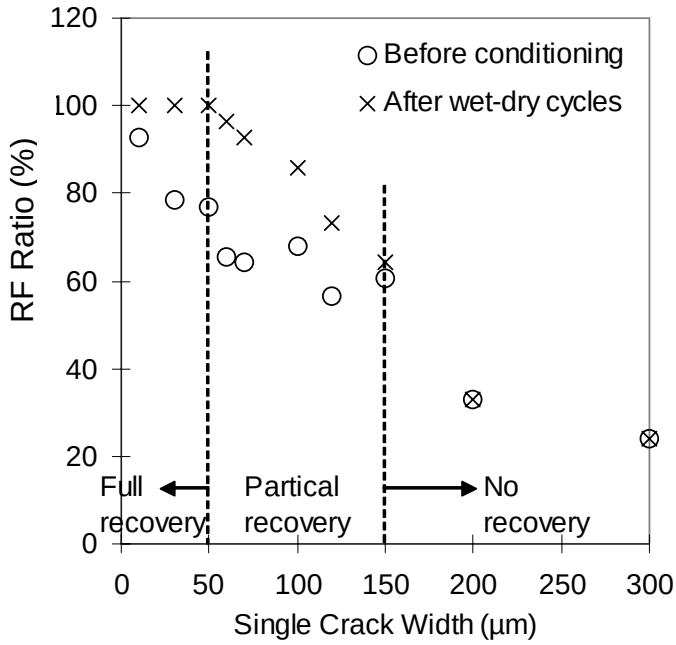

Fig. 4.4 – Resonant frequency (RF) ratio as a function of crack width

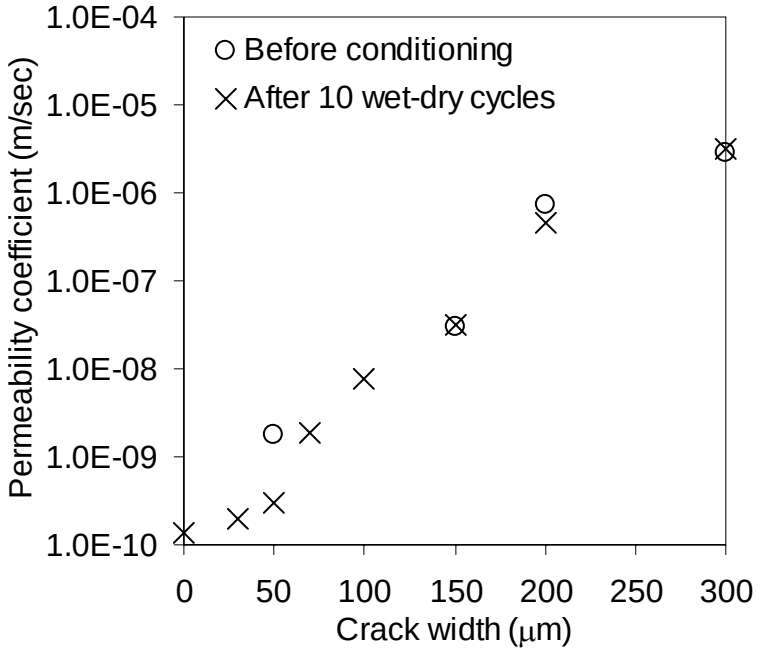

Fig. 4.5 – Permeability coefficient as a function crack width before and after exposure

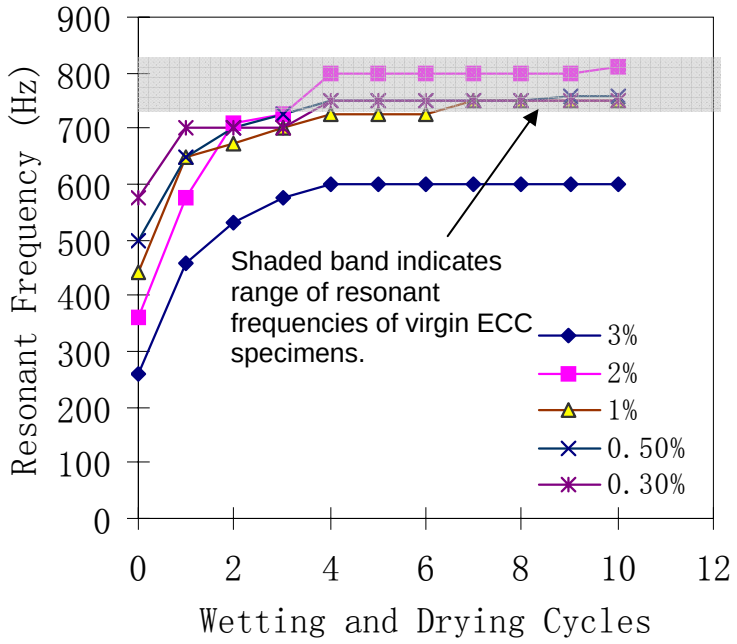

(a) Resonant frequency recovery under CR1 (water/air cycle)

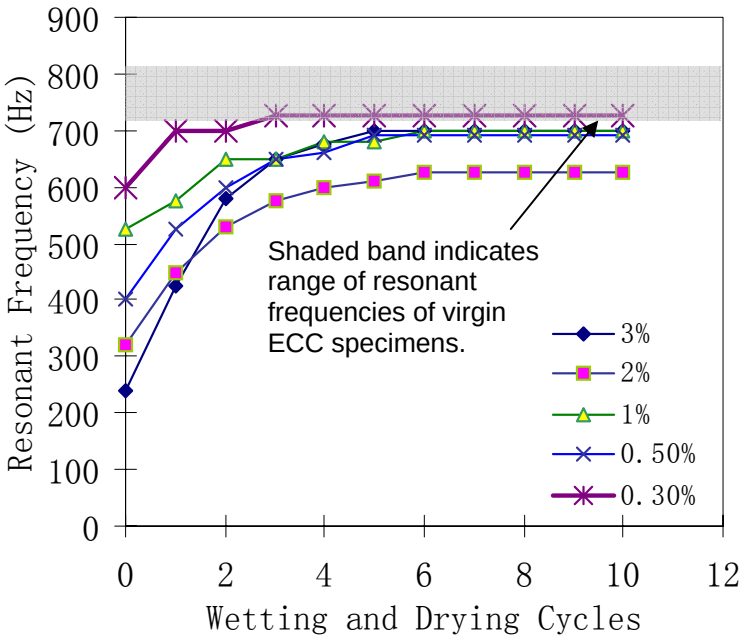

(b) Resonant frequency recovery under CR2 (water/hot air cycle)

Fig. 4.6 – Self-healing rate of ECC under cyclic wetting and drying

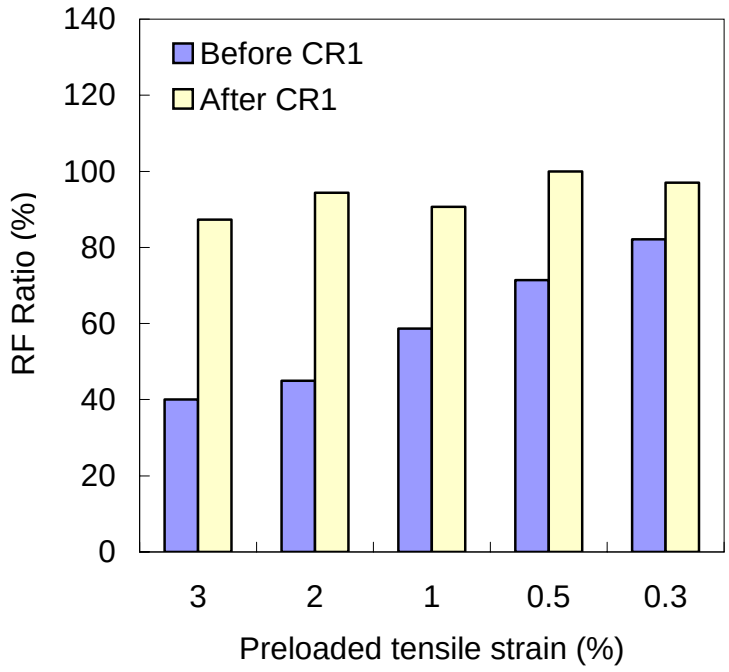

(a) Extent of self-healing in ECC under CR1 (water/air cycle)

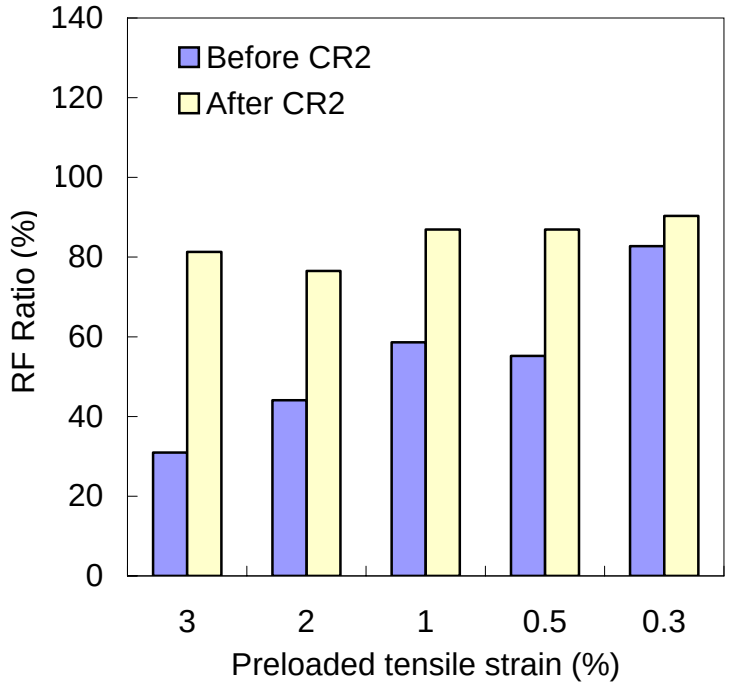

(b) Extent of self-healing in ECC under CR2 (water/hot air cycle)

Fig. 4.7 – Extent of self-healing in ECC under cyclic wetting and drying

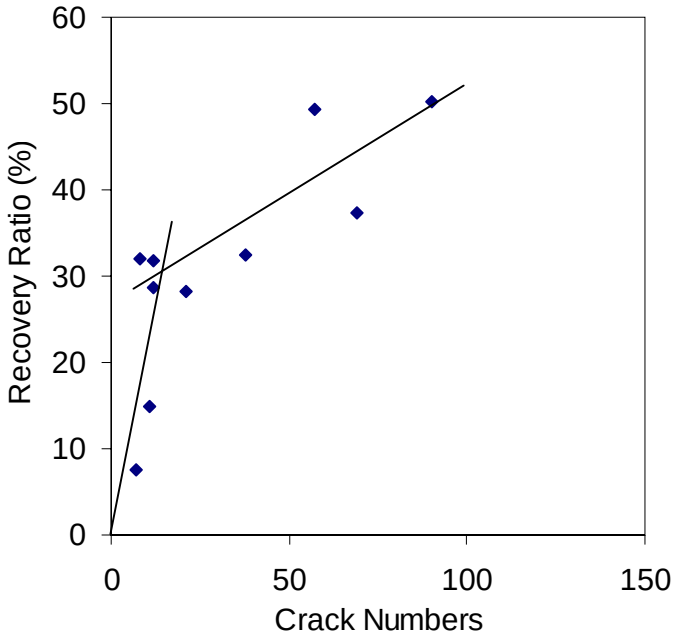

Fig. 4.8 – Rebound in resonant frequency versus number of cracks within the ECC specimen

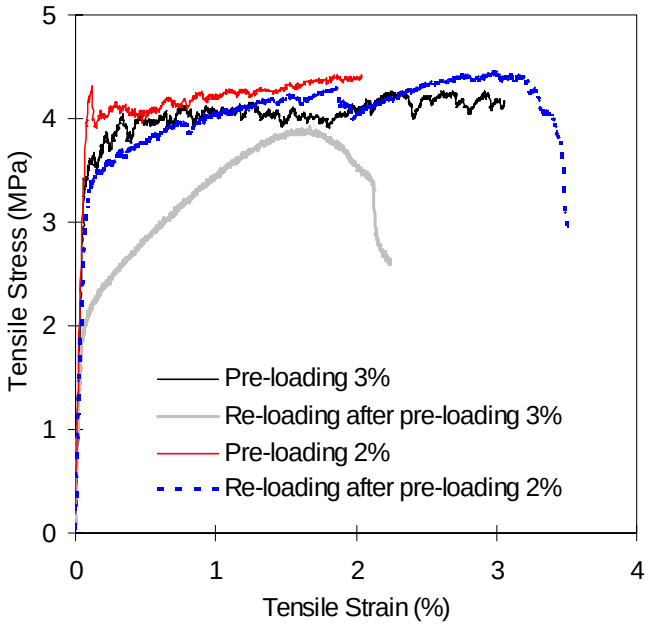

(a) Specimen with preloading to above 1%

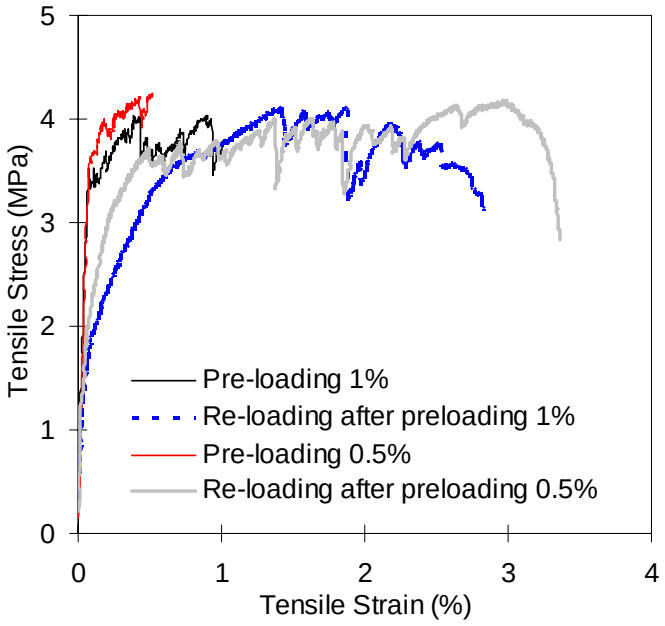

(b) Specimens with preloading to 1% or below

Fig. 4.9 – Preloading and reloading after 10 CR1 (water/air) cycles tensile stress-strain relations of ECC specimens

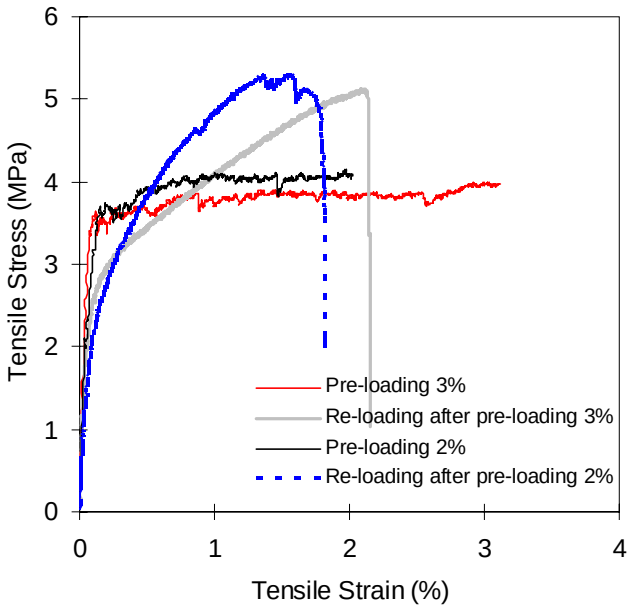

(a) Specimen with preloading to above 1%

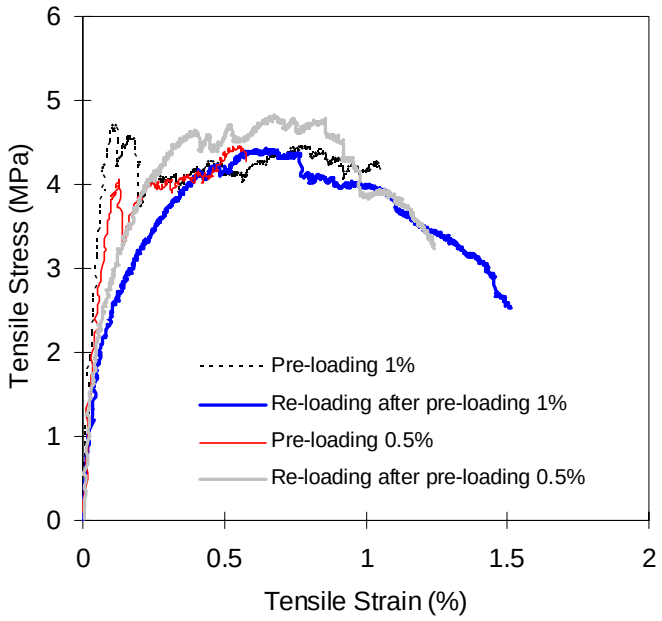

(b) Specimen with preloading to 1% or below

Fig. 4.10 – Preloading and reloading after 10 CR2 (water/hot air) cycles tensile stress-strain relations of ECC specimens

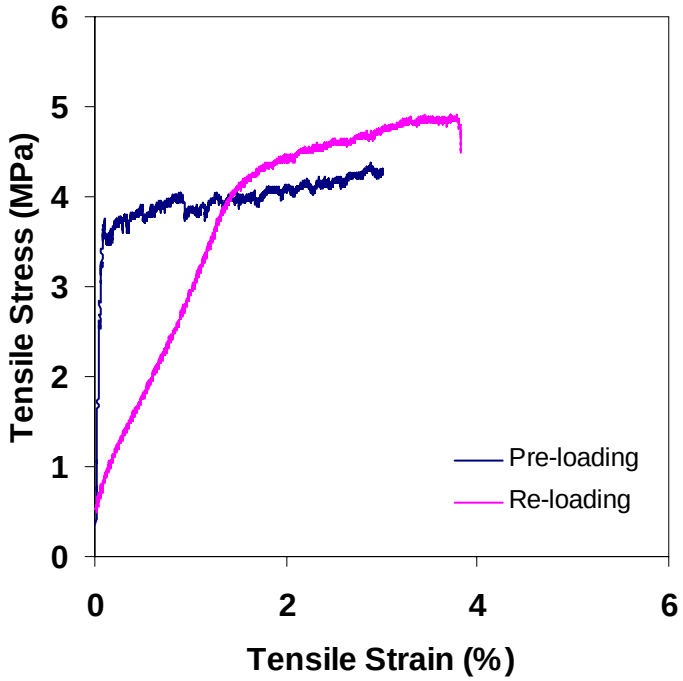

Fig. 4.11 – Preloading and reloading without self-healing tensile stress-strain curve of ECC specimen

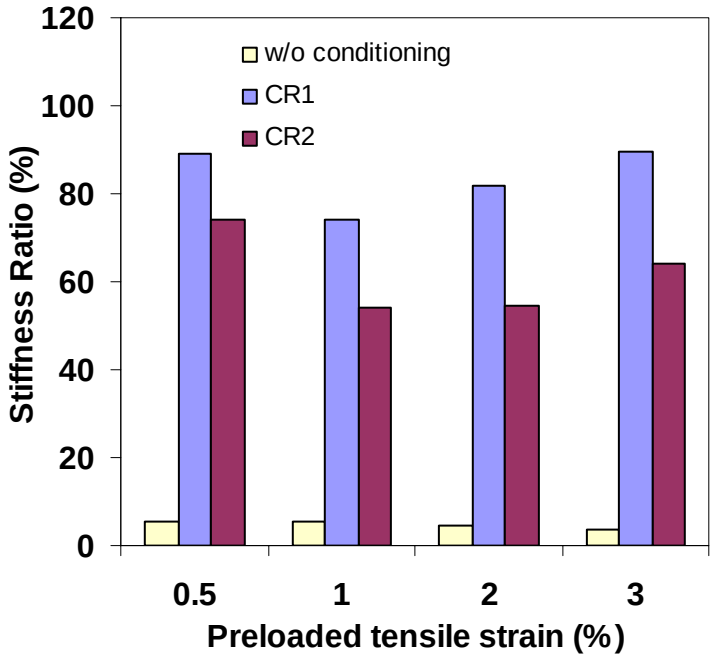

Fig. 4.12 – Stiffness recovery of ECC under different exposure regime

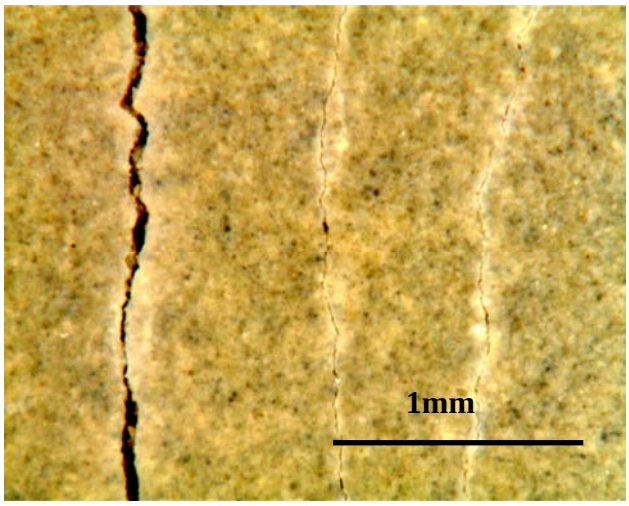

Fig. 4.13 – Cracks through self-healed material due to reloading after wet-dry cycles

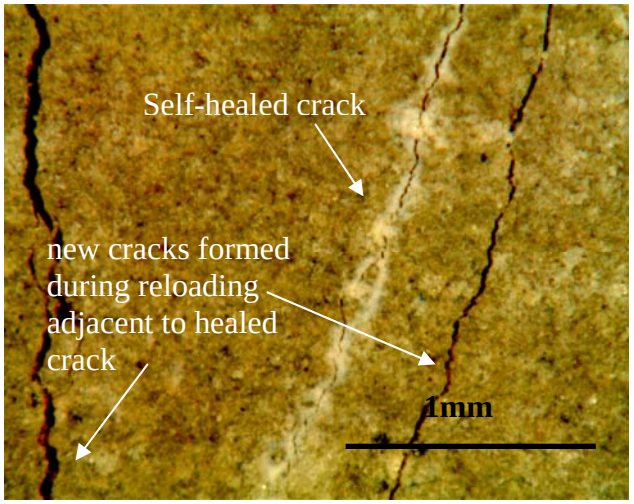

Fig. 4.14 – Cracks through virgin ECC material adjacent to a self-healed crack held tight by self-healing material

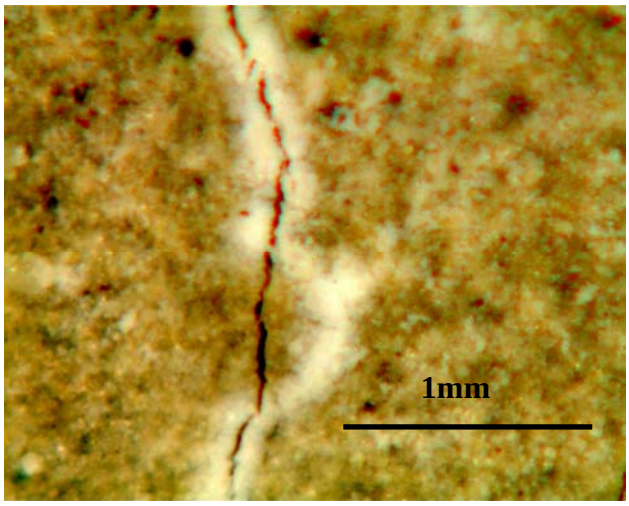

Fig. 4.15 – Meandering new crack path partially deviating from previously self-healed crack

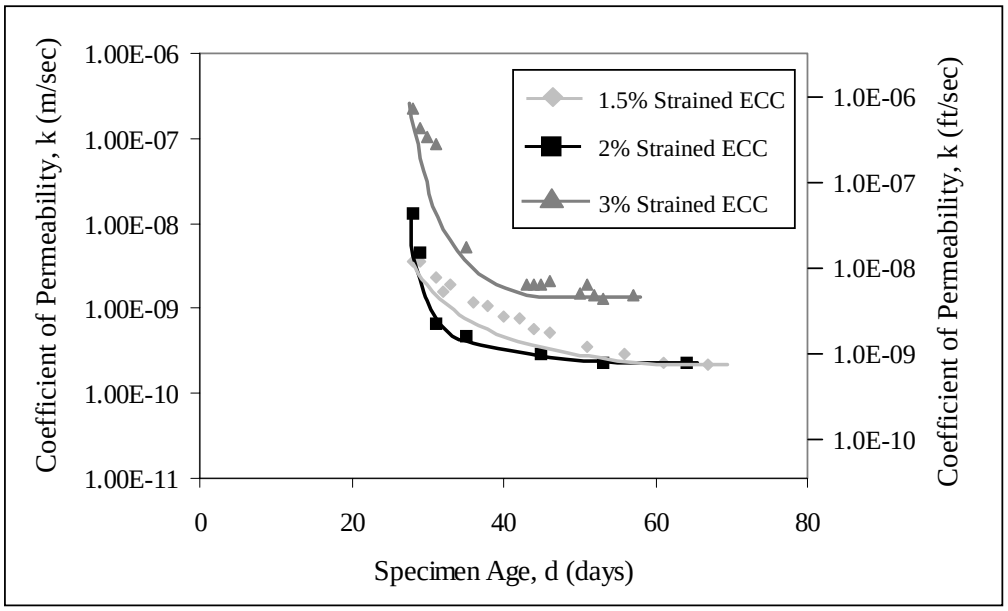

Fig. 4.16 – Development of Permeability for ECC Strain to 1.5%, 2%, and 3% (After [42])

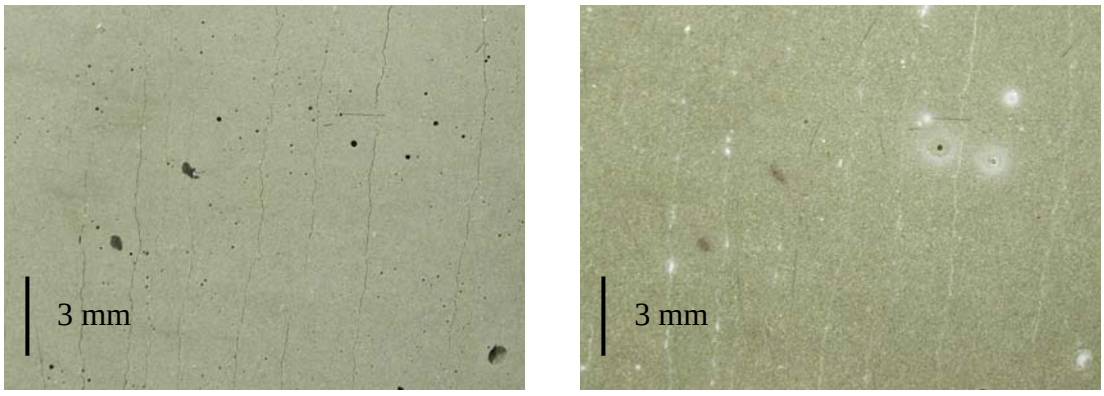

(a) (b)

Fig. 4.17 – Appearance of ECC permeability speciemens (a) before permeability testing, and (b) after permeability testing (After [42])

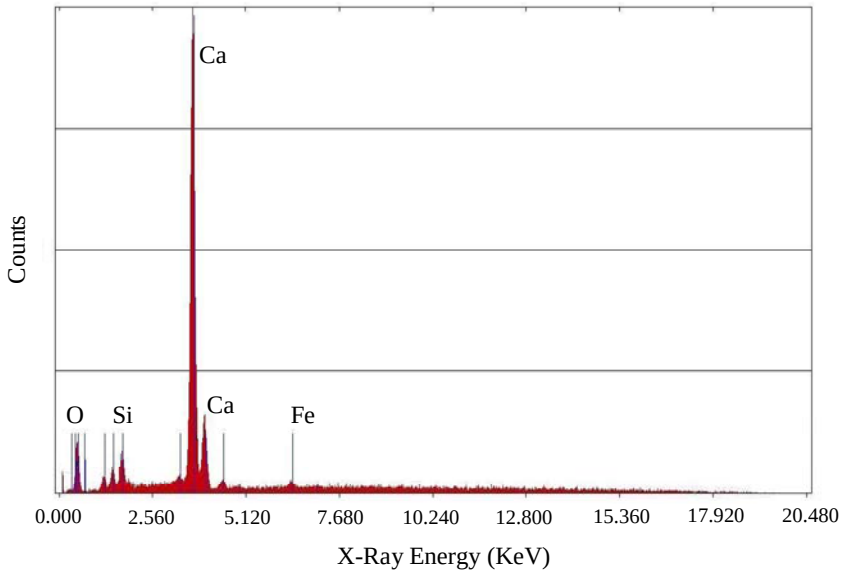

Fig. 4.18 – ESEM Surface Chemical Composition Analysis (EDX) of Self-Healing Crack Formations (After [42])

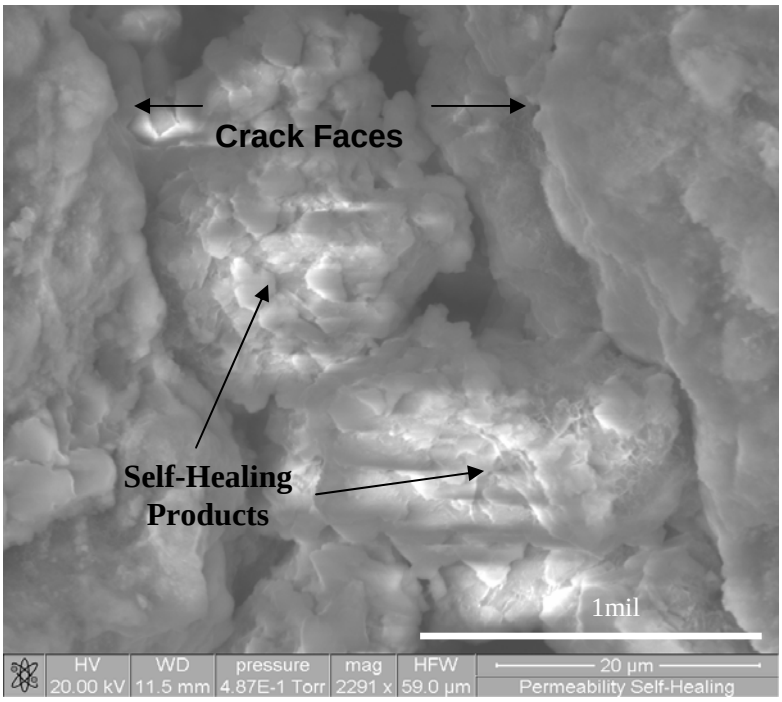

(a) Autogenous self-healing crystalline formations in ECC crack after permebaility testing

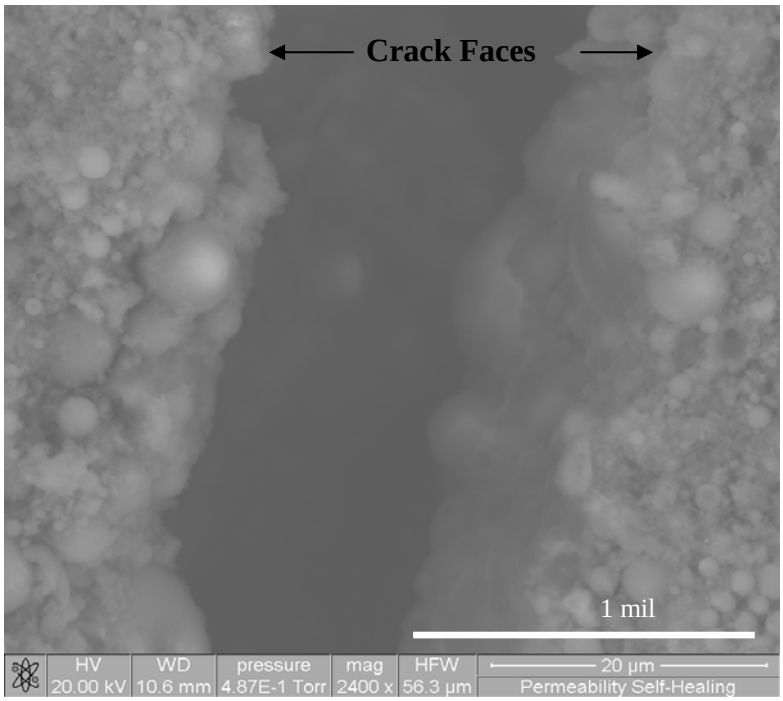

(b) ECC crack before permeability testing

Fig. 4.19 – Morphology of crack within ECC specimen from ESEM (After [42])

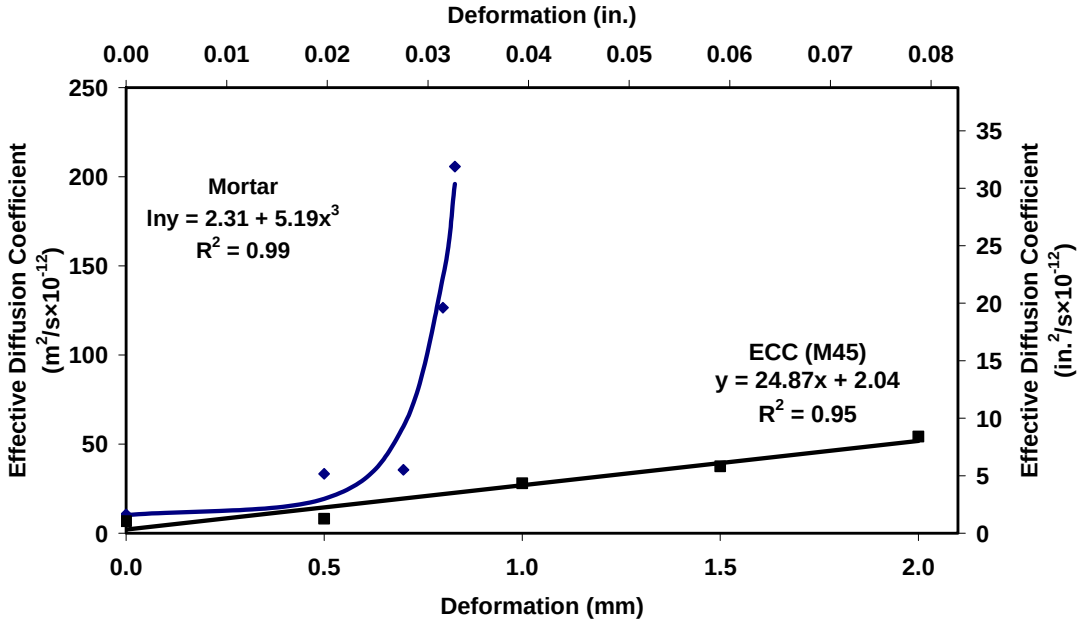

Figure 4.20 – Diffusion coefficient versus preloading deformation level for ECC and mortar (After [10])

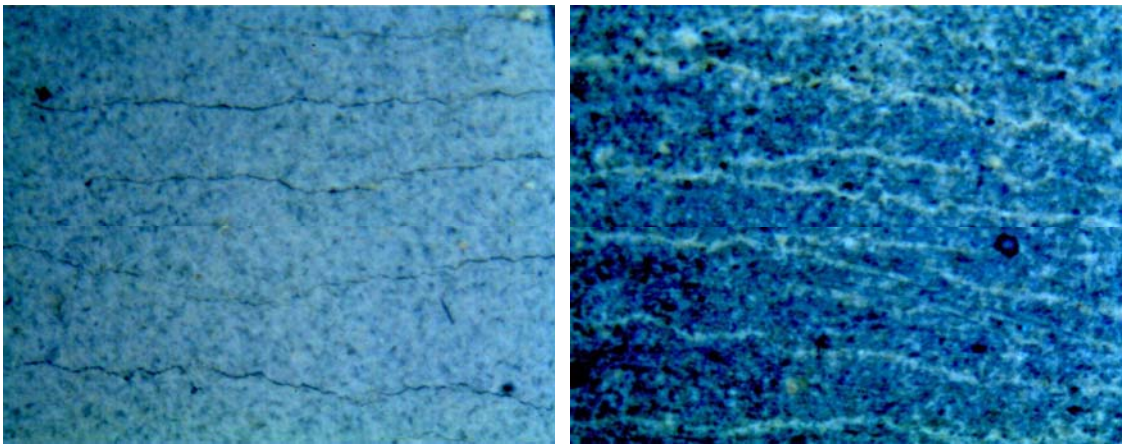

(a) (b)

Fig. 4.21 – Self healing products in ECC microcracks (a) before, and (b) after salt ponding test at 30days exposure (After [10])

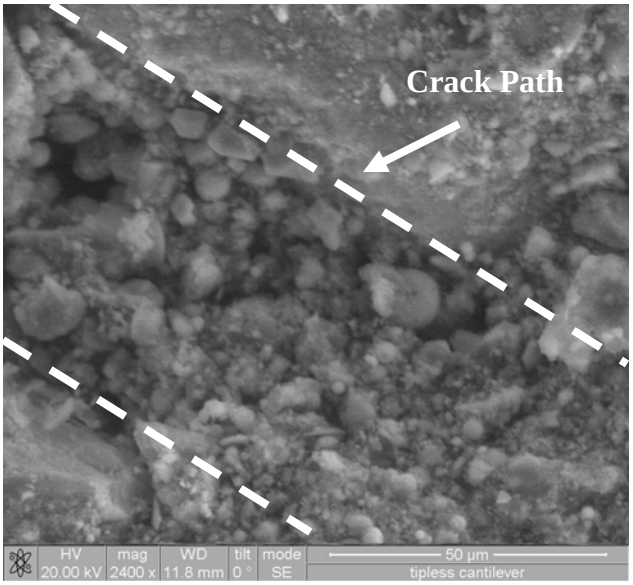

Fig. 4.22 – ESEM micrograph of rehydration products in a self-healed crack (After [10])

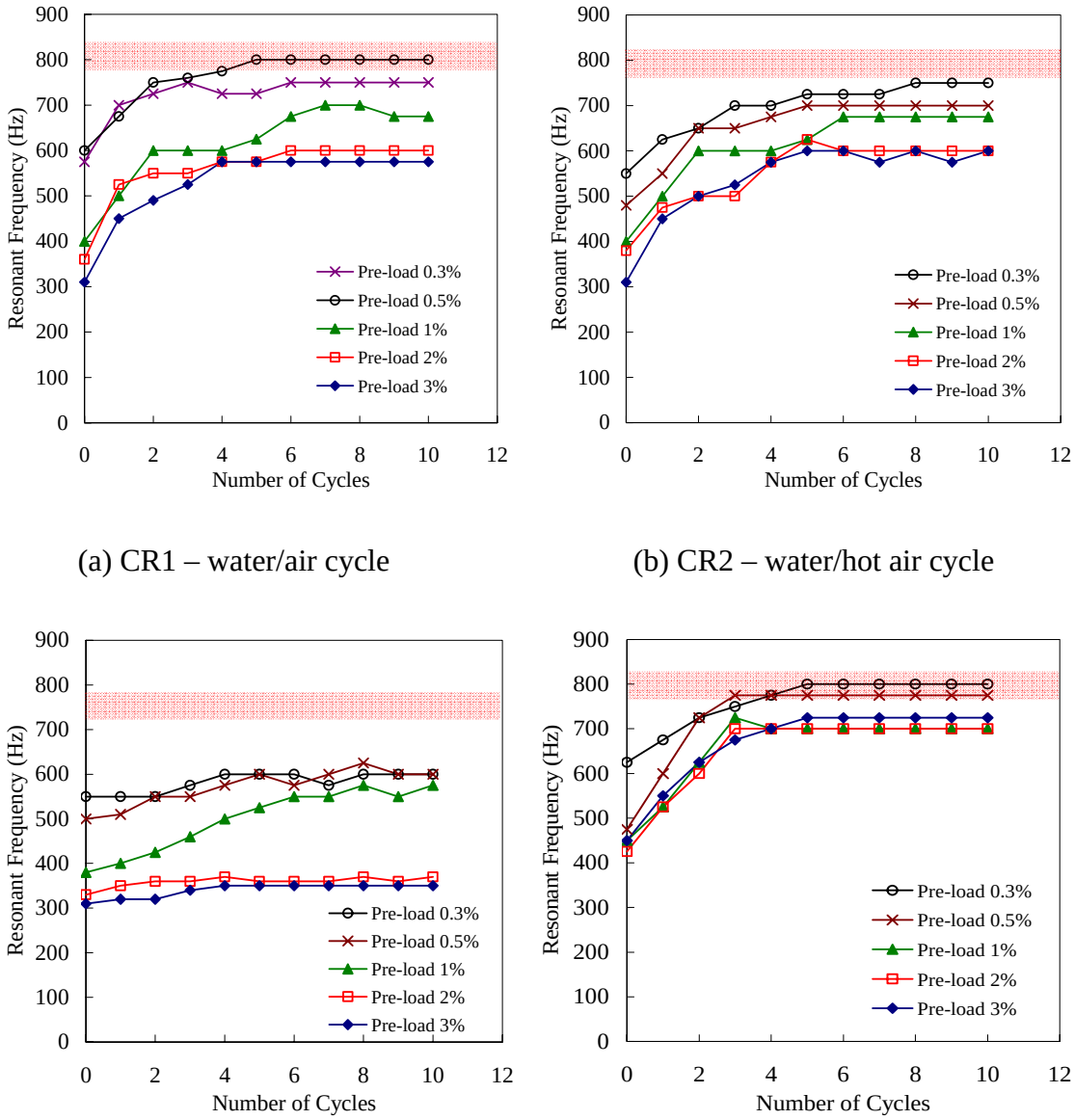

(a) CR1 – water/air cycle

(b) CR2 – water/hot air cycle

(c) CR3 – 90%RH/air cycle

(d) CR4 – water

Fig. 4.23 – ECC autogenous healing rate/process (i.e. resonant frequency vs number of cyclic exposure regime) at different environmental exposures at early ages

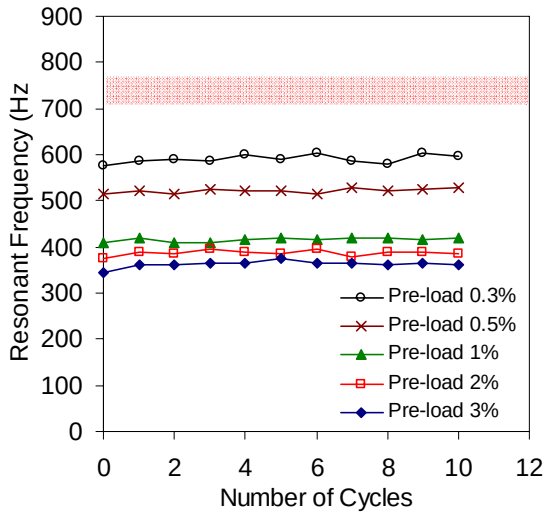

(d) CR5 – air

Fig. 4.23 – ECC autogenous healing rate/process (i.e. resonant frequency vs number of cyclic exposure regime) at different environmental exposures at early ages

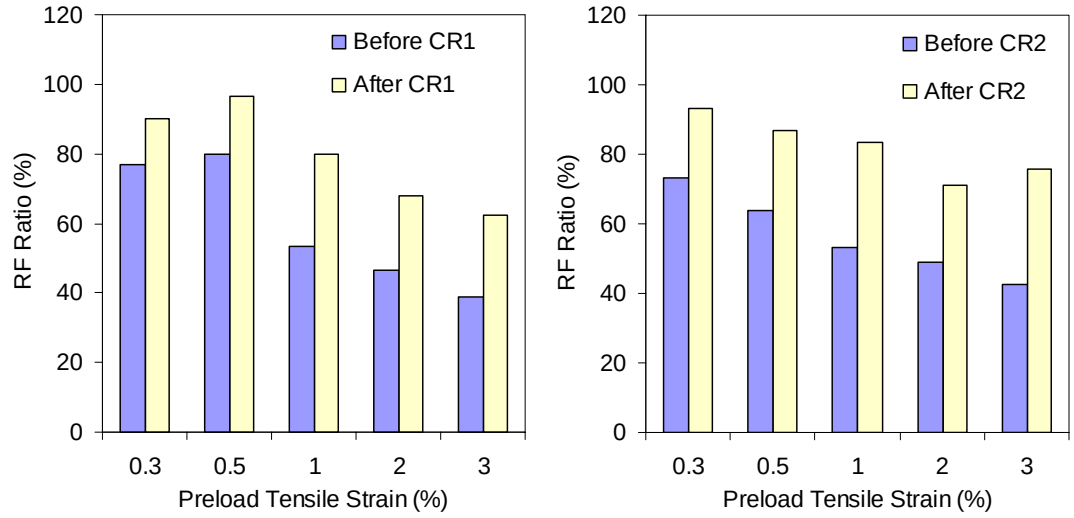

(a) CR1 – water/air cycle (b) CR2 – water/hot air cycle

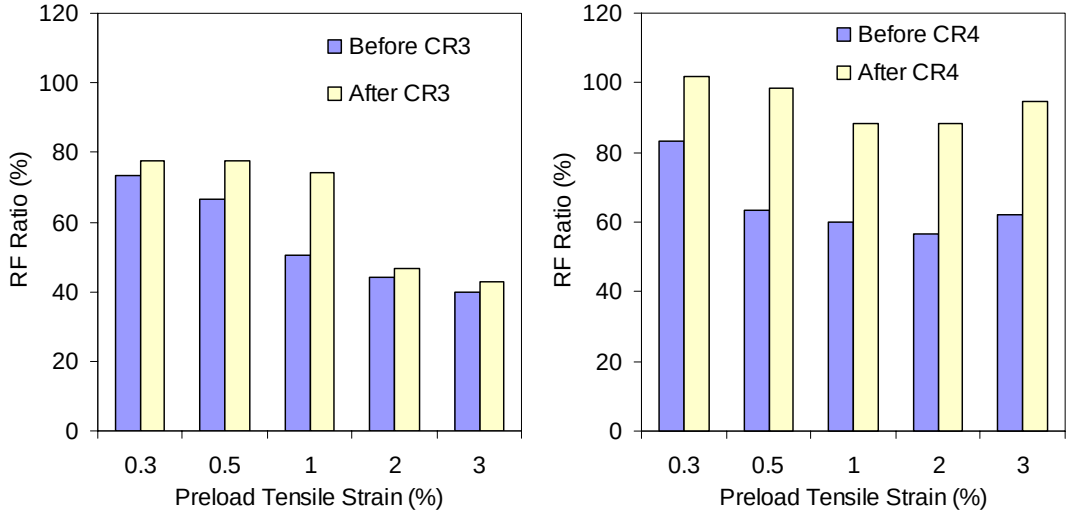

(c) CR3 – 90%RH/air cycle (d) CR4 – water

Fig. 4.24 – Extent of ECC self-healing (i.e. resonant frequency ratio) under different environmental exposures

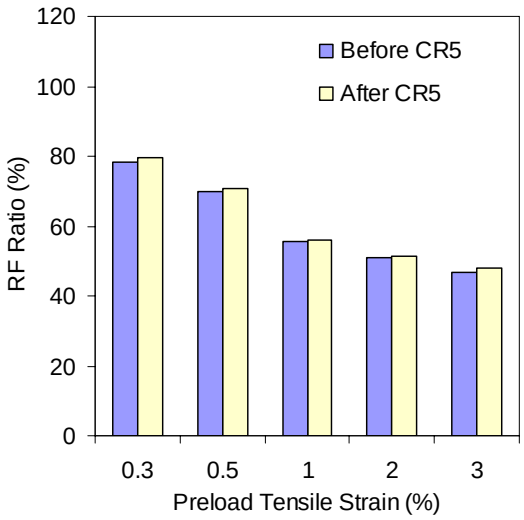

(e) CR5 – air

Fig. 4.24 – Extent of ECC self-healing (i.e. resonant frequency ratio) under different environmental exposures

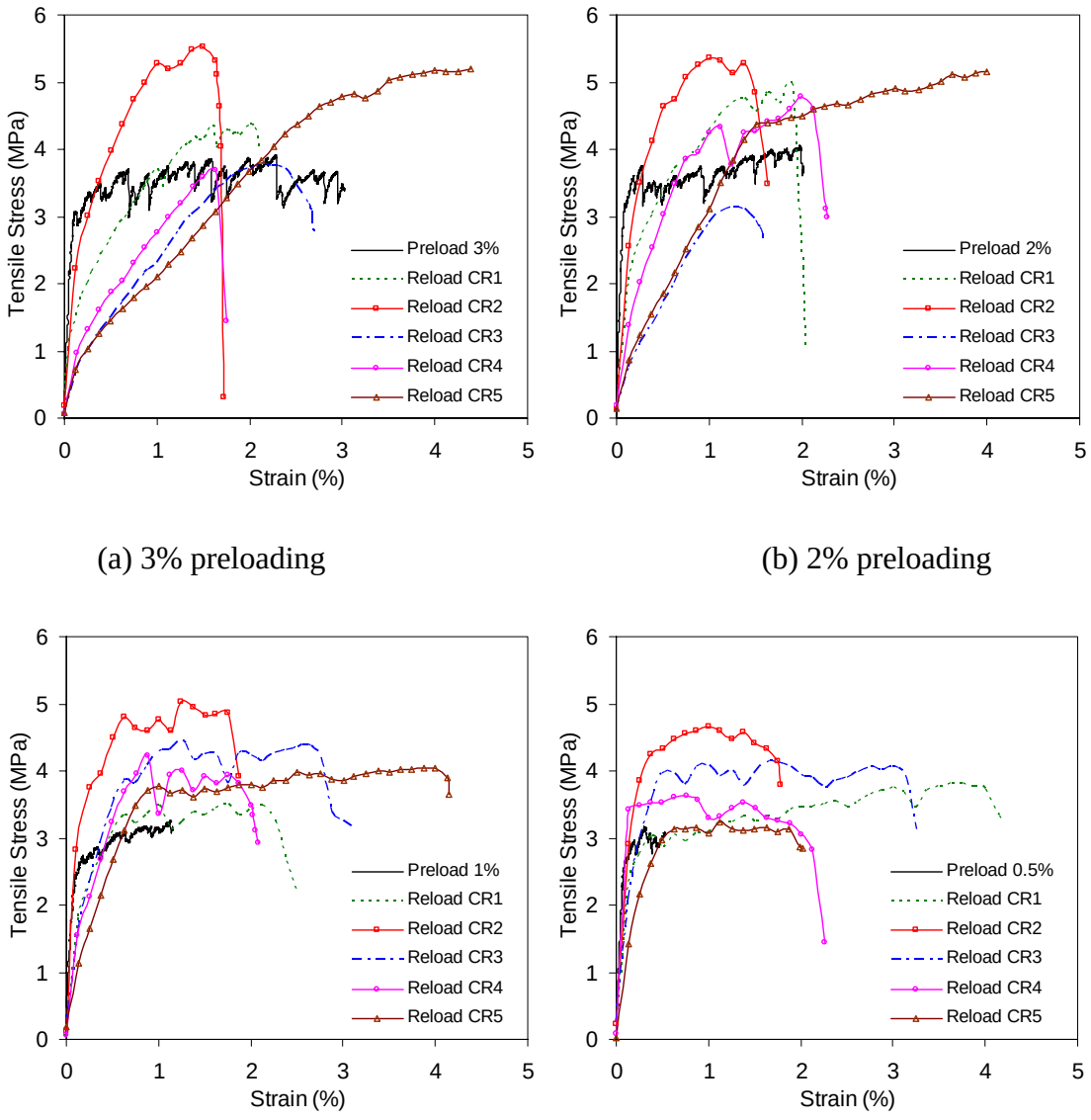

(a) 3% preloading

(b) 2% preloading

(c) 1% preloading

(d) 0.5% preloading

Fig. 4.25 – Typical preloading and reloading tensile stress-strain curve of ECC with pre-determined tensile deformation of (a) 3%, (b) 2%, (c) 1%, (d) 0.5%, (e) 0.3%, and (f) 0%, after different environmental exposures

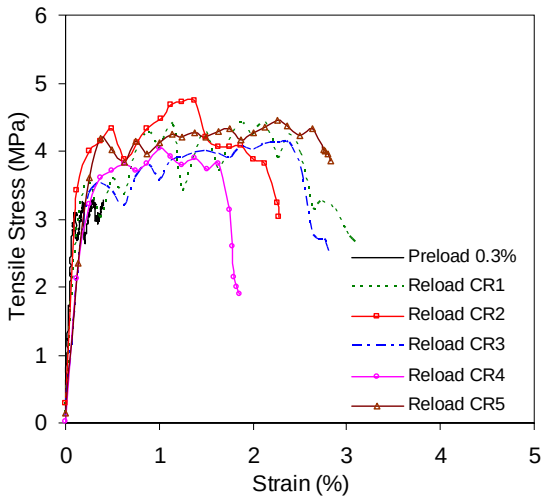

(e) 0.3% preloading

Fig. 4.25 – Typical preloading and reloading tensile stress-strain curve of ECC with pre-determined tensile deformation of (a) 3%, (b) 2%, (c) 1%, (d) 0.5%, (e) 0.3%, and (f) 0%, after different environmental exposures

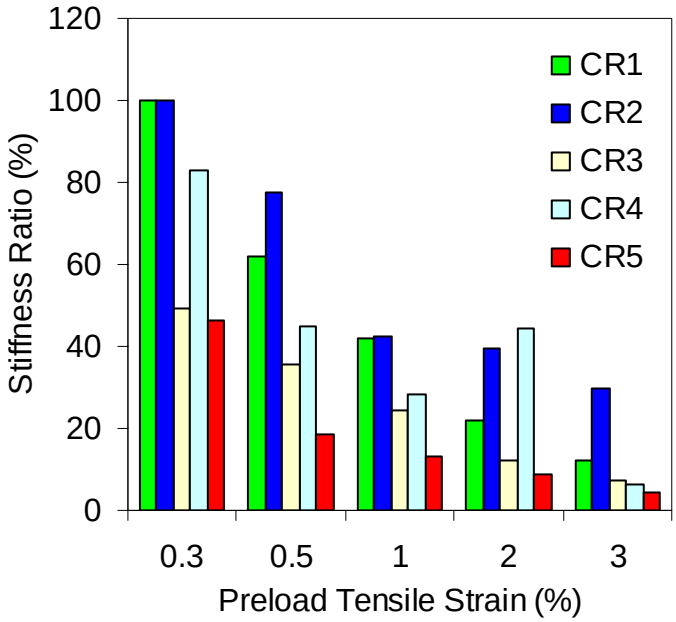

Fig. 4.26 – ECC stiffness ratio under different environmental exposures, for specimens with different pre-loading levels

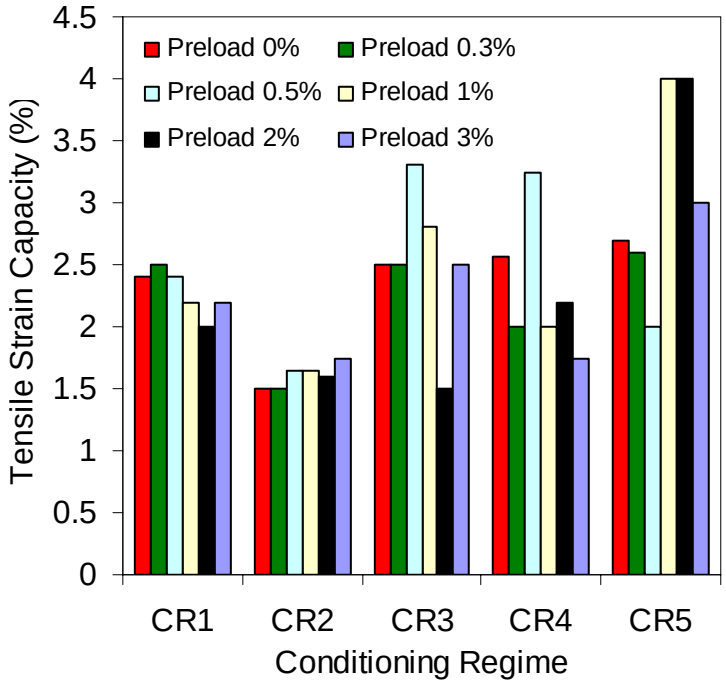

Fig. 4.27 – ECC tensile strain capacity of reloading under different environmental exposures

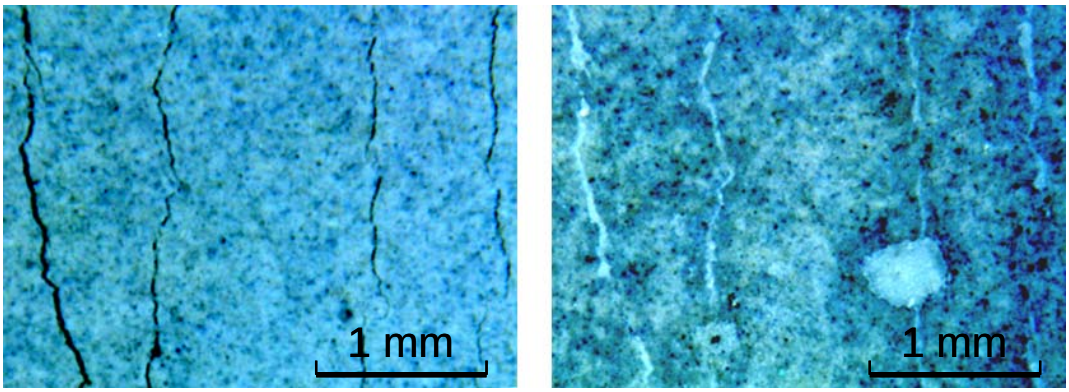

(a) (b)

Fig. 4.28 – (a) Controlled microcrack damage of preloaded ECC specimen and (b) autogenous healing of ECC specimen subjected to CR4 (water)

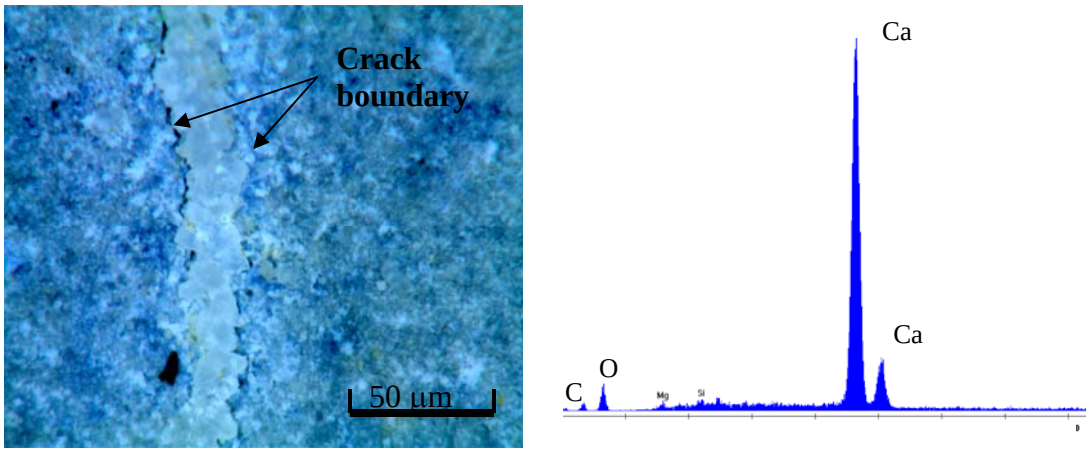

(a) (b)

Fig. 4.29 – (a) Reheal product and (b) its EDX spectrum

References

[1] Edvardsen, C., "Water Permeability and Autogenous Healing of Cracks In Concrete," *ACI Materials J.*, vol.96, pp.448-455, 1999

[2] Reinhardt, H., Joos, M., "Permeability and Self-healing of Cracked Concrete as a Function of Temperature and Crack Width," *J. of Cement and Concrete Research,* vol.33, pp.981-985, 2003

[3] Pimienta, P., and Chanvillard, G., "Retention of the mechanical performances of Ductal® specimens kept in various aggressive environments," *Fib Symposium,* 2004

[4] Granger, S., Pijaudier-Cabot, G., and Loukili, A., "Mechanical behavior of self-healed Ultra High Performance Concrete: from experimental evidence to modeling," *accepted for publication in Proc. FRAMCOS 6*, Catalina, Italy, 2007

[5] Ter Heidi, N., Schlangen, E., and van Breugel, K., "Experimental Study of Crack Healing of Early Age Cracks," *Proc., Knud Hojgaard Conference on Advanced Cement-Based Materials: Research and Teaching*, M.G. O.M. Jensen, and H. Stang ed., Lyngby, Denmark, pp.311-322, 2006

[6] White, S.R., N.R. Sottos, P.H. Geubelle, J.S. Moore, M.R. Kessler, S.R. Sriram, E.N. Brown, and S. Viswanathan, "Autonomic healing of polymer composites," *Nature*, vol.409, pp.794-797, 2001

[7] Kessler, M.K., Sottos, N.R., and White, S.R., "Self-healing structural composite material," *Composites Part A: Applied Science and Manufacturing*, vol.34, no.8, pp.743-753, 2003

[8] Dry, C., "Matrix Crack Repair and Filling Using active and Passive Model for Smart Time Release of Chemicals from Fibers into Cement Matrixes," *Journal of Smart Materials and Structure*, pp.118-123, 1994

[9] Dry, C., "Procedures Developed for Self-Repair of Polymer Matrix Composite Materials," *Composite Structure*, vol.35, pp.236-269, 1996

[10] Sahmaran, M., Li, M., and Li, V.C., "Transport Properties of ECC under Chloride Exposure," *accepted, ACI Materials J.*, 2007

[11] Dry, C., "Release of Smart Chemicals for the In-Service Repair of Bridges and Roadways," *Proc. Symposium on Smart Materials, Structures and MEMS*, pp.140-144, 1996

[12] Lee, J.Y., G.A. Buxton, and A.C. Balazs, "Using Nanoparticles to Create Self-healing Composites," *Journal of Chemical Physics*, vol.121, no.11, pp.5531-5540, 2004

[13] Nishiwaki, T., H. Mihashi, B.K. Jang, and K. Miura, "Development of Self-Healing System for Concrete with Selective Healing around Crack," *J. Advanced Concrete Technology*, vol.4, no.2, pp.267-275, 2006

[14] Bang, S.S., Galinat, J.K., and Ramakrishnan, V., "Calcite precipitation induced by polyurethane-immobilized Bacillus pasteurii," *Enzyme and Microbial Technology*, vol.28, pp.404-409, 2001

[15] Rodriguez-Navarro, C., Rodriguez-Gallego, M. Chekroun, K.B., and Gonzalez-Munoz, M.T., "Conservation of Ornamental Stone by Myxococcus santhus-Induced Carbonate Biomineralization," *Applied and Environmental Microbiology*, pp.2182-2193, 2003

[16] Clear, C.A., *The Effects of Autogenous Healing Upon the leakage of Water Through Cracks In Concrete*, 1985, 28 pp pp

[17] Nanayakkara, A., "Self-healing of Cracks in Concrete Subjected to Water Pressure," *New Technologies for Urban Safety of Mega Cities in Asia*, Tokyo, 2003

[18] Institute, A.C., *Building Code Requirements for Structural Concrete (ACI318-95) and Commentary (ACI318R-95)*, 1995,

[19] Jooss, M., "Leaching of Concrete Under Thermal Influence," *Otto-Graf-Journal*, vol.12, pp.51-68, 2001

[20] Hannant, D.J., and J.G. Keer, "Autogenous Healing of Thin Cement Based Sheets," *Cement and Concrete Research*, vol.13, pp.357-365, 1983

[21] Farage, M.C.R., Sercombe, J., and Galle, C., "Rehydration and microstructure of cement paste after heating at temperatures up to 300ºC," *J. of Cement and Concrete Research*, vol.33, pp.1047-1056, 2003

[22] Cowie, J., and F.P. Glassert, "The Reaction Between Cement and Natural Water Containing Dissolved Carbon Dioxide," *Advances in Cement Research*, vol.14, no.15, pp.119-134, 1992

[23] Ter Heide, N., *Crack Healing in Hydrating Concrete*, MSc-thesis Dissertation, TU Delft, MSc-thesis, 2005

[24] Schiessl, P., and Brauer, N., "Influence of Autogenous Healing of Cracks on Corrosion of Reinforcement," *Durability of Building Materials and Components 7*, pp.542-552, 1996

[25] Mangat, P.S., and K. Gurusamy, "Permissible Crack Widths in Steel Fiber Reinforced Marine Concrete," *J. of Materials and Structures*, vol.20, pp.338-347, 1987

[26] Jacobsen, S., Marchand, J., and Boisvert, L., "Effect of Cracking and Healing on Chloride Transport in OPC Concrete," *J. of Cement and Concrete Research*, vol.26, pp.869-881, 1996

[27] Jacobsen, S., Marchand, J., and Homain, H., "SEM Observations of The Microstructure of Frost Deteriorated and Self-healed Concrete," *J. of Cement and Concrete Research*, vol.25, pp.1781-1790, 1995

[28] Ismail, M., A.Toumi, R. Francois, and R. Gagne, "Effect of crack opening on local diffusion of chloride inert materials," *Cement and Concrete Research*, vol.34, pp.711-716, 2004

[29] Aldea, C., Song, W., Popovics, J.S., and Shah, S.P., "Extent of Healing of Cracked Normal Strength Concrete," *J. of Materials In Civil Engineering*, vol.12, pp.92-96, 2000

[30] Yang, E., Yang, Y., and Li, V.C., "Use of High Volumes of Fly Ash to Improve ECC Mechanical Properties and Material Greenness," *ACI Materials J., accepted*, July, 2007

[31] Lepech, M.D.a.V.C.L., "Long Term Durability Performance of Engineered Cementitious Composites," *Int'l J. for Restoration of Buildings and Monuments*, vol.12, no.2, pp.119-132, 2006

[32] Kunieda, M., and K. Rokugo, "Recent Progress on HPFRCC in Japan, Required Performance and Applications," *J. Advanced Concrete Technology*, vol.4, no.1, pp.19-33, 2006

[33] Ramm, W., and Biscoping, M., "Autogenous Healing and Reinforcement Corrosion of Water-penetrated Separation Cracks in Reinforced Concrete," *J. of Nuclear Engineering and Design*, vol.179, pp.191-200, 1998

[34] Reinharde, H., Jooss, M., "Permeability and Self-healing of Cracked Concrete as a Function of Temperature and Crack Width," *J. of Cement and Concrete Research*, vol.33, pp.981-985, 2003

[35] Wang, K., Nelsena, D.E., and Nixon, W., "Damaging effects of deicing chemicals on concrete materials," *Cement and Concrete Composites*, vol.28, no.2, pp.173-188, 2006

[36] Lepech, M.D., and Li, V.C., "Water Permeability of Cracked Cementitious Composites," *ICF 11*, Turin, Italy, Paper 4539 of Compendium of Papers CD ROM, 2005

[37] Jacobsen, S., and Sellevold, E.J., "Self Healing of High Strength Concrete After Deterioration By Freeze/Thaw," *J. of Cement and Concrete Research*, vol.26, pp.55-62, 1996

[38] Yang, Y., Lepech, M., and Li, V. C.,, "Self -healing of ECC under Cyclic Wetting and Drying," *Proceedings of Int'l Workshop on Durability of Reinforced Concrete under Combined Mechanical and Climatic Loads*, Qingdao, China, pp.231-242, 2005

[39] Cernica, J.N., in *Geotechnical Engineering*, Holt, Reinhart & Winston, New York, pp.97-99, 1982

[40] Lepech, M.D., *A Paradigm for Integrated Structures and Materials Design for Sustainable Transportation Infrastructure*, Ph.D. Dissertation, Department of Civil and Environmental Engineering, University of Michigan, Ann Arbor, 2006

[41] Weimann, M.B., and Li, V.C., "Drying Shrinkage and Crack Width of ECC," *BMC 7*, Poland, pp.37-46, 2003

[42] Lepech, M.D., *A Paradigm for Integrated Structures and Materials Design for Sustainable Transportation Infrastructure*, Ph.D. Dissertation, Department of Civil and Environmental, University of Michigan, Ann Arbor, PhD Thesis, 2006

[43] Drabik, M., and R. Slade, "Macrodefect-free Materials: Modification of Interfaces in Cement Composites by Polymer Grafting," *Interface Science*, vol.12, no.4, pp.375-379, 2004

[44] Rangan, B.V., "High-performance High-strength Concrete: Design Recommendations," *Concrete International*, vol.20, no.11, pp.63-68, 1998

[45] Metha, P.K., *Concrete: Structure, Properties, and Materials*, Englewood Cliffs, N.J., Prentice-Hall, 450 pp, 1986

[46] Hwang, C.L., J.J. Liu, L.S. Lee, and F.Y. Lin, "Densified Mixture Design Algorithm and Early Properties of High Performance Concrete," *Journal of the Chinese Institute of Civil and Hydraulic Engineering*, vol.8, no.2, pp.217-229, 1996

[47] ACI_Committee_363, *State-of-the-Art Report on High-Strength Concrete*, American Concrete Institute, 1992,

[48] Wiegrink, K., S. Marikunte, and S.P. Shah, "Shrinkage Cracking of High-Strength Concrete," *ACI Materials Journal*, vol.93, no.5, pp.409-415, 1996

[49] Shah, S.P., K. Wang, and W.J. Weiss, "Is High Strength Concrete Durable?," in *Concrete Technology for a Sustainable Development in the 21st Century*, O.E. Gjørv, and K. Sakai ed., pp.102-114, 2000

[50] Mihashi, H., and J.P.B., De Leite, "State-of-the-art Report on Control of Cracking in Early Age Concrete," *Journal of Advanced Concrete Technology*, vol.2, no.2, pp.141-154, 2004

[51] Neville, A., "Autogenous Healing - A Concrete Miracle?," *Concrete International*, vol.24, no.11, pp.76-82, 2002

[52] Lauer, K.R., and F.O. Slate, "Autogenous Healing of Cement Paste," *ACI Journal*, vol.52, no.10, pp.1083-1097, 1956

[53] Haque, M.N., and D.J. COOK, "The Effect of Water Sorption on the Dynamic Modulus of Elasticity of Desiccated Concrete Materials," *Journal of Materials and Structure*, vol.9, no.6, pp.407-410, 1976

[54] Van Den Abeele, K.E.-A., J. Carmeliet, P.A. Johnson, and B. Zinszer, "The Influence of Water Saturation on the Nonlinear Elastic Mescopic Response in Earth Materials, and Implications," *Journal of Geophysical Research*, vol.107, no.B6, pp.ECV4-1-11, 2002

[55] Mindess, S., J.F. Young, and D. Darwin, *Concrete*, 2nd ed, Prentice Hall, 644 pp, 2002

CHAPTER 5

DESIGNING IMPACT RESISTANCE FUNCTION IN ECC

This chapter presents the results of a preliminary investigation on the effectiveness of impact resistant ECCs to enhance the impact resistance of structures. Rate dependency in ECC is investigated and rate dependent strain-hardening criteria are established. ECC is retailored to maintain its tensile ductility under high strain rate loading. Drop weight impact loadings were conducted to examine the structural performance of the resulting ECCs in the form of thin ECC circular plate, ECC beam, reinforced ECC (R/ECC) panel, and R/ECC beam. In each test series, concrete or mortar and/or FRC specimens were tested as controls. The results showed that ECC designed for high rate loading can effectively suppress the brittle fracture failure mode, and therefore enhance the structural performance in terms of structural load and energy absorption capacity under drop weight impacts.

5.1 Introduction

Terrorist attacks and natural hazards highlight the need for assuring human safety in large structures under extreme loading such as bomb blasts and flying object impacts. While concrete has served as an eminently successful construction material for many years, reinforced concrete (R/C) infrastructure can be vulnerable under severe dynamic loading [1]. The collapse of a large portion of the Alfred P. Murrah Federal Building in Oklahoma City in 1996, for example, demonstrates the vulnerability of R/C structure when subjected to bomb blasts.

Many catastrophic failures of R/C structures subjected to blast/impact are associated with the brittleness of concrete material in tension [2]. Although a compressive stress wave is generated on the loading side of the structure by impact/blast, it reflects as a tensile stress wave on arrival at a free boundary on the back side of the structural element. In addition, the tensile strength of concrete is typically much lower (by about an order of magnitude) than its compressive strength. Therefore, concrete tensile properties generally govern concrete failure under impact/blast as suggested by Malvar and Ross [2]. Brittle failures, such as cracking, spalling, and fragmentation, of concrete are often observed in R/C structures when subjected to blast/impact [3], and can lead to severe loss of structural integrity [4]. Apart from that, high speed spalling debris ejected from the back side of the structural elements can cause serious injury to personnel behind the structural elements.

Extensive research has been conducted on impact/blast response of R/C structural elements [5, 6] and mitigation design of R/C structure against impact/blast [7-16] loading. Current practice [9], such as thickening the dimension of structural members, increasing

the amount of steel reinforcement, special reinforcement detailing, installing additional shear walls etc., places emphasis on structural design and detailing, and/or adding redundancy to reduce the chance of progressive collapse after an attack [8, 12]. An alternative solution to resolve some of the above mentioned challenges is to embed tensile ductility intrinsically into the concrete material. Ductile concrete would be highly desirable to suppress the brittle failure modes and enhance the efficiency and performance of current design approaches.

R/ECC structural members show superior structural load carrying and energy absorption capacity and extreme high damage tolerance under monotonic and cyclic loading, when compared with normal R/C structures [17-19]. For example, **Fig. 5.1a** shows the load-deformation response of R/ECC column under reversed cyclic loading. When compared with R/C column (**Fig. 5.1b**), R/ECC column exhibits higher load carrying capacity, ductility, and energy absorption even when there are no shear stirrups in the R/ECC column. This significantly enhanced performance of R/ECC structural elements is a direct result of the ultra-ductility of ECC, which suppresses the brittle failure mode, maintains the structural integrity, and promotes the synergistic interaction between steel reinforcement and surrounding ductile ECC material. Also, the high energy absorption observed in R/ECC members is a result of the plastic yielding of longer segments of the steel reinforcement in comparison to that in normal R/C members. The engagement of a longer segment of steel yielding is due to the compatible deformation between rebar and ECC in an R/ECC element even when the member undergoes large deformation. For example, **Fig. 5.2a** shows plastic yield deformation in the steel while ECC undergoes strain-hardening in a tension-stiffening specimen [17]. In

contrast, the R/C element (**Fig. 5.2b**) under similar loading shows localized concrete fracture and bond splitting between rebar and concrete. It is plausible that this high energy absorption feature of R/ECC structure may be maintained when subjected to impact or blast loading, as long as the deformation compatibility behavior just described could be retained. This in turn depends on retaining the tensile ductility of ECC under high rate loading.

Based on the above discussions on the ductile material and structural behavior, ECC can be a potential material solution to enhance structural performance subjected to severe impact/blast loading. In the following sections, the principles of impact-resistant ECC material design are first highlighted. This is followed by a summary of preliminary test performances of simple ECC and R/ECC structural elements subjected to drop weight impacts.

5.2 Rate Dependent Strain-Hardening Cretia

The theoretical foundation behind the multiple cracking phenomenon as described in **Chapter 2** was first explored by Aveston et al [20], whose work was later extended by Marshall and Cox [21]. These investigations focus on brittle matrix composites reinforced with continuous and aligned fibers with relatively simple bridging laws. Emphasis is placed on the conditions for steady state matrix cracking – extension of bridged crack length with flat crack surfaces so that the bridging elements remain intact after the passage of a crack, thus allowing load transfer from the bridging fibers back into the matrix to activate additional flaw sites into new microcracks. Especially transparent

in Marshall and Cox [21], the steady state crack analysis employs the concept of energy balance between external work, crack tip energy absorption through matrix breakdown (matrix toughness), and crack flank energy absorption through fiber/matrix interface debonding.

Under high loading rates; however, cracks propagate in a much faster manner [22] and the energy required to drive the crack tip (or the inertia effect of a fast moving crack tip) has to be considered [23]. Also, rate dependency of matrix and fiber bridging properties may play an important role in formulating the rate dependent steady-state cracking criterion [24]. Cui [24] extended the work of Marshall and Cox [21] to analyze dynamic steady state matrix cracking behavior in continuous and aligned fiber reinforced ceramics. The analysis accounts for the viscoplastic effects of bridging fibers and the inertial effect of a dynamically propagating crack. The bridging law adopted has the form shown in **Eqn. 5.1**

$$\sigma_B(x) = \sqrt{\left(\eta\dot{\delta} + \beta^2\delta\right)\Big/ 2} \tag{5.1}$$

in which η represents the viscosity parameter and the β parameter is dependent on the fiber and interface properties.

Formulation of the boundary value problem of a steadily propagating matrix crack with crack opening sensitive surface traction results in the integral equation:

$$\sigma^{\infty} - \frac{\mu}{\pi\alpha_d}\frac{c_s^2}{\mathrm{v}^2} D \int_{-\infty}^{0} \frac{1}{2(x-\xi)}\frac{\partial\delta}{\partial\xi} d\xi = \sqrt{-\frac{\eta\mathrm{v}}{2}\frac{\partial\delta}{\partial x} + \frac{\beta^2}{2}\delta} \tag{5.2}$$

where $D = 4\alpha_d\alpha_s - \left(1+\alpha_s^2\right)^2$, σ^{∞} is the ambient stress, v is crack tip velocity, μ is shear modulus, $\alpha_s = \sqrt{1-\left(\mathrm{v}/c_s\right)^2}$, and $\alpha_d = \sqrt{1-\left(\mathrm{v}/c_d\right)^2}$ where c_s and c_d are the velocities of

longitudinal and shear waves in the composite medium, respectively. The left hand side of **Eqn. 5.2** represents the net pressure on the crack flank, the difference between the ambient load and the total back stress due to propagating dislocations distributed to form the crack opening. The right hand side is the crack bridging stress due to fibers and results from **Eqn. 5.1** when steady state cracking prevails. In **Eqn. 5.2** both σ^{∞} and $\delta(x)$ are unknowns to be solved for a given crack velocity v. The problem formulation was completed by imposing an energy based dynamic crack growth criterion, equating the dynamic driving force to fracture resistance:

$$\left(\pi\mu c_s^2 / 4\alpha_d \mathrm{v}^2\right) D\left[\lim \sqrt{-x}\left(\partial\delta/\partial x\right)\right]^2 = \left(1 - V_f\right) G_m \tag{5.3}$$

where G_m is the critical energy release rate for fracture in the matrix. Numerical solution of **Eqns. 5.2** and **5.3** leads to the determination of matrix cracking stress σ^{∞} as a function of the crack speed v.

Although Cui's work provides helpful background, the final result is cast in a form not amenable for material design. In this section, an alternative formulation which can produce a mathematically more tractable rate dependent steady-state cracking criterion, similar to that under static loading condition (**Eqn. 2.1**), is derived (see Appendix).

This rate dependent steady-state cracking can be derived from a dynamic version of the J-integral analysis analogous to that used in Marshall & Cox's analysis [21], except that the kinetic energy of a moving crack tip and the rate sensitivity of fiber bridging and matrix properties should be accounted for in the analysis [23, 24]. **Equation 5.4** shows the resulting rate dependent steady-state cracking criterion. Detailed derivation based on J-integral can be found in the **Appendix A to D**.

$$G_{tip} \le \sigma_0 \delta_0 - \int_0^{\delta_0} \sigma(\delta) d\delta \equiv G_b^{'} \tag{5.4}$$

where G_{tip} is the matrix toughness and $G^{'}_{b}$ is the complementatry energy. It can be seem that **Eqns. 5.4** and **2.1** have the same form. However, the matrix toughness is now not only a function of matrix composition but also a function of loading rates. Similarly, fiber bridging spring law is now dependent upon fiber and interfacial preporties as well as loading rates. This result is indeed consistent with Cui's finding, in which the dynamic steady-state matrix cracking stress becomes independent of cracking speed for rate-insensitive bridging fibers. In the case of rate sensitive bridging law; however, the inertial effects play a role through its interaction with viscoplastic effects of the bridging elements, which is the case for most polymeric fibers.

The strength criterion determines whether a crack will initiate from a pre-existing flaw site, or not, and should have the same form as that under static loading condition. However, matrix tensile cracking strength σ_c and maximum fiber bridging strength σ_0 are now functions of loading rates.

$$\sigma_c < \sigma_0 \tag{5.5}$$

where σ_0 is influenced by rate dependent fiber bridging strength and σ_c is influenced by rate dependent matrix toughness.

In summary, the rate dependent strain-hardening criteria derived here has the same form as that of static strain-hardening criteria described in **Chapter 2**. However, micromechanics parameters are now dependent on loading rates. This micromechanics-based theroy will be used to identify the rate dependency in ECC and material re-design to conteract the rate effect in the following sections.

5.3 Rate Dependency in ECC

Similar to concrete and many other engineering materials [2, 25-31], ECC has mechanical properties which exhibit rate dependency [32, 33]. **Figure 5.3a** plots the tensile stress-strain curve of ECC M45, the most widely studied version of ECC in current engineering practice, subjected to different strain rates. The strain rate ranges from 10^{-5} to 10^{-1} s^{-1}, corresponding to quasi-static loading to low speed impact. A descending trend of tensile ductility with increasing strain rate was found for M45 as depicted in **Fig. 5.3b**. Tensile ductility reduces from 3% to 0.5% at the highest strain rate. Both first cracking strength and ultimate tensile strength were found to increase with increasing strain rate.

To trace the source of rate dependency in ECC composite macroscale behavior, investigations have been conducted in revealing the rate dependency in material microscale, i.e. fiber, matrix, and interface, by means of single fiber test, matrix toughness test, and single fiber pullout test. It was found that fiber modulus E_f and strength σ_f, mortar matrix toughness J_{tip}, and interface chemical bond G_d are sensitive to the loading rate. These parameters increase with rate as shown in **Figs. 5-4**, **5-8**, **5-11**, and **5-14**, respectively. Interestingly, the frictional bond and the slip-hardening coefficient of the fiber/matrix interface showed negligible rate dependencies over the range of loading speed tested. The fibers used in ECC M45 are polyvinyl alcohol (PVA) fiber and it is well know that polymeric fibers have a strong rate dependency. Calculations are carried out to evaluate the effect of microscale rate dependency on the fiber bridging constitutive law $\sigma(\delta)$ as shown in **Figs. 5-5**, **5-9**, and **5-12**. The resulting $\sigma(\delta)$ curve is then used as inputs (**Fig. 5.6**) to calculate the matrix cracking strength σ_c by

means of the numerical cohesive cracking model as described in **Chpter 2**. In this calculation, a traction-free *interface one* (**Fig. 2.5**) with 2.5 mm in length is used to simulate an inherent defect site of 5 mm which is commonly found in ECC matrix. Total cohesive traction as depicted in **Fig. 5.6** is assigned to the *interface two* (**Fig. 2.5**). **Figs. 5-6**, **5-10**, and **5-13** give the calculation results of effect of microscale rate dependency on the matrix cracking strength. Two important properties, J'_b and σ_0, can be calculated from the $\sigma(\delta)$ relation. Combined with σ_c and J_{tip}, we can now utilize **Eqns. 5.4** and **5.5** to explain the rate dependency in ECC composite macroscale by insights gained from material microscale rate sensitivity.

The rate dependencies of fiber, matrix and interface properties have different effects on the strain hardening indices J'_b/J_{tip} and σ_0/σ_c. In general, increase of fiber modulus E_f results in reduction of J'_b and an increase in σ_c. From the analytical $\sigma(\delta)$ calculation, it was found that the maximum bridging strength σ_0 remains the same and was independent of the increase of E_f. It was concluded that the rate dependency of E_f is unfavorable to ECC multiple cracking since J'_b/J_{tip} and σ_0/σ_c diminish with rate. In case of fiber strength σ_f, it is the opposite. Increase of σ_f introduces high J'_b and σ_0. Based on the cohesive crack model calculation, σ_c remains constant and does not change with σ_f. Therefore, the rate dependency of σ_f in PVA fiber is favorable to ECC multiple cracking. The increase of chemical bond G_d also leads to loss of J'_b and increase in σ_c. Since σ_0 remains the same and is independent of G_d, the rate dependency of G_d is unfavorable to ECC multiple cracking. Overall, the combined effect of rate dependency in E_f, σ_f, G_d and J_{tip} introduces lower J'_b/J_{tip} and σ_0/σ_c as shown in **Figs. 5.15** to **5.17**. This explains from a micromechanics viewpoint why ECC M45 exhibits lower ductility at higher loading rates.

5.4 Development of Ductile ECC for Protective Structures Applications

Although fiber modulus and strength also exhibit rate dependency, not much can be done in terms of modifying rate dependency in these parameters. Therefore, attention was given to modifying interface chemical bond G_d and matrix toughness J_{tip}. Several attempts have been made to re-tailor ECC for high rate applications and results are summarized here.

One approach is to eliminate the chemical bond between fiber and matrix. If no chemical bond exists, no rate dependency can exist in G_d. It is well known that polyethylene (PE) fibers show no chemical bond in cement-based composite due to its hydrophobic nature. Hence, a lower rate dependency in PE ECC is expected when compared with PVA ECC. As discussed above, increase of chemical bond G_d can result in a higher cracking strength σ_c and a lower complementary energy J'_b. Both tendencies are unfavorable to ECC strain-hardening. Therefore, the second approach to material re-engineering is to minimize the rate dependency by lowering G_d and J_{tip}, and therefore imposing a larger J'_b/J_{tip} in advance.

5.4.1 Experimental Program

Five example mixes are prepared and the mix proportions can be found in **Table 5.1**. The cement used is Type I Portland Cement from Holcim Cement Co., MI, USA. The water reducing agent used is superplasticizer available as ADVA Cast 530 from W. R. Grace & Co., IL, USA. Two types of discontinuous polymer fibers, K-II REC ™ polyvinyl alcohol (PVA) fiber through Kuraray Co. Ltd of Osaka, Japan, and Spectra 900 high strength high modulus polyethylene (PE) fiber through Honeywell Inc., USA, are used at

2% volume fraction. The properties of the PVA and PE fibers can be found in **Table 5.2**. Pozzolanic admixture used is a low calcium Class F fly ash from Boral, TX, USA. Two types of fine aggregate, silica sand and recycled corbitz sand, are used. The silica sand with a size distribution from 50 to 250 μm, available as F110 through US Silica Co., MV, USA, is used in some mixes. Corbitz is a byproduct from chemically bonded lost foam sand casting techniques and often contains high amount of carbon particles. Lightweight filler used is a commercially available glass bubble, Scotchlite™ S60, from 3M Co., Minnesota, USA.

The five mix compositions examined here have been guided by the insights gained from the theoretical model discussed in Section 5.3 above to achieve a lower chemical bond G_d and/or a lower matrix toughness. Specifically, PE spectra fibers were used in Mixes 4 and 5 to eliminate chemical bond. Fly ash was used in Mixes 1 and 4 to reduce the interface chemical bond and matrix toughness (**Chapter 3**). Lightweigth aggregate (glass bubble) was used in Mixes 2 and 5 to lower matrix toughness [34] and the corbitz sand was used in Mix 3 to reduce the inteface chemical bond due to the presence of carbon particles. All of these measure are meant to reduce the rate dependency of chemical bond and/or impose a larger margign of J'_b/J_{tip} in advance.

The mixture was prepared in a Hobart mixer with a planetary rotating blade. Solid ingredients, except fiber, were dry mixed for approximately 1-2 minutes, and then water and the superplasticizer was added and mixed another 2 minutes. The fibers were then slowly added, until all fibers were dispersed into the cementitious matrix. The fresh mixture was cast into plexiglas molds. Specimens were demolded after 24 hours and

then cured in sealed bags at room temperature for 7 days. The specimens were then cured in the air until the predetermined testing age of 28 days.

Uniaxial tensile test was conducted to characterize the tensile behavior of the composite. Since some quasi-brittle FRCs show apparent strain hardening behavior under flexural loading, direct uniaxial tensile test is considered the most convincing way to confirm strain hardening behavior of the composite. The coupon specimen used here measures 304.8 mm x 76.2 mm x 12.7 mm. Aluminum plates were glued to the coupon specimen ends to facilitate gripping. Tests were conducted in an MTS machine with 25KN capacity under displacement control. The test strain rate ranges from 10^{-5} to 10^{-1} s^{-1}, corresponding to quasi-static loading to low speed impact. Two external LVDTs (Linear Variable Displacement Transducer) were attached to the specimen surface with a gage length of 100 mm to measure the displacement.

5.4.2 Results and Discussion

The test results are summarized in **Table 5.3**, including tensile strain capacity and strength at the highest test rate, and compressive strength at quasi-static loading for each Example mix. Complete tensile stress versus strain curves of these composites are illustrated in **Figs. 5.18** to **5.22**, and all of them exhibit significant strain-hardening behavior when subjected to strain rate ranges from 10^{-5} to 10^{-1} s^{-1}. The results show that there is a substantial increase in the ultimate tensile strength with increasing strain rate, while the strain capacity can be retained with similar multiple cracking behavior as those for the static test. The high strain rate does not seem to negatively affect the strain-hardening behavior of these ECCs under uniaxial tension.

As discussed in **Ch. 3**, adoption of fly ash reduces interface chemical bond G_d and matrix toughness J_{tip} significantly. The high amount of carbon particles in the Corbitz sand can lower G_d and J_{tip}. Glass bubble was also found to reduce the matrix toughness [34]. Therefore, ECCs incorporating these ingredients provide a larger margin for strain-hardening condition. The concept of using PE fiber to eliminate rate dependency of chemical bond is supported by Mixes 4 and 5. Similar result was also reported by Maalej et al [35] who investigated the behavior of a hybrid-fiber ECC (1.5 vol% PE and 0.5 vol% steel fibers) subjected to dynamic tensile loading. **Figure 5.23** shows the tensile stress-strain behavior of the hybrid-fiber ECC subjected to six different loading rates.

5.5 Impact Resistance of Simple ECC and R/ECC Structural Elements

To demonstrate the impact resistance, Mix 1 with high amount of fly ash was used to build simple structural elements. Drop weight impact tests were then performed to evaluate the impact resistance of simple structural elements in the form of circular plate, beams and steel rebar reinforced beams. In all tests, concrete or mortar specimens were used as controls. Zhang et al. [36] investigated the impact resistance of R/ECC panels using the hybrid-fiber ECC [35]. Their results are also summarized in this section.

5.5.1 Impact resistance of ECC circular plate

Circular plate specimens were tested under drop weigh impacts to evaluate their impact resistance. Mix 1 and mortar (f_{cube} = 35MPa) were used as materials for the preparation of circular plates. The plates (diameter = 350mm, thickness = 13mm) were supported

along the perimeter at a span of 330mm. The striking mass was a 35mm, 977 gram steel cylinder with flat ends. At each test the striking mass was dropped from various heights up to 1.4 m. The dropping heights were 50, 75, 100, 125, and 140 cm and the corresponding strain rates were 0.23, 1.11, 2.05, 3.53 and 4.28 s^{-1} (striking velocities ranged from 1.2 to 5 m/sec). After each drop the plates were visually examined to determine viability of the next drop.

The control mortar plate withstood the first 50-cm drop but failed under the 2nd impact of 75-cm drop (the 2nd impact) with severe cracking and fragmentation (**Fig. 5.24a**), whereas the test on Mix 1 plates were aborted after a series of drops (two dropping series of 50, 75, 100, 125 and 140 cm, total 10 impacts) with only minor damage caused. Again, Mix 1 plates showed superior impact resistance when compared with mortar specimens. While the control mortar plate withstood only a single impact, Mix 1 plates withstood all impact levels (i.e. from all drop heights) without significant damage after the first test series (five drops). The Mix 1 specimens remained without major damage and showed significant load carrying capacity in the second series of drops as shown in **Table 5.4**. Only fine multiple microcracks were found on the backside of the plates as shown in **Fig. 5.24b**.

5.5.2 Impact Resistance of ECC and R/ECC Beams

Beams and steel rebar reinforced beams measuring 305mm x 76mm x 51mm (length x height x depth) were tested under three-point-bending drop weight impacts to evaluate their impact resistance. Mix 1 and concrete (f'_c = 40MPa) were used as materials for the preparation of beams and steel rebar reinforced beams. In the case of steel rebar

reinforced beams, a single 5mm diameter steel bar with no ribs was used as reinforcement. The steel bar was placed close to the bottom side with a clear cover of 18mm. The reinforcing ratio of both steel bar reinforce Mix 1 (R/Mix 1) beam and steel bar reinforced concrete (R/C) beam was 0.5%.

A 50kg impact tup with flat impact surface was lifted to a height of 50cm and allowed to drop freely under its free weight onto the center of the specimen. The mass and height were chosen so that the specimen failed in one single impact. The specimens were supported with a span of 254mm. A steel roller was glued in the middle span and on the top surface of the specimen so that a uniform line load was applied to the specimen when the tup contacted the roller. 1 mm thick hard rubber pads were placed in between the specimen, the roller, and the tup. The rubber pads were meant to eliminate potential inertia effect during impact [37, 38].

Figure 5.25 shows the load-deformation curve of concrete, Mix 1, R/C, and R/Mix 1 beams and **Table 5.5** summarizes their load carry and energy absorption capacity. The energy absorption of beams without reinforcement was the area below the full load-deformation curve until the load is zero. In case of reinforced beams, the failure state was defined as a crack penetrates through the depth of the specimen, which was characterized by a constant load capacity (~ 5 kN) due to pullout of steel reinforcing bar (i.e. green dots in **Fig. 5.25b**). Therefore, the energy capacity of R/C and R/Mix 1 beams was the area below the load-deformation curve until the green dots. As can be seen, Mix 1 and R/Mix 1 beams show improved load and energy capacity (e.g. 102 N-m for R/Mix 1) than that of concrete and R/C beam (e.g. 17 N-m for R/C), respectively. Interestingly, the load and energy capacity improvement due to reinforcements in Mix 1 specimen is

much more significant than that of concrete specimen. This can be attributed to the ultra tensile ductility of Mix 1 material so that a compatible deformation between steel reinforcement and Mix 1 in the R/Mix 1 beam can be achieved during impact, and therefore a longer segment of steel yielding. The synergetic interaction between steel reinforcement and ultra ductile Mix 1 material results in a significant increase in the load and energy capacity of R/Mix 1 beams.

To evaluate the resistance of R/C and R/Mix 1 beams under multiple impacts, the same test configuration was adopted except that a 12 kg impact tup was chosen and the drop height was reduced to 20 cm. Again, the R/Mix 1 beams showed much improved impact resistance than that of R/C beams. **Figure 5.26** shows the damage of R/C and R/Mix 1 after impact testing. As can be seen, one single crack with large crack width appeared in the R/C beam after the first impact. The crack penetrated through the beam causing severe loss of structural integrity and load carrying capacity. In contrast, only very fine microcracks were found in R/Mix 1 specimen even after 10 impacts. **Figure 5.27** summarizes the load capacity of R/C and R/Mix 1 beams in each impact. It was found that R/C failed after the first impact at about 9 kN (the data point showing load capacity ~5 kN at the 2^{nd} impact is due to the pullout of reinforcing bar). However, the load capacity of R/Mix 1 remains roughly constant at about 20 kN over the ten impacts.

5.5.3 Impact resistance of R/ECC panel

Drop weight tests were conducted on R/ECC (f'_c = 74MPa), R/FRC (f'_c = 75MPa) as well as normal strength R/C (f'_c = 40MPa) panels [36]. In this series of test, hybrid-fiber ECC [35] was used to construct the R/ECC. All panels measuring 2m x 1m x 0.1m

(length x width x thickness) were reinforced orthogonally with 8 mm diameter mild steel bars spaced at 150 mm center to centre (ρ = 0.6%). A clear cover of 15 mm was maintained for both the top and bottom layer of bars using plastic spacers. For each impact, a 45 kg hammer with a hemispherical tip of diameter 95 mm was raised to a height of 4 m and allowed to drop freely under its own weight onto the centre of the specimen. The same drop height of 4 m was maintained for each impact. For each specimen, the impact resistance (impact force, crater diameter, penetration depth, cracking and fragmentation) under multiple impacts were monitored.

For R/C and R/FRC panels, multiple impact tests were repeatedly performed until the panel was finally perforated by the drop hammer, while the test on R/ECC panel were aborted after the tenth impact in view of the minor damage caused. Generally, R/ECC panels were found to show significantly improved impact and fragmentation resistance. In the case of R/C, typical damage on the distal face after the 2^{nd} and 3^{rd} impacts is shown in **Fig. 5.28**. The second impact on the R/C specimen caused serious scabbing and large debris on the distal face and the third impact perforated the panel completely. R/FRC panel showed improved impact resistance and was perforated after the 7^{th} impact as shown in **Fig. 5.29a**. However, ten impacts on the R/ECC panel caused only minor damage with no debris as shown in **Fig. 5.29b**, where the micro-cracks were highlighted using a thick marker. This prompted the abortion of the test instead of attempting to perforate the specimen.

After each impact test, the damage level was evaluated and characterized based on the average crater diameter, indentation depth, crack propagation as well as spalling, scabbing and debris conditions. The first two parameters were measured directly from

the specimens after each test, while the rest were observed qualitatively from high-speed video and digital camera recordings. Post-experiment examinations of the specimens showed that under the drop weight impact, the R/ECC panels exhibited improved resistance and reduced damage characterized in the following aspects:

- On the impact face, R/ECC panels exhibited much smaller indentation depth and crater size than those on the R/C and R/FRC panels as shown in **Fig. 5.30a** and **5.30b**, respectively. **Figure 5.31** shows the damage on the impact face of R/C panel after the third impact, R/FRC panel after the 7^{th} impact, and R/ECC panel after the 10^{th} impact.
- Significant improvement was observed in the cracking behavior of R/ECC panel over that of R/C and R/FRC panels. No macro-cracks leading to serious scabbing and debris of the specimens were observed for the R/ECC panels. Instead, the cracks were almost invisible due to their very fine width. The crack patterns as shown in **Fig. 5.29b** can only be seen after being highlighted with a thick marker. A distributed micro-cracking zone on R/ECC panels was found (**Fig. 5.29b**) to extend beyond the impact region showing that more material in the ECC panel was involved in energy absorption, thus achieving better resistance compared to only a few wide cracks obtained for the case of R/C and R/FRC panels (**Fig. 5.28** and **5.29a**).
- After the initial impact, the capability of the R/ECC panel to provide resistance against multiple impacts remains largely unimpaired unlike the R/C and R/FRC panels as shown in **Fig. 30c**. Within the first 10 impacts on the R/ECC specimens, the structural integrity of the specimen remains largely intact except for a minor indent around the point of impact and the very fine micro-cracks. The R/ECC panel is able to resist multiple impacts.

5.6 Conclusions

This chapter reports the development of impact resistant ECCs which exhibit tensile strain-hardening behavior even when the material is subjected to high strain rate loading. Drop weight impacts were performed to evaluate the impact resistance of simple ECC and R/ECC structural elements. Significantly improved impact and fragmentation resistance as well as structural load and energy absorption capacity were observed. It can be expected that incorporation of ductile ECC in protective structural design technologies can enhance the damage tolerance and safety of a broad range of civil and military infrastructure systems. While the current study confirms the effectiveness of micromechanics based design of ECC for impact resistance at low speed impact, further research is needed to verify the potency of ECC for impact resistance at high rate impact. The following specific conclusions may be drawn from the current preliminary studies:

- ECC tensile properties may exhibit rate dependency – The tensile properties of ECC M45 exhibit strong rate dependence. The tensile strain capacity decreases from 3% to 0.5% when the loading rate increases from quasi-static to low speed impact.
- The magnitude and tendency of the rate dependency are dependent on the microstructure and material composition – The fiber strength σ_f, fiber modulus E_f, matrix toughness J_{tip}, and interface chemical bond G_d of M45 show strong rate dependencies that contribute to the composite rate dependency.
- Extreme ductility of ECC could be retained under dynamic loading, when the composite microstructures are properly re-tailored. Direct tension tests of re-tailored ECC shows tensile strain capacity at 2-7% at impact loading rate of 0.1 s^{-1}.
- Drop weight impact tests indicate significant improved impact and fragmentation

resistance and load and energy absorption capacity of ECC and R/ECC structural elements both on single and multiple impacts. This is attributed to the ultra ductility of the re-tailored ECC materials that suppress the brittle failure mode normally observed in R/C structures, and therefore elevate the structural load and energy absorption capacity under impact/blast. The multiple cracking observed in both ECC and R/ECC structural elements indicates a larger volume of material involved in energy absorption and improved synergy with steel reinforcement plastic energy dissipation for better impact resistance.

Table 5.1 – Mix proportions of Examples, parts by weight

Mix No.	Cement	Water	Sand	Corbitz Sand	Fly Ash	Glass Bubble	SP	PE Fiber by volume	PVA Fiber by volume
1	1	1	1.4	0	2.8	0	0.013	0	0.02
2	1	0.45	0	0	0	0.2	0.01	0	0.02
3	1	0.56	0.8	0.05	1.2	0	0.01	0	0.02
4	1	0.68	0	0	1.6	0	0.013	0.02	0
5	1	0.75	0	0	0	0.5	0.013	0.02	0

Table 5.2 – Properties of KII-REC PVA and Spectra 900 PE Fibers

Fiber Type	Nominal Strength (MPa)	Diameter (μm)	Length (mm)	Modulus of Elasticity (GPa)
PVA	1620	39	12	42.8
PE	2400	38	38.1	66

Table 5.3 – Properties of Examples

Mix No.	Tensile strength (MPa)	Tensile strain capacity (%)	Compressive strength (MPa)
1	5.94	3.84	39.6
2	5.65	3.35	41.7
3	5.98	4.31	45.2
4	4.19	3.21	48.4
5	3.31	6.24	21.8

Table 5.4 – Load cell peak impact force of ECC plate (Courtesy of D. Yanklevsky et al., Technion-Isreal Institute of Technology)

	Drop Height (cm)				
	50	75	100	125	140
1st series	0.7 kN	1.8 kN	2.5 kN	3.0 kN	3.1 kN
2nd series	0.8 kN	1.8 kN	1.6 kN	1.9 kN	2.2 kN

Table 5.5 – Load and energy capacity of concrete, R/C, ECC, and R/ECC beams subjected to drop weight impacts

	Concrete	R/C	Improvement due to reinforcement	ECC	R/ECC	Improvement due to reinforcement
Load capacity (kN)	13	22	9	18	29	11
Energy capacity (N-m)	4	17	13	69	102	33

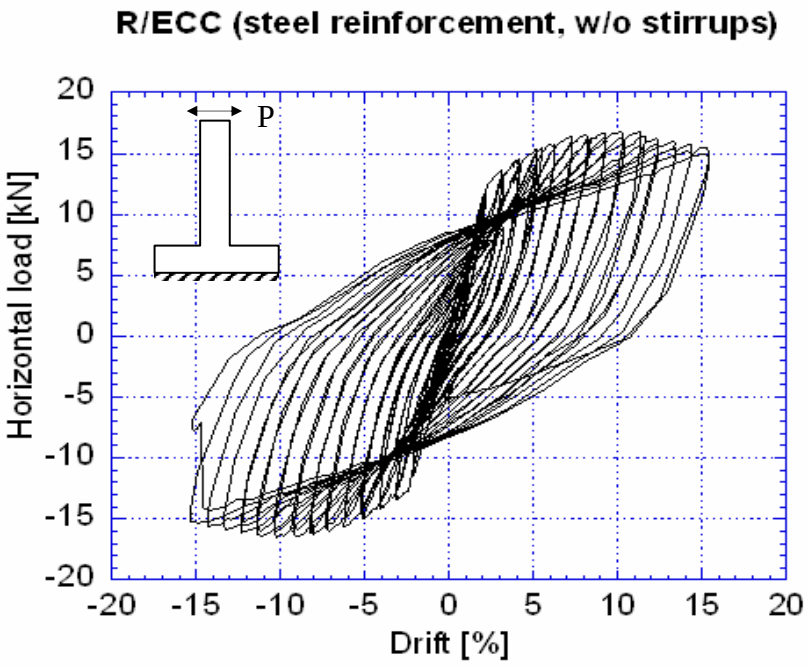

(a)

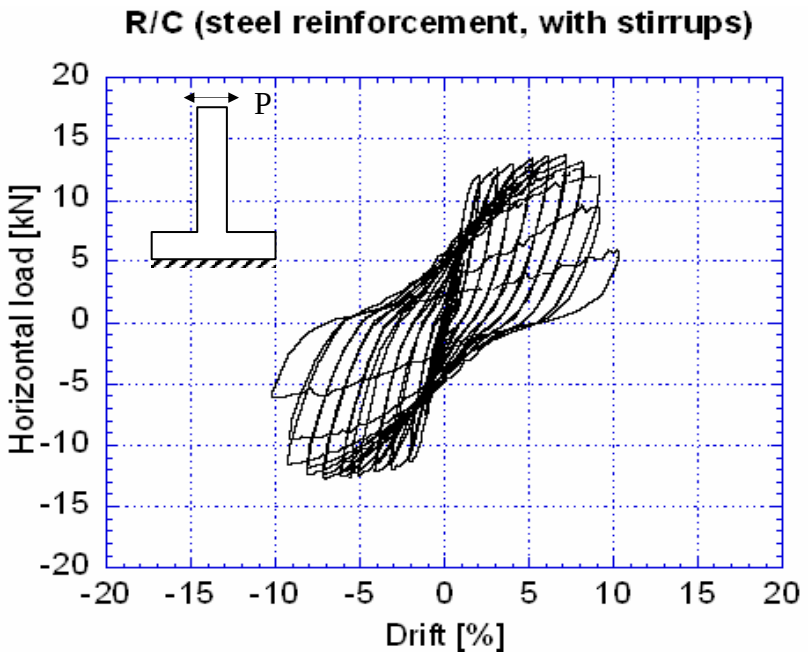

(b)

Fig. 5.1 – Load-deformation response of (a) R/ECC column without stirrups and (b) R/C column with stirrups subjected to reversed cyclic loading (After [17])

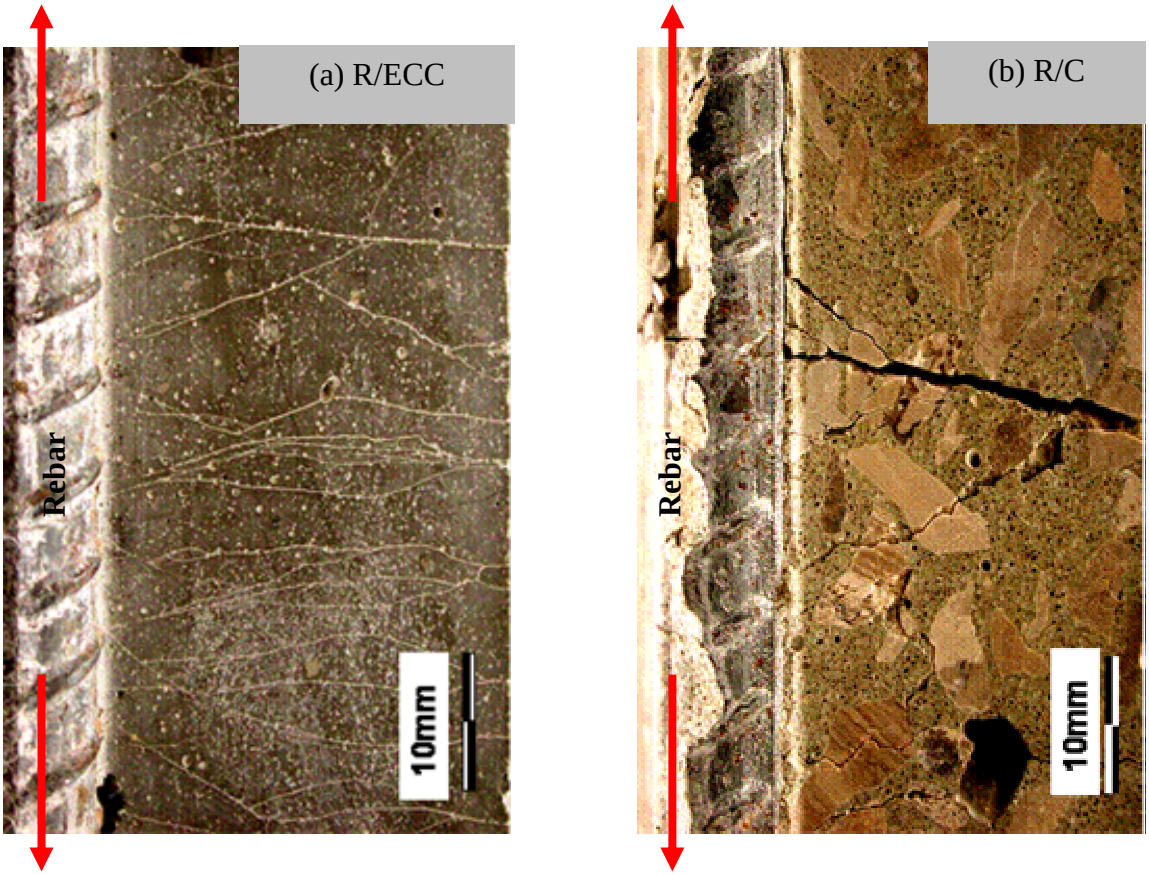

Fig. 5.2 – (a) Compatibility of deformation in R/ECC elements, and (b) localized crack and bond splitting in R/C elements under uniaxial tension (After [39])

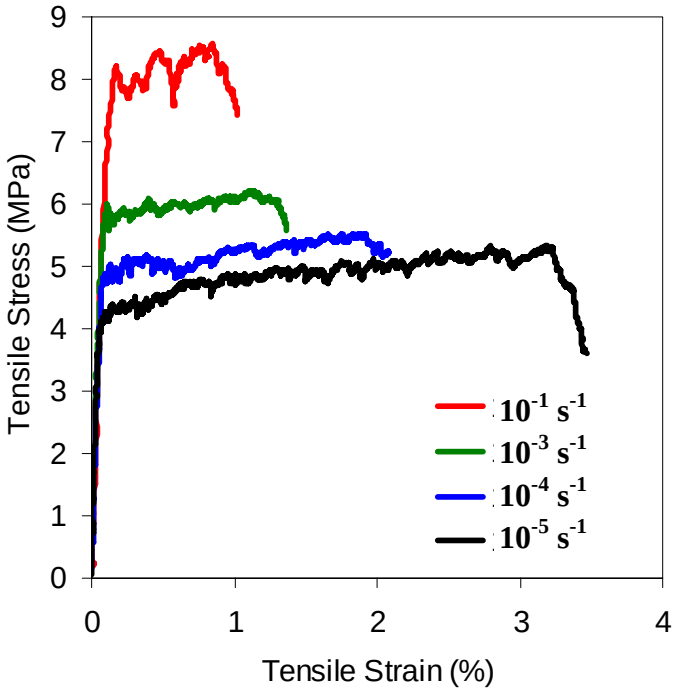

(a)

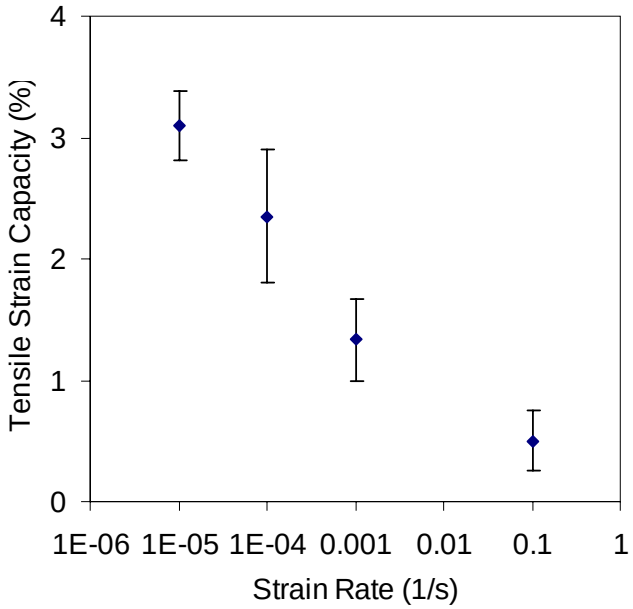

(b)

Fig. 5.3 – Rate dependency in ECC M45 composite (a) tensile stress-strain curve and (b) tensile ductility at four different strain rates

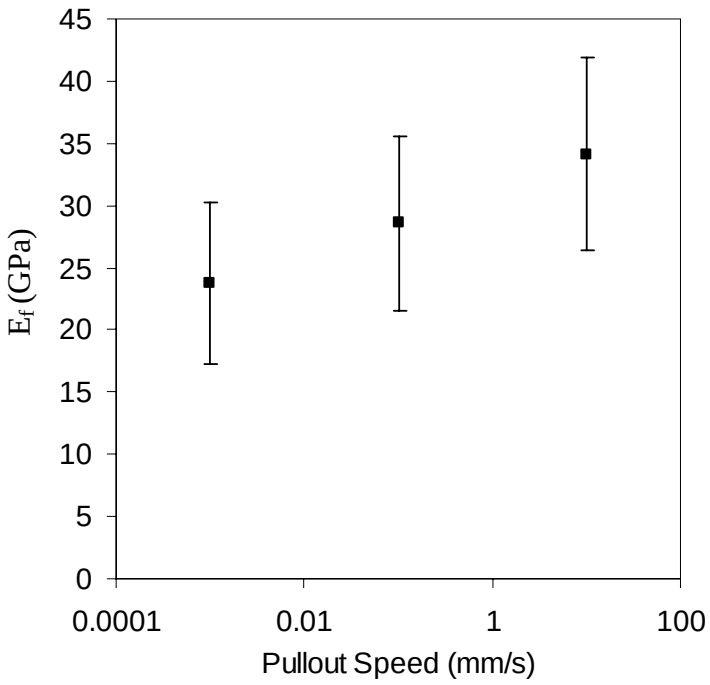

Fig. 5.4 – Rate dependency of PVA fiber modulus

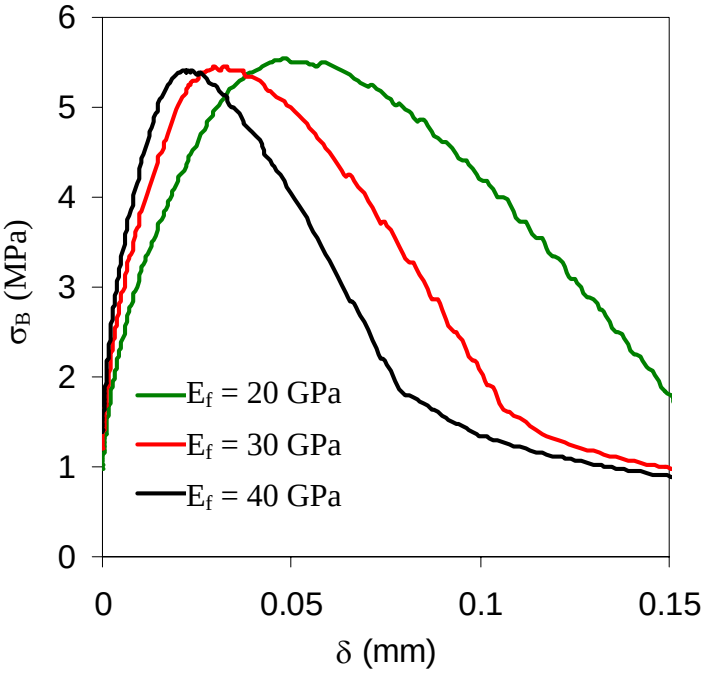

Fig. 5.5 – Parametric study on the effect of fiber modulus on fiber bridging spring law σ-δ curve

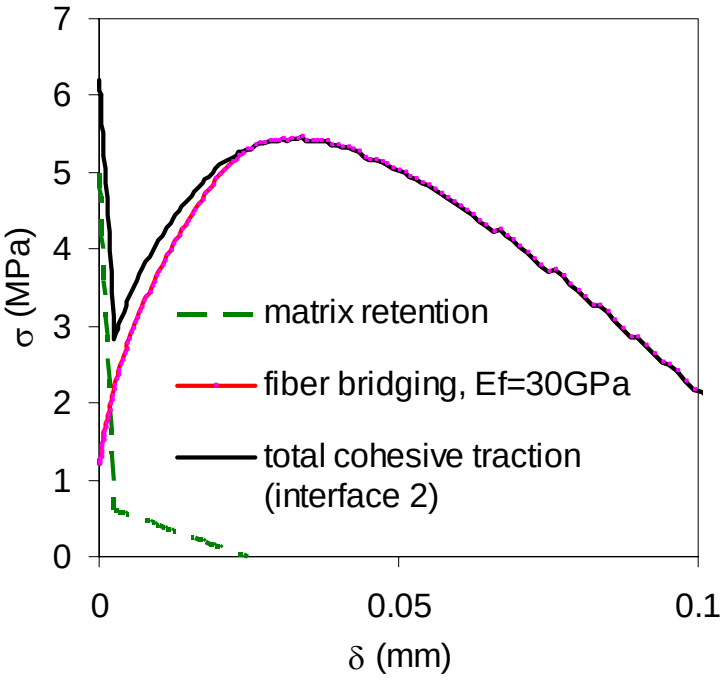

Fig. 5.6 – Cohesive traction model .

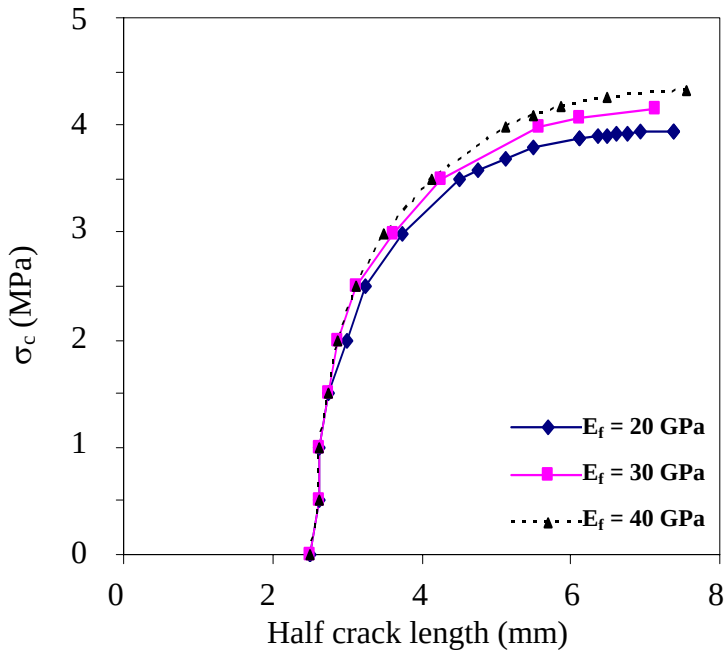

Fig. 5.7 – Parametric study on the effect of fiber modulus on matrix cracking strength.

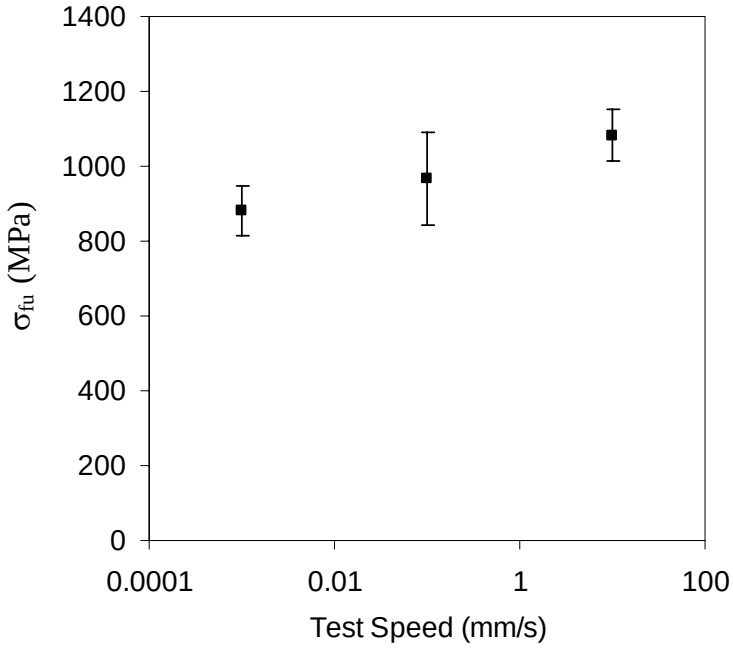

Fig. 5.8 – Rate dependency on in-situ PVA fiber tensile strength

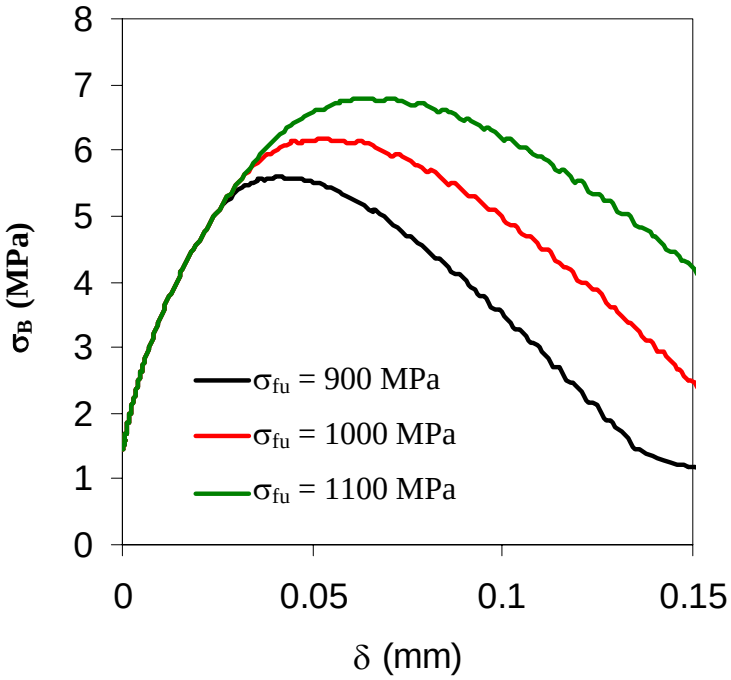

Fig. 5.9 – Parametric study on the effect of fiber strength on fiber bridging spring law σ-δ curve

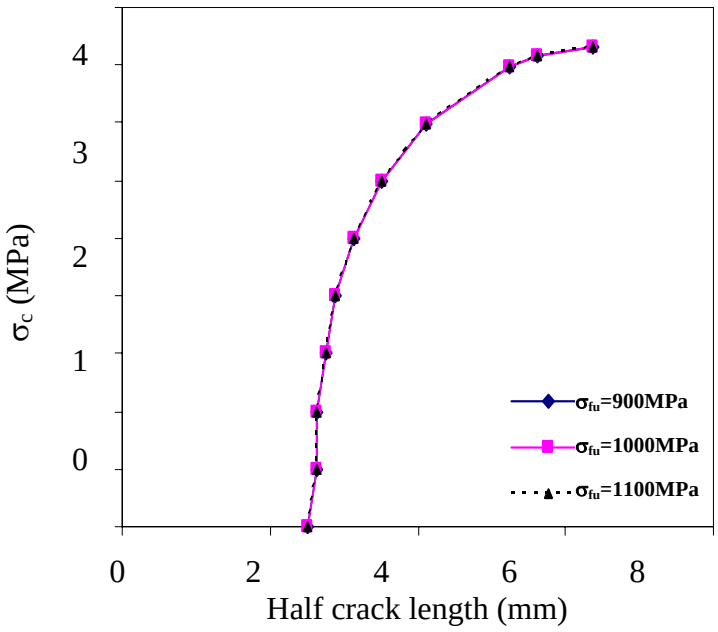

Fig. 5.10 – Parametric study on the effect of fiber strength on matrix cracking strength

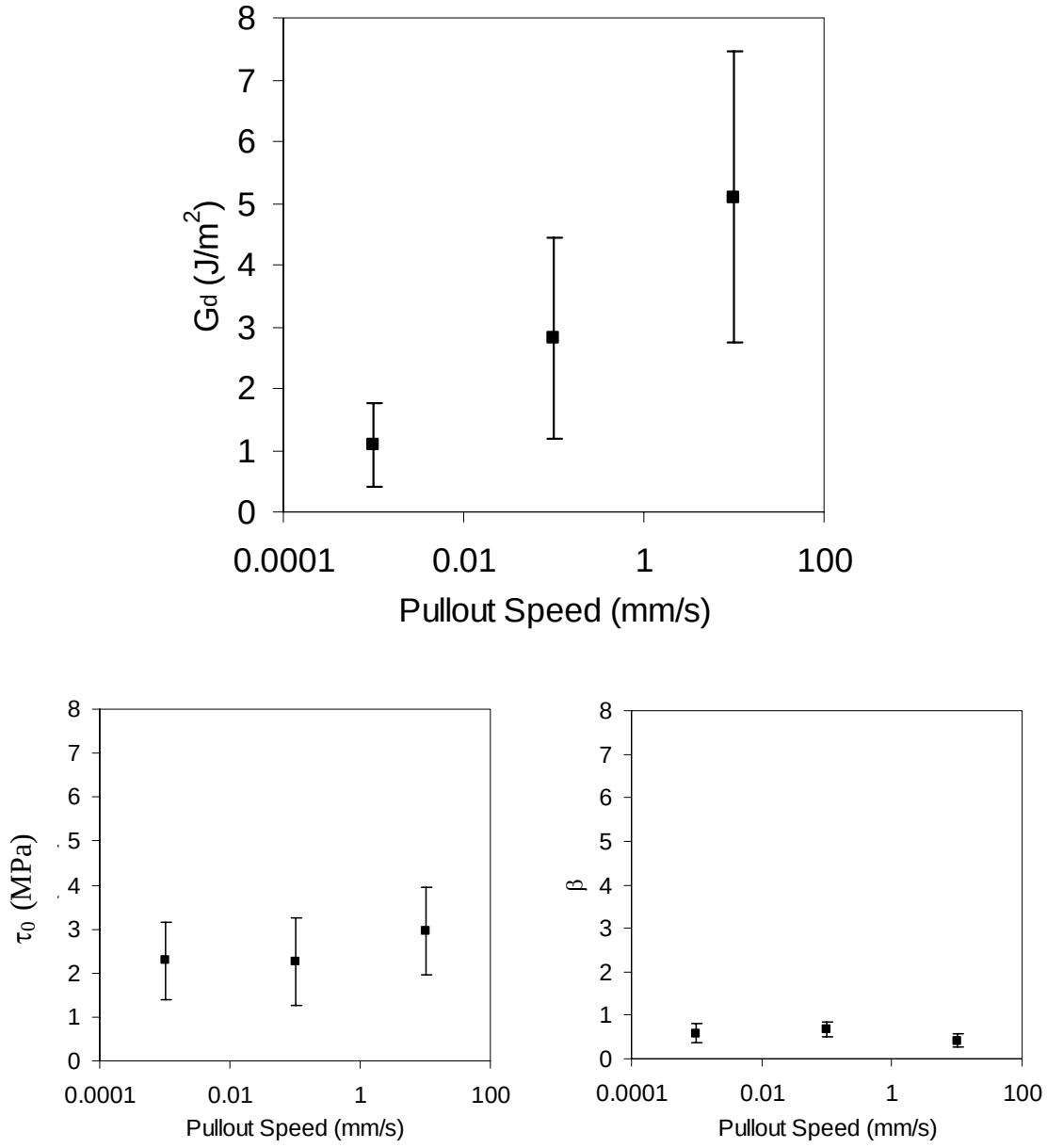

Fig. 5.11 – Rate dependency on interfacial bond properties (a) chemical bond, (b) frictional bond, and (c) slip-hardening coefficient

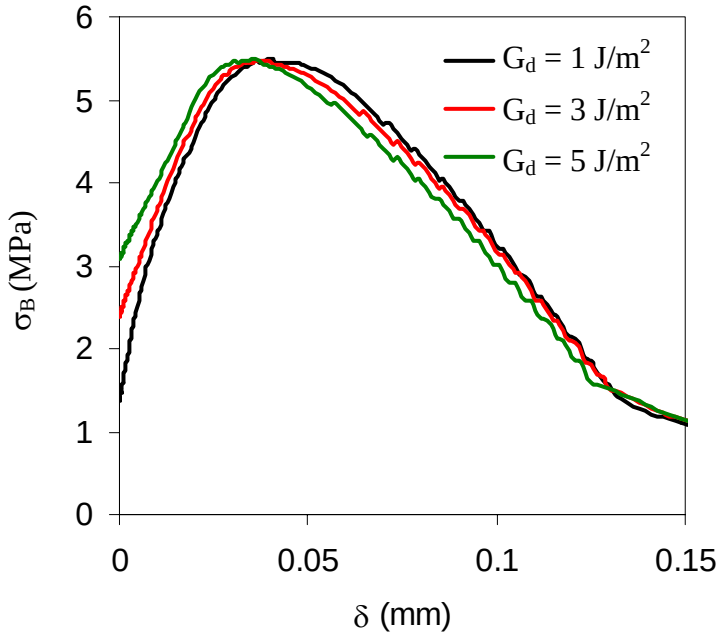

Fig. 5.12 – Parametric study on the effect of interfaical chemical bond strength on fiber bridging spring law σ-δ curve

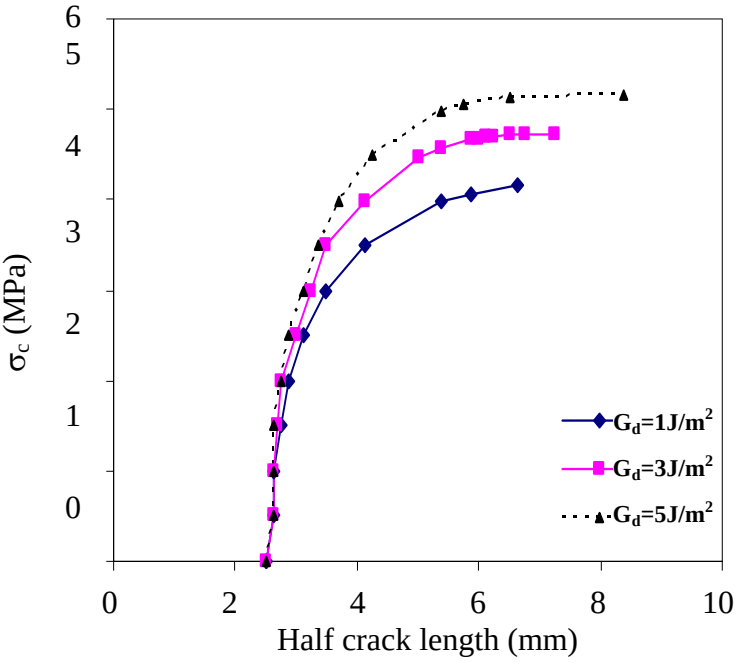

Fig. 5.13 – Parametric study on the effect of interfacial chemical bond on matrix cracking strength

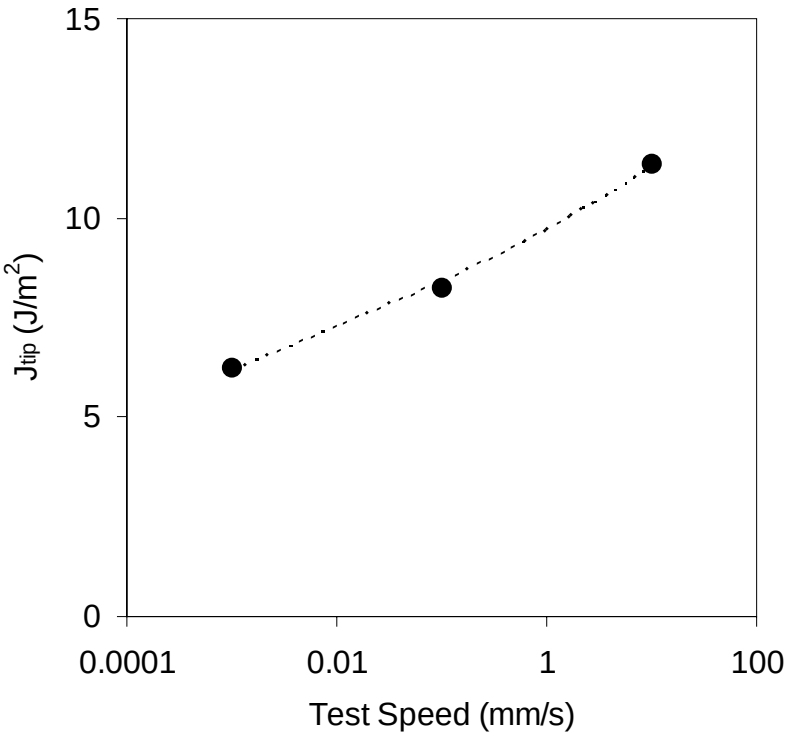

Fig. 5.14 – Matrix toughness at three different loading rates

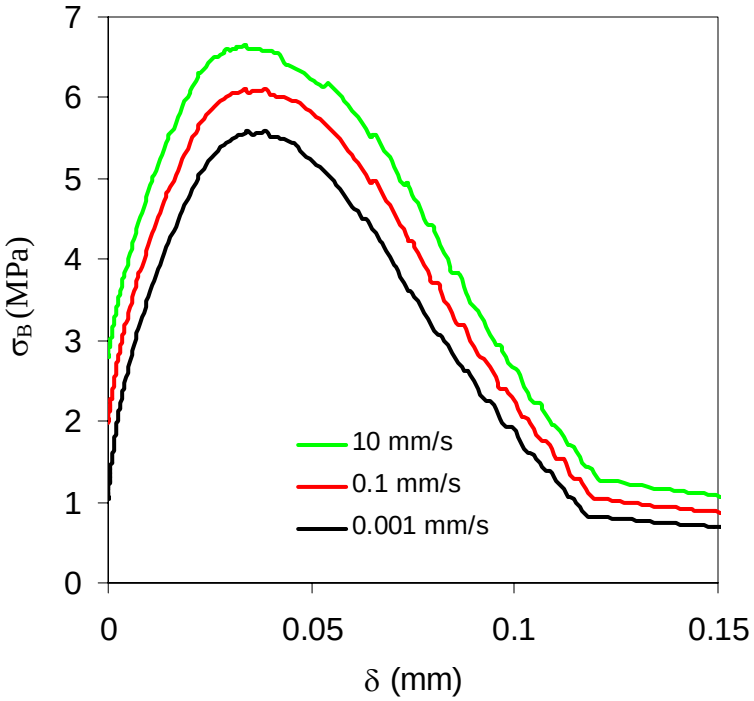

Fig. 5.15 – Preidcted fiber bridging spring law σ-δ curve of three different loading rates

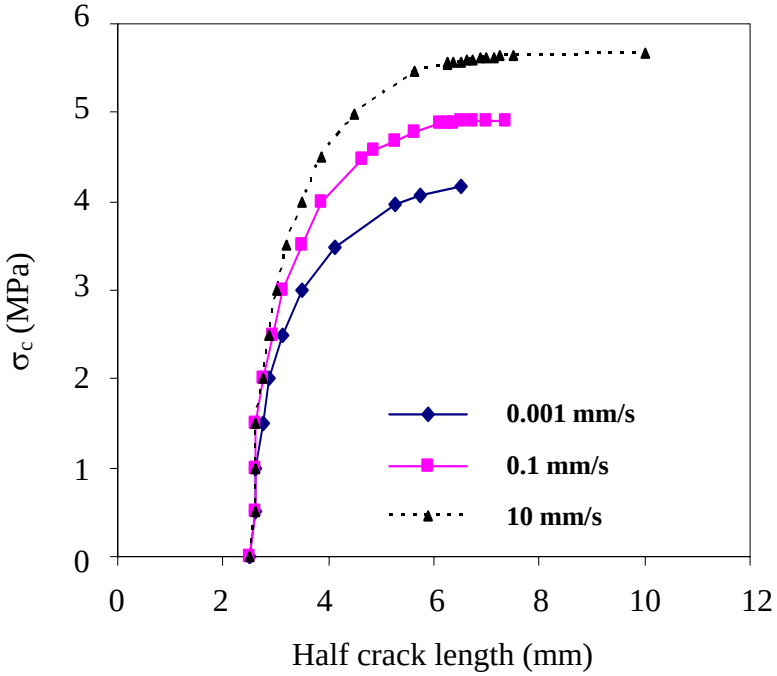

Fig. 5.16 – Preidcted matrix cracking strength of three different loading rates

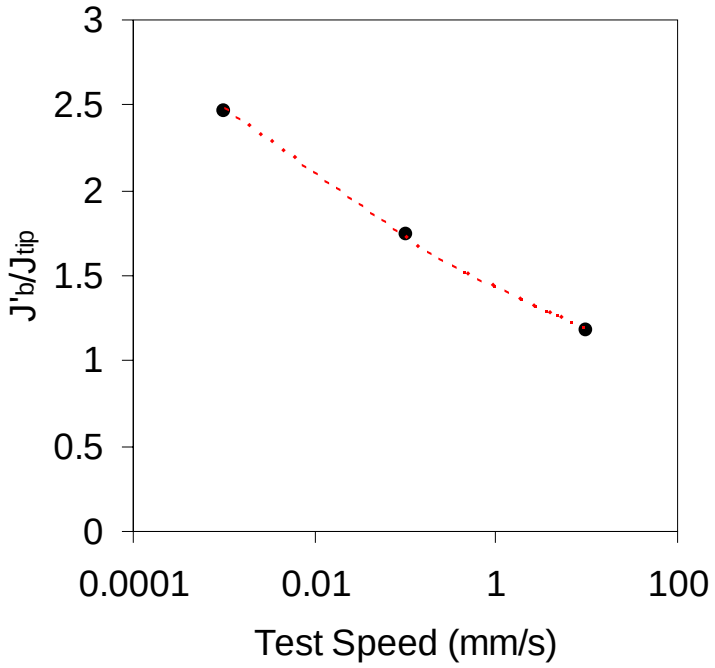

(a)

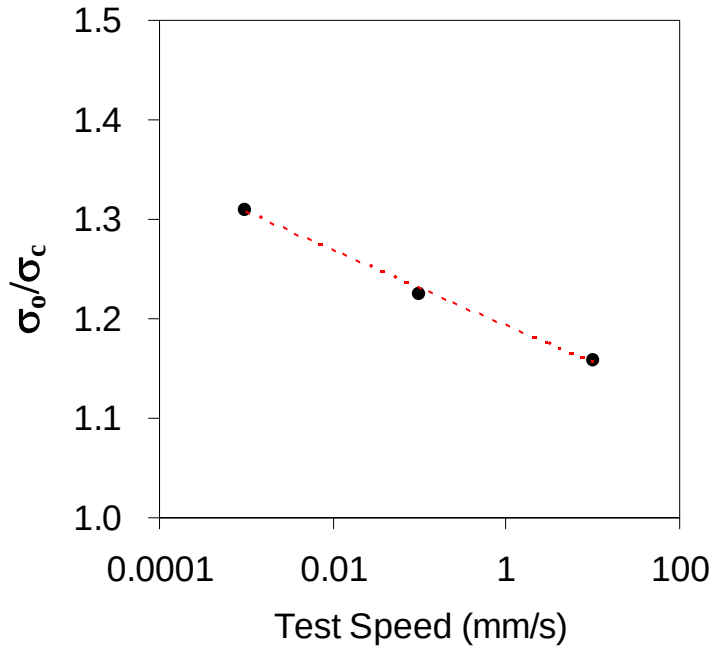

(b)

Fig. 5.17 – ECC strain hardening indices (J'_b/J_{tip} and σ_0/σ_c) against loading rates

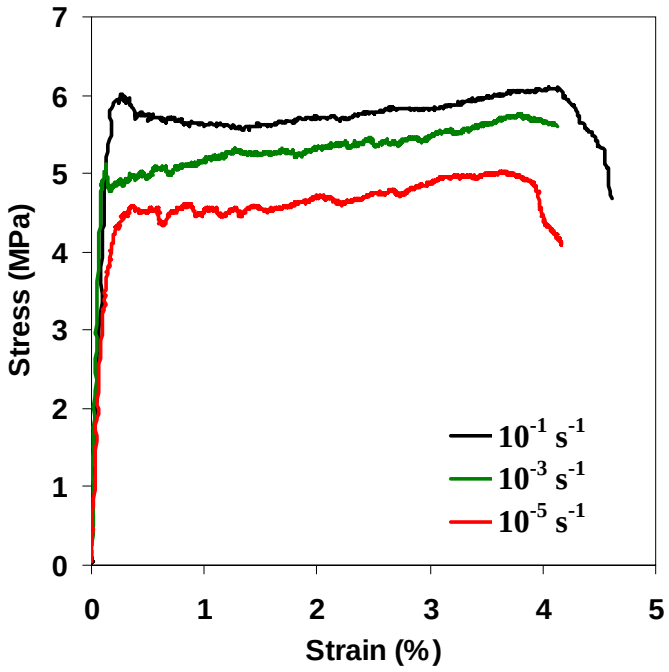

Fig. 5.18 – Tensile stress-strain curves of Mix 1 subjected to three different strain rates

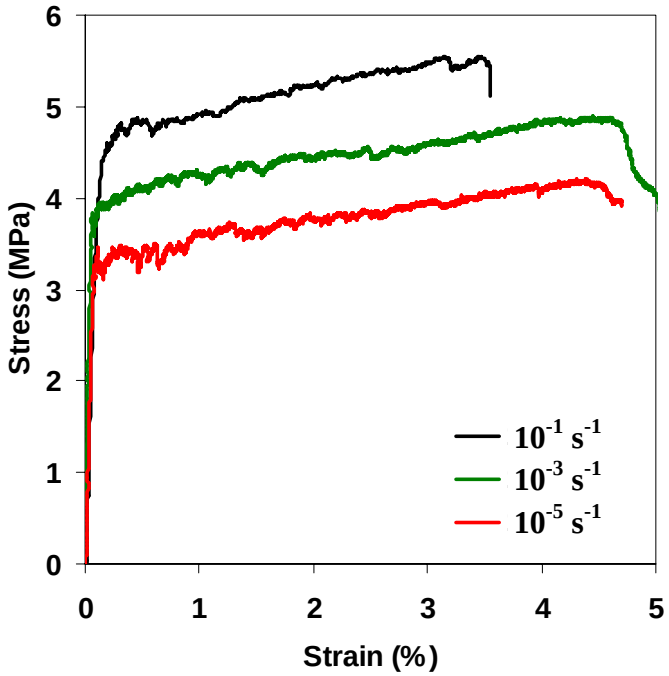

Fig. 5.19 – Tensile stress-strain curves of Mix 2 subjected to three different strain rates

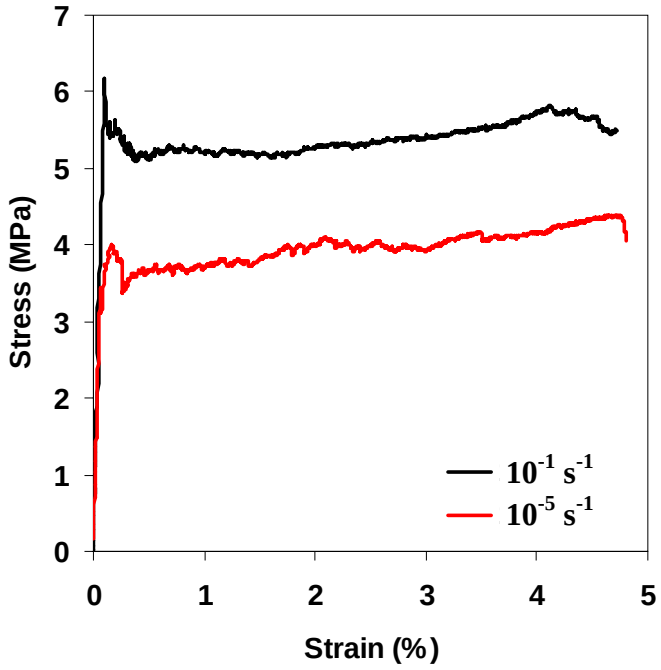

Fig. 5.20 – Tensile stress-strain curves of Mix 3 subjected to two different strain rates

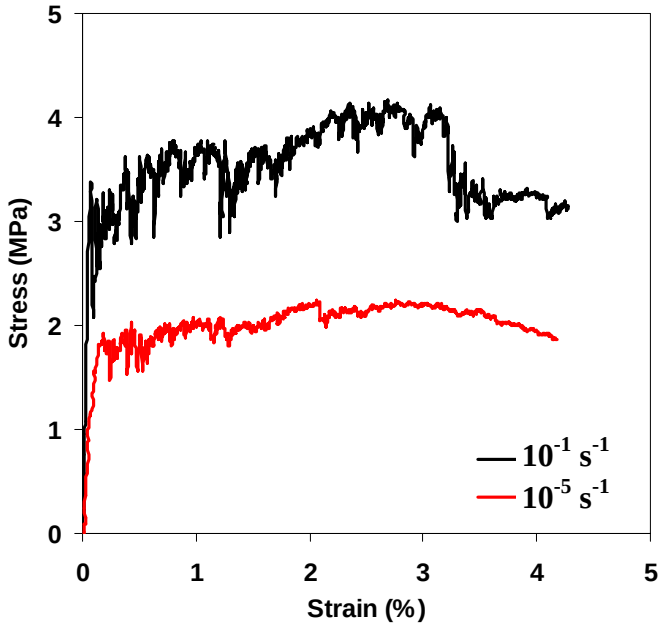

Fig 5.21 – Tensile stress-strain curves of Mix 4 subjected to two different strain rates

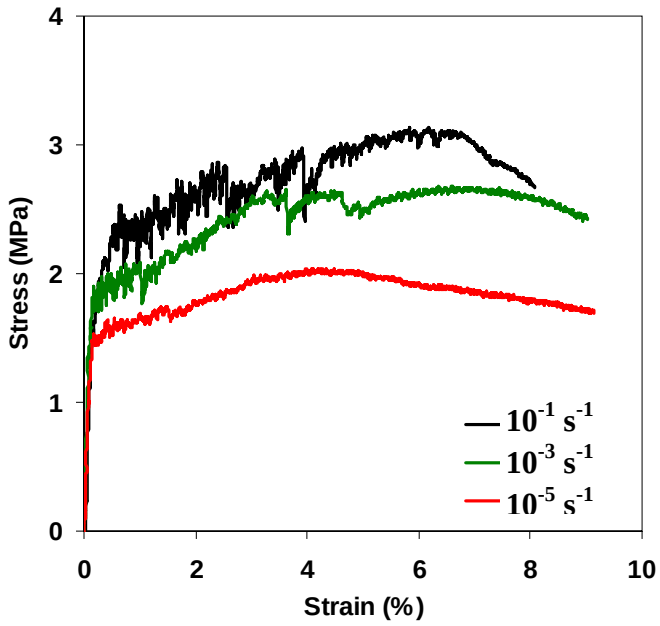

Fig. 5.22 – Tensile stress-strain curves of Mix 5 subjected to three different strain **rates**

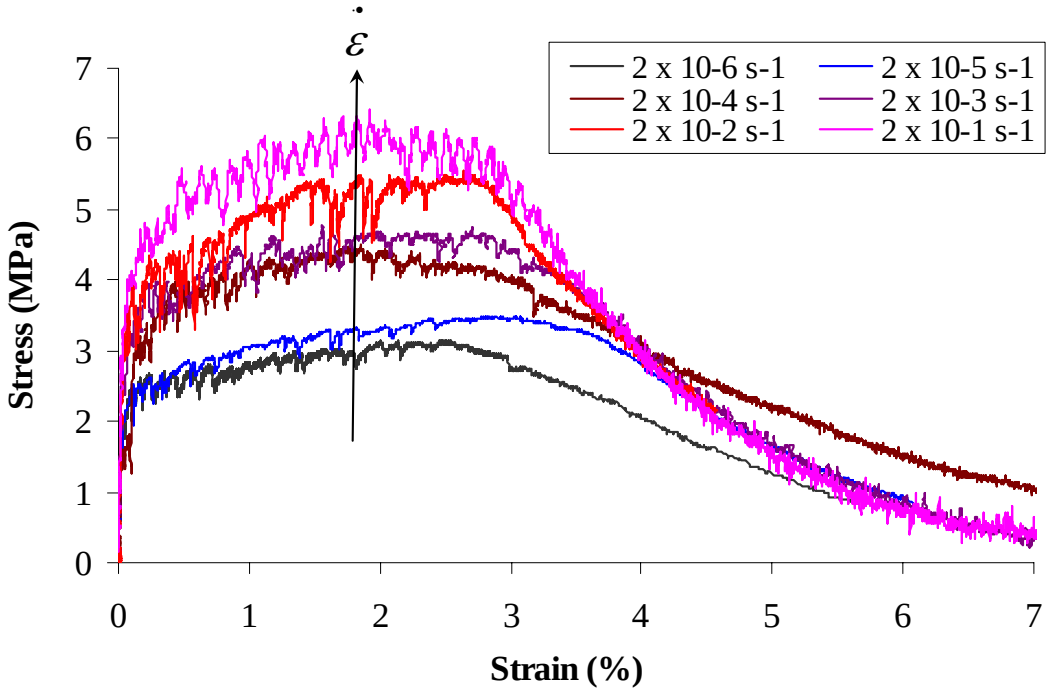

Fig 5.23 – Tensile stress-strain curve of hybrid-fiber ECC subjected to 6 different strain rates (After [35])

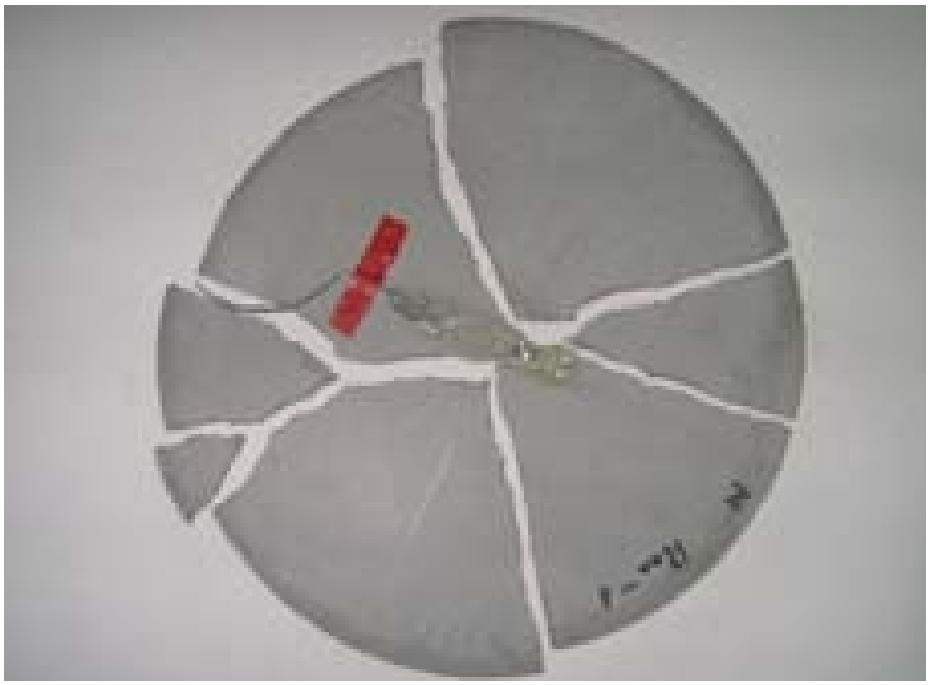

(a)

(b)

Fig. 5.24 – (a) Mortar plate after the 2nd impact (cracking & fragmentation) and (b) back side of ECC plate after 10 impacts (fine cracks only) [Courtesy of D. Yanklevsky et al., Technion-Isreal Institute of Technology]

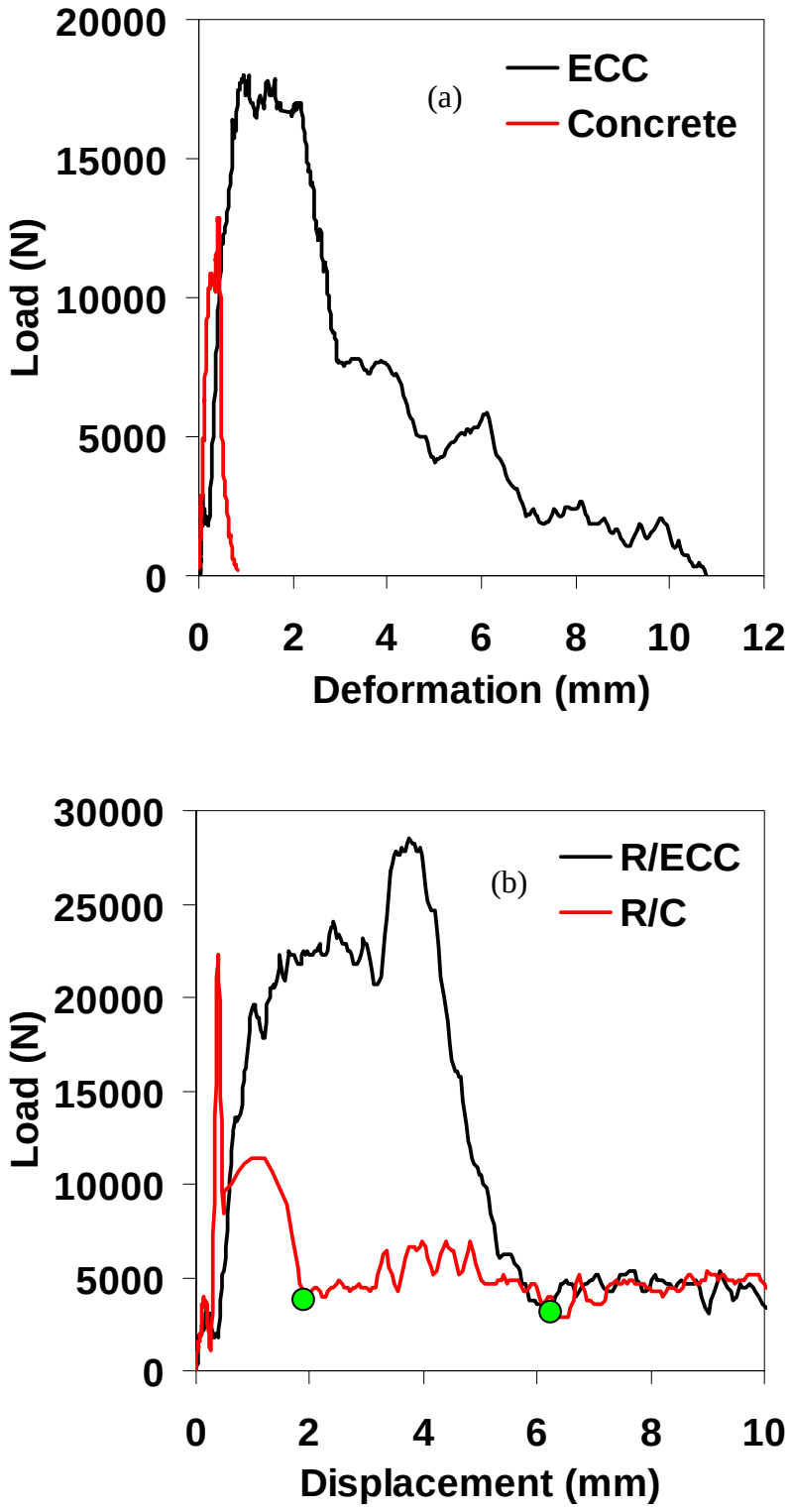

Fig. 5.25 – Load-deformation curve of (a) ECC and concrete beams and (b) R/ECC and R/C beams

(a)

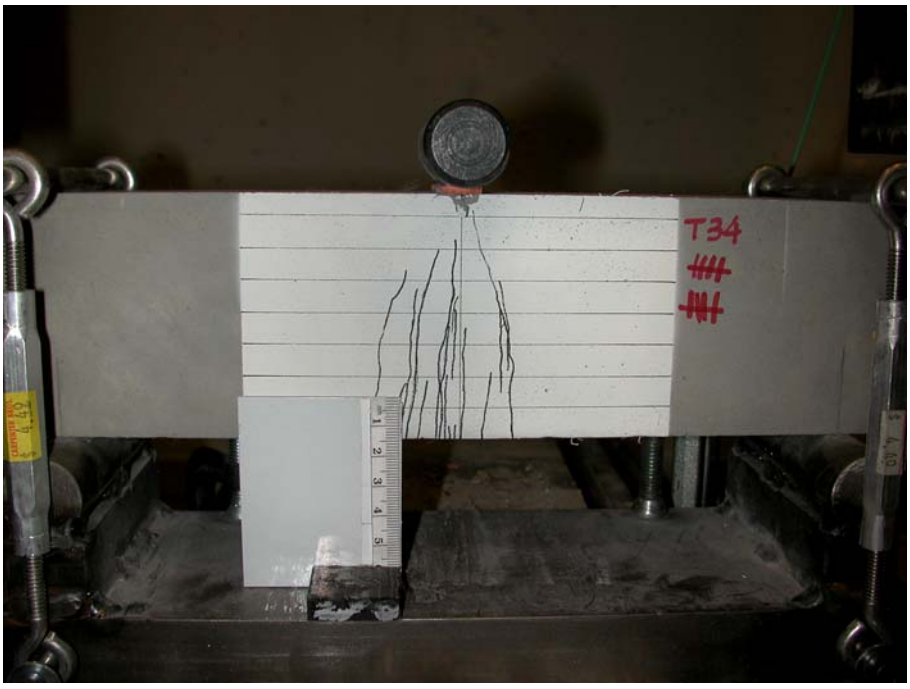

(b)

Fig 5.26 – Damage of (a) R/C beam after the 1st impact (cracking penetrates through the specimen) and (b) R/ECC beam after the 10th impact (fine cracks only highlighted by a thick marker)

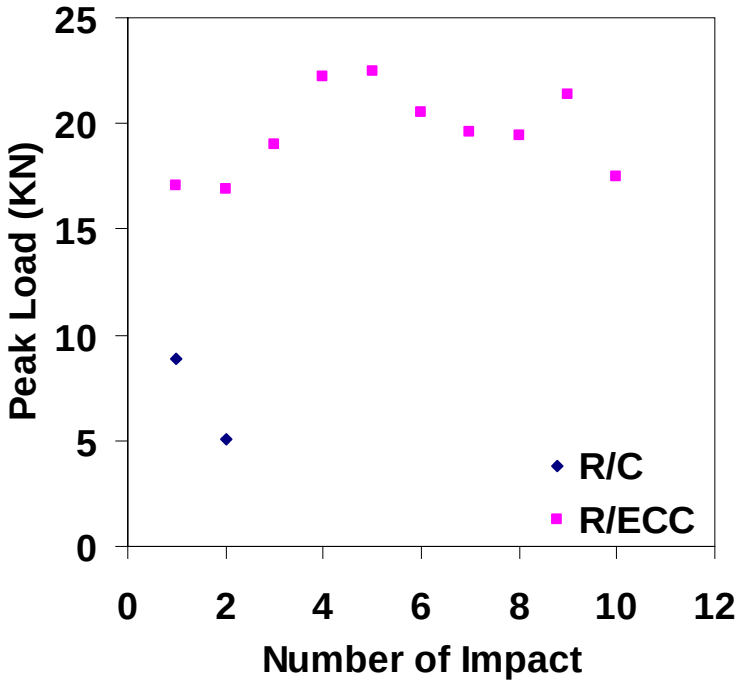

Fig. 5.27 – Load capacity of R/C and R/ECC beams against number of impact

(a)

(b)

Fig 5.28 – Damage of R/C panel on distal face (a) after 2nd impact (serious scabbing) and (b) after 3rd impact (perforated with big shear cone; cracking pattern) (After [36])

(a)

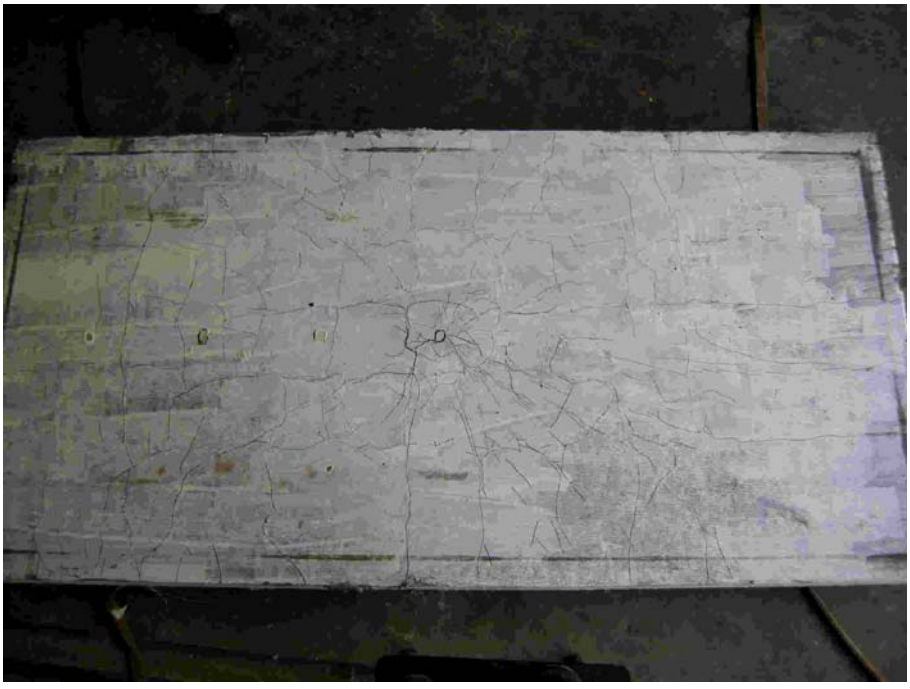

(b)

Fig 5.29 – Damage of (a) R/FRC panel on distal face after the 7th impact (perforated with big shear cone), and (b) R/ECC panel on distal face after 10 impacts (only very fine cracks developed, highlighted using a thick marker (After [36])

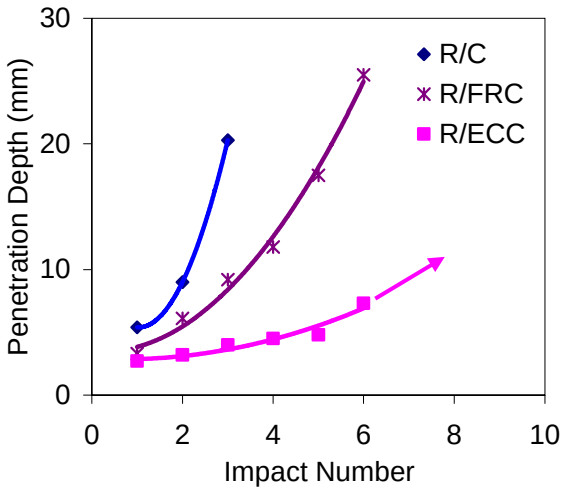

(a)

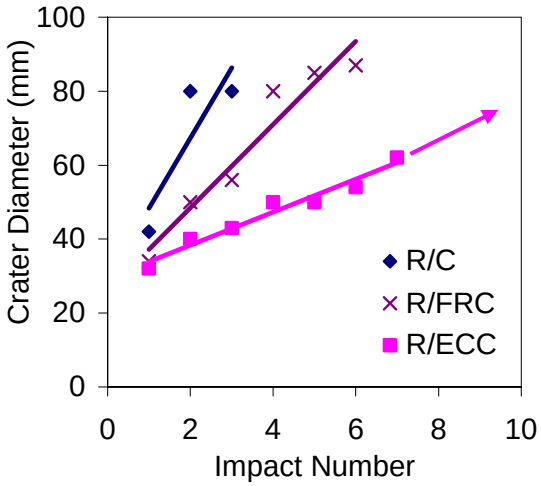

(b)

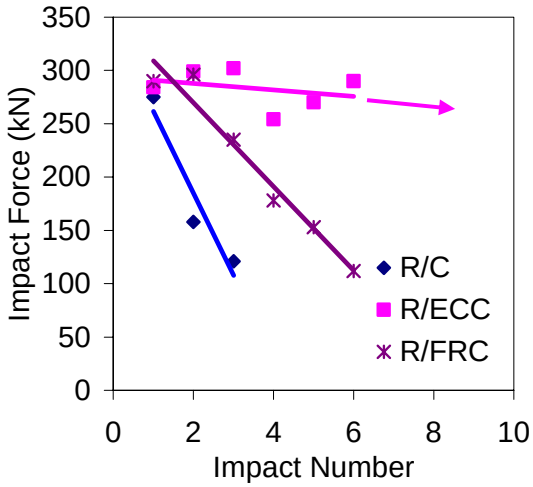

(c)

Fig 5.30 – (a) Indentation depth, (b) crater size, and (c) load cell peak impact force against number of impacts (After [36])

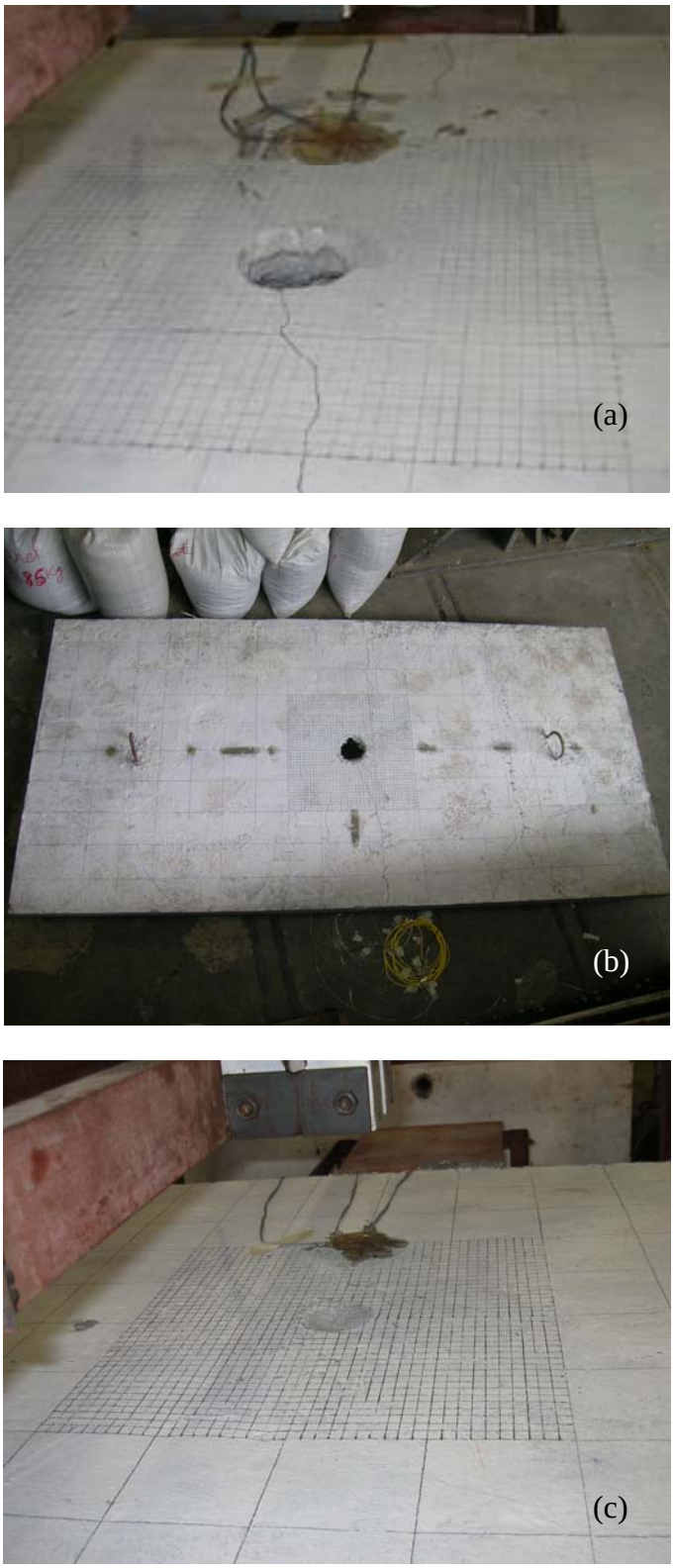

Fig 5.31 – Damage on the impact face of (a) R/C panel after 3rd impact, (b) R/FRC panel after 7th impact, and (c) R/ECC panel after 10th impact (After [36])

Appendix A: Dynamic energy release rate

For a propagating crack in an elastic body, the dynamic energy release rate, G, can be defined as the rate of mechanical energy flow out of the body and into the crack tip per unit crack advance. It is found that

$$G(\Gamma^*) = \lim_{\Gamma^* \to 0} \int_{\Gamma^*} \left[(W + T) n_1 - \sigma_{ij} n_j \frac{\partial u_i}{\partial x} \right] ds$$

is not a path-independent integral, where W is the strain energy density and T is the kinetic energy density, respectively.

$$T = \frac{1}{2} \rho \dot{u}_i \dot{u}_i$$

If other path, Γ, is chosen,

$$G(\Gamma) = \lim_{\Gamma^* \to 0} \left\{ \int_{\Gamma} \left[(W + T) n_1 - \sigma_{ij} n_j \frac{\partial u_i}{\partial x} \right] ds + \int_{A - A^*} \left[\rho \ddot{u}_i \frac{\partial u_i}{\partial x} - \rho \dot{u}_i \frac{\partial^2 u_i}{\partial t \partial x} \right] dA \right\}$$

$$G(\Gamma) - G(\Gamma^*) = \lim_{\Gamma^* \to 0} \int_{A - A^*} \left[\rho \ddot{u}_i \frac{\partial u_i}{\partial x} - \rho \dot{u}_i \frac{\partial^2 u_i}{\partial t \partial x} \right] dA \neq 0 \quad \text{…….. Path dependency}$$

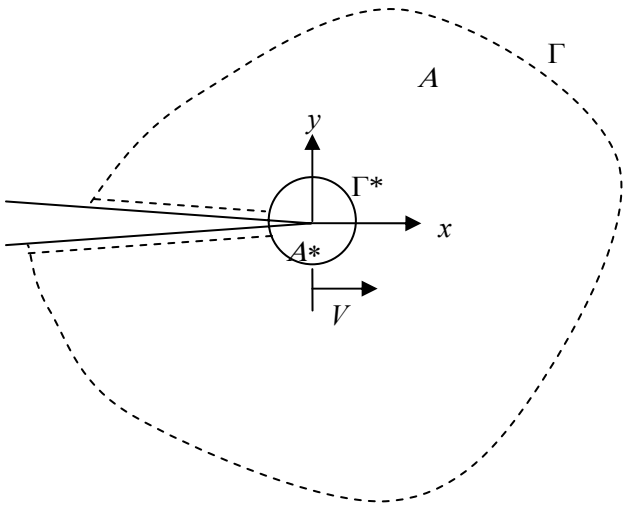

, where *x*-*y* is a coordinate system attached to and moving with the crack tip at speed *V*.

To calculate *G* for a propagating crack in an arbitrary contour, the displacement field within the region of A-A* should be known.

Special Case: Under conditions of steady-state crack propagation, the area integral vanishes and *G* is indeed path-independent.

$$G = \int_{\Gamma} (W + T)dy - \sigma_{ij} n_j \frac{\partial u_i}{\partial x} ds$$

The steady-state crack propagation here means that the mechanical fields are time invariant in a reference frame traveling with the crack tip in the *x*-direction at a uniform speed, *V* [23].

Appendix B: Review of static steady-state cracking criterion

$$J \equiv \int_{\Gamma} W dy - \sigma_{ij} n_j \frac{\partial u_i}{\partial x} ds$$

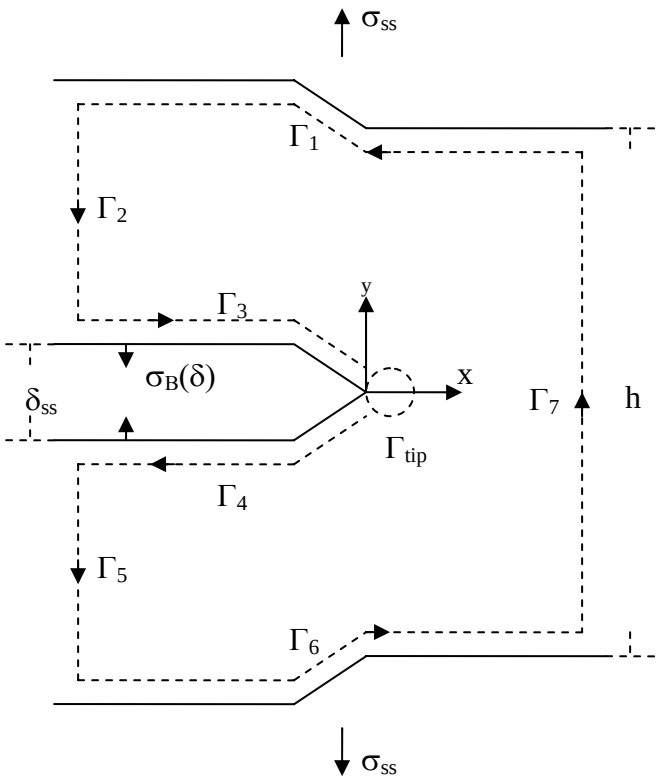

$J_{\Gamma 1}+J_{\Gamma 2}+J_{\Gamma 3}+J_{\Gamma 4}+J_{\Gamma 5}+J_{\Gamma 6}+J_{\Gamma 7} = J_{tip}$

Path Γ_1:

dy=0, ds=-dx

$n_1=0$, $n_2=1$

$\sigma_{11}=\sigma_{12}=\sigma_{21}=0$, $\sigma_{22}=\sigma_{ss}$

$$J_{\Gamma_1} = \int_{\Gamma_1} \sigma_{22} du_2$$
$$= \int_{\Gamma_1} \sigma_{ss} du_2$$
$$= \sigma_{ss} u_2 \Big|_{\frac{h}{2}}^{\frac{h}{2}+\frac{\delta_{ss}}{2}}$$
$$= \frac{\sigma_{ss}\delta_{ss}}{2}$$

Path Γ_2:

$n_2=0$

$\sigma_{11}=\sigma_{12}= \sigma_{21}=0$,

$$J_{\Gamma_2} = \int_{\Gamma_2} W dy$$

where $W = \int_0^{\varepsilon} \sigma_{ij} d\varepsilon_{ij} = \int_0^{\varepsilon_{22}} \sigma_{22} d\varepsilon_{22} = \frac{\sigma_{ss}^2}{2E}$

$$J_{\Gamma_2} = \int_{\Gamma_2} W dy = \frac{\sigma_{ss}^2}{2E} y\Big|_{\frac{h}{2}+\frac{\delta_{ss}}{2}}^{\frac{\delta_{ss}}{2}} = -\frac{\sigma_{ss}^2 h}{4E}$$

Path Γ_3:

dy=0, ds=dx

n_1=0, n_2=-1

$\sigma_{11}=\sigma_{12}=\sigma_{21}=0$, $\sigma_{22}=\sigma_B(\delta)$

$$J_{\Gamma_3} = \int_{\Gamma_3} \sigma_{22} du_2 = \int_{\Gamma_3} \sigma_B(u_2) du_2 = \int_{\frac{\delta_{ss}}{2}}^{0} \sigma_B(u_2) du_2$$

Path Γ_4:

dy=0, ds=-dx

n_1=0, n_2=1

$\sigma_{11}=\sigma_{12}=\sigma_{21}=0$, $\sigma_{22}=\sigma_B(\delta)$

$$J_{\Gamma_4} = \int_{\Gamma_4} \sigma_{22} du_2 = \int_{\Gamma_4} \sigma_B(u_2) du_2 = \int_{0}^{-\frac{\delta_{ss}}{2}} \sigma_B(u_2) du_2$$

Path Γ_5:

n_2=0

$\sigma_{11}=\sigma_{12}=\sigma_{21}=0$,

$$J_{\Gamma_5} = \int_{\Gamma_5} W dy$$

where $W = \int_0^{\varepsilon} \sigma_{ij} d\varepsilon_{ij} = \int_0^{\varepsilon_{22}} \sigma_{22} d\varepsilon_{22} = \frac{\sigma_{ss}^2}{2E}$

$$J_{\Gamma_5} = \int_{\Gamma_5} W dy = \frac{\sigma_{ss}^2}{2E} y\Big|_{-\frac{\delta_{ss}}{2}}^{-\frac{h}{2}-\frac{\delta_{ss}}{2}} = -\frac{\sigma_{ss}^2 h}{4E}$$

Path Γ_6:

dy=0, ds=dx

$n_1=0$, $n_2=-1$

$\sigma_{11}=\sigma_{12}=\sigma_{21}=0$, $\sigma_{22}=\sigma_{ss}$

$$J_{\Gamma_6} = \int_{\Gamma_6} \sigma_{ss} du_2 = \sigma_{ss} u_2\Big|_{-\frac{h}{2}-\frac{\delta_{ss}}{2}}^{-\frac{h}{2}} = \frac{\sigma_{ss}\delta_{ss}}{2}$$

Path Γ_7:

$n_2=0$

$\sigma_{11}=\sigma_{12}=\sigma_{21}=0$,

$$J_{\Gamma_7} = \int_{\Gamma_7} W dy$$

where $W = \int_0^{\varepsilon} \sigma_{ij} d\varepsilon_{ij} = \int_0^{\varepsilon_{22}} \sigma_{22} d\varepsilon_{22} = \frac{\sigma_{ss}^2}{2E}$

$$J_{\Gamma_7} = \int_{\Gamma_7} W dy = \frac{\sigma_{ss}^2}{2E} y\Big|_{-\frac{h}{2}}^{\frac{h}{2}} = \frac{\sigma_{ss}^2 h}{2E}$$

$$\begin{aligned} J_{tip} &= J_{\Gamma_1} + J_{\Gamma_2} + J_{\Gamma_3} + J_{\Gamma_4} + J_{\Gamma_5} + J_{\Gamma_6} + J_{\Gamma_7} \\ &= \frac{\sigma_{ss}\delta_{ss}}{2} + \left(-\frac{\sigma_{ss}^2 h}{4E}\right) + \int_{-\frac{\delta_{ss}}{2}}^{0} \sigma_B(u_2) du_2 + \int_0^{-\frac{\delta_{ss}}{2}} \sigma_B(u_2) du_2 + \left(-\frac{\sigma_{ss}^2 h}{4E}\right) + \frac{\sigma_{ss}\delta_{ss}}{2} + \left(\frac{\sigma_{ss}^2 h}{2E}\right) \\ &= \sigma_{ss}\delta_{ss} - \int_0^{\delta_{ss}} \sigma_B(\delta) d\delta \equiv J_b^{'} \end{aligned}$$

Appendix C: Dynamic steady-state cracking criterion

$$G = \int_{\Gamma} (W + T)dy - \sigma_{ij} n_j \frac{\partial u_i}{\partial x} ds$$
$$= \int_{\Gamma} \left(W + \frac{1}{2} \rho V^2 \frac{\partial u_i}{\partial x} \frac{\partial u_i}{\partial x} \right) dy - \sigma_{ij} n_j \frac{\partial u_i}{\partial x} ds$$

Check: When $V = 0$, this equation reduces to the J-integral.

$G_{\Gamma 1}+G_{\Gamma 2}+G_{\Gamma 3}+G_{\Gamma 4}+G_{\Gamma 5}+G_{\Gamma 6}+G_{\Gamma 7} = G_{tip}$

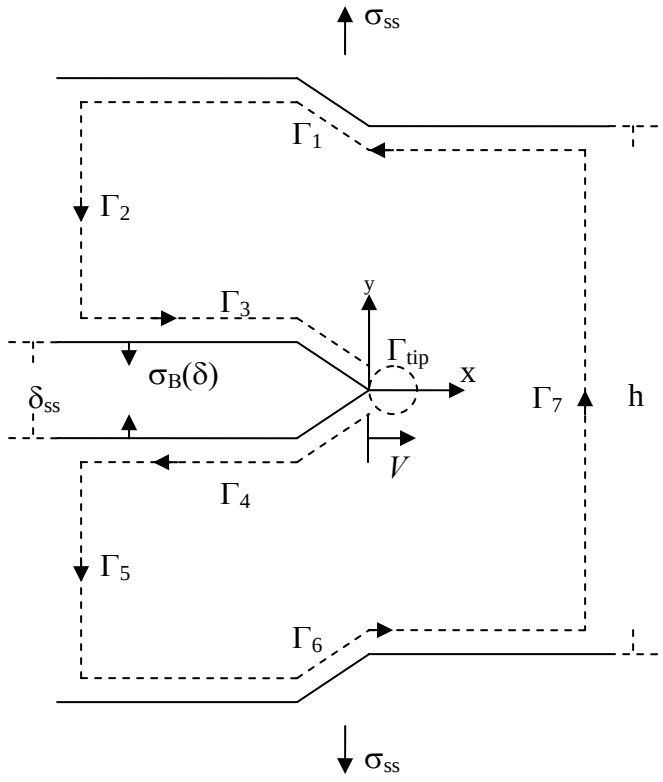

Path Γ_1:

dy=0, ds=-dx

$n_1=0$, $n_2=1$

$\sigma_{11}=\sigma_{12}=\sigma_{21}=0$, $\sigma_{22}=\sigma_{ss}$

$$G_{\Gamma_1} = \int_{\Gamma_1} \sigma_{22} du_2$$
$$= \int_{\Gamma_1} \sigma_{ss} du_2$$
$$= \sigma_{ss} u_2 \Big|_{\frac{h}{2}}^{\frac{h}{2}+\frac{\delta_{ss}}{2}}$$
$$= \frac{\sigma_{ss}\delta_{ss}}{2}$$

Path Γ_2:

$n_2=0$

$\sigma_{11}=\sigma_{12}= \sigma_{21}=0$,

$$\frac{\partial u_i}{\partial x} = 0$$

$$G_{\Gamma_2} = \int_{\Gamma_2} (W + T) dy$$

$$W = \int_0^{\varepsilon} \sigma_{ij} d\varepsilon_{ij} = \int_0^{\varepsilon_{22}} \sigma_{22} d\varepsilon_{22} = \frac{\sigma_{ss}^2}{2E}$$

where

$$T = \frac{1}{2} \rho V^2 \frac{\partial u_i}{\partial x} \frac{\partial u_i}{\partial x} = 0$$

$$G_{\Gamma_2} = \int_{\Gamma_2} W dy = \frac{\sigma_{ss}^2}{2E} y \Big|_{\frac{h}{2}+\frac{\delta_{ss}}{2}}^{\frac{\delta_{ss}}{2}} = -\frac{\sigma_{ss}^2 h}{4E}$$

Path Γ_3:

dy=0, ds=dx

n_1=0, n_2=-1

$\sigma_{11}=\sigma_{12}=\sigma_{21}=0$, $\sigma_{22}=\sigma_B(\delta)$

$$G_{\Gamma_3} = \int_{\Gamma_3} \sigma_{22} du_2 = \int_{\Gamma_3} \sigma_B(u_2) du_2 = \int_{\frac{\delta_{ss}}{2}}^{0} \sigma_B(u_2) du_2$$

Path Γ_4:

dy=0, ds=-dx

n_1=0, n_2=1

$\sigma_{11}=\sigma_{12}=\sigma_{21}=0$, $\sigma_{22}=\sigma_B(\delta)$

$$G_{\Gamma_4} = \int_{\Gamma_4} \sigma_{22} du_2 = \int_{\Gamma_4} \sigma_B(u_2) du_2 = \int_0^{-\frac{\delta_{ss}}{2}} \sigma_B(u_2) du_2$$

Path Γ_5:

n_2=0

$\sigma_{11}=\sigma_{12}=\sigma_{21}=0$,

$$\frac{\partial u_i}{\partial x} = 0$$

$$G_{\Gamma_5} = \int_{\Gamma_5} (W + T) dy$$

where
$$W = \int_0^{\varepsilon} \sigma_{ij} d\varepsilon_{ij} = \int_0^{\varepsilon_{22}} \sigma_{22} d\varepsilon_{22} = \frac{\sigma_{ss}^2}{2E}$$

$$T = \frac{1}{2} \rho V^2 \frac{\partial u_i}{\partial x} \frac{\partial u_i}{\partial x} = 0$$

$$G_{\Gamma_5} = \int_{\Gamma_5} W dy = \frac{\sigma_{ss}^2}{2E} y \Big|_{-\frac{\delta_{ss}}{2}}^{-\frac{h}{2}-\frac{\delta_{ss}}{2}} = -\frac{\sigma_{ss}^2 h}{4E}$$

Path Γ_6:

dy=0, ds=dx

$n_1=0$, $n_2=-1$

$\sigma_{11}=\sigma_{12}=\sigma_{21}=0$, $\sigma_{22}=\sigma_{ss}$

$$G_{\Gamma_6} = \int_{\Gamma_6} \sigma_{ss} du_2 = \sigma_{ss} u_2 \Big|_{-\frac{h}{2}-\frac{\delta_{ss}}{2}}^{-\frac{h}{2}} = \frac{\sigma_{ss} \delta_{ss}}{2}$$

Path Γ_7:

$n_2=0$

$\sigma_{11}=\sigma_{12}= \sigma_{21}=0$,

$$\frac{\partial u_i}{\partial x} = 0$$

$$G_{\Gamma_7} = \int_{\Gamma_7} (W + T) dy$$

$$W = \int_0^{\varepsilon} \sigma_{ij} d\varepsilon_{ij} = \int_0^{\varepsilon_{22}} \sigma_{22} d\varepsilon_{22} = \frac{\sigma_{ss}^2}{2E}$$

where

$$T = \frac{1}{2}\rho V^2 \frac{\partial u_i}{\partial x}\frac{\partial u_i}{\partial x} = 0$$

$$G_{\Gamma_7} = \int_{\Gamma_7} W dy = \frac{\sigma_{ss}^2}{2E} y\Big|_{-\frac{h}{2}}^{\frac{h}{2}} = \frac{\sigma_{ss}^2 h}{2E}$$

$$\begin{aligned} G_{tip} &= G_{\Gamma_1} + G_{\Gamma_2} + G_{\Gamma_3} + G_{\Gamma_4} + G_{\Gamma_5} + G_{\Gamma_6} + G_{\Gamma_7} \\ &= \frac{\sigma_{ss}\delta_{ss}}{2} + \left(-\frac{\sigma_{ss}^2 h}{4E}\right) + \int_{\frac{\delta_{ss}}{2}}^{0} \sigma_B(u_2) du_2 + \int_0^{-\frac{\delta_{ss}}{2}} \sigma_B(u_2) du_2 + \left(-\frac{\sigma_{ss}^2 h}{4E}\right) + \frac{\sigma_{ss}\delta_{ss}}{2} + \left(\frac{\sigma_{ss}^2 h}{2E}\right) \\ &= \sigma_{ss}\delta_{ss} - \int_0^{\delta_{ss}} \sigma_B(\delta) d\delta \equiv G_b^{'} \end{aligned}$$

Appendix D: Derivation from the definition of energy release rate or energy exchange point of view for the dynamic steady-state cracking criterion (Check)

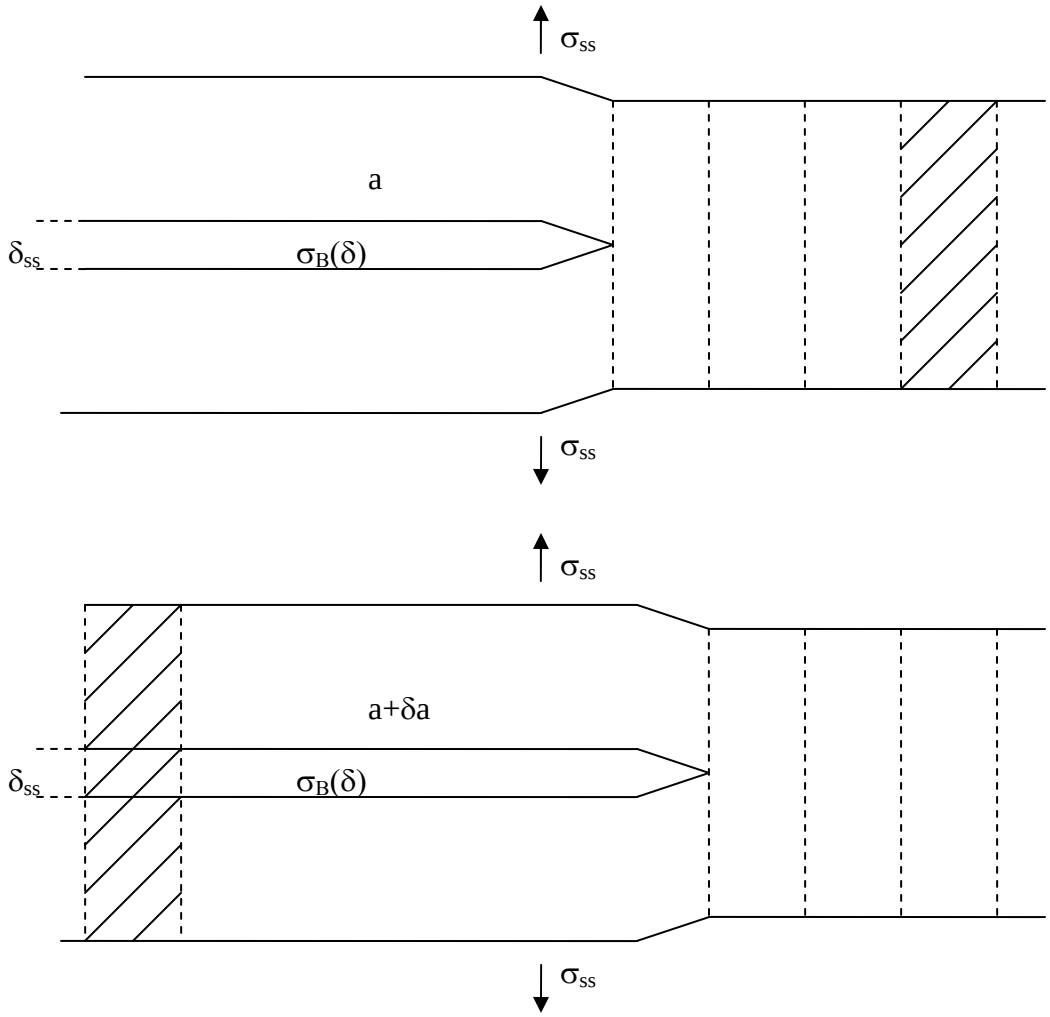

G definition:

$$G \equiv -\frac{\delta \pi_p}{\delta a}$$

, where π_p is the potential energy

$$\delta\pi_p = (U+T-W)_{after} - (U+T-W)_{before}$$
$$= (U_a - U_b) + (T_a - T_b) - (W_a - W_b)$$
$$= \left(\int_0^{\delta_{ss}} \sigma_B(\delta) d\delta + 0 - \sigma_{ss}\delta_{ss} \right) \delta a$$

$$G \equiv -\frac{\delta\pi_p}{\delta a}$$
$$= \sigma_{ss}\delta_{ss} - \int_0^{\delta_{ss}} \sigma_B(\delta) d\delta \equiv G_b^{'}$$

$G^{'}_b = G_{tip}$ for steady-state cracking criterion

Or

Energy exhange:

$dW = (\Delta a)\delta_{ss}\sigma_{ss}$

$$dU = (\Delta a)\int_0^{\delta_{ss}} \sigma_B(\delta) d\delta$$

$dT = 0$

$dE_s = (\Delta a) G_{tip}$

From energy balance ➔ $G_{tip} = \sigma_{ss}\delta_{ss} - \int_0^{\delta_{ss}} \sigma_B(\delta) d\delta \equiv G_b^{'}$

References

[1] Magnusson, J., and M. Hallgren, "Reinforced High Strength Concrete Beams Subjected to Air Blast Loading," *Structures and Materials*, vol.15, pp.53-62, 2004

[2] Malvar, L.J., and C.A. Ross, "Review of Strain Rate Effects for Concrete in Tension," *ACI Materials Journal*, vol.95, no.6, pp.735-739, 1998

[3] Clifton, J.R., *Penetration Resistance of Concrete – A Review*, 1984,

[4] Zhang, J., M. Maalej, S.T. Quek, and Y.Y. Teo, "Drop Weight Impact on Hybrid-fiber ECC Blast/Shelter Panels," *Proceedings of Construction Materials,* Vancouver, Canada, pp.CD-paper, 2005

[5] Toutlemonde, F., C. Boulay, C., and C. Gourraud, "Shock-tube Tests of Concrete Slabs," *Materials and Structures /Materiaux et Construction*, vol.26, no.155, pp.38-42, 1993

[6] Lan, S., and L. Heng, "Composite Structural Components under Blast Loading," *Structures and Materials*, vol.11, pp.13-21, 2002

[7] Krauthammer, T., "Structural Concrete Connections for Blast Containment," *Proceedings of the 3rd International Conference on Structures under Shock and Impact III,* pp.107, 1994

[8] Rittenhouse, T., "Design Terrorist-Resistant Buildings," *Fire Engineering*, vol.148, no.11, pp.103-105, 1995

[9] Ettouney, M., R. Smilowitz, and T. Rittenhouse, "Blast Resistant Design of Commercial Buildings," *Practice Periodical on Structural Design and Construction*, vol.1, no.1, pp.31-39, 1996

[10] Krauthammer, T., "Blast Mitigation Technologies: Developments and Numerical Considerations for Behavior Assessment and Design," *International Conference on Structures under Shock and Impact,* pp.3-12, 1998

[11] Conrath, E., T. Krauthammer, K.A. Marchand, and P.F. Mlakar, ed. *Structural Design for Physical Security: State of the Practice*. 1999, ASCE, Structural Institute.

[12] Muszynski, L.C., and M.R. Purcell, "Composite Reinforcement to Strengthen Existing Concrete Structures Against Air Blast," *Journal of Composites for Construction*, vol.7, no.2, pp.93-97, 2003

[13] TM5-1300, *Structures to Resist the Effects of Accidental Explosions*. 1990, US Dept of the Army, the Navy and the Air Force.

[14] TM5-855-1, *Fundamentals of Protective Design for Conventional Weapons*. 1992, USAWES.

[15] Biggs, J.M., *Structural Dynamics*, New York, McGraw-Hill Inc., 1964

[16] *Conwep Computer Code*. 1992, USAWES.

[17] Fischer, G., and Li, V.C., "Influence of Matrix Ductility on the Tension-Stiffening Behavior of Steel Reinforced Engineered Cementitious Composites (ECC)," *ACI Structural Journal*, vol.99, no.1, pp.104-111, 2002

[18] Kesner, K., and S.L. Billington, "Experimental Response of Precast Infill Panels Made with DFRCC," *DFRCC-2002 International Workshop,* Takayama, Japan, pp.289-298, 2002

[19] Parra-Montesinos, G., and J.K. Wight, "Seismic Response of Exterior RC Column-to-Steel Beam Connections," *Journal of Structural Engineering*, vol.126, no.10, pp.1113-1121, 2000

[20] Aveston, J., Cooper, G., and Kelly, A., "Single and Multiple Fracture," *Properties of Fiber Composites,* Guildford, UK, IPC Science and Technology Press, pp.15-24, 1971

[21] Marshall, D.B., and Cox, B.N., "A J-Integral Method for Calculating Steady-State Matrix Cracking Stresses in Composites," *Mechanics of Materials*, no.8, pp.127-133, 1988

[22] Ross, C.A., Tedesco, J.W., and Kuennen, S.T., "Effects of Strain Rate on Concrete Strength," *ACI Materials Journal*, vol.92, no.1, pp.37-47, 1995

[23] Freud, L.B., *Dynamic Fracture Mechanics*, Cambridge, New York, Cambridge University Press, 1990

[24] Cui, Y.L., "Dynamic Matrix Cracking in Fiber Reinforced Ceramics," *Journal of the Mechanics and Physics of Solids*, vol.43, no.12, pp.1875-1886, 1995

[25] Reinhardt, H.W., "Concrete under Impact Loading – Tensile Strength and Bond," *HERON*, vol.27, no.3, 1982

[26] Shah, S.P., "Concrete and Fiber Reinforced Concrete Subjected to Impact Loading," *Cement Based Composites: Strain Rate Effect on Fracture, MRS Symposium Proceedings,* pp.181-202, 1986

[27] Bischoff, P.H., and S.H. Perry, "Compressive Behavior of Concrete at High Strain Rates," *Materials and Structures*, vol.24, pp.425-450, 1991

[28] Chandra, D., and T. Krauthammer, "Strength Enhancement in Particulate Solids under High Loading Rates," *Earthquake Engineering and Structural Dynamics*, vol.24, pp.1609-1622, 1995

[29] Naaman, A.E., and V.S. Gopalaratnam, *Impact Properties of Steel Fibre Reinforced Concrete in Bending*, in *Construction Press*. 1983. p. 225-233.

[30] Banthia, N., V. Bindiganavile, and S. Mindess, "Impact Resistance of Fiber Reinforced Concrete: A Progress Report," *Proceedings of HPFRCC 4,* a.H.W.R. A.E. Naaman ed., Ann Arbor, Michigan, pp.117-132, 2003

[31] Suaris, W., and S.P. Shah, "Properties of Concrete Subjected to Impact," *Journal of Structural Engineering*, vol.109, no.7, pp.1727-1741, 1983

[32] Yang, E., and V.C. Li, "Rate Dependencies in Engineered Cementitious Composites," *Proceedings of International Workshop on HPFRCC in Structural Applications,* Honolulu, Hawaii, USA, pp.83-92, 2005

[33] Douglas, K.S., and S.L. Billington, "Rate Dependence in High-Performance Fiber-Reinforced Cement-Based Composites for Seismic Applications," *Proceedings of Int'l RILEM workshop on HPFRCC in structural applications,* pp.17-25, 2005

[34] Wang, S., and Li, V.C., "Lightweight ECC," *in Proceedings of High Performance Fiber Reinforced Cementitious Composite (HPFRCC 4),* A.E. Naaman, and H.W. Reinhardt ed., Ann Arbor, Michigan, Chapman & Hull, pp.379-390, 2003

[35] Maalej, M., S.T. Quek, and J. Zhang, "Behavior of Hybrid-Fiber Engineered Cementitious Composites Subjected to Dynamic Tensile Loading and Projectile Impact," *Jounal of Materials in Civil Engineering*, vol.17, no.2, pp.143-152, 2005

[36] Zhang, J., M. Maalej, S.T. Quek, and Y.Y. Teo, "Drop Weight Impact on Hybrid-fiber ECC Blast/Shelter Panels," *Proceedings of Construction Materials,* Vancouver, Canada, 2005

[37] Suaris, W., and Shah, S.P., "Inertia Effects in the Instrumented Impact Testing of Cementitious Composites," *ASTM Journal of Cement, Concrete and Aggregates,* vol.3, no.2, pp.77-83, 1981

[38] Suaris, W., and S.P. Shah, "Strain-rate Effects in Fibre-Reinforced Concrete Subjected to Impact and Impulsive Loading," *Composites*, vol.13, no.2, pp.153-159, 2003

[39] Fischer, G., *Deformation behavior of reinforced ECC flexural members under reversed cyclic loading conditions*, Ph.D. Dissertation, Civil and Environmental Engineering, University of Michigan, 2002

CHAPTER 6

CONCLUDING REMARKS

This research has focused on the development of a new material design approach in which new attributes can be added into materials without losing their basic properties. Specifically, new performance requirements were embedded into ECC while maintaining its tensile ductility. The ability to achieve this goal is due to realizing the connection between material macroscopic properties and material microstructures. Once established, the model-based linking provides a backward path for component re-tailoring and ingredients re-selection so that both ductility and new performance requirement can be achieved.

Research activities can be divided into two task groups, namely micromechanics (Chapter 2) and illustrations (Chapter 3, 4, and 5) with specific added functions relevant to the three major challenges civil engineering infrastructure faces – safety, durability and sustainability. In micromechanics, the fundamental requirement for ECC tensile strain-hardening was numerically verified through an FEM cohesive traction model. An

enhanced fiber bridging model with better crack width prediction was proposed and verified experimentally. This improvement was particularly relevant to the investigation on crack width design for self-healing, as discussed in Chapter 4. In addition, the strain-hardening criteria for quasi-static loading was extended to dynamic loading, important for the investigation of rate dependent material response under impact, as discussed in Chapter 5. Chapters 3 to 5 gives the details of how the extended micromechanical model was deployed to facilitate ECC re-design when new performance requirements were added into ECC material.

The second task group involved the detailed development of several ECCs with new added functions, e.g. material greenness (Chapter 3), self-healing (Chapter 4), and impact resistance (Chapter 5). Table 6.1 summarized the results of three ECCs with newly added functions. Microstructure tailoring under the guidance of micromechanics models was emphasized in the design of these ECCs. In particular, the influences of new change on material microstructure were quantified and correlated to composite behavior. The most critical microstructure property relevant to the individual performance targets was identified, and performance optimization was made through control of fiber, matrix, and interfacial bond properties.

6.1 Findings and Accomplishments

Significant findings and accomplishments made in this thesis are summarized in the following section.

6.1.1 ECC Micromechanics-based Design Theory Improvement

Three aspects of progress were made in this research, namely verifying the condition of steady-state cracking through numerical analyses of crack propagation mode, modeling and verification of fiber bridging stress-crack opening relation, and establishing the rate-dependent strain-hardening criteria. The latter two are essential to provide a quantitative base of the design guideline for added functions described in this thesis.

The well-know criterion for steady-state cracking, i.e. complementary energy of the fiber bridging relation J'_b should be larger than crack tip toughness, is a fundamental requirement for ECC tensile strain-hardening. However, the two crack propagation modes (Griffith type vs steady state flat crack) have never being observed or captured experimentally due to the difficulty of the test itself. An FEM cohesive traction model with two types of interface was used to study these crack propagation modes by assigning different traction laws to the interfaces. The condition for steady-state crack propagation, $J'_b > J_{tip}$, was therefore verified through the numerical results for the first time.

One important contribution to the ECC micromechanics-based design theory in this research is the improvement in the modeling of fiber bridging constitutive law. The new model improves over an earlier version by including three new mechanisms of fiber/matrix interactions in order to accurately predict the $\sigma(\delta)$ curve of ECC in general, and improve accuracy of crack opening prediction in particular. The fiber bridging σ-δ

relation supplies two important composite parameters to the strain-hardening criteria – fiber bridging strength and complementary energy. In addition, it predicts the steady-state crack opening, which is one of the design targets in the self-healing ECCs detailed in Chapter 4. The new model was verified by comparison with experimentally determined fiber bridging σ-δ curves.

Another significant contribution to ECC design theory in this research is the establishment of the rate-dependent strain-hardening criterion that extends current static strain-hardening criterion and is essential for designing the ductile ECC subjected to high rate loading. The rate-dependent strain-hardening criterion was applied in designing impact-resistant ECCs in Chapter 5.

A new class of ECC reinforced with polypropylene fibers was developed through micromechanics-based composites optimization and component tailoring technology. The model indicated that increase in frictional bonding and fiber strength greatly enhances composite performance when PP fiber is utilized. Experimental data show significant improvements in composite ductility (4-5%) when these fibers are properly tailored, thus confirming the effectiveness of the micromechanics approach. Although applied to two specific fiber types, the theoretical tools developed are expected to be applicable to a wide range of fiber types and brittle matrix types.

6.1.2 Green ECC

As large scale application of ECC is emerging in the field, material sustainability becomes a design concern. The approach in this study involved reducing cement usage and/or using lower processing energy fibers in ECC mix. Specifically, a large amount of

cement is substituted by a high volume of recycled class F fly ash (up to 85% by weight), a coal combustion by-product. While the objective was to develop a greener version of ECC with balanced performance in sustainability, ductility and strength, emphasis was placed on the understanding of the micromechanical linkage between mix composition and performance targets.

In the course of this study, it was discovered that fly ash possesses a number of remarkable advantageous effects to ECC development. Specifically, the micromechanics study showed that the presence of fly ash reduced the fiber/matrix interfacial chemical bond while simultaneously lowered the matrix toughness, thus improving strain-hardening potential J'_b/J_{tip}. In addition, it was found that fly ash induced a high interface frictional bond τ_0 that restrained fiber slippage and promoted tight crack width. Microstructure analysis revealed that the higher τ_0 was a result of densely packed interface transition zone by unhydrated fly ash particles. Finally, high volume fly ash contributed to lowering the composite shrinkage.

However, high volumes of fly ash tend to lower the compressive and tensile strength. By targeting the compressive strength performance similar to typical structural concrete, the designed green ECC mix contained less cement than typical concrete, while delivering robust tensile strain capacity at 2-3% and tensile strength above 4 MPa. The degree of greenness in this high volume fly ash ECC was found to achieve material sustainability indices 50% above those of previous "standardized" version of ECC – M45.

This study demonstrated that sacrifice of high material performance was not inevitable when using low quality substitutions or industrial by-products, as long as the governing micromechanics parameters were carefully controlled. In the present study,

using recycling class F fly ash actually improves many properties of ECC, especially reduced drying shrinkage, tighter crack width and more robust tensile strain ductility. However, the use of fly ash does limit the compressive strength and tensile strength of ECC. Therefore, understanding the underlying micromechanics of critical composite properties is the key to successfully take sustainability into consideration in the design of construction materials.

6.1.3 Self-healing ECC

Crack formation due to loading, shrinkage, thermal deformation is inevitable in reinforced concrete structures. The presence of cracks results in the reduction of structural stiffness, load capacity, water tightness, and durability. Therefore, a concrete material which can recover its mechanical and/or transport properties autogenously without external intervention after damage is highly desirable.

It was found that crack width plays an important role in engaging self-healing behavior. Complete recovery of both mechanical and transport properties subject to wetting and drying cycles were observed when the crack width is below 50 microns. No recovery when the crack width is above 150 microns. Partial recovery when the crack width is in between these limits.

The chemical make-up and the ability to design self-controlled tight crack width below 50 microns makes self-healing prevails in a variety of environmental conditions even when ECC is deliberately damaged by tensioning to several percent strain. In ECCs, the chemical make-up is one of large amount of unhydrated cement grains with expectedly long shelf life. When fly ash is employed, as investigated in conjunction with

added greenness (Chapter 3), a large amount of pozzolan can also be expected. These chemical reservoirs provide the basic ingredients for further hydration and pozzolanic reactions to create self-healed products in cracks in ECC. With high fly ash content, steady state crack width down to 20 μm were attained. The combination of engineered tight crack width, presence of chemical reservoirs, and water and CO_2 in air, was found to be responsible for robust self-healing in ECC.

Several techniques were adopted in this thesis study to quantify the quality of ECC self-healing, including resonant frequency test, uniaxial tensile test, water permeability test, ESEM, and EDX. Self-healing takes place automatically at cracked locations without external intervention. Self-healing in terms of both mechanical and transport properties recovery of pre-damaged composite is revealed in a variety of environmental exposures both at early and later ages. Apart from the work of Li and Chan [1] that uses encapsulated polymer for rehealing, this is the first time that true autogenous healing of a mechanical nature has been revealed. Based on the ESEM and EDX analyses, it is likely that the rehealed product is a mix of calcium carbonate and calcium hydroxide.

Embedding self-healing functionality into ECC to produce a virtually crack free concrete material was demonstrated in this research task. The establishment of self-healing in ECC looks to improve the long term ductility and durability of ECC after cracking, and to establish a much more durable civil engineering material subjected to various environmental conditions.

6.1.4 Impact-resistant ECC

The brittleness of concrete in tension makes reinforced concrete structure vulnerable under extreme loading such as impact and blast. A plausible solution is to embed tensile ductility intrinsically into concrete materials to prevent spalling and fragmentation when concrete structure is subjected to high rate loading. This research resulted in an impact-resistant ECC that shows extreme tensile ductility even at high loading rate.

Although ECC has shown extreme tensile ductility in static loading, the strain capacity tends to reduce with strain rate, e.g. the tensile strain capacity decreases from 3% to 0.5% for ECC mix 45 when the loading rate increases from 10^{-5} s^{-1} to 10^{-1} s^{-1}. It was found that the magnitude and tendency of the rate dependency are dependent on the microstructure and material composition. In the case of ECC M45, the fiber strength σ_f, fiber modulus E_f, matrix toughness J_{tip}, and interface chemical bond G_d of M45 show strong rate dependencies that contribute to the overall diminishing of strain-hardening potential (J'_b/J_{tip} and σ_c/σ_0), and therefore composite tensile strain capacity. It was demonstrated that extreme ductility of ECC could be retained under dynamic loading, when the composite microstructures are properly re-tailored. Five different version of impact resistant ECCs has been developed by eliminating the rate sensitivity of chemical bond and/or increasing the margin of strain-hardening potential. The tensile tests of re-tailored ECC shows tensile strain capacity at 2-7% and tensile strength at 3 to 6 MPa at impact loading rate of 0.1 s^{-1}.

Drop weight impact tests indicate significant improved impact and fragmentation resistance and load and energy absorption capacity of ECC and R/ECC structural elements both on single and multiple impacts. This is attributed to the ultra ductility of

the re-tailored ECC materials that suppress the brittle failure mode normally observed in R/C structures, and therefore elevate the structural load and energy absorption capacity under impact/blast. The multiple cracking observed in both ECC and R/ECC structural elements indicates a larger volume of material involved in energy absorption and improved synergy with steel reinforcement plastic energy dissipation for better impact resistance.

6.2 Impact of Research

A systematic approach of adding functions on top of basic material properties has been developed. This research demonstrates the ability to add new attributes into ECC without losing its basic properties. Although the focus was placed on embedding new functions into Engineered Cementitious Composites while maintaining the tensile ductility, this design approach can be applied to other material systems as well.

The study further completes the ECC theoretical framework, including simulation of steady-state crack propagation, improving the fiber bridging constitutive model, and establishing the rate-dependent strain-hardening criteria. The first part establishes without a doubt that the steady state-cracking criterion is a fundamental principle that must be satisfied for ductilizing brittle matrix composites via multiple cracking. The second part significantly improves the prediction of steady-state crack opening, one of the vital design targets for self-healing. The third part establishes the basis for re-design impact-resistant ECC which shows extreme tensile ductility even when subjected to high rate loading.

Three ECCs with added functions, namely material greenness, self-healing, and impact-resistant, have been developed in this thesis research through the proposed design approach. While these new versions of ECC with added functions are expected to contribute greatly to enhancing the safety, durability, and sustainability of infrastructure built with ECC, the complete solution of these broad challenges is beyond the scope of this thesis.

6.3 Recommendations for Future Research

The ECC micromechanics-based design framework is rather complete except for the deterministic nature of the micromechanics-based analytical model for the composite constitutive law, even though the present model already accounts for fiber uniform randomness. Due to the non-uniform random nature of fiber dispersion and other variability such as intrinsic flaw size distribution in ECC, the stress-strain-crack width relation should incorporate statistical information of these parameters, so that reliability measures of composite ultimate tensile strength and strain capacity and crack width can be adopted for more realistic structural design.

Despite its wider availability, lower cost, and more environmental friendly, the current version of PP-ECC has relatively low tensile strength when compared with PVA-ECC. Although the interfacial bond of the current high tenacity PP fiber is higher than ordinary high tenacity PP, it is still in the lower end of the model-predicted optimized value. It is recommended to increase the interfacial bond by further densifying the interface transition zone (ITZ). Several ways may achieve this goal including lowering

water to binder ratio and incorporating ultra find high reactive pozzolans such as silica fume.

While the free drying shrinkage shows significant reduction when high volumes of fly ash are incorporated, the effect of fly ash in autogenous shrinkage is unknown. Systematic studies of autogenous shrinkage of ECC systems with high fly ash content at early age are needed. Furthermore, a detailed examination of the mechanical properties of the ITZ (e.g. using nano-indentation method) as a function of fly ash content is needed for more effective control of the interface properties.

At the microscale level, the detailed ECC self-healing process and self-healing product need to be examined through ESEM and X-ray diffraction technology. This information will be very useful in terms of ingredients re-selection to further ensure robust self-healing. At the macroscale level, the repeatability of self-healing is still unknown. Also, the laboratory self-healing test was performed in the unloaded state. Given that structures in the field are likely to be in the loaded state, self-healing behavior in the loaded state will need to be evaluated and established. In addition, ECC self-healing under field condition has never been demonstrated and need to be further confirmed both in the loaded and unloaded state.

Impact-resistant ECC shows extreme tensile ductility when subjected to strain rate up to 0.1 s^{-1}. To confirm that this tensile ductility is retained under high rate impact and blast loading, the present test results need to be reconfirmed with experiments conducted at strain rates up to 100 s^{-1}. In addition, structural level test with realistic projectile impact and blast wave loading will be required to ascertain the high speed impact- and blast-resistant performance of such ECC structures. Future development of impact-

/blast-resistant ECC should focus on improving hardness, compressive and tensile strength, and heat resistance on top of tensile ductility at high loading rates.

Table 6.1 – Summary of the three ECCs with newly added functions

Starting Material	Added Function	Metric (quantifiable difference from M-45)	Trade-off if any	Remarks
M-45	Greenness	MSI reduced by 10-50%	Reduction in tensile strength 5-40%	
	Self healing	Recovery in RF = 85-100% Recovery in Transport = 85-95% Recovery in Mechanical = 75-90%		
	Impact resistance	Tensile ductility maintained at 3-6 %, for loading rate up to 0.1 s^{-1}		Higher tensile strength attained

Reference

[1] Li, V.C., Lim, Y.M., and Chan, Y., "Feasibility Study of a Passive Smart Self-healing Cementitious Composite," *Composites Part B*, vol.29B, pp.819-827, 1998